

JOURNAL OF RESEARCH OF THE U.S. GEOLOGICAL SURVEY

JULY-AUGUST 1973
VOLUME 1, NUMBER 4

*Scientific notes and summaries
of investigations in geology,
hydrology, and related fields*



U.S. DEPARTMENT OF THE INTERIOR



UNITED STATES DEPARTMENT OF THE INTERIOR

ROGERS C. B. MORTON, Secretary

GEOLOGICAL SURVEY

V. E. McKelvey, Director

For sale by the Superintendent of Documents, U.S. Government Printing Office, Washington, D.C., 20402. Order by SD Catalog No. JRGS. Annual subscription rate, effective July 1, 1973, \$15.50 (plus \$3.75 for foreign mailing). Single copy \$2.75. Make checks or money orders payable to the Superintendent of Documents.

Send all subscription inquiries and address changes to the Superintendent of Documents at the above address.

Purchase orders should not be sent to the U.S. Geological Survey library.

Library of Congress Card No. 72-600241

The Journal of Research consists of six issues a year (January-February, March-April, May-June, July-August, September-October, November-December) published in Washington, D.C., by the U.S. Geological Survey. It contains papers by members of the Geological Survey on geologic, hydrologic, topographic, and other scientific and technical subjects.

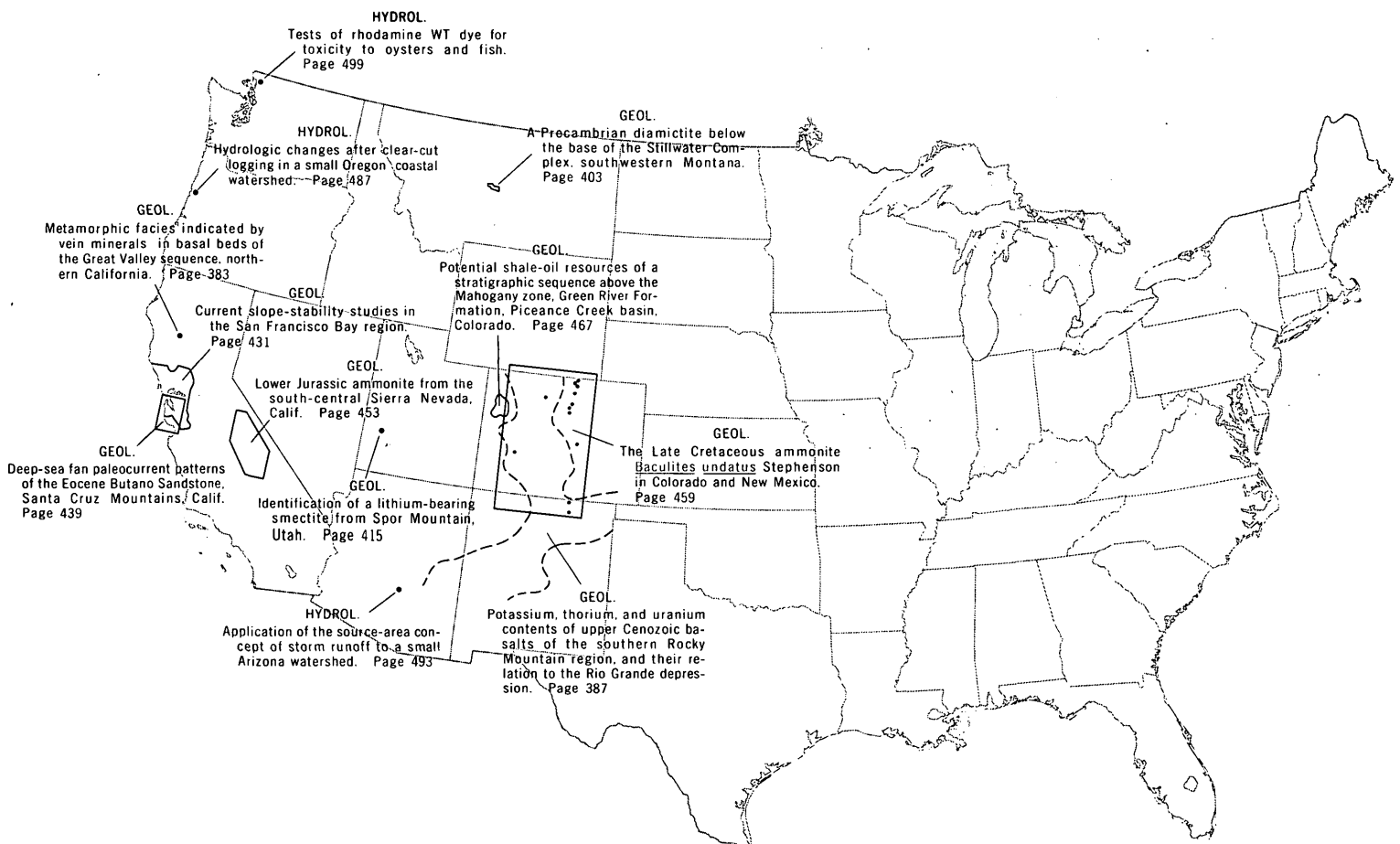
The Journal supersedes the short-papers chapters (B, C, and D) of the former Geological Survey Research ("Annual Review") series of professional papers. The

synopsis chapter (A) of the former Geological Survey Research series will be published as a separate professional paper each year.

Correspondence and inquiries concerning the Journal (other than subscription inquiries and address changes) should be directed to the Managing Editor, Journal of Research, Publications Division, U.S. Geological Survey, Washington, D.C. 20244.

Papers for the Journal should be submitted through regular Division publication channels.

The Secretary of the Interior has determined that the publication of this periodical is necessary in the transaction of the public business required by law of this Department. Use of funds for printing this periodical has been approved by the Director of the Office of Management and Budget through February 11, 1975.



GEOGRAPHIC INDEX TO ARTICLES

[See Contents for articles concerning areas outside the United States and articles without geographic orientation]

JOURNAL OF RESEARCH

of the
U.S. Geological Survey

Vol. 1 No. 4

July-Aug. 1973

CONTENTS

Abbreviations and symbols II

GEOLOGIC STUDIES

Boron-bearing potassium feldspar of authigenic origin in closed-basin deposits . . . <i>R. A. Sheppard and A. J. Cude 3d</i>	377
Metamorphic facies indicated by vein minerals in basal beds of the Great Valley sequence, northern California <i>E. H. Bailey and D. L. Jones</i>	383
Potassium, thorium, and uranium contents of upper Cenozoic basalts of the southern Rocky Mountain region, and their relation to the Rio Grande depression <i>P. W. Lipman, C. M. Bunker, and C. A. Bush</i>	387
A Precambrian diamictite below the base of the Stillwater Complex, southwestern Montana <i>N. J. Page and R. A. Koski</i>	403
Identification of a lithium-bearing smectite from Spor Mountain, Utah <i>H. C. Starkey and Wayne Mountjoy</i>	415
Stream-profile analysis and stream-gradient index <i>J. T. Hack</i>	421
Current slope-stability studies in the San Francisco Bay region <i>T. H. Nilsen and E. E. Brabb</i>	431
Deep-sea fan paleocurrent patterns of the Eocene Butano Sandstone, Santa Cruz Mountains, California <i>T. H. Nilsen and T. R. Simoni, Jr.</i>	439
Lower Jurassic ammonite from the south-central Sierra Nevada, California. <i>D. L. Jones and J. G. Moore</i>	453
The Late Cretaceous ammonite <i>Baculites undatus</i> Stephenson in Colorado and New Mexico <i>W. A. Cobban</i>	459
Potential shale-oil resources of a stratigraphic sequence above the Mahogany zone, Green River Formation, Piceance Creek basin, Colorado <i>J. K. Pitman and J. R. Donnell</i>	467
Spectrochemical computer analysis—Instrumentation <i>A. W. Helz</i>	475
Solubility of cryolite at 25°C and 1 atmosphere pressure <i>C. E. Roberson and J. D. Hem</i>	483

HYDROLOGIC STUDIES

Hydrologic changes after clear-cut logging in a small Oregon coastal watershed <i>D. D. Harris</i>	487
Application of the source-area concept of storm runoff to a small Arizona watershed <i>F. E. Arteaga and S. E. Rantz</i>	493
Tests of rhodamine WT dye for toxicity to oysters and fish <i>G. G. Parker, Jr.</i>	499
Recent publications of the U.S. Geological Survey	Inside of back cover

ABBREVIATIONS

[Singular and plural forms for abbreviations of units of measure are the same]

A	angstrom units	lb	pounds
A ³	cubic angstroms	m	meters
a-c	alternating current	<i>m</i>	molal (concentration)
amp	amperes	m ²	square meters
atm	atmospheres	m ³	cubic meters
bbl	barrels	<i>M</i>	molar (concentration)
B.C.	Before Christ	me	milliequivalents
B.P.	Before Present	MeV	million electron volts
b.y.	billion years	mg	milligrams
c	crystalline state	mgd	million gallons per day
C _x	molal concentration (of substance x)	mi ²	square miles
cal	calories	min	minutes
cfs	cubic feet per second	ml	milliliters
Ci	Curies	mm	millimeters
cm	centimeters	mol	moles
cm ²	square centimeters	mr	milliroentgens
cm ³	cubic centimeters	mV	millivolts
cpm	counts per minute	m.y.	million years
cu ft	cubic feet	μ	microns
cu mi	cubic miles	μm	micrometers
d-c	direct current	μmho	micromhos
emu	electromagnetic units	n	neutrons
eV	electron volts	<i>N</i>	normal
ft	feet	ng	nanograms
ft ³	cubic feet	nm	nanometers
g	grams	Oe	oersteds
gal	gallons	pCi	picocuries
gpd	gallons per day	pH	pH (measure of hydrogen ion activity)
gpm	gallons per minute	ppb	parts per billion
hr	hours	ppm	parts per million
in.	inches	rad	radiometric
kb	kilobars	rpm	revolutions per minute
kg	kilograms	sec	seconds
km	kilometers	sq ft	square feet
km ²	square kilometers	sq mi	square miles
km ³	cubic kilometers	yr	years
kV	kilovolts	v	volts
l	liters	wt	weight

BORON-BEARING POTASSIUM FELDSPAR OF AUTHIGENIC ORIGIN IN CLOSED-BASIN DEPOSITS

By RICHARD A. SHEPPARD and ARTHUR J. GUDE 3d,
Denver, Colo.

Abstract.—Silicic vitric tuffs in saline, alkaline lacustrine deposits are commonly altered to a variety of zeolites and potassium feldspar. The tuffs generally show a lateral gradation, in a basinward direction, of fresh glass to zeolites and then to potassium feldspar. Zeolites were formed early in diagenesis by reaction of the glass with the interstitial water. The feldspar, however, was formed later by reaction of the zeolites with interstitial water, and its formation can be correlated with water of relatively high salinity and alkalinity. Semiquantitative spectrographic analyses for boron in the zeolites and potassium feldspar show that most of the boron resides in the relatively late feldspar. The boron content of the zeolites is commonly less than 100 ppm, whereas the boron content of the potassium feldspar is commonly greater than 1,000 ppm. Boron apparently substitutes for aluminum in the feldspar structure and causes distortion of the monoclinic unit cell such that the *b* and *c* dimensions are shortened. These boron-bearing potassium feldspars having anomalous cell parameters seem unique to saline, alkaline lacustrine deposits and could serve as a prospecting aid for locating buried saline minerals.

Authigenic silicate minerals in silicic vitric tuffs of closed-basin deposits show a consistent distribution pattern (Hay, 1966). In a general way, there is a lateral gradation, basinward, of fresh glass to zeolites and then to potassium feldspar. The authigenic silicate minerals in the tuffs of Pleistocene Lake Tecopa, Inyo County, Calif. (Sheppard and Gude, 1968), are characteristic of this distribution pattern. Fresh glass occurs along the margin and at the inlets of the ancient lake. The glass is succeeded inwardly first by a zone of zeolites and then, in the central part of the lake basin, by potassium feldspar. Zeolites in the Lake Tecopa deposits are chiefly phillipsite, erionite, and clinoptilolite. At Lake Tecopa, the tuffs containing authigenic potassium feldspar also commonly contain searlesite ($\text{NaBSi}_2\text{O}_6 \cdot \text{H}_2\text{O}$).

A variation in the distribution pattern of authigenic silicate minerals in tuffs of closed-basin deposits is illustrated by the Pliocene Big Sandy Formation (Sheppard and Gude, 1972). The Big Sandy Formation consists of lacustrine strata that were deposited in the valley of the Big Sandy River near Wikieup, Mohave County, Ariz. A nonalcalimic zeolite facies occurs along the margin of the ancient lacustrine deposit and is succeeded basinward first by the analcime facies and then by

the potassium feldspar facies. Zeolites in the nonalcalimic zeolite facies are chiefly chabazite, clinoptilolite, erionite, and phillipsite. A similar distribution pattern of authigenic silicate minerals was recognized in the Miocene Barstow Formation of California (Sheppard and Gude, 1969a) and in the Eocene Green River Formation of Wyoming (Surdam and Parker, 1972).

GENESIS OF THE SILICATE MINERALS

The zeolites and potassium feldspar in the originally silicic tuffs formed during diagenesis; the probable paragenetic sequence is shown schematically in figure 1. The silicic glass

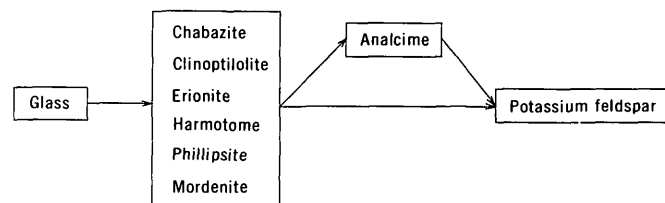


Figure 1.—Schematic representation of the paragenetic sequence that leads to the crystallization of potassium feldspar in tuffs of closed-basin deposits.

reacted with the alkaline and saline interstitial water to form all of the zeolites except analcime. Mariner and Surdam (1970) recently suggested that aluminosilicate gels may be an intermediate stage between the glass and the zeolites. Analcime formed later by the reaction of these relatively early zeolites with the interstitial fluids. The potassium feldspar is the end product of the series of reactions and formed from analcime as well as directly from the other zeolites. The formation of potassium feldspar can be correlated with interstitial water of the highest salinity and pH (Sheppard and Gude, 1969a).

BORON CONTENT OF THE SILICATE MINERALS

While studying the authigenic silicate minerals in tuffs of the Miocene Barstow Formation, Mud Hills, Calif., in 1964, we

Table 1.—Boron, in parts per million, in authigenic zeolites and potassium feldspars from closed-basin deposits

[Number of specimens analyzed is given in parentheses]

Deposit	Boron			
	Zeolites		Potassium feldspar	
	Range	Average	Range	Average
Pleistocene Lake Tecopa, near Shoshone, Inyo County, Calif.	50–200	130 (6)	1,000–2,000	1,700 (3)
Unnamed deposit of Pliocene age, near Rome, Malheur County, Oreg.	0–150	90 (6)	700–1,500	1,050 (4)
Pliocene Big Sandy Formation, near Wikieup, Mohave County, Ariz.	0–150	40 (26)	500–1,500	950 (6)
Miocene Barstow Formation, Mud Hills, San Bernardino County, Calif.	0–150	30 (11)	1,000–5,000	3,400 (9)

discovered that the potassium feldspar contains substantial amounts of boron and is deficient in aluminum (Sheppard and Gude, 1965). The boron substitutes for aluminum in the feldspar structure. Inasmuch as there were insufficient data on the boron contents of zeolites and feldspars, we obtained semiquantitative spectrographic analyses of these minerals from the Barstow Formation and several other closed-basin deposits.

The boron contents of the authigenic zeolites and potassium feldspars from these deposits are shown in table 1. The analyses were performed either on pure separates or on bulk samples of tuff that were monomineralic as determined by X-ray powder diffraction. The average and the range of boron contents are shown for the zeolites and potassium feldspar from each of these closed-basin deposits, which range in age from Pleistocene to Miocene. The boron content of the zeolites is much lower than that of the feldspars. The boron content is commonly less than 100 ppm in the zeolites, whereas it is commonly greater than 1,000 ppm in the feldspar. Although analcime, chabazite, clinoptilolite, erionite, harmotome, mordenite, and phillipsite were analyzed, no consistent difference in the boron content of the different zeolites was found.

DESCRIPTION OF THE POTASSIUM FELDSPAR-RICH TUFFS

The potassium feldspar-rich tuffs are difficult to identify as such in the field because of their fine crystallinity. Commonly, vitroclastic texture in the feldspathic tuffs is poorly preserved in contrast with that of most of the zeolitic tuffs. If the feldspar-rich tuffs are free of opal, quartz, or searlesite, they are generally friable—much more so than their zeolitic counterparts. Tuffs altered chiefly to potassium feldspar are generally white to light gray or locally pastel shades of green or yellow. Nearly monomineralic feldspathic tuffs range in thickness from less than an inch to several feet.

Thin sections of the potassium feldspar-rich tuffs do not reveal much about the character of the feldspar except that it is finely crystalline; most crystals are less than 10 μm in size. We examined feldspathic tuffs from closed-basin deposits that range in age from Quaternary to Eocene and found that all

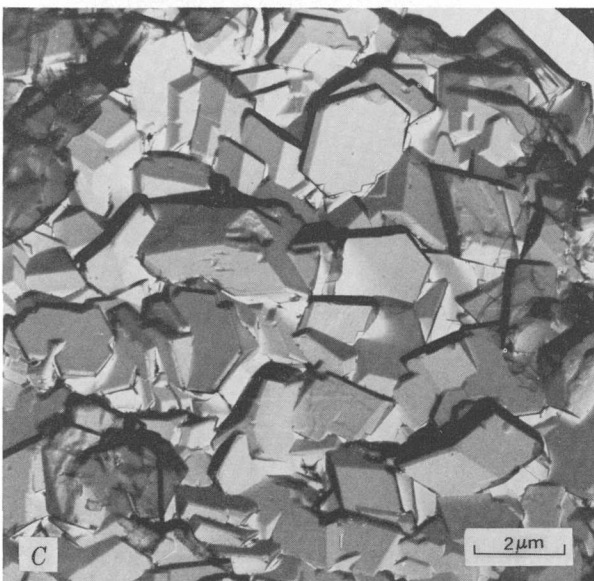
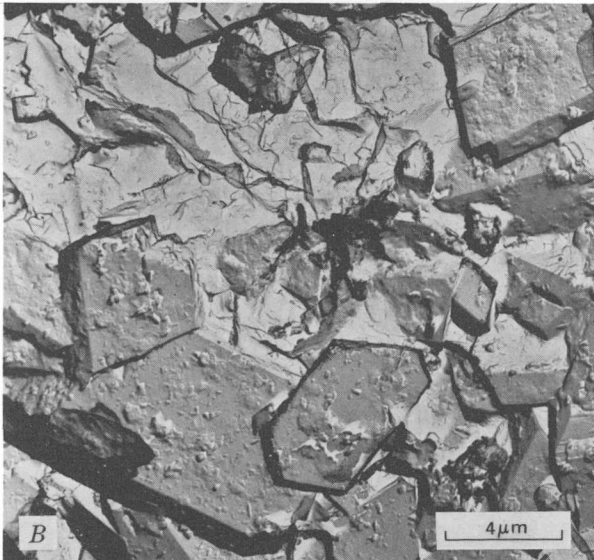
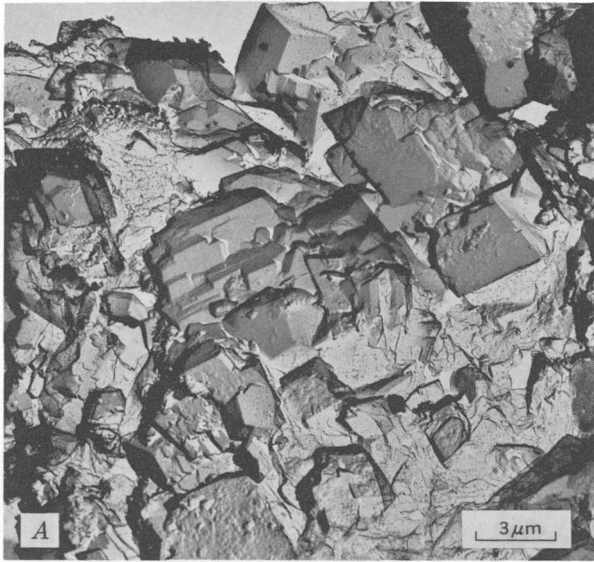
samples have about the same range in crystal size. Optically, the feldspar seems to occur as aggregates of minute anhedral crystals, somewhat resembling chert. Electron microscopy, however, has shown that the feldspar occurs as subhedral to euhedral crystals. The well-developed crystal forms of this authigenic potassium feldspar from three different deposits are shown in figure 2.

Potassium feldspar in the tuffs is most easily identified by X-ray powder diffraction techniques. A typical X-ray diffractometer trace of a bulk sample of monomineralic feldspathic tuff from the Miocene Barstow Formation is shown in figure 3.

CELL DIMENSIONS OF THE FELDSPAR

The boron-bearing authigenic potassium feldspar, first recognized in the Barstow Formation, has a distorted monoclinic unit cell (Sheppard and Gude, 1965). Cell parameters were obtained by a least-squares refinement of X-ray powder diffractometer data of 14 specimens from four deposits by use of the U.S. Geological Survey's FORTRAN IV computer program W9214. The cell parameters and the boron contents of these authigenic potassium feldspars are given in table 2. The cell parameters show the following ranges: $a=8.570$ – 8.611 A, $b=12.957$ – 12.998 A, $c=7.156$ – 7.179 A, $\beta=115^\circ 54.7'$ – $116^\circ 8.9'$, and $V=715.0$ – 721.1 A³.

The b and c dimensions for feldspars from the four closed-basin deposits are plotted in figure 4, the potassic portion of Wright and Stewart's (1968) b - c quadrilateral for alkali feldspars. All these authigenic potassium feldspars plot near the high sanidine corner but well within the quadrilateral. On the basis of the potassic composition of the feldspars as determined by chemical analyses and inferred from the indices of refraction, the feldspars would be expected to plot along the maximum microcline–high sanidine sideline. Inasmuch as the authigenic feldspars are monoclinic, they would be expected to plot at the high sanidine corner. Thus, the feldspars have an anomalous unit cell, and b is shortened by as much as about 0.07 A and c is shortened by as much as about 0.02 A. The a dimension is not plotted in figure 4; however, a is consistent with the potassic composition of the feldspar. Another measure of the distortion of the monoclinic unit cell is shown by the a dimension inferred from the b - c plot. The



measured a dimension is about 8.57–8.61 Å, but the inferred a dimension is about 8.32–8.40 Å.

Two possible explanations for the distortion are: (1) Inasmuch as the feldspar formed from zeolites, some relict structure may have been inherited from the zeolites, or (2) the substitution of boron for aluminum in the framework may have distorted the feldspar structure. Martin (1971) confirmed the second possibility. On the basis of cation exchange and heating experiments on natural specimens from Lake Tecopa and the Barstow Formation, as well as the synthesis of a series of boron-bearing potassium feldspars, Martin concluded that substitution of relatively small amounts of boron for aluminum in the authigenic feldspar causes appreciable distortion of the unit cell. Eugster and McIver (1959) had previously synthesized a potassium feldspar having boron completely replacing aluminum.

POTENTIAL PROSPECTING GUIDE TO SALINE DEPOSITS

Localities where similar authigenic potassium feldspars have been found in tuffs of lacustrine deposits of the Western United States are shown in figure 5. The deposits range in age from Pleistocene to Eocene, and many contain bedded saline minerals of economic interest such as borax, colemanite, halite, nahcolite, and trona, or molds of saline minerals. A careful search at those deposits where saline minerals have not been reported may also reveal saline minerals or their molds.

With respect to authigenic zeolites and potassium feldspar, boron resides chiefly in the relatively late feldspar. The boron apparently remains in the interstitial fluid in the tuff and eventually enters the feldspar structure, causing distortion of the unit cell. This boron-bearing potassium feldspar seems unique to saline lacustrine deposits. Thus, the recognition of this distinctive authigenic feldspar in lacustrine deposits may be useful as a prospecting guide for the location of buried saline minerals.

Figure 2.—Electron micrographs of authigenic potassium feldspar in tuffs. *A*, Pleistocene Lake Tecopa deposit, California. *B*, Pliocene Big Sandy Formation, Arizona. *C*, Miocene Barstow Formation, California. Electron micrographs by Paul D. Blackmon.

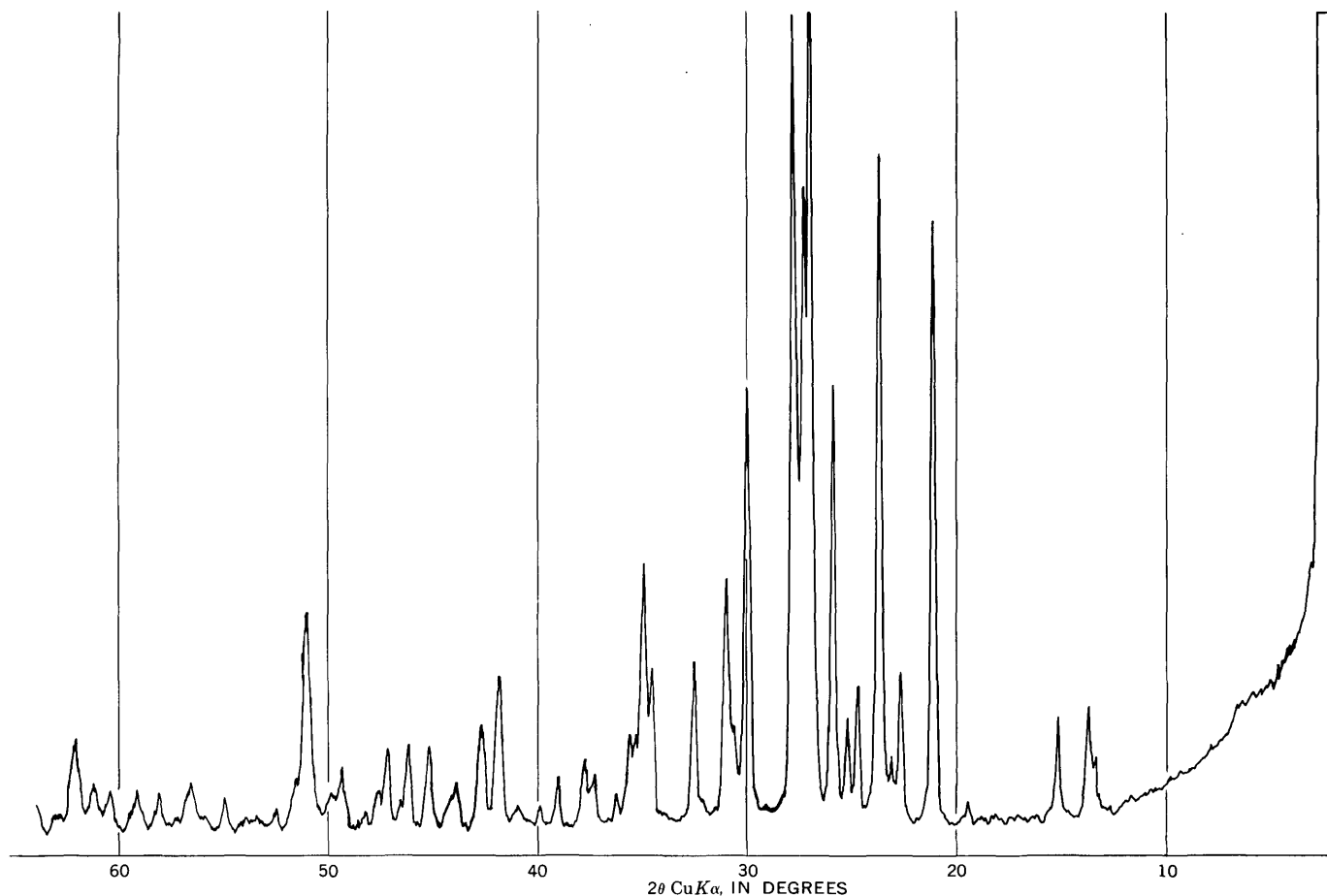


Figure 3.—X-ray diffractometer trace of authigenic potassium feldspar from a tuff in the Barstow Formation of California.

Table 2.—Unit cell parameters and boron contents of authigenic potassium feldspars from closed-basin deposits

[Cell parameters were obtained by a least-squares refinement of X-ray diffractometer data, by use of the U.S. Geological Survey's FORTRAN IV computer program W9214. The boron content was determined by semiquantitative spectrographic analysis by L. A. Bradley, W. B. Crandel, J. C. Hamilton, B. W. Lanthorn, Harriet Neiman, and Barbara Tobin]

Deposit	Sample	<i>a</i> (Å)	<i>b</i> (Å)	<i>c</i> (Å)	β	<i>V</i> (Å ³)	Boron content (ppm)
Pleistocene Lake Tecopa, near Shoshone, Inyo County, Calif.	1	8.583±0.003	12.969±0.003	7.169±0.002	115°59.9'±2.0'	718.2±0.3	2,000
	2	8.576±0.004	12.990±0.006	7.169±0.002	116°5.3'±2.6'	717.3±0.5	1,000
Unnamed deposit of Pliocene age, near Rome, Malheur County, Oreg.	3	8.604±0.005	12.983±0.004	7.175±0.002	116°6.7'±2.2'	719.8±0.4	1,000
	4	8.601±0.010	12.988±0.010	7.174±0.005	116°2.0'±5.6'	720.1±1.0	1,000
Pliocene Big Sandy Formation, near Wikieup, Mohave County, Ariz.	5	8.589±0.003	12.976±0.003	7.164±0.001	115°59.2'±1.2'	717.7±0.2	1,000
	6	8.583±0.004	12.974±0.003	7.167±0.002	116°0.6'±1.8'	717.2±0.3	1,000
	7	8.578±0.004	12.986±0.004	7.170±0.003	116°3.2'±1.4'	717.6±0.3	500
	8	8.589±0.002	12.984±0.002	7.169±0.002	115°59.3'±1.4'	718.6±0.2	1,500
	9	8.589±0.002	12.982±0.002	7.168±0.002	115°55.7'±1.0'	718.8±0.2	700
	10	8.573±0.003	12.966±0.006	7.167±0.002	116°1.4'±1.1'	715.9±0.3'	1,000
Miocene Barstow Formation, Mud Hills, San Bernardino County, Calif.	11	8.593±0.002	12.967±0.003	7.165±0.001	116°3.3'±1.0'	717.2±0.2	1,500
	12	8.582±0.004	12.962±0.005	7.158±0.002	116°2.3'±2.5'	715.4±0.4	2,000
	13	8.592±0.003	12.976±0.005	7.164±0.003	116°0.4'±1.6'	717.8±0.3	5,000
	14	8.590±0.003	12.986±0.004	7.171±0.003	116°0.9'±1.7'	718.9±0.3	2,000

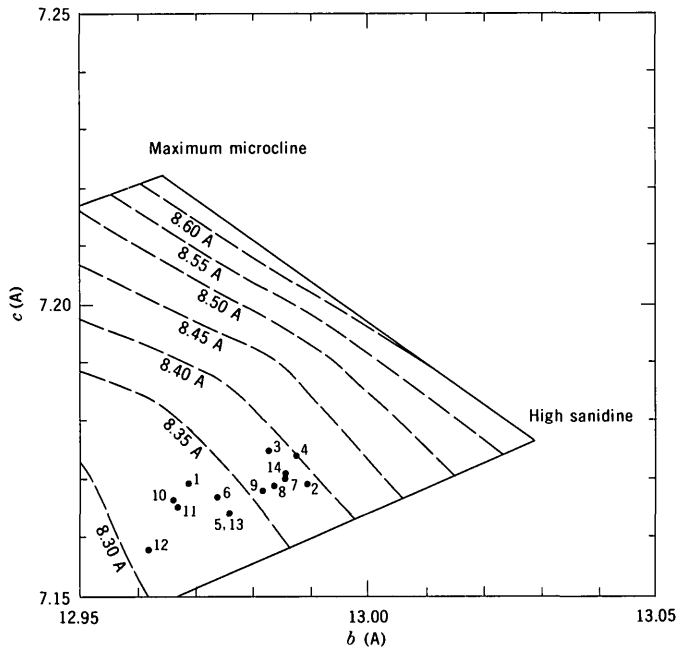


Figure 4.—Potassium-rich portion of Wright and Stewart's (1968) *b-c* quadrilateral for alkali feldspars which has been contoured for *a* (dashed). The *b-c* dimensions are plotted for the 14 specimens given in table 2.



Figure 5.—Map showing occurrences of authigenic potassium feldspar in tuffs of lacustrine deposits. Closed circle, potassium feldspar associated with saline minerals or their molds; open circle, potassium feldspar not associated with saline minerals or their molds. Data for numbered localities are as follows:

1. Unnamed deposit of Pliocene age, near Durkee, Baker County, Oreg. (Sheppard and Gude, unpub. data).

Figure 5—Continued

2. Danforth Formation of Pliocene age, Harney Lake, Harney County, Oreg. (Walker and Swanson, 1968).
3. Unnamed deposit of Pliocene age, near Rome, Malheur County, Oreg. (Sheppard and Gude, 1969b).
4. Unnamed deposit of Pliocene age, Jersey Valley, Pershing County, Nev. (Sheppard and Gude, unpub. data).
5. Horse Camp Formation of Miocene to Pliocene age, near Currant, Nye County, Nev. (Moore, 1968).
6. Unnamed deposit of Pliocene age, Silver Peak Range, Esmeralda County, Nev. (Robinson, 1966).
7. Unnamed deposit of Pleistocene Lake Tecopa, near Shoshone, Inyo County, Calif. (Sheppard and Gude, 1968).
8. Mixed layer of Pleistocene Searles Lake, San Bernardino County, Calif. (Hay and Moiola, 1963; Smith and Haines, 1964).
9. Unnamed deposit of Miocene age, near Kramer, San Bernardino County, Calif. (Hay, 1966).
10. Barstow Formation of Miocene age, Mud Hills, San Bernardino County, Calif. (Sheppard and Gude, 1969a).
11. Big Sandy Formation of Pliocene age, near Wikieup, Mohave County, Ariz. (Sheppard and Gude, 1972).
12. Unnamed deposit of Eocene age, Lysite Mountain, Hot Springs County, Wyo. (Bay, 1969).
13. Wagon Bed Formation of Eocene age, Beaver Rim, Fremont County, Wyo. (Boles, 1968).
14. Green River Formation of Eocene age, near Green River, Sweetwater County, Wyo. (Iijima and Hay, 1968; Surdam and Parker, 1972).
15. Green River Formation of Eocene age, Piceance Creek basin, Rio Blanco County, Colo. (Hite and Dyni, 1967; Brobst and Tucker, 1973).

REFERENCES CITED

- Bay, K. W., 1969, Stratigraphy of Eocene sedimentary rocks in the Lysite Mountain area, Hot Springs, Fremont, and Washakie Counties, Wyoming: Wyoming Univ., unpub. Ph. D. thesis, 181 p.
- Boles, J. R., 1968, Zeolites and authigenic feldspar along a part of the Beaver Rim, Fremont County, Wyoming: Wyoming Univ., unpub. M.S. thesis, 64 p.
- Brobst, D. A., and Tucker, J. D., 1973, X-ray mineralogy of the Parachute Creek Member, Green River Formation, in the northern Piceance Creek basin, Colorado: U.S. Geol. Survey Prof. Paper 803 (In press).
- Eugster, H. P., and McIver, N. L., 1959, Boron analogues of alkali feldspars and related silicates [abs.]: Geol. Soc. America Bull., v. 70, no. 12, pt. 2, p. 1598–1599.
- Hay, R. L., 1966, Zeolites and zeolitic reactions in sedimentary rocks: Geol. Soc. America Spec. Paper 85, 130 p.
- Hay, R. L., and Moiola, R. J., 1963, Authigenic silicate minerals in Searles Lake, California: Sedimentology, v. 2, no. 4, p. 312–332.
- Hite, R. J., and Dyni, J. R., 1967, Potential resources of dawsonite and nahcolite in the Piceance Creek basin, northwest Colorado: Colorado School Mines Quart., v. 62, no. 3, p. 25–38.
- Iijima, Azuma, and Hay, R. L., 1968, Analcime composition in tuffs of the Green River Formation of Wyoming: Am. Mineralogist, v. 53, nos. 1–2, p. 184–200.
- Mariner, R. H., and Surdam, R. C., 1970, Alkalinity and formation of zeolites in saline alkaline lakes: Science, v. 170, no. 3961, p. 977–980.
- Martin, R. F., 1971, Disordered authigenic feldspars of the series $KAlSi_3O_8$ - $KBSi_3O_8$ from southern California: Am. Mineralogist, v. 56, nos. 1–2, p. 281–291.

- Moore, E. M., 1968, Mio-Pliocene sediments, gravity slides, and their tectonic significance, east-central Nevada: *Jour. Geology*, v. 76, no. 1, p. 88–98.
- Robinson, P. T., 1966, Zeolitic diagenesis of Mio-Pliocene rocks of the Silver Peak Range, Esmeralda County, Nevada: *Jour. Sed. Petrology*, v. 36, no. 4, p. 1007–1015.
- Sheppard, R. A., and Gude, A. J., 3d, 1965, Potash feldspar of possible economic value in the Barstow Formation, San Bernardino County, California: *U.S. Geol. Survey Circ.* 500, 7 p.
- 1968, Distribution and genesis of authigenic silicate minerals in tuffs of Pleistocene Lake Tecopa, Inyo County, California: *U.S. Geol. Survey Prof. Paper* 597, 38 p.
- 1969a, Diagenesis of tuffs in the Barstow Formation, Mud Hills, San Bernardino County, California: *U.S. Geol. Survey Prof. Paper* 634, 35 p.
- 1969b, Authigenic fluorite in Pliocene lacustrine rocks near Rome, Malheur County, Oregon, in *Geological Survey Research* 1969: *U.S. Geol. Survey Prof. Paper* 650-D, p. D69–D74.
- 1972, Big Sandy Formation near Wikieup, Mohave County, Arizona: *U.S. Geol. Survey Bull.* 1354-C, 10 p.
- Smith, G. I., and Haines, D. V., 1964, Character and distribution of nonclastic minerals in the Searles Lake evaporite deposit, California: *U.S. Geol. Survey Bull.* 1181-P, 58 p.
- Surdam, R. C., and Parker, R. D., 1972, Authigenic aluminosilicate minerals in the tuffaceous rocks of the Green River Formation, Wyoming: *Geol. Soc. America Bull.*, v. 83, no. 3, p. 689–700.
- Walker, G. W., and Swanson, D. A., 1968, Summary report on the geology and mineral resources of the Harney Lake and Malheur Lake areas of the Malheur National Wildlife Refuge, north-central Harney County, Oregon: *U.S. Geol. Survey Bull.* 1260-L, 17 p.
- Wright, T. L., and Stewart, D. B., 1968, X-ray and optical study of alkali feldspar—[Pt.] I. Determination of composition and structural state from refined unit-cell parameters and $2V$: *Am. Mineralogist*, v. 53, nos. 1–2, p. 38–87.



METAMORPHIC FACIES INDICATED BY VEIN MINERALS IN BASAL BEDS OF THE GREAT VALLEY SEQUENCE, NORTHERN CALIFORNIA

By EDGAR H. BAILEY and DAVID L. JONES, Menlo Park, Calif.

Abstract.—A reexamination of reported blueschist mineral localities in the basal strata of the Great Valley sequence revealed only prehnite-pumpellyite facies minerals. Franciscan graywacke thrust below the Great Valley rocks contains lawsonite-quartz blueschist assemblages. At a common pressure of about 4 kb, the Franciscan blueschists formed at lower temperatures than the overlying Great Valley prehnite-bearing rocks, lending support to tectonic models that involve rapid subduction of the Franciscan rocks.

The Great Valley sequence in California consists of a conformable section of about 50,000 feet (15,000 m) of marine sedimentary rock of Late Jurassic and Cretaceous age deposited on an ophiolite sequence having basalt, or locally keratophyre, in its upper part, gabbro below, and serpentinized ultramafic rocks at the base (Bailey and others, 1970). Beneath the serpentinite lies the Coast Range thrust, a late Mesozoic subduction zone along which eugeosynclinal Franciscan rocks have been thrust under the Great Valley rocks. The Franciscan rocks beneath the Coast Range thrust are converted to blueschist metamorphic assemblages in which lawsonite, jadeite, glaucophane, and aragonite are key minerals (Blake and others, 1967). In contrast, the Great Valley rocks above the Coast Range thrust typically are altered only to zeolite, or locally prehnite-pumpellyite facies (Bailey and Blake, 1969; Dickinson and others, 1969). The Franciscan blueschists are believed to require temperatures of 150°–300°C and pressure of about 5 kb or more for their formation (Taylor and Coleman, 1968; Ernst and others, 1970), whereas the formation of zeolite (laumontite) or prehnite-pumpellyite facies of the Great Valley rocks are generally believed to be indicative of slightly lower temperatures and significantly less pressure (Crawford and Fyfe, 1965; Fyfe, 1970; Coombs and others, 1970). Thus, the difference in metamorphic facies across the Coast Range thrust, particularly as it has been interpreted to indicate major pressure difference, is striking (Bailey and Blake, 1969; Ernst, 1971a).

In one area, veins containing the key blueschist minerals lawsonite and aragonite have been reported from the basal sedimentary rocks of the Great Valley sequence above the Coast Range thrust (McKee, 1965). As the pressure-temperature significance of the metamorphic mineral assem-

blages became better known, their occurrence in an environment that had not been subjected to shearing or metamorphic pressures other than those resulting from the load of 50,000 feet (15,000 m) of overlying sediments seemed anomalous. To reevaluate this apparently unique find, we obtained through the generous cooperation of Bates McKee, University of Washington, one of his original thin sections and locality data that permitted us to reexamine these blueschist mineral occurrences.

The chief localities are near the north end of the Sacramento Valley about 5 miles northwest of Paskenta in two canyons at the west edges of secs. 23 and 26, T. 24 N., R. 7 W., Mount Diablo base line (fig. 1). In both canyons graywacke and shale of the Great Valley sequence lie on basaltic breccia and contain mafic and ultramafic clasts. Small discontinuous veins and veinlets are conspicuous in the sedimentary rocks within tens of meters of the contact. Most veins are chiefly quartz, although carbonate veins also are common. Rarer albite and albite-quartz veins traverse the sedimentary strata. Prehnite forms crystals several millimeters long in some quartz-calcite veins, and larger barite crystals occur in coarsely crystalline

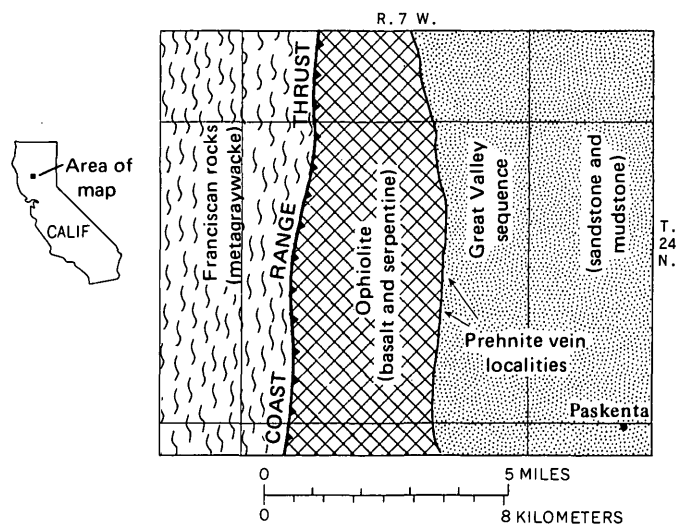


Figure 1.—Sketch map showing location of prehnite-quartz veins.

calcite veins. Both prehnite and barite were confirmed by X-ray, spectroscopic, and optical examination. No lawsonite was found, but as seen in both specimens and thin sections, the blades of prehnite might be easily mistaken for tablets of lawsonite (fig. 2). Some of the carbonate mineral shows a little separation of isogyres in optic axial interference figures, but all specimens we checked by X-ray proved to be calcite, not aragonite. Three miles farther south along Thomes Creek, indurated mudstone near the same contact contains abundant veins of laumontite.

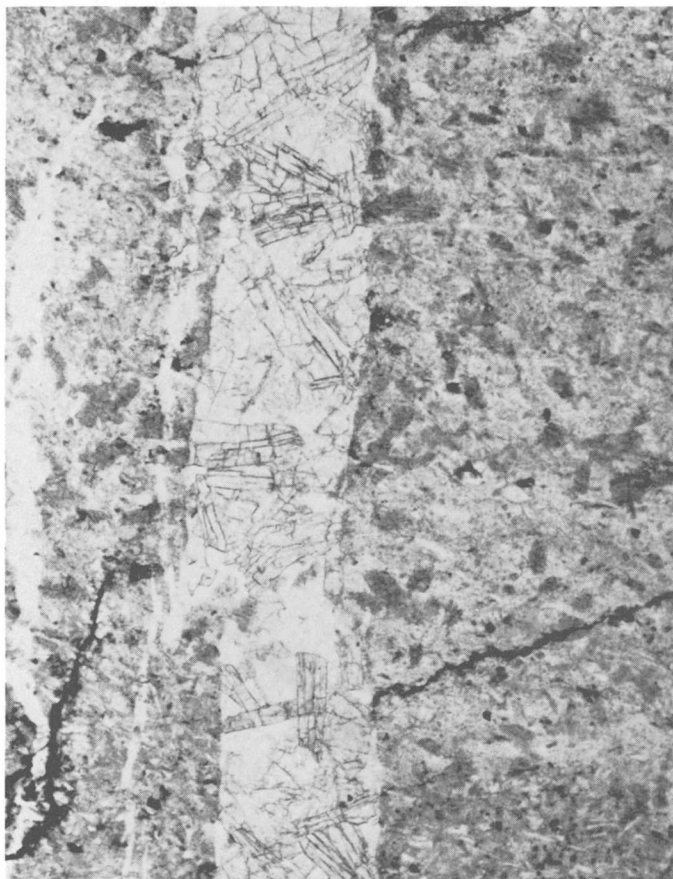


Figure 2.—Prehnite-quartz vein in metagraywacke of the Great Valley sequence. Width of vein is ½ mm.

The mineral assemblages of the veinlets in these sedimentary rocks clearly are representative of conditions under which the Great Valley strata have been altered. Where we found quartz-prehnite veins, the host graywackes also contained prehnite, and where albite veins occur, the feldspar clasts are albitized. We know of no other alleged occurrences of blueschist minerals above the Coast Range thrust in the basal sedimentary rocks of the Great Valley sequence. Until such an occurrence can be documented, the metamorphic facies above the thrust should be regarded as of no higher grade than prehnite-pumpellyite. Veins in the basalts of the ophiolite

immediately below the sedimentary rocks of the Great Valley sequence also locally contain quartz, prehnite, pumpellyite, thomsonite, and epidote, but one cannot be certain that they did not form prior to the deposition of the sedimentary strata under different pressure-temperature conditions. Certainly some epidote formed earlier, as it occurs as detrital grains in the lowest beds of the Great Valley sequence.

The Franciscan metagraywackes below these Great Valley sequence localities contain a lawsonite-plus-quartz mineral assemblage (Blake and others, 1967). The experimental work of Liou (1971) on the stability field of prehnite indicates that at 4 kb fluid pressure, prehnite and quartz are stable between 300° and 400°C, and at the same pressure lawsonite plus quartz is stable at temperatures below 300°C. The presence of the lower temperature assemblage in the Franciscan plate below the Coast Range thrust doubtless is the result of rapid subduction of colder Franciscan rocks beneath the warmer Great Valley sequence (fig. 3), and lends support to the tectonic models of Bailey and Blake (1969), Hamilton (1969), and Ernst (1970). However, where jadeite plus quartz occurs directly beneath rock of the prehnite-pumpellyite-bearing Great Valley sequence rocks, a metamorphic pressure discontinuity seems to exist (Ernst, 1971b).

REFERENCES CITED

- Bailey, E. H., and Blake, M. C., 1969, Tectonic development of western California during the late Mesozoic: *Geotektonika*, pt. 3, p. 17–30; pt. 4, p. 24–34.
- Bailey, E. H., Blake, M. C., Jr., and Jones, D. L., 1970, On-land Mesozoic oceanic crust in California Coast Ranges, in *Geological Survey Research 1970*: U.S. Geol. Survey Prof. Paper 700-C, p. C70–C81.
- Blake, M. C., Jr., Irwin, W. P., and Coleman, R. G., 1967, Upside-down metamorphic zonation, blueschist facies, along a regional thrust in California and Oregon, in *Geological Survey Research 1967*: U.S. Geol. Survey Prof. Paper 575-C, p. C1–C9.
- Coombs, D. S., Horodyski, R. J., and Naylor, R. S., 1970, Occurrence of prehnite-pumpellyite facies metamorphism in northern Maine: *Am. Jour. Sci.*, v. 268, p. 142–156.
- Crawford, W. A., and Fyfe, W. S., 1965, Lawsonite equilibria: *Am. Jour. Sci.* v. 263, p. 262–270.
- Dickinson, W. R., Ojakangas, R. W., and Stewart, R. J., 1969, Burial metamorphism of the late Mesozoic Great Valley sequence, Cache Creek, California: *Geol. Soc. America Bull.*, v. 80, p. 519–526.
- Ernst, W. G., 1970, Tectonic contact between the Franciscan mélange and the Great Valley sequence—crustal expression of late Mesozoic Benioff zone: *Jour. Geophys. Research*, v. 75, no. 5, p. 886–901.
- 1971a, Metamorphic zonations on presumably subducted lithospheric plates from Japan, California, and the Alps: *Contr. Mineralogy and Petrology*, v. 34, p. 43–59.
- 1971b, Do mineral parageneses reflect unusually high-pressure conditions of Franciscan metamorphism?: *Am. Jour. Sci.*, v. 270, p. 81–108.
- Ernst, W. G., Seki, Y., Onuki, H., and Gilbert, M. C., 1970, Comparative study of low-grade metamorphism in the California Coast Ranges and the outer metamorphic belt of Japan: *Geol. Soc. America Mem.* 124, 276 p.

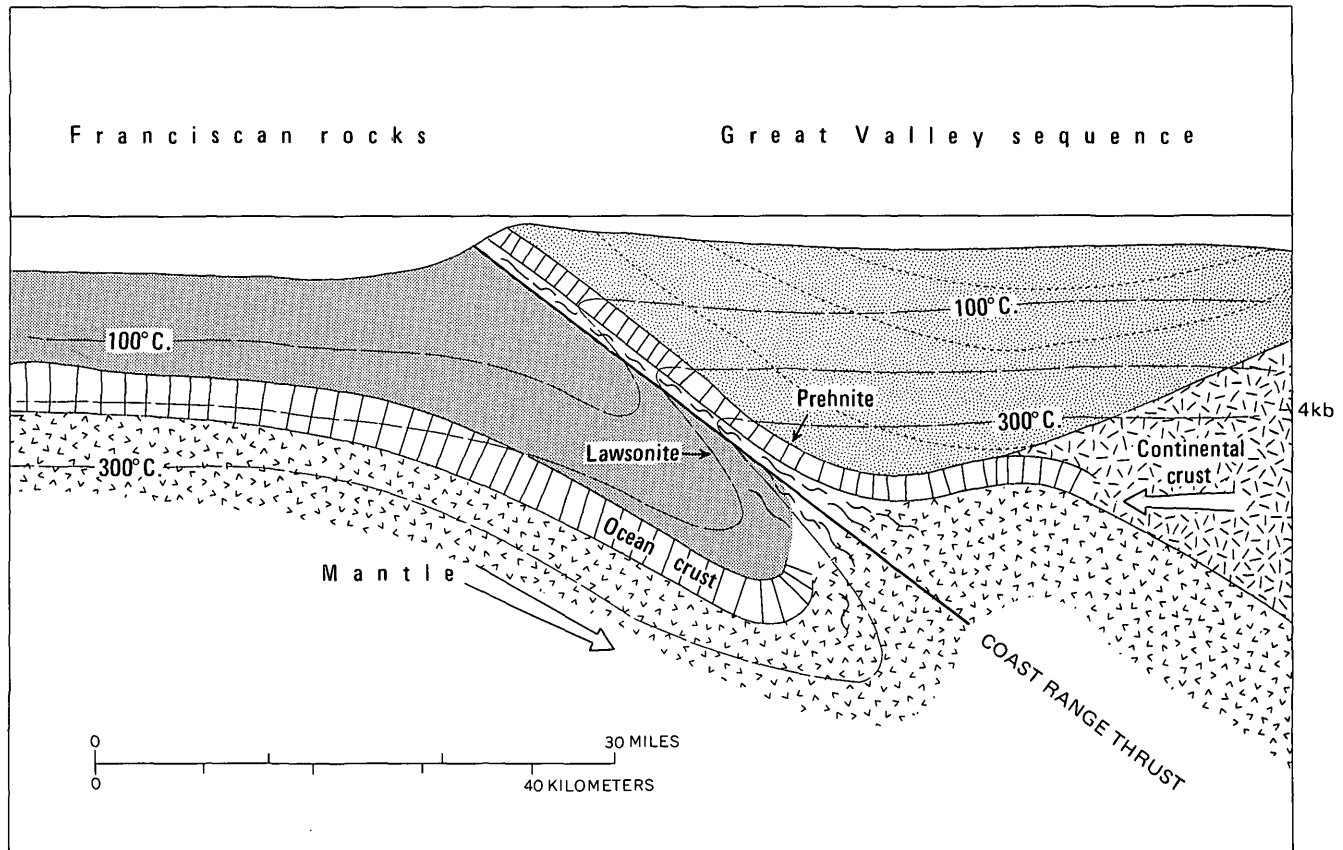


Figure 3.—Schematic section showing the Coast Range thrust subduction zone and Franciscan rocks plunging beneath rocks of the Great Valley sequence. Complex internal deformation of Franciscan rocks is not shown. Rapid underthrusting results in depression of isotherms beneath the subduction zone. At the 4-kb pressure level, prehnite developed in the rocks of the upper plate while lawsonite developed in the colder Franciscan rocks beneath the Coast Range thrust.

- Fyfe, W. S., 1970, Phase changes in the earth's crust—the record of crustal geophysics: *Sci. Progress*, v. 58, p. 47–70.
 Hamilton, Warren, 1969, Mesozoic California and the underflow of Pacific Mantle: *Geol. Soc. America Bull.*, v. 80, p. 2409–2430.
 Liou, J. G., 1971, Synthesis and stability relations of prehnite, $\text{Ca}_2\text{Al}_2\text{Si}_3\text{O}_{10}(\text{OH})_2$: *Am. Mineralogist*, v. 56, p. 507–531.

- McKee, Bates, 1965, Knoxville-Franciscan contact near Paskenta, western Sacramento Valley, California: *Geol. Soc. America Spec. Paper* 87, p. 215–216.
 Taylor, H. P., and Coleman, R. G., 1968, $\text{O}^{18}/\text{O}^{16}$ ratios of coexisting minerals in glaucophane-bearing metamorphic rocks: *Geol. Soc. America Bull.*, v. 79, p. 1727–1756.



POTASSIUM, THORIUM, AND URANIUM CONTENTS OF UPPER CENOZOIC BASALTS OF THE SOUTHERN ROCKY MOUNTAIN REGION, AND THEIR RELATION TO THE RIO GRANDE DEPRESSION

By PETER W. LIPMAN, CARL M. BUNKER,
and CHARLES A. BUSH, Denver, Colo.

Abstract.—Late Cenozoic basaltic volcanism in southern Colorado and northern New Mexico was most intense near the Rio Grande rift depression but extended onto stable platforms to the west (Colorado Plateau) and to the east (High Plains). Tholeiitic rocks are largely confined to the Rio Grande depression, and the basalts become increasingly alkalic with distance from the depression. The K, Th, and U contents and the Th/K and U/K ratios consistently increase away from the depression, and Th/U ratios also tend to increase slightly. Geographically distinct suites of petrographically related basalts that are very similar in major-oxide compositions are readily distinguishable by K, Th, and U contents. Sialic crustal contamination did not contribute significantly to development of these compositional variations, and the lateral change from tholeiitic to alkalic basaltic volcanism may be related to different depths of or degrees of partial melting in the mantle. The compositions and compositional ranges of basalts in the southern Rocky Mountain region are similar to those of many Pacific islands, despite the contrasting geologic settings.

querque basin is a similar asymmetrical graben with its axis shifted en echelon to the west. South of Socorro, the Rio Grande depression merges with the Basin and Range province and is a less pronounced structure than to the north.

Previous reconnaissance studies have suggested that upper Cenozoic basaltic rocks in the southern Rocky Mountain region vary in petrology with distance from the Rio Grande depression (Lipman, 1969; Kudo and others, 1971). In general, basalt and basaltic andesite of alkalic affinities are thought to have erupted east and west of the depression concurrently with its formation, whereas tholeiitic basalt flooded parts of the depression late in its history. We here report additional chemical data on 170 samples (see table 2 at end of article), mainly K, Th, and U concentrations determined by gamma-ray spectrometry, that demonstrate more precisely some aspects of these petrologic variations.

ANALYTICAL TECHNIQUES

Basaltic volcanism and extensional block faulting have been the dominant volcano-tectonic association in the Western United States over much of late Cenozoic time (Christiansen and Lipman, 1972). In much of this region, extensional faulting occurred across a broad zone, as in the Basin and Range province, but in the southern Rocky Mountains the Rio Grande depression (Bryan, 1938; Kelley, 1952, 1956; Chapin, 1971) forms a well-defined rift valley that separates the stable platforms of the Colorado Plateau and the High Plains in its central part and extends northward at least as far as central Colorado (fig. 1).

In Colorado and northern New Mexico, the San Luis Valley segment of the Rio Grande depression is a complexly faulted graben containing as much as 8 km of sedimentary fill, as indicated by gravity data (Gaca and Karig, 1966). The major bounding fault system is on the east side of the graben against the Sangre de Cristo Mountains, and the west boundary is a dip slope of eastward-tilted volcanic rocks of the San Juan Mountains. From Sante Fe to Socorro, N. Mex., the Albu-

Samples weighing at least 4–5 kg were collected by sledge hammer, trimmed of all weathered surfaces, and crushed to -30 mesh. So far as possible, porous vesicular parts of flows were avoided in sampling. Samples were sealed in an aluminum container consisting of a double-walled cylinder closed on one end. A 2.5-cm-thick layer of sample is contained between the annuli and within the closed end; this amount of material weighs 3,000–5,000 g, depending on the bulk density of the powdered rock. The sample container is placed on and around a 12.5-cm-diameter by 10-cm-thick sodium iodide crystal. The radiation penetrating the crystal is sorted by the spectrometer system and stored in a 100-channel memory. The spectra were interpreted with the aid of a linear least-squares computer method which matches the spectrum from a sample to a library of radioelement standards and calculates the concentrations of the radioelement in the sample; the computer method is a modification of a program written by Schonfeld (1966). The spectrometer data are calibrated to U and Th

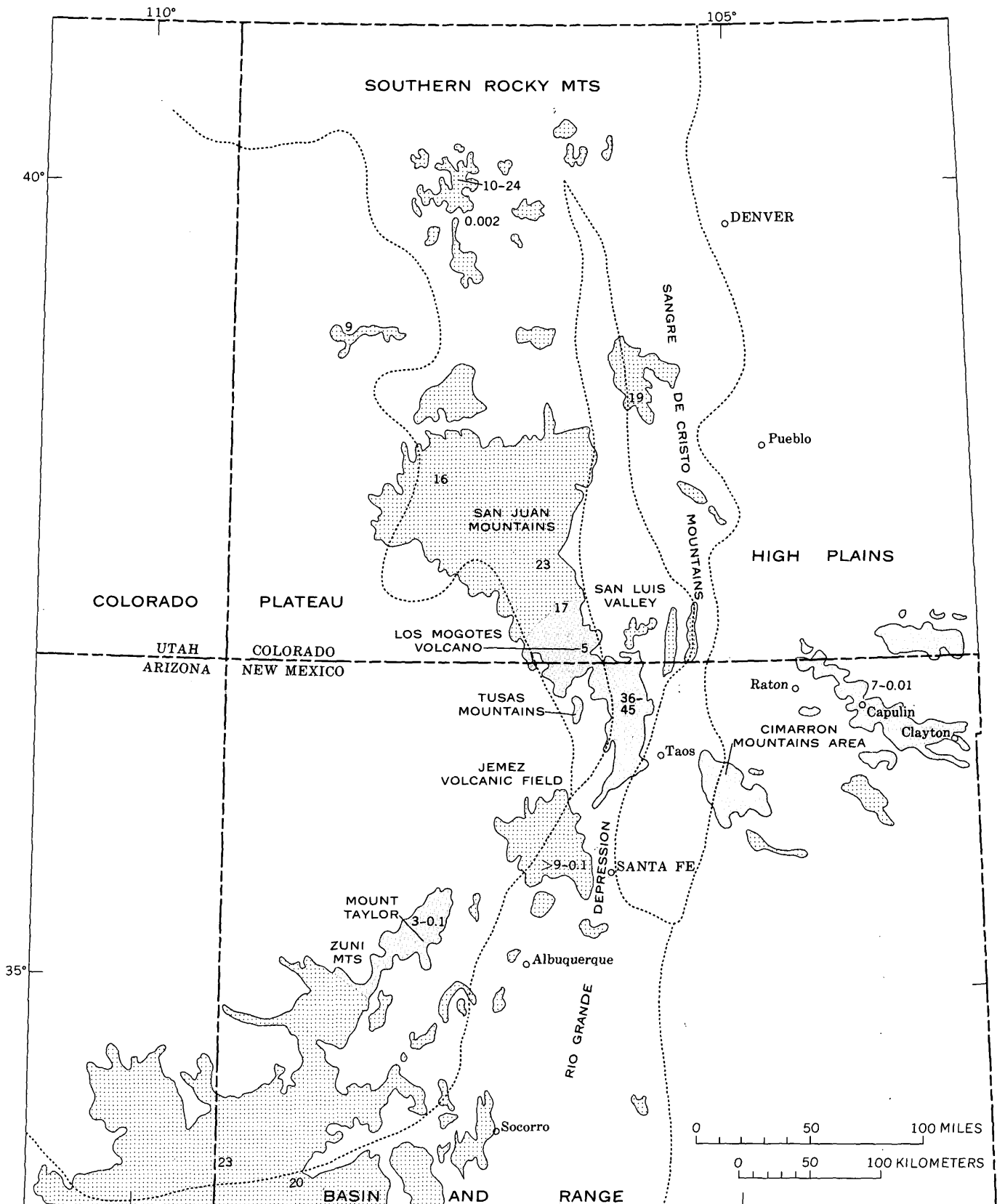


Figure 1.—Index map of the southern Rocky Mountain region, showing general distribution of upper Cenozoic volcanic rocks (coarse pattern; modified from Cohee, 1961), major structural provinces (Kelley, 1952), and areas discussed in this report (fine pattern). Numbers indicate K-Ar ages, in millions of years, of upper Cenozoic basaltic rocks; these are taken from references cited in text.

standards measured by isotope dilution and mass or alpha spectrometry in a group of rocks.

Uranium concentrations are determined indirectly by measuring the radium daughters to obtain radium-equivalent uranium (RaeU) values. Radium-equivalent uranium is the amount of uranium, under the assumption of radioactive equilibrium, required to support the amount of daughter products that emit the radioactivity measured in a sample; disequilibrium in unaltered mafic igneous rocks is unlikely to exceed 5–10 percent. Throughout the report where “U” and “uranium” are used, “radium-equivalent uranium” is implicit. Although thorium is also measured from daughter products, disequilibrium is improbable because of short half-lives, and the concentrations are considered to be a direct measurement of parent thorium. Potassium is determined from its K^{40} constituent which is proportional to total potassium. The coefficients of variation for the accuracy of the data included in this report, when compared to samples analyzed by isotope-dilution techniques, are about 5 percent for U and Th and about 3 percent for K. At low concentrations these percentages are in addition to minimum standard deviations of about 0.01 ppm U, 0.02 ppm Th, and 0.01 percent K.

Acknowledgments.—We thank Robert J. Kirkpatrick for assistance in collecting the basalt samples and Gerald T. Cebula for help in sample preparation.

BASALTS

Basalts in the southern Rocky Mountain region range in age from Miocene to Holocene (Lipman and others, 1970; Strangway and others, 1969; Christiansen and Lipman, 1972), approximately contemporaneous with the period of extensional block faulting. These basalts represent the latest phase of widespread Cenozoic volcanism in the southern Rocky Mountains. The earlier volcanism was more silicic, ranging from andesite to rhyolite, and was mainly Oligocene in age (Steven and Epis, 1968).

For convenience, the basalt data are discussed in six geographic groups (fig. 1): (1) tholeiitic basalts, alkalic basalts, and xenocrystic basaltic andesites of the Rio Grande depression, (2) alkalic basalts of Los Mogotes volcano in the southeastern San Juan Mountains, (3) the alkalic Brazos Basalt (of Doney, 1968) in the Tusas Mountains, (4) several basalt groups from the Mount Taylor area, (5) alkalic basalt of the Cimarron Mountains, and (6) the alkalic Raton, Clayton, and Capulin Basalts (of Collins, 1949) on the High Plains of northeastern New Mexico.

Rio Grande depression

Mafic flows that flood the southern San Luis Valley are divisible into three distinct types: olivine tholeiite, silicic alkalic basalt, and xenocrystic alkalic basaltic andesite.

The flows of olivine tholeiite are volumetrically the most abundant (Aoki, 1967a; Lipman, 1969). They form an impressive volcanic plateau north of Taos, N. Mex., and constitute the dominant basalt type in sections as much as 200 m thick in the Rio Grande gorge, where they have been dated as 3.6 to 4.5 m.y. old (Ozima and others, 1967). These basalts are coarse grained, porous, and characterized by diktytaxitic textures. They are also distinctive chemically in comparison with all the alkalic rocks of the region, being characterized by higher Fe, Al, Mg, and lower Ti, P, Sr, Ba, Rb, K, U, and Th (Lipman, 1969). Total alkalis are sufficiently low that these rocks plot within the field of tholeiitic basalts of Hawaii (fig. 2A). The contents of K, U, and Th are the lowest in the region and are only slightly variable (fig. 3A).

Interlayered in the Rio Grande gorge with the typical diktytaxitic olivine tholeiites are subordinate flows of fine-grained dense silicic alkali-olivine basalt (Aoki, 1967a, table 1, Nos. 11, 14, 15). Cinder-cone vents for similar flows are exposed along the west margin of the southern San Luis Valley in northernmost New Mexico, but it is not clear whether the alkalic basalts exposed along the Rio Grande gorge were erupted from vents within the main part of the rift or whether they flowed in from the sides. All these flows petrologically resemble the nearby alkalic basalts in the Tusas Mountains and southeastern San Juan Mountains: in addition to higher total alkalis than the tholeiites (fig. 2A), they contain higher contents of K, Th, and U (table 1; fig. 3A).

Also exposed along the west margin of the San Luis Valley, near the Colorado-New Mexico line, are several distinctive flows of alkalic basaltic andesite that are characterized by abundant xenocrysts of quartz and plagioclase. These flows are similar to upper Cenozoic xenocrystic basalts that occur farther northwest in the San Juan volcanic field (Larsen and others, 1938; Doe and others, 1969; Lipman, 1969, pls. 1, 2). Some of these xenocrystic flows are clearly older than the olivine tholeiite flows, for example the Dorado Basalt of Butler (1971) that is exposed along the east edge of the Tusas Mountains. Other xenocrystic flows farther east within the Rio Grande depression may be younger than some of the tholeiitic basalts or, alternatively, these flows may represent older hills partly buried by the tholeiitic basalts. The xenocrystic flows of basaltic andesite are only slightly higher in K than the nonxenocrystic alkalic basalts of the same general area, but they are distinctly higher in Th and U (fig. 3A).

Southeastern San Juan Mountains

Basaltic lavas of the Miocene-Pliocene Hinsdale Formation are the dominant type of late Cenozoic volcanism throughout the San Juan Mountains, but interpretation of these rocks is hampered by uncertain location of the vents for many flows. All analyses reported here are of samples from Los Mogotes volcano, a small 5-m.y.-old shield (Lipman and others, 1970) near the west edge of the San Luis Valley in the southeastern

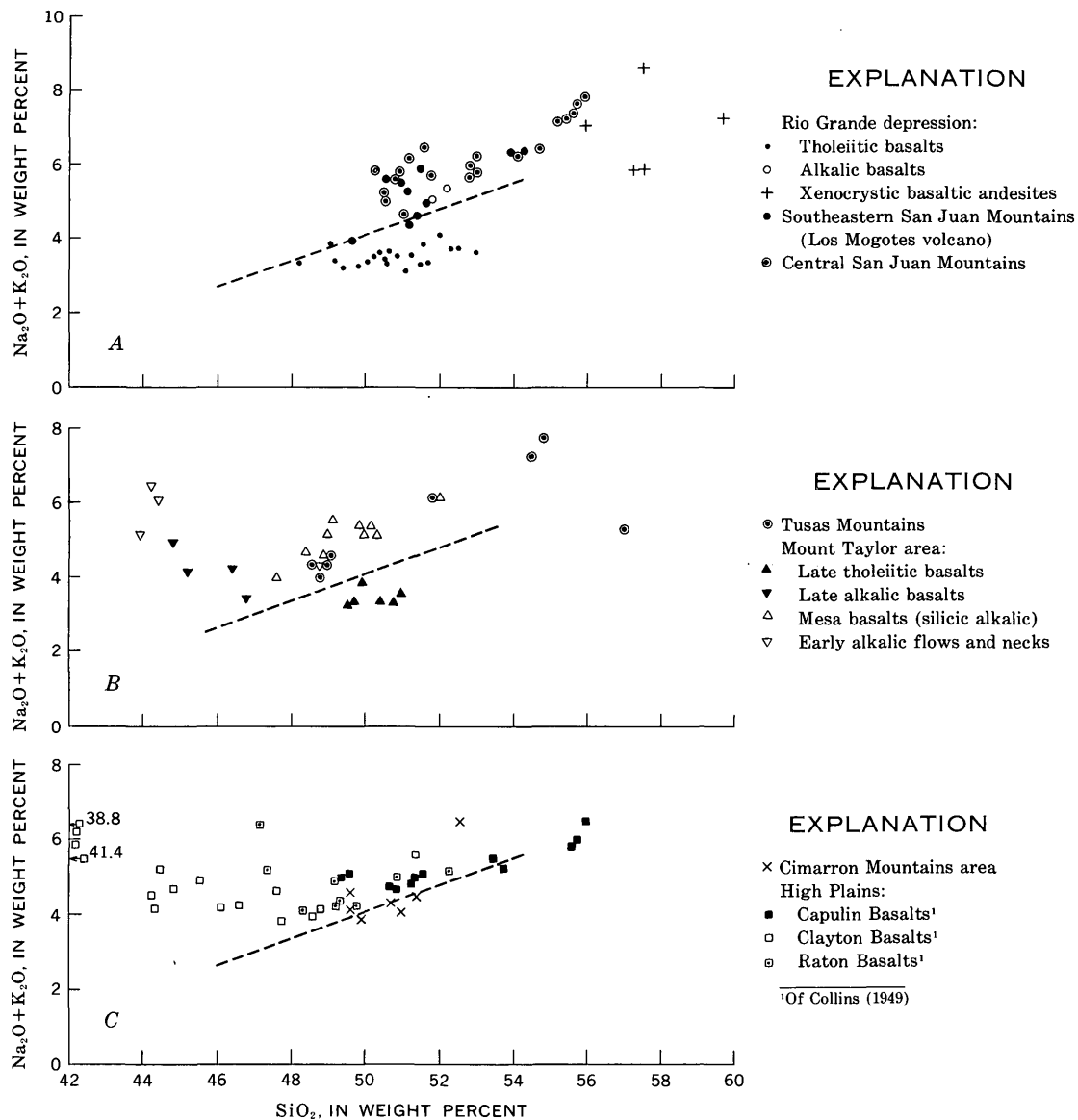


Figure 2.—Plots of total alkalis and SiO_2 for basalts of the southern Rocky Mountain region. Data from Aoki (1967a, b), Renault (1970), Laughlin and others (1971), Baldwin and Muehlberger (1959), Larsen and Cross (1956), Stormer (1972), Lipman and Moench (1972), and Lipman (1969 and unpub. data). All analyses plotted have been recalculated to 100 percent without H_2O or CO_2 . Dashed line separates fields of Hawaiian tholeiitic and alkalic basalts (Macdonald and Katsura, 1964). Although arbitrary, this field boundary is used because it emphasizes seemingly significant petrographic and geographic distinctions; alternative boundaries (Kudo and others, 1971) result in slightly different nomenclature for the basalts of the region.

- A. Basalts of the Rio Grande depression and the southeastern and central San Juan Mountains.
 B. Basalts west of the Rio Grande depression (Tusas Mountains and Mount Taylor areas).
 C. Basalts east of the Rio Grande depression (Cimarron Mountains and High Plains areas).

San Juan Mountains (fig. 1). Basaltic lava flows originally extended outward 15–20 km in all directions from a central cinder cone, but the shield has been tilted about 5° toward the San Luis Valley and asymmetrically dissected. Where the flank of the volcano has been cut across by the canyon of the Conajos River, at least 10 individual basalt flows are exposed. In the field these flows appear to be monotonously uniform

dense basalt with sparse olivine phenocrysts, but chemical analyses indicate that they decrease systematically upward in silica, alkalis, and other elements—from about 54 percent silica at the base of the sequence to less than 50 percent silica for the latest erupted flows (P. W. Lipman, unpub. data). The Los Mogotes flows are relatively silicic alkali-olivine basalts, generally similar in petrography and chemistry to the other basalts

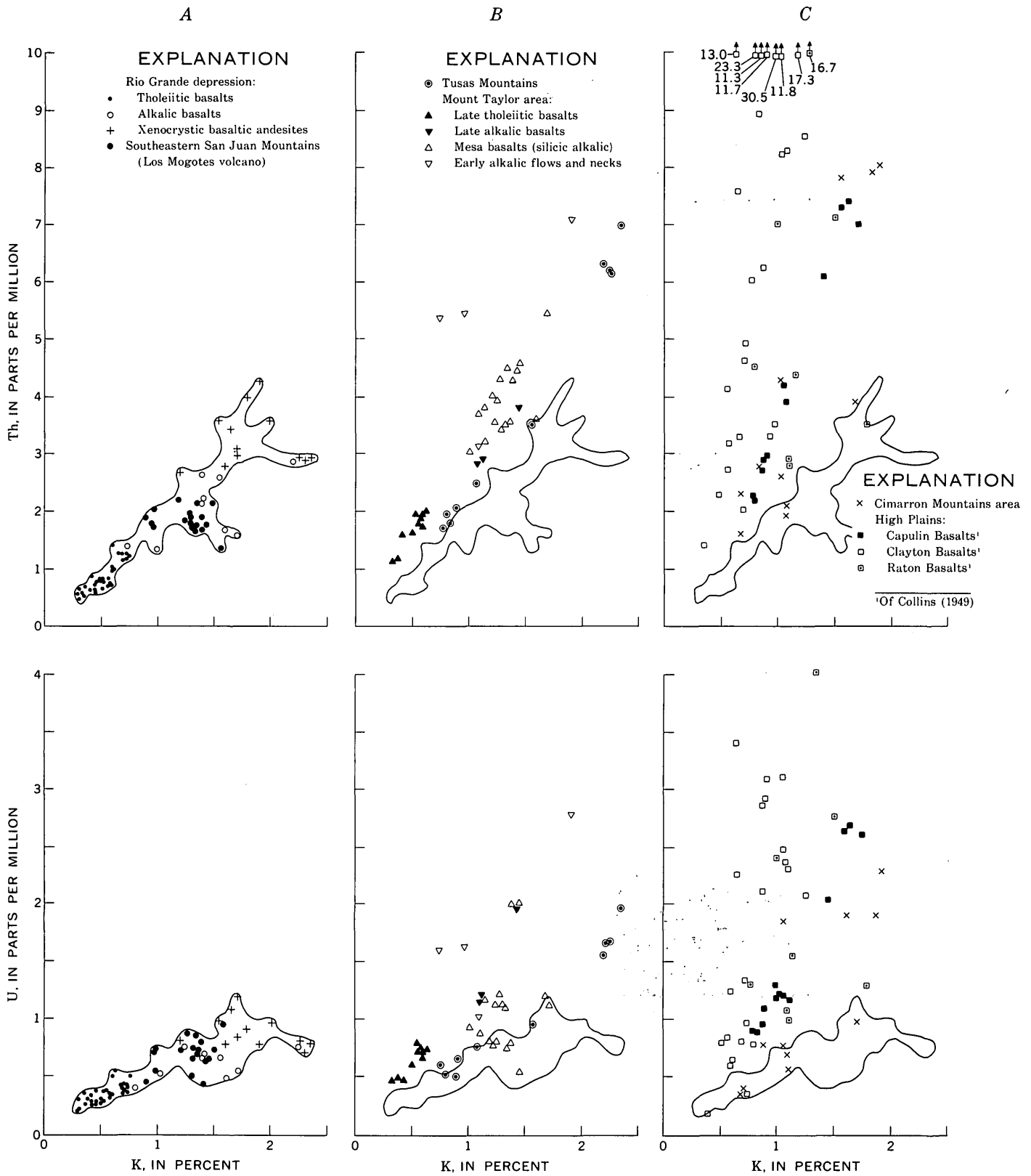


Figure 3.—Plots of K, Th, and U contents of basalts of the southern Rocky Mountain region. Data from table 2.

- Basalts of the Rio Grande depression and the southeastern San Juan Mountains. Empirically estimated field boundary of Rio Grande depression basalts is repeated in B and C.
- Basalts west of the Rio Grande depression (Tusas Mountains and Mount Taylor areas).
- Basalts east of the Rio Grande depression (Cimarron Mountains and High Plains areas).

of the Hinsdale Formation. Their contents of K, Th, and U are generally similar to those of nearby alkalic basalts within the Rio Grande depression (fig. 2A).

Tusas Mountains

A north-trending zone of at least five little-eroded cinder cones and related lava flows of probable Pleistocene age along the west flank of the Tusas Mountains in northern New Mexico, which have been termed the Brazos Basalt by Doney (1968), forms a partial link between the San Juan volcanic field and the Jemez field to the south. Although younger than any known basalt of the Hinsdale Formation of the San Juan Mountains, the Brazos Basalt is a generally similar type of silicic alkali-olivine basalt (fig. 2B). The most silicic flows of Brazos Basalt contain sparse xenocrysts of quartz and plagioclase. The Brazos Basalt, which is well west of the Rio Grande depression, is slightly higher in U and Th contents than otherwise petrographically similar alkalic basalts along the west edge of the San Luis Valley and in the Rio Grande gorge (fig. 3B).

Mount Taylor area

Petrologically diverse Pliocene and younger basalts occur in the vicinity of Mount Taylor (Lipman and Moench, 1972), near the south margin of the Colorado Plateau, about 50 km west of the Rio Grande depression (fig. 1).

The oldest basalts in this area are flows and necks, mainly low-silica nepheline-normative alkali-olivine basalt (fig. 2B), that were emplaced prior to the formation of the Mount Taylor stratovolcano. Flows of intermediate age (mesa basalts), which now cap erosional mesas around Mount Taylor, consist of silicic alkalic basalt that is generally similar in mineralogy, texture, and major-oxide composition to basalts of the San Juan Mountains and Tusas Mountains (fig. 2). Pleistocene and Holocene basalts of the Mount Taylor area, which occur near modern drainage levels, include both alkalic and tholeiitic types. Diktytaxitic olivine tholeiites that are similar to the tholeiitic basalts of the Rio Grande depression in mineralogy, texture, and major-oxide composition occur around the southwest, south, and southeast margins of the Mount Taylor area (Lipman and Moench, 1972; Renault, 1970). Late alkalic basalts, some sufficiently low in silica to be nepheline normative, are closely associated with olivine tholeiites in the Zuni Mountains, about 30 km southwest of Mount Taylor (Renault, 1970; Kudo and others, 1971; Laughlin and others, 1971).

These diverse basalts in the Mount Taylor area are predictably variable in K, Th, and U contents (fig. 3B; table 1), but at any K content, both Th and U are distinctly higher than for basalts near or within the Rio Grande depression (fig. 3A). Especially striking are the distinctly separate fields for the olivine tholeiites from the two areas, and also the virtually

complete separation of the two groups of silicic alkalic basalts (fig. 3B). The low-silica alkalic basalts from the Mount Taylor area are especially rich in Th and U; no petrologically comparable basalts occur within or near the Rio Grande depression to the east.

Cimarron Mountains area

On the east side of the Rio Grande depression, a large basalt field that extends from near Wagon Mound, N. Mex., across the Cimarron Mountains, to the flank of the southern Sangre de Cristo Mountains (fig. 1), is virtually unstudied except for reconnaissance geochemical sampling (Kudo and others, 1971; this report). Most of the flows are late Cenozoic, as indicated by limited erosional dissection, but no radiometric ages are available. These basalts are mostly silicic alkalic types (fig. 2C), similar in texture and mineralogy to those of Los Mogotes volcano, the Tusas Mountains, and the mesas of the Mount Taylor area. Although a few of the samples analyzed for this study have diktytaxitic textures, megascopically resemble the tholeiites of the Rio Grande depression, and plot marginally within the field of Hawaiian tholeiitic basalts (fig. 2C), none are as low in alkalis and other dispersed elements as the tholeiites of the depression. In contents of K, Th, and U, basalts of the Cimarron Mountains are rather like the silicic alkalic basalts of the Mount Taylor area: they are distinctly enriched in U and Th at any given K content, in comparison with otherwise similar rocks within or near the Rio Grande depression (fig. 3A). Xenocrystic basaltic andesites, which are common in the western Cimarron Mountains, contain exceptionally high K, Th, and U contents.

High Plains of northeastern New Mexico

The large area of Pliocene to Holocene basaltic lavas in northeastern New Mexico (fig. 1) has been described by Lee (1922), Collins (1949), Stobbe (1949), Baldwin and Muehlberger (1959), Aoki (1967b), and Stormer (1972). The older basalts cap high mesas and have been extensively eroded, but the younger basalts follow present drainages and are only slightly eroded. Several of the older flows have yielded K-Ar ages of 7–8 m.y. (Stormer, 1972). One of the youngest basaltic centers of this area, Capulin cone, was active between 8,000 and 2,500 B.C. (Baldwin and Muehlberger, 1959).

These basalts can be divided into several groups on the basis of petrology and age. The oldest, the Raton Basalts of Collins (1949), are mostly silicic alkalic basalts similar in chemistry and petrography to the basalts of the San Juan Mountains and the mesa basalts of the Mount Taylor area (fig. 2). The intermediate-age Clayton Basalts of Collins (1949) consist in part of silicic alkalic basalt similar to the Raton Basalts, but they also include distinctive highly alkalic basalts low in silica and containing feldspathoids in the groundmass. These feldspathoidal basalts are generally like the nepheline-normative

early basalts of the Mount Taylor area (fig. 2B), but some are even more mafic and alkalic, with silica contents of 40 percent or less. The youngest lavas, the Capulin Basalts of Collins (1949), are silicic alkalic basalts chemically and petrographically similar to the Raton Basalts. These flows contain olivine phenocrysts, and some flows from Capulin cone contain abundant xenocrysts of quartz and plagioclase.

All these High Plains basalts are rich in Th and U, in comparison with otherwise petrologically similar basalts nearer the Rio Grande depression (fig. 3). The feldspathoidal Clayton Basalts are the most enriched, containing as much as 30.0 ppm Th and 7.2 ppm U, but even the more ordinary silicic alkalic flows of Clayton Basalts are much higher in these elements than any of the basalts near the Rio Grande depression. The Raton and Capulin Basalts, which are restricted to western parts of the High Plains basalt field, have contents of Th and U that are intermediate between those of the Clayton Basalts and basalt fields nearer the Rio Grande depression (fig. 3). The Clayton Basalts that are lowest in K, Th, and U have fine-grained diktytaxitic textures, generally resembling some tholeiites of the Rio Grande depression, but the Th/K and most of the U/K ratios of these Clayton Basalts are much higher (fig. 3C; table 1).

DISCUSSION

The most interesting general feature of the distribution of K, Th, and U in basalts of the southern Rocky Mountain region is the increase in Th and U with respect to K with distance from the Rio Grande depression. The volumetrically predominant olivine tholeiites of the depression have the lowest K, Th, and U contents of any basalts in the region. The less abundant alkalic basalts and xenocrystic basaltic andesites of the western Rio Grande depression have higher contents of these elements but the Th/K and U/K ratios remain very low, averaging about 1.7×10^{-4} and 0.5×10^{-4} , respectively (table 1).

Away from the Rio Grande depression, tholeiitic rocks low in K, Th, and U are rare in the southern Rocky Mountain region. The only major exception would seem to be the olivine tholeiites south of Mount Taylor, which are similar to tholeiites of the depression in texture, mineralogy, and major-oxide chemistry (fig. 2B), but which have distinctly higher average Th/K and U/K ratios, about 3.1×10^{-4} and 1.1×10^{-4} (table 1, fig. 3). The presence of tholeiitic basalts near Mount Taylor has been interpreted as related to the structural discontinuity between the Colorado Plateau and Basin and Range provinces (Lipman, 1969; Lipman and Moench, 1972). Compositionally transitional basalts with diktytaxitic textures, that are low-potassium components of the basalt suites in the Cimarron Mountains and in the Clayton Basalts on the High Plains, are also distinctly enriched in Th and U relative to K, in comparison with similar-textured tholeiites of the Rio Grande depression (fig. 3).

These large variations in K, Th, and U contents and ratios between suites of olivine tholeiites from different geographic regions, and similar variations between suites of silicic alkalic basalts from different regions, permit distinctions among basalt suites that are very similar in texture, mineralogy, and major-oxide chemistry.

The silicic alkalic basalts that are the dominant type in the southern Rocky Mountain region all have higher K, Th, and U contents than the tholeiitic basalts. In addition, the Th/K and U/K ratios of these basalts increase with distance from the Rio Grande depression (table 1). The lowest ratios of these elements occur in the basalts of Los Mogotes volcano on the west margin of the Rio Grande depression and in the sparse similar silicic alkalic basalts interlayered with the tholeiitic basalts farther south within the depression (fig. 3A). Concentrations and ratios of these elements increase westward across the San Juan volcanic field: preliminary results of our minor-element studies, currently in progress on western San Juan basalts, indicate average U/K and Th/K ratios of 0.86 and

Table 1.—Averages and ranges of Th/U, U/K, and Th/K in basalts of the southern Rocky Mountain region

[Data from table 2; U/K and Th/K ratios $\times 10^{-4}$]

Area and rock type	No. of samples	Th/U	U/K	Th/K
Rio Grande depression:				
Tholeiitic basalts	31	2.7 (1.9–3.8)	0.64 (0.51–1.1)	1.7 (1.3–2.3)
Alkalic basalts	9	3.4 (2.7–3.8)	.45 (.28–.67)	1.6 (1.0–2.3)
Xenocrystic basaltic andesites	12	4.0 (2.9–4.6)	.46 (.27–.63)	1.8 (1.2–2.3)
Southeastern San Juan Mountains	18	2.9 (1.5–4.6)	.51 (.30–.67)	1.5 (.87–2.1)
Tusas Mountains	10	3.7 (3.0–4.3)	.67 (.56–.83)	2.5 (2.2–2.9)
Mount Taylor area:				
Early alkalic flows and necks	4	3.3 (2.9–3.6)	1.4 (.87–2.0)	4.8 (2.8–7.0)
Mesa basalts	17	4.2 (2.3–9.2)	.75 (.33–1.3)	2.9 (2.1–3.3)
Late tholeiitic basalts	10	2.8 (2.5–3.6)	1.1 (.87–1.3)	3.1 (2.4–3.6)
Late alkalic basalts	3	2.3 (2.2–2.5)	1.1 (.92–1.2)	2.4 (2.1–2.7)
Cimarron Mountains	11	4.0 (2.5–6.4)	.79 (.48–1.6)	3.1 (1.7–4.8)
High Plains:				
Raton Basalts	8	3.1 (2.3–4.1)	1.6 (.69–2.9)	5.0 (1.8–12.2)
Clayton Basalts	23	4.5 (3.2–9.4)	2.3 (.35–7.6)	9.4 (2.5–26.4)
Capulin Basalts	14	2.9 (2.5–4.4)	1.2 (.86–1.6)	3.6 (2.8–4.5)

2.8, respectively, for these rocks (compare with table 1). These ratios also are higher in the silicic alkalic basalts of the Cimarron and Tusas Mountains, east and west of the Rio Grande depression, respectively; they are even higher in the otherwise petrologically similar mesa basalts of the Mount Taylor area and Capulin Basalts of the High Plains at greater distances from the Rio Grande depression. Extremely high Th

and U contents—as much as 30 and 7 ppm, respectively—and high Th/K and U/K ratios occur only at large distances from the Rio Grande depression; on the High Plains to the east and at Mount Taylor on the southeastern Colorado Plateau. High Th/K and U/K ratios characterize basalts of the western Colorado Plateau region (fig. 4A), as noted by Best, Hamblin, and Brimhall (1966, 1969) and Best and Brimhall (1970); the

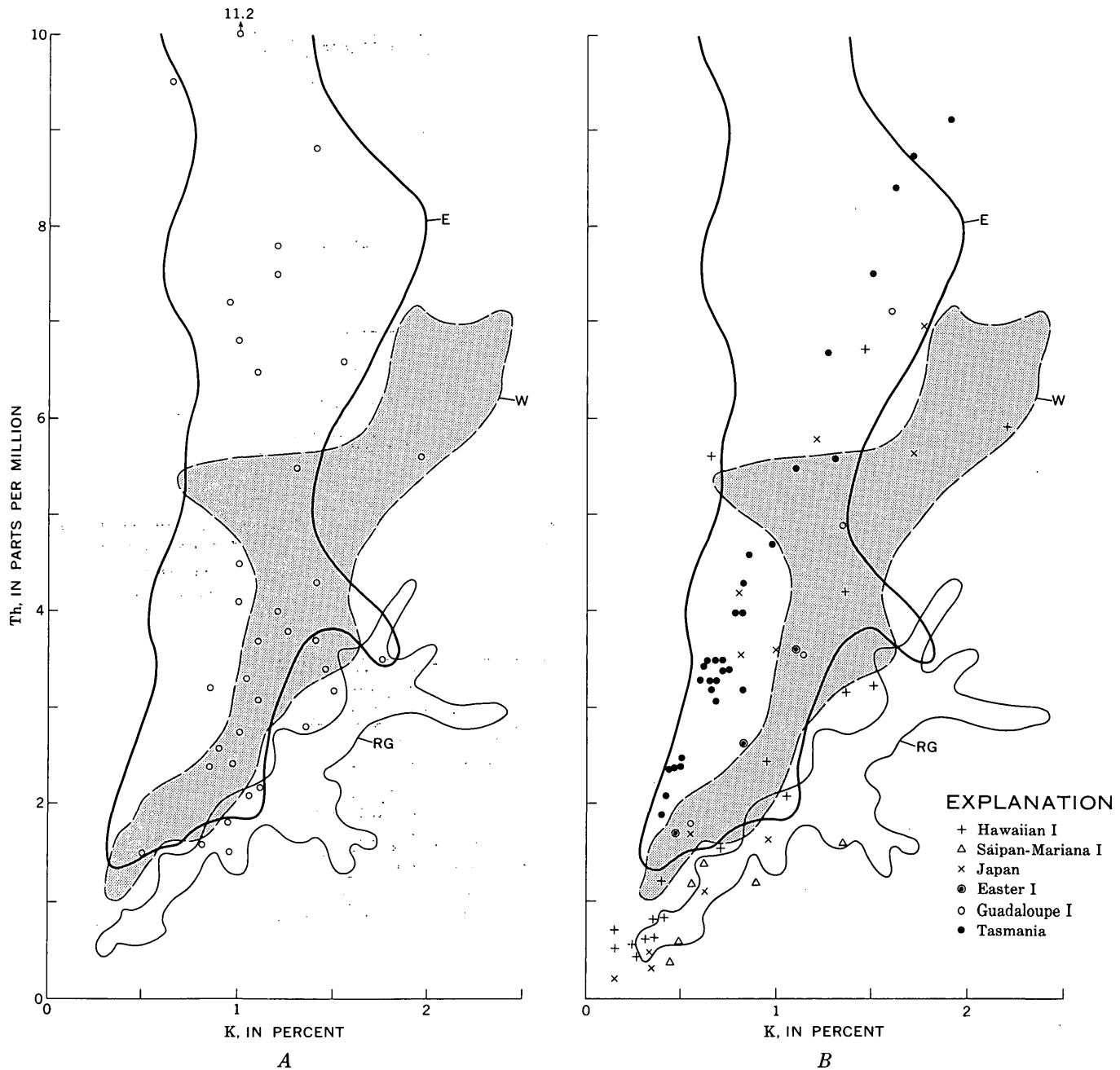


Figure 4.—Comparisons of K and Th contents of basalts of the southern Rocky Mountain region with mafic volcanic rocks from other regions. Plots of K and U also show similar patterns for these regions. Empirically estimated field boundaries for basalts of the Rio Grande depression (RG), basalts west of the depression (W), and basalts east of the depression (E) are taken from figure 3.

A. Western Grand Canyon region. Data are from Best, Hamblin, and Brimhall (1966) and Embree (1970).

B. Oceanic-island and island-arc basalts. Data are from Heier and Rogers (1963), Heier, McDougall, and Adams (1964), Heier, Compston, and McDougall (1965), Tatsumoto (1966a, b), Gottfried, Moore, and Campbell (1963), and Hedge and Knight (1969).

western Colorado Plateau basalts seem generally petrologically similar to basalts of the Mount Taylor and High Plains areas discussed in this report.

Large variations in U and Th contents and ratios within some individual lava flows have been interpreted as related to oxidation and leaching processes (Watkins and Haggerty, 1967; Watkins and others, 1967; Heier and Rogers, 1963), but processes of this type seem unlikely to have affected significantly the basalts studied here. Paired samples of black cinders (reduced) and red cinders (oxidized) from four individual cinder cones differ only slightly in Th, K, and U contents or ratios (table 2, Nos. 45–47, 160–161, 164–165, and 165–166). A detailed study by Embree (1970) also found only insignificant lateral variation and only slight vertical variation within a single large basalt flow in the western Grand Canyon region.

The Th/K and U/K ratios of basalts of the southern Rocky Mountain region vary by more than an order of magnitude (table 1), a larger range than has previously been reported for basaltic rocks in general (Heier and Rogers, 1963). The geochemical coherence of these elements seems less ideal than previously thought, and the present data show a closer coherence between Th (and U) and Sr (fig. 5) than between Th (and U) and K (fig. 3). The highest Th/K and U/K ratios of the basalts approach those of lunar basalts (Fanale and Nash, 1971) and terrestrial ultramafic rocks (Fisher, 1970), although the concentrations of these elements are much greater in the basalts of the southern Rocky Mountain region.

The Th/U ratios are also quite variable, although less so than the Th/K or U/K ratios (table 1). In general, the most alkalic basalts have the highest Th/U ratios, and the tholeiitic rocks have low ratios. Significant exceptions are the late alkalic basalts of the Mount Taylor area, which have atypically low Th/U ratios, apparently because of anomalously high U contents. These variations in Th/U ratios in basalts of the southern Rocky Mountain region are interesting, as most of the values are below the estimated mantle ratio (3.9–4.1) required to generate observed ranges of Pb-isotopic compositions through time (Russell and Farquhar, 1960; Patterson and Tatsumoto, 1964). In the ocean basins, the ridge tholeiites also have lower Th/U ratios than the more alkalic island basalts, and the Th/U ratios of the ridge tholeiites are too low to have generated their observed Pb-isotopic ratios (Tatsumoto, 1966a). Sparse available Pb-isotopic data (Doe and others, 1969) suggest the possibility of a similar relation for the low Th/U basalts of the southern Rocky Mountain region. Either the mantle underlying the southern Rocky Mountain region has been variably depleted in Th relative to U by pre-late Cenozoic events, or varying conditions of melting during generation of the upper Cenozoic basalts were capable of significantly fractionating the Th/U ratios.

The variations in K, Th, and U are parallel to the major-oxide chemical variations of the southern Rocky Mountain basalts, which become generally more alkalic away from the Rio Grande depression (Lipman, 1969; Kudo and others, 1971): basalts and basaltic andesites of alkalic affinities were

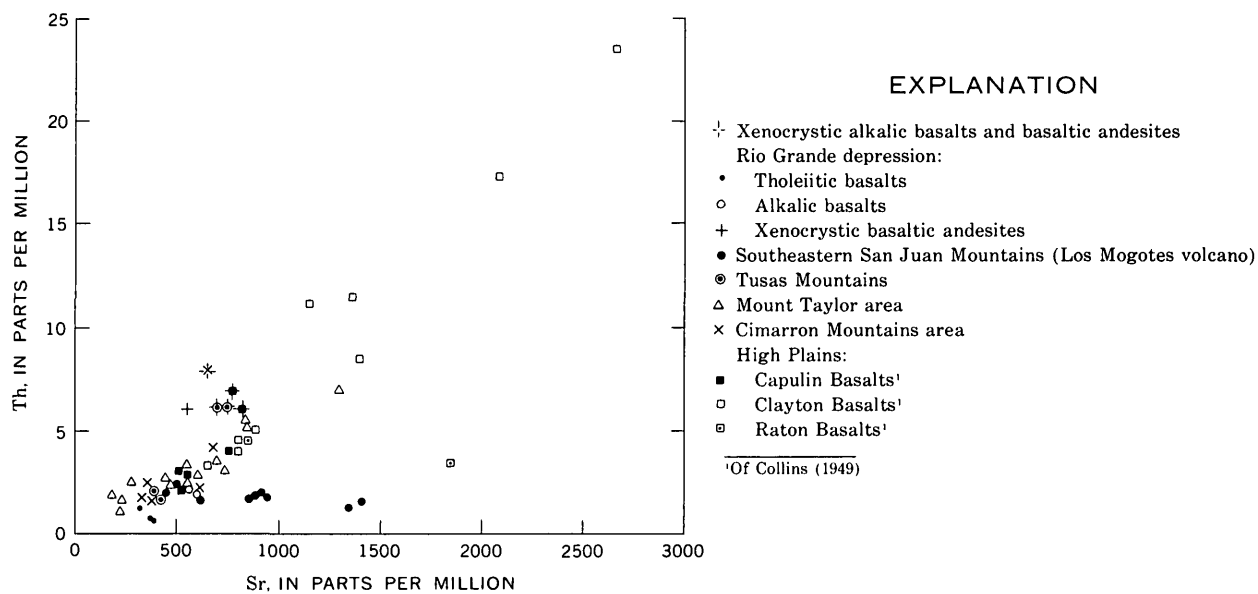


Figure 5.—Plot of Th and Sr for basalts of the southern Rocky Mountain region, showing general coherence of these two elements. The major exceptions are samples from Los Mogotes volcano, which define a divergent trend in which Sr increases as Th remains nearly constant; the Los Mogotes rocks are also atypical in several other elemental trends (P. W. Lipman and C. E. Hedge, unpub. data). Also, xenocrystic alkalic basalts and basaltic andesites tend to contain higher Th contents than nonxenocrystic basalts of similar Sr content from the same area. Sr concentrations are by X-ray fluorescence (C. E. Hedge, written commun., 1971) except for Mount Taylor (Lipman and Moench, 1972) and Cimarron Mountains (Lipman, unpub. data), which are by emission-spectrographic methods.

erupted east and west of the depression concurrently with its formation, and tholeiitic basalts filled parts of the depression late in its history. Nepheline-normative alkalic basalts occur only at distances of about 100 km or more from the depression. Extremely alkalic rocks are present in the interior of the Colorado Plateau (Williams, 1936) and on the High Plains (Clayton Basalts). Thus, the increasing Th/K and U/K ratios of the basalts of the southern Rocky Mountain region correlate well with alkalinity of the basalt suites. This correlation is probably valid for basalts in general. A similar increase in Th and U in basalts across Japan, as the basalts change from tholeiitic to alkalic (Kuno, 1959; Sugimura, 1960), was noted by Heier and Rogers (1963), and systematic correlation between Th and U contents and alkali-lime indices has been demonstrated for igneous suites in general by Tilling and Gottfried (1969, fig. 6).

The overall range in compositions, both major oxides and minor elements, in basalts of the southern Rocky Mountain region is large and encompasses virtually the entire known range of oceanic-island or other continental basalts (Hedge and Lipman, 1972). This similarity seems especially evident for the K, Th, and U data (fig. 4), although adequate analyses are sparse for many regions. The only conspicuous exceptions are the oceanic ridge tholeiites, which are extremely low in elements such as K, Th, U, Sr, Rb, and Ba (Engel and others, 1965; Tatsumoto, 1966a; Kay and others, 1970), and even here the tholeiitic basalts of the Rio Grande depression are transitional toward the ridge tholeiites (Cohen and others, 1967; Lipman, 1969), containing contents of these minor elements as low as or lower than most Hawaiian or Japanese tholeiites (fig. 4B; Hedge and Lipman, 1972). The low-silica alkalic basalts of the High Plains and the Mount Taylor areas are generally similar to the nepheline-normative alkalic basalts of oceanic islands. The silicic alkalic basalts, although generally similar in elemental composition to hawaiites and mugearites of oceanic islands, form a significantly greater proportion of the total basalt accumulation in the southern Rocky Mountains, and for that matter throughout the Western United States (Lipman, 1969; Leeman and Rogers, 1970).

The diversity of basalt types in the southern Rocky Mountain region seems most plausibly interpreted as related to depth of magma generation (Lipman, 1969; Lipman and Moench, 1972; Stormer, 1972). The general trends of chemical variations from tholeiitic to nepheline-normative alkalic basalts, involving increase of alkalis as silica decreases, cannot be produced by crystal-liquid fractionation at low pressures (Powers, 1935; Yoder and Tilley, 1962). Furthermore, compositional variations within basalt sequences related to some individual centers, such as Los Mogotes volcano, cannot be accounted for by addition or subtraction of the low-pressure phenocryst phases present in the basalts, and seemingly must also be due to high-pressure fractionation (P. W. Lipman and C. E. Hedge, unpub. data). It therefore appears likely that much of the chemical variation among basalts of the southern

Rocky Mountain region reflects fundamental differences in the conditions of magma generation at depth in the source area, presumably in the mantle. Either the source area differs in composition roughly symmetrically across the area of the Rio Grande depression or, more likely, the pressure-temperature conditions of magma generation vary symmetrically across the region.

Crystallization experiments on basalts at high pressures (Green and Ringwood, 1967; Green, 1968; Kushiro, 1968) have shown that basaltic magmas can be generated by partial melting of probable mantle constituents and that the composition of the basaltic melt is determined by the depth of melting and the depth at which the melt last equilibrates with the refractory residuum (O'Hara and Yoder, 1967). Experimental fraction trends at different pressures suggest that tholeiitic basalt should be generated at lesser depths than alkalic basalt, and these relations have been cited to interpret the origin of compositionally varied basalt associations in the Western United States like those of the southern Rocky Mountain region (Wise, 1969; Leeman and Rogers, 1970; Condie and Barsky, 1972) and also to account for basalt variations in oceanic areas (Kuno, 1959, 1968; Jackson and Wright, 1970).

Effects of sialic crustal contamination on basalts of the southern Rocky Mountain region, although locally significant in affecting concentrations and isotopic compositions of some elements (Doe and others, 1969; Laughlin and others, 1972), seem generally to have played an insignificant role in generation of the diversity of basalt types. In the present study the rocks with the highest Th and U contents are the low-silica alkalic basalts; these high Th and U values cannot be due to contamination by sialic crust, which would have concurrently increased the silica contents of these basalts. Interpretation of Sr data leads to similar conclusions: the rocks richest in U and Th also have the highest Sr contents—as much as 2,500 ppm Sr, in contrast with 250–300 ppm Sr in the Th- and U-poor olivine tholeiites (C. E. Hedge, written commun., 1971)—but contamination by any plausible crustal material would lower the Sr concentration in these basalts, not increase it. The Sr-poor rocks should also be much more sensitive to effects of contamination than the Sr-rich rocks, yet the Sr^{87}/Sr^{86} ratios of the most Sr-rich Clayton Basalts of the High Plains (0.7041–0.7049; four samples) bracket the radiogenic Sr of the Sr-poor tholeiitic basalts of the Rio Grande depression (0.7042–0.7048; four samples); data from Hedge and Lipman (1972 and unpub. data).

Perhaps the slightly high Th/K and U/K ratios of the xenocrystic basaltic andesites of the Rio Grande depression, in comparison with silicic alkalic basalts from the same area (fig. 2A), are due to effects of sialic crustal contamination, as Pb-isotopic comparisons of similar rocks show significant differences (Doe and others, 1969). However, the origin of such xenocrystic rocks is in doubt. In addition to possible derivation from Precambrian sialic crust, they may represent

disequilibrium remnants from high-pressure crystallization in the upper mantle (Nicholls and others, 1971) or result from mixing with phenocryst-bearing rhyolitic magma, as can be demonstrated for a few small basalt rhyolite mix-lava complexes in the southeastern San Juan Mountains (Lipman, unpub data).

Table 2.—Analyses of K, Th, and U in basalts of the southern Rocky Mountain region

No.	Field sample No.	U (ppm)	Th (ppm)	K (percent)	Th/U	U $K \times 10^{-4}$	Th $K \times 10^{-4}$
Rio Grande depression—tholeiitic basalt							
1.	68L-10....	0.51	1.02	0.62	1.99	0.82	1.65
2.	14A...	.36	.81	.60	2.25	.60	1.35
3.	14B...	.36	.83	.53	2.31	.68	1.57
4.	14C...	.36	.86	.55	2.39	.65	1.56
5.	14D...	.38	1.17	.71	3.08	.54	1.65
6.	14E...	.50	1.21	.77	2.42	.65	1.57
7.	14F...	.38	1.27	.69	3.34	.55	1.84
8.	14G...	.39	1.30	.68	3.33	.57	1.91
9.	14H...	.38	1.29	.75	3.39	.51	1.72
10.	18B4..	.29	.81	.53	2.79	.55	1.53
11.	19....	.52	1.42	.62	2.73	.84	2.29
12.	111....	.23	.52	.32	2.26	.72	1.62
13.	112....	.32	.63	.38	1.97	.84	1.66
14.	113....	.37	.79	.62	2.14	.60	1.27
15.	114....	.29	.88	.51	3.03	.57	1.73
16.	119C..	.26	.80	.47	3.08	.55	1.70
17.	119D..	.42	1.20	.75	2.86	.56	1.60
18.	119E..	.36	1.03	.63	2.86	.57	1.63
19.	119F..	.18	.69	.31	3.83	.58	2.23
20.	119G..	.28	.70	.54	2.50	.52	1.30
21.	120....	.24	.73	.37	3.04	.65	1.97
22.	121....	.27	.63	.34	2.33	.79	1.85
23.	125....	.30	.71	.42	2.37	.71	1.69
24.	126....	.32	.76	.58	2.38	.55	1.31
25.	127....	.24	.64	.46	2.67	.52	1.39
26.	128....	.32	.94	.42	2.94	.76	2.24
27.	129....	.34	1.14	.62	3.35	.55	1.84
28.	140....	.32	.62	.30	1.94	1.07	2.07
29.	145A..	.31	.89	.59	2.87	.53	1.51
30.	145B..	.35	1.00	.61	2.86	.57	1.64
31.	147....	.38	.79	.45	2.14	.82	1.76
Rio Grande depression—alkalic basalt							
32.	68L-116....	0.76	2.62	1.24	3.45	0.61	2.11
33.	119A..	.65	2.17	1.43	3.34	.45	1.52
34.	119B..	.64	2.17	1.40	3.39	.46	1.55
35.	137....	.57	1.59	1.70	2.79	.34	.94
36.	138....	.81	3.10	1.57	3.83	.52	1.97
37.	139....	.79	2.95	2.27	3.73	.35	1.30
38.	141....	.50	1.71	.75	3.42	.67	2.28
39.	142....	.42	1.41	1.04	3.36	.40	1.36
40.	146....	.45	1.64	1.63	3.64	.28	1.01
Rio Grande depression—xenocrystic basaltic andesite							
41.	67L-102....	0.77	4.29	1.94	5.56	0.40	2.21
42.	68L-115....	.74	2.83	1.64	3.82	.45	1.73
43.	117....	.69	2.68	1.21	3.88	.57	2.21
44.	118....	.91	3.55	1.58	3.90	.58	2.25
45.	122A..	.86	2.83	2.28	3.29	.38	1.24
46.	122B1..	.63	2.93	2.36	4.65	.27	1.24
47.	122B2..	.74	2.98	2.39	4.03	.31	1.25
48.	123....	.92	3.63	2.05	3.95	.45	1.77
49.	131....	1.09	3.17	1.72	2.91	.63	1.84
50.	143A..	.88	4.05	1.80	4.60	.49	2.25
51.	143B..	1.03	3.49	1.65	3.39	.62	2.12
52.	144....	.80	2.99	1.73	3.74	.46	1.73
Southeastern San Juan Mountains							
53.	67L-12....	0.71	2.08	1.53	2.93	0.46	1.36
54.	13....	.59	1.73	1.48	2.93	.40	1.17
55.	16....	.54	2.04	1.01	3.78	.53	2.02
56.	103....	.42	1.91	1.40	4.55	.30	1.36

Table 2.—Analyses of K, Th, and U in basalts of the southern Rocky Mountain region—Continued

No.	Field sample No.	U (ppm)	Th (ppm)	K (percent)	Th/U	U $K \times 10^{-4}$	Th $K \times 10^{-4}$
Southeastern San Juan Mountains—Continued							
57.	68L-16A...	0.69	2.17	1.20	3.14	0.58	1.81
58.	16B...	.72	2.19	1.21	3.04	.60	1.81
59.	17B2..	.48	1.76	1.30	3.67	.37	1.35
60.	134A..	.68	1.78	1.01	2.62	.67	1.76
61.	134B..	.68	1.77	1.01	2.60	.67	1.75
62.	134C..	.85	1.91	1.27	2.25	.67	1.50
63.	134D..	.73	1.97	1.32	2.70	.55	1.49
64.	134E..	.90	1.38	1.59	1.53	.57	.87
65.	134F..	.65	1.67	1.36	2.57	.48	1.23
66.	134G..	.70	1.79	1.38	2.56	.51	1.30
67.	134H..	.78	2.17	1.40	2.78	.56	1.55
68.	134I..	.83	1.78	1.35	2.14	.61	1.32
69.	135....	.58	1.69	1.44	2.91	.40	1.17
70.	136....	.44	1.89	.90	4.30	.49	2.10
Tusas Mountains							
71.	68L-92....	0.51	2.09	0.91	4.10	0.56	2.30
72.	93....	1.43	6.20	2.23	4.34	.64	2.78
73.	94....	1.58	6.25	2.28	3.96	.69	2.74
74.	95....	.50	1.81	.83	3.62	.60	2.18
75.	96....	.71	2.52	1.10	3.55	.65	2.29
76.	97....	1.62	6.55	2.25	4.04	.72	2.91
77.	98....	1.96	6.86	2.35	3.50	.83	2.92
78.	99....	.57	1.75	.79	3.07	.72	2.22
79.	100....	.89	3.51	1.61	3.94	.55	2.18
80.	101....	.63	2.04	.83	3.24	.76	2.46
Mount Taylor area—early alkalic flows and necks							
81.	68L-202A..	0.99	3.14	1.14	3.17	0.87	2.75
82.	202B..	1.53	5.35	.77	3.50	1.99	6.95
83.	215....	2.47	7.10	1.96	2.87	1.26	3.62
84.	217....	1.51	5.48	.98	3.63	1.54	5.59
Mount Taylor area—mesa basalts							
85.	68L-7A....	1.07	5.42	1.75	5.07	0.61	3.10
86.	7B(2)..	.83	3.69	1.12	4.45	.74	3.29
87.	7C....	.79	3.14	1.22	3.97	.65	2.57
88.	7D....	.76	3.56	1.40	4.68	.54	2.54
89.	200A..	.73	3.54	1.27	4.85	.57	2.79
90.	200B..	.73	4.06	1.24	5.56	.59	3.27
91.	200C..	.73	4.42	1.36	6.05	.54	3.25
92.	200D..	1.14	3.58	1.70	3.14	.67	2.11
93.	201A..	1.84	4.33	1.42	2.35	1.30	3.05
94.	201B..	1.87	4.52	1.47	2.42	1.27	3.07
95.	201C..	1.03	3.97	1.27	3.85	.81	3.13
96.	202C..	.49	4.52	1.49	9.22	.33	3.03
97.	202D..	1.17	4.25	1.31	3.63	.89	3.24
98.	203....	1.09	3.78	1.18	3.47	.92	3.20
99.	205....	.89	3.05	1.06	3.43	.84	2.88
100.	216A..	1.05	3.54	1.36	3.37	.77	2.60
101.	216B..	1.06	3.44	1.34	3.25	.79	2.57
Mount Taylor area—late tholeiitic basalts							
102.	68L-8....	0.44	1.60	0.45	3.64	0.98	3.56
103.	206....	.43	1.13	.35	2.63	1.23	3.23
104.	207....	.47	1.24	.40	2.64	1.17	3.10
105.	208....	.67	1.95	.61	2.91	1.10	3.20
106.	209....	.67	1.89	.60	2.82	1.12	3.15
107.	213....	.71	2.03	.65	2.86	1.09	3.12
108.	214....	.76	1.92	.57	2.53	1.33	3.37
109.	218....	.57	1.66	.51	2.91	1.12	3.25
110.	219....	.62	1.72	.62	2.77	1.00	2.77
111.	220....	.66	1.83	.76	2.77	.87	2.41
Mount Taylor area—late alkalic basalts							
112.	68L-210....	1.16	2.93	1.16	2.53	1.00	2.53
113.	211....	1.82	3.92	1.46	2.15	1.25	2.68
114.	212....	1.05	2.43	1.14	2.31	.92	2.13
Cimarron Mountains							
115.	68L-187....	0.38	1.58	0.71	4.16	0.54	2.23
116.	188....	1.70	4.24	1.07	2.49	1.59	3.96

Table 2.—Analyses of K, Th, and U in basalts of the southern Rocky Mountain region—Continued

No.	Field sample No.	U (ppm)	Th (ppm)	K (percent)	Th/U	$\frac{U}{K \times 10^{-4}}$	$\frac{Th}{K \times 10^{-4}}$
Cimarron Mountains—Continued							
117.	68L-189...	0.76	2.76	0.90	3.63	0.84	3.07
118.	190...	.64	2.62	1.07	4.09	.60	2.45
119.	191...	.92	3.91	1.73	4.25	.53	2.26
120.	192...	.37	2.38	.70	6.43	.53	3.40
121.	193...	.62	1.93	1.12	3.11	.55	1.72
122.	194...	2.12	7.97	1.96	3.76	1.08	4.07
123.	195...	1.71	7.86	1.91	4.60	.90	4.12
124.	196...	1.85	7.86	1.64	4.25	1.13	4.79
125.	228...	.54	2.10	1.13	3.89	.48	1.86
High Plains—Raton Basalts							
126.	68L-1A....	1.04	2.93	1.12	2.82	0.93	2.62
127.	1B.....	.92	2.82	1.13	3.07	.81	2.50
128.	148....	4.08	16.92	1.39	4.15	2.94	12.17
129.	149....	1.50	4.36	1.16	2.91	1.29	3.76
130.	156A..	2.99	6.94	1.51	2.32	1.98	4.60
131.	156B..	2.28	7.14	1.02	3.13	2.24	7.00
132.	164....	1.25	3.25	1.80	2.60	.69	1.81
133.	197....	1.27	4.41	.79	3.47	1.61	5.58
High Plains—Clayton Basalts							
134.	68L-151...	4.54	17.29	1.25	3.81	3.63	13.83
135.	157....	6.74	23.46	.89	3.48	7.57	26.36
136.	160....	1.88	8.47	1.33	4.51	1.41	6.37
137.	165....	2.73	11.55	.96	4.23	2.84	12.03
138.	167....	7.22	30.02	1.23	4.16	5.87	24.41
139.	168....	2.99	12.81	.68	4.28	4.40	18.84
140.	169....	2.55	11.21	.91	4.40	2.80	12.32
141.	170....	2.59	11.40	1.09	4.40	2.38	10.46
142.	171....	.88	4.93	.80	5.60	1.10	6.16
143.	172....	.73	3.27	.73	4.48	1.00	4.48
144.	174....	1.19	4.49	.76	3.77	1.57	5.91
145.	175....	.31	2.00	.79	6.45	.39	2.53
146.	176....	.15	1.41	.43	9.40	.35	3.28
147.	177....	2.57	8.70	.88	3.39	2.92	9.89
148.	178....	1.11	4.07	.64	3.67	1.73	6.36
149.	179....	.63	3.20	.63	5.08	1.00	5.08
150.	180....	.82	6.04	.78	7.37	1.05	7.74
151.	181....	2.16	8.16	1.13	3.78	1.91	7.22
152.	182....	2.19	8.09	1.18	3.69	1.86	6.86
153.	183....	.76	2.70	.61	3.55	1.25	4.43
154.	184....	.71	2.28	.55	3.21	1.29	4.15
155.	185....	1.97	7.52	.69	3.82	2.86	10.90
156.	186....	1.83	6.19	.91	3.38	2.01	6.80
High Plains—Capulin Basalts							
157.	68L-2.....	0.96	4.18	1.11	4.35	0.86	3.77
158.	152....	2.72	6.82	1.76	2.51	1.55	3.88
159.	153....	1.07	3.85	1.12	3.60	.96	3.44
160.	154A..	2.66	7.15	1.60	2.69	1.66	4.47
161.	154B..	2.47	7.42	1.68	3.00	1.47	4.42
162.	155....	2.03	5.96	1.48	2.94	1.37	4.03
163.	158....	1.08	2.90	.92	2.69	1.17	3.15
164.	159A..	1.19	3.74	1.03	3.14	1.16	3.63
165.	159B..	1.15	3.49	1.08	3.03	1.06	3.23
166.	161A..	1.18	3.34	.98	2.83	1.20	3.41
167.	161B..	1.11	3.24	1.00	2.92	1.11	3.24
168.	162....	.86	2.65	.89	3.08	.97	2.98
169.	163....	1.18	2.91	.90	2.47	1.31	3.23
170.	166....	.79	2.27	.82	2.87	.96	2.77

Basalt sample localities and comments:

1. Low cliff, east side of north-trending arroyo, 0.5 km southeast of San Antonio, Colo.
- 2–9. Sequence of flow units or separate rapidly erupted lava flows, from top of section down; nose of ridge between Rio de los Pinos and Rio San Antonio, 0.4 km southeast of Ortiz, N. Mex.
10. La Jara Canyon road, 4 km southwest of Capulin, Colo., at bend in road around low cliff of basalt.
11. South of road intersection, 1.5 km south of Capulin, Colo.

12. 1.6 km east of U.S. Route 285 on gravel road; lat 36°58' N., long 105°59' W.; at spot elevation 8,073 ft. Especially coarse grained.
13. Same road 5 km east of U.S. 285; 36°57' N., 105°56' W.; at spot elevation 7,953 ft. Zeolite vesicle coatings.
14. Same road, about 9 km east of U.S. 285; 36°57' N., 105°54' W.; west side of small hill with spot elevation 7,967 ft.
15. Road through saddle about 2 km west of No. 13; at 8,050 ft on west side of 8,113-ft hill. Relatively dense and fine grained.
- 16–20. Rio Grande gorge at Dunn Bridge; sequence of five flows, from base up. Lowest flow (Nos. 33–34) is alkalic basalt.
21. Road to Dunn Bridge, at first main arroyo, about 4.5 km southeast of intersection with N. Mex. 111.
22. Along N. Mex. 111, about 0.5 km southeast of intersection with Dunn Bridge road; first roadcut.
23. Roadcut, U.S. 285, west of La Segita Peaks, 0.2 km south of spot elevation 8,460 ft.
24. N. Mex. 111, 1.3 km east of Tres Piedras intersection, at Arroyo Aguaje de la Petaca.
25. Roadcut, U.S. 285, at arroyo 4.5 km northeast of Cerro Mojimo.
26. South slope of Cerro Mojimo, at about 7,750-ft elevation. Cerro Mojimo is a small tholeiitic shield volcano.
27. Roadcut, U.S. 285, 2 km south of Stong, N. Mex.
28. Lower flow, Arroyo Aguaje de la Petaca, along gravel road 1.5 km northeast of Red Hill.
- 29–30. Lower and upper flows in roadcut, U.S. 285, 0.2 km north of Arroyo Aguaje de la Petaca, 0.9 km north of No Agua mill road.
31. Rio Grande gorge bridge, N. Mex. 111, west abutment.
32. Southeast Pinabetoso Peak; thin lava flow interlayered with cinders in dissected remnant of old cone.
- 33–34. Rio Grande gorge at Dunn Bridge; base and top of lowest flow, overlain by tholeiitic flows (Nos. 16–20).
35. Red Hill, flow on north ridge at 8,560 ft.
36. Red Hill, red cinders from most northwesterly prospect on east side, at about 8,560 ft.
37. Same locality as No. 28, upper flow; zeolitic vesicle linings.
38. Los Cerritos de la Cruz, northwest cone; cinders from pit on southeast side at about 9,020 ft.
39. Los Cerritos de la Cruz; flow in arroyo 0.9 km southeast of northwest cone, at 8,850-ft elevation.
40. Roadcut, U.S. 285, west of No Agua Peaks, 0.2 km north of Baretta Canyon. Fine-grained dense texture.
41. Mouth, Ra Jadero Canyon, west of La Jara, Colo.; same locality as analyzed sample (Lipman, 1969, table 1, No. 7).
42. Same locality as No. 15; from top of hill. Uncertain whether older or younger than flanking tholeiitic flows.
43. Crest of north La Segita Peak.
44. North La Segita Peak, south slope at 8,540 ft. Flattened vesicles partly filled by zeolite.
- 45–47. Cinder cone at northeast base of San Antonio Mountain. No. 45, black cinders; Nos. 46–47, two different horizons of red cinders.
48. Northeast side of San Antonio Mountain; flow along road to cinder quarry, at about 8,340-ft elevation.
49. Flow on Petaca Mesa; talus block along road about 1.0 km north of Petaca, N. Mex.
- 50–51. Los Cerritos de la Cruz, east slope of south cone at about 8,900 ft. No. 50, upper flow, is rather oxidized; No. 51, lower flow, appears less oxidized but has zeolite-coated vesicles.
52. Flow, 1.5 km northeast of south cone, Los Cerritos de la Cruz, knob south of road; probably erupted from this cone.
53. Southeast flank of Los Mogotes volcano, top flow on mesa rim, along road, 2.5 km northwest of Mecitas, Colo.
54. Flow at base of dissected main cone, along road, about 1 km east of central peak.
55. North rim of crater; fairly coarse interior of dense flow.
56. Ridge south of Ra Jadero Canyon, west of La Jara, Colo.; knob east of logging road, at about 8,850 ft.
- 57–58. Lower La Jara Canyon, lower and upper parts of lowest flow, mouth of Vicente Canyon. May not have been erupted from Los Mogotes volcano.
59. Lower La Jara Canyon, middle flow; along road about 3.5 km northeast of locality 57–58.
- 60–68. Sequence of nine flows, from top down, on south mesa rim about 5 km west of Mecitas, south flank of Los Mogotes volcano.
69. Flow along road, east flank of main cone; about same locality as 54.
70. Flow on north crater rim; about same locality as 55.

71. Tierra Amarilla flow; roadcut, U.S. 84, at 7,400-ft elevation, just south of Park View, N. Mex.
72. Cebolla flow; along logging road at 8,750 ft, about 6 km east of Cebolla, N. Mex.
73. Cebolla flow; along logging road at about 8,500 ft, about 5 km east of Cebolla, N. Mex.
74. Tierra Amarilla flow; north of road (N. Mex. 112), 1.0 km northeast of La Puente, N. Mex.
75. Tierra Amarilla flow; along N. Mex. 112, 2.2 km southwest of La Puente.
76. Agua Fria flow; south of road, about 1 km west of junction of Rito de Tierra Amarilla and Rito de Agua Fria. Rather vesicular.
77. Agua Fria flow; about 1 km above mouth of Rito de Agua Fria.
- 78–80. Cluster of cinder cones, about 4 km southeast of Brazos Box. No. 78 is agglutinate spatter from near the crest of the west cone; No. 79 is a flow on the southwest side of the north cone; and No. 80 is a flow on the west side of the east cone.
81. Flow 1; see Lipman and Moench (1972, table 1, No. 1).
82. Flow 2; see Lipman and Moench (1972, table 1, No. 2).
83. Picacho Peak plug; see Lipman and Moench (1972, table 1, No. 4).
84. Flow 2; see Lipman and Moench (1972, table 1, No. 3).
85. Flow 4; same locality as Lipman and Moench (1972, table 1, No. 7).
86. Flow 6; see Lipman and Moench (1972, table 1, No. 7).
87. Flow 8; see Lipman and Moench (1972, table 1, No. 8).
88. Flow 13; same locality as Lipman and Moench (1972, table 1, No. 7).
89. Flow 3? Rio Paguete, about 1 km northeast of Evans Ranch.
90. Flow 5? Same locality as 89.
91. Flow 6; same locality as 89.
92. Flow 8? Same locality as 89.
93. Flow 9; see Lipman and Moench (1972, table 1, No. 9).
94. Flow 11; see Lipman and Moench (1972, table 1, No. 10).
95. Flow 4? See Lipman and Moench (1972, table 1, No. 6).
96. Flow 4; see Lipman and Moench (1972, table 1, No. 5).
97. Flow 5; same locality as 96.
98. High basalt of La Jara Mesa: Lobo Canyon road, San Mateo quadrangle.
99. Basalt of Horace Mesa; see Lipman and Moench (1972, table 1, No. 11).
100. Flow 12; see Lipman and Moench (1972, table 1, No. 12).
101. Flow 13; see Lipman and Moench (1972, table 1, No. 13).
102. Laguna flow at Laguna, N. Mex., just east of bridge across Rio San Jose.
103. Bluewater flow; roadcut, U.S. 66, about 1.5 km west of Anaconda mill.
104. Bluewater flow; see Lipman and Moench (1972, table 1, No. 16).
105. Fine-grained vesicular flow, southeast end of Zuni uplift; N. Mex. 53, at about 6,800-ft elevation.
106. Olivine-rich flow, N. Mex. 53, at about 7,250 ft just east of Continental Divide.
107. McCarty flow; see Lipman and Moench (1972, table 1, No. 15).
108. McCarty flow; roadcut, U.S. 66, 11 km southeast of Grants, north end of Las Ventanas Ridge.
109. Laguna flow; see Lipman and Moench (1972, table 1, No. 14).
110. Diktytaxitic flow; N. Mex. 6, 8 km southeast of intersection with U.S. 66.
111. Fine-grained porous flow with large olivine phenocrysts; N. Mex. 6, about 10 km east of Rio Puerco.
112. Roadcut, N. Mex. 53, just west of Continental Divide.
113. Junction of Zuni and La Jara Canyons; flow came down La Jara Canyon.
114. Zuni Canyon flow; see Lipman and Moench (1972, table 1, No. 17).
115. High flow, U.S. 85, 1.5 km north of Wagon Mound, N. Mex.
116. High flow, in quarry 2 km east of Wagon Mound.
117. Maxson flow, roadcut, U.S. 85, at hillcrest southeast of Maxson crater.
118. Dense basalt, probably welded spatter; eroded cinder cone 0.5 km north of N. Mex. 120, 13 km northwest of Wagon Mound.
119. Xenocrystic basalt on low mesa; just north of N. Mex. 120, 1.5 km east of Naranjos, N. Mex.
120. Diktytaxitic flow; N. Mex. 21, 1 km south of Ocate.
121. Dense fine-grained flow; N. Mex. 21, about 2 km south of Ojo Felix.
122. Xenocrystic flow; N. Mex. 38, about 3.5 km north of Guadalupe.
123. Basaltic andesite; N. Mex. 38, at pass south of Black Lakes.
124. Basaltic andesite(?); outlet of Black Lake.
125. Low flow; west of U.S. 85, about 9 km north of Wagon Mound, N. Mex.
- 126–127. Northwest end of Mesa de Maya, 5 km south of Tobe, Colo., upper and lower flows.
128. Johnson Mesa, upper flow; roadcut, N. Mex. 72, about 3 km northwest of Windrow Peak at about 8,000-ft elevation.
129. Johnson Mesa, pressure ridge, top of flow; roadcut, just south of intersection with N. Mex. 72, 1.5 km west of Windrow Peak.
- 130–131. Mesa rim, 2.5 km northwest of Capulin cone. No. 130 is top blocky ledge; 131 is lower ledge of denser and finer grained basalt. Probably same locality as that of sample analyzed by Baldwin and Muehlberger (1959, table 4, RBC).
132. East rim of Johnson Mesa; first major roadcut, N. Mex. 72, at about 7,400 ft. Probably same locality as that of sample analyzed by Aoki (1967b, table 1, No. 1).
133. Bartlett Mesa; talus block on slope at Raton Pass, rest area on I-25.
134. Flow from Yankee volcano; south of N. Mex. 72 at Yankee, N. Mex. Approximately same locality as that of samples analyzed by Lee (1922).
135. Mud Hill cinder cone; small fine-grained dense flow on west side.
136. Purvine Mesa flow; from vent No. 4 (south of main line of cones) in Purvine Hills.
137. Bellisle Mountain flow; N. Mex. 72, at west boundary of Union County.
138. East Big Hill; N. Mex. 325, about 5 km northeast of Folsom, N. Mex. May be a dike within the cinder cone.
139. Emory Peak flow; underlies sample 138 at same locality.
140. Emory Peak flow; west end of flow at falls over Baby Capulin flow. Locality of sample analyzed by Baldwin and Muehlberger (1959, table 4, EP).
141. Bellisle Mountain flow; N. Mex. 325, about 3 km northeast of Folsom, N. Mex.
142. Robinson Mountain flow; about 4 km west of Folsom, N. Mex., at about 6,400-ft elevation, in tributary of Dry Cimarron Creek; fine diktytaxitic texture.
143. Jose Butte flow, as mapped by Baldwin and Muehlberger (1959), but appears continuous with Robinson Mountain flow locality 142; collected 0.5 km upstream from locality 142.
144. Van Cleve flow, at Weatherly Lake; about same locality as that of sample analyzed by Baldwin and Muehlberger (1959, table 4, VC).
145. Gaps flow; 5 km south of Weatherly Lake, from scarp west of road; fine-grained diktytaxitic texture.
146. At road intersection, 1.5 km northeast of Greenville, N. Mex.; fairly coarse diktytaxitic texture.
147. Flow from Cienquilla del Barro Mountain; at railway cut, 1.5 km east of Mount Dora. A few large quartz xenocrysts; some zeolites in vesicles.
148. Flow at Royce; along gravel road, about 0.1 km north of railway. Some calcite-filled vesicles. Near locality of sample analyzed by Aoki (1967b, table 1, No. 7).
149. Roadcut, N. Mex. 370, about 3 km northwest of Clayton, N. Mex.
150. Mesa rim flow, south of Clayton Reservoir, on access road.
151. Middle-level flow; N. Mex. 370, about 4 km northwest of Rabbit Ear Mountain, at 4,900-ft elevation; erupted from Rabbit Ear vent.
152. High flow; N. Mex. 370, about 1.5 km west of Rabbit Ear Mountain, at 4,500 ft; erupted from Rabbit Ear vent.
153. Carrizo flow; N. Mex. 56, about 20 km southwest of Clayton, N. Mex.
154. Flow at southeast edge of San Carlos Hills; N. Mex. 56, just west of Passamonte Ranch.
155. Similar flow; N. Mex. 56, about 4 km east of Gladstone, N. Mex.
156. Higher level flow; N. Mex. 56, about 10 km east of Gladstone, N. Mex.
157. Capulin cone; dense flow, at campground on south side of cone.
158. Xenocrystic flow from Capulin cone; roadcut, N. Mex. 64. Probably locality of sample analyzed by Aoki (1967b, table 1, No. 8).
159. Capulin cone; flow or large block within scoria fall on south side of cone.
- 160–161. Capulin cone; scoria fall along road 0.1 km north of crater parking lot. No. 160 is red cinders; 161, black cinders.
162. Capulin cone; xenocrystic flow on west side; roadcut, N. Mex. 325.
163. Baby Capulin; flow on west side of cone, about 0.1 km east of N. Mex. 325.

- 164–165. Baby Capulin; scoria fall, east quarry pit. No. 164 is red cinders; 165, black cinders.
 166–167. Twin Mountain; scoria fall, east quarry pit. No. 166 is red cinders; 167, black cinders.
 168. Flow probably from west Purvine Hill vent; 0.5 km east of Twin Mountain, on cinder quarry road.
 169. Twin Mountain flow; tumulus south of paved road, just north of Twin Mountain.
 170. Baby Capulin flow near toe; along Cimarron River south of Devoys Peak. Probably near locality of sample analyzed by Baldwin and Muehlberger (1959, table 4, BC).

REFERENCES CITED

- Aoki, Ken-ichiro, 1967a, Petrography and petrochemistry of latest Pliocene olivine-tholeiites of Taos area, northern New Mexico, U.S.A.: *Contr. Mineralogy and Petrology*, v. 14, no. 3, p. 190–203.
 ——— 1967b, Alkaline and calc-alkaline basalts from Capulin Mountain, northeastern New Mexico, U.S.A.: *Japanese Assoc. Mineralogists, Petrologists and Econ. Geologists Jour.*, v. 58, no. 4, p. 143–151.
 Baldwin, Brewster, and Muehlberger, W. R., 1959, *Geologic studies of Union County, New Mexico*: New Mexico Bur. Mines and Mineral Resources Bull. 63, 171 p.
 Best, M. G., and Brimhall, W. H., 1970, Late Cenozoic basalt types in the western Grand Canyon region, in Hamblin, W. K., and Best, M. G., eds., *The western Grand Canyon district*: Utah Geol. Soc. Guidebook 23, p. 57–74.
 Best, M. G., Hamblin, W. K., and Brimhall, W. H., 1966, Preliminary petrology and chemistry of Late Cenozoic basalts in the western Grand Canyon region: *Brigham Young Univ. Geology Studies*, v. 13, p. 109–123.
 ——— 1969, Late Cenozoic basalts on the western margin of the Colorado Plateaus, Utah and Arizona: *Brigham Young Univ. Research Rept.* 69-1, 39 p.
 Bryan, Kirk, 1938, Geology and ground water conditions of the Rio Grande depression in Colorado and New Mexico, in *Regional planning*, Pt. 6, Rio Grande joint investigation in the upper Rio Grande Basin: Washington, Natl. Resources Comm., v. 1, pt. 2, sec. 1, p. 197–225.
 Butler, A. P., Jr., 1971, Tertiary volcanic stratigraphy of the eastern Tuzas Mountains, southwest of the San Luis Valley, Colorado-New Mexico, in *New Mexico Geol. Soc. Guidebook 22d Field Conf.*: p. 289–300.
 Chapin, C. E., 1971, The Rio Grande Rift, Pt. I—Modifications and additions, in *New Mexico Geol. Soc. Guidebook 22d Field Conf.*: p. 191–202.
 Christiansen, R. L., and Lipman, P. W., 1972, Cenozoic volcanism and plate-tectonic evolution of the Western United States—II. Late Cenozoic: *Royal Soc. London Philos. Trans.*, v. 271, no. 1213, p. 249–284.
 Cohee, G. V., chm., and others, 1961, Tectonic map of the United States, exclusive of Alaska and Hawaii: U.S. Geol. Survey and Am. Assoc. Petroleum Geologists, scale 1:2,500,000 [1962].
 Cohen, L. H., Ito, Keisuke, and Kennedy, G. C., 1967, Melting and phase relations in an anhydrous basalt to 40 kilobars: *Am. Jour. Sci.*, v. 265, no. 6, p. 475–518.
 Collins, R. F., 1949, Volcanic rocks of northeastern New Mexico: *Geol. Soc. America Bull.*, v. 60, no. 6, p. 1017–1040.
 Condie, K. C., and Barsky, C. K., 1972, Origin of Quaternary basalts from the Black Rock Desert region, Utah: *Geol. Soc. America Bull.*, v. 83, no. 2, p. 333–352.
 Doe, B. R., Lipman, P. W., Hedge, C. E., and Kurasawa, Hajime, 1969, Primitive and contaminated basalts from the southern Rocky Mountains, U.S.A.: *Contr. Mineralogy and Petrology*, v. 21, no. 2, p. 142–156.
 Doney, H. H., 1968, Geology of the Cebolla quadrangle, Rio Arriba County, New Mexico: *New Mexico State Bur. Mines and Mineral Resources Bull.* 92, 114 p.
 Embree, G. F., 1970, Lateral and vertical variations in a Quaternary basalt flow—Petrography and chemistry of the Gunlock flow, southwestern Utah: *Brigham Young Univ. Geology Studies*, v. 17, pt. 1, p. 67–115.
 Engel, A. E. J., Engel, C. G., and Havens, R. G., 1965, Chemical characteristics of oceanic basalts and the upper mantle: *Geol. Soc. America Bull.*, v. 76, no. 7, p. 719–734.
 Fanale, F. P., and Nash, D. B., 1971, Potassium-uranium systematics of Apollo 11 and Apollo 12 samples—Implications for lunar material history: *Science*, v. 171, no. 3968, p. 282–284.
 Fisher, D. E., 1970, Homogenized fission track analysis of uranium in some ultramafic rocks of known potassium content: *Geochim. et Cosmochim. Acta*, v. 34, no. 5, p. 630–634.
 Gaca, J. R., and Karig, D. E., 1966, Gravity survey in the San Luis Valley area, Colorado: U.S. Geol. Survey open-file report, 43 p.
 Gottfried, David, Moore, Roosevelt, and Campbell, Esma, 1963, Thorium and uranium in some volcanic rocks from the circum-Pacific province: Art. 202 in *U.S. Geol. Survey Prof. Paper 450-E*, p. E85–E89.
 Green, D. H., 1968, Origin of basaltic magmas, in Hess, H. H., and Poldervaart, Arie, eds., *Basalts—The Poldervaart treatise on rocks of basaltic composition*, V. 2: New York and London, Intersci. Publishers, p. 835–862.
 Green, D. H., and Ringwood, A. E., 1967, The genesis of basaltic magmas: *Contr. Mineralogy and Petrology*, v. 15, no. 2, p. 103–190.
 Hedge, C. E., and Knight, R. J., 1969, Lead and strontium isotopes in volcanic rocks from northern Honshu, Japan: *Geochem. Jour.*, v. 3, no. 1, p. 15–24.
 Hedge, C. E., and Lipman, P. W., 1972, Upper Cenozoic basalts of the southern Rocky Mountain region—Pt. 2, Strontium isotopes and the geochemistry of Sr, Rb, and Ba: *Geol. Soc. America, Cordilleran Sec., Abs. with Programs*, v. 4, no. 3, p. 169.
 Heier, K. S., Compston, W., and McDougall, I., 1965, Thorium and uranium concentrations, and the isotopic composition of strontium in the differentiated Tasmanian dolerites: *Geochim. et Cosmochim. Acta*, v. 29, no. 6, p. 643–659.
 Heier, K. S., McDougall, Ian, and Adams, J. A. S., 1964, Thorium, uranium and potassium concentrations in Hawaiian lavas: *Nature*, v. 201, no. 4916, p. 254–256.
 Heier, K. S., and Rogers, J. J. W., 1963, Radiometric determination of thorium, uranium and potassium in basalts and in two magmatic differentiation series: *Geochim. et Cosmochim. Acta*, v. 27, no. 2, p. 137–154.
 Jackson, E. D., and Wright, T. L., 1970, Xenoliths in the Honolulu volcanic series, Hawaii: *Jour. Petrology*, v. 11, pt. 2, p. 405–430.
 Kay, R., Hubbard, N. J., and Gast, P. W., 1970, Chemical characteristics and origin of oceanic ridge volcanic rocks: *Jour. Geophys. Research*, v. 75, no. 8, p. 1585–1614.
 Kelley, V. C., 1952, Tectonics of the Rio Grande depression of central New Mexico, in *New Mexico Geol. Soc. Guidebook 3d Field Conf.*, Rio Grande Country, central New Mexico, 1952: p. 93–105.
 ——— 1956, The Rio Grande depression from Taos to Santa Fe, in *New Mexico Geol. Soc. Guidebook 7th Field Conf.*, southeastern Sangre de Cristo Mountains, New Mexico, 1956: p. 109–114.
 Kudo, A. M., Aoki, Ken-ichiro, and Brookins, D. G., 1971, The origin of Pliocene-Holocene basalts of New Mexico in the light of strontium-isotope and major-element abundances: *Earth and Planetary Sci. Letters*, v. 13, no. 1, p. 200–240.
 Kuno, Hisashi, 1959, Origin of Cenozoic petrographic provinces of Japan and surrounding areas: *Bull. Volcanol.*, ser. 2, v. 20, p. 37–76.

- 1968, Differentiation of basalt magmas, in Hess, H. H., and Poldervaart, Arie, eds., *Basalts—The Poldervaart treatise on rocks of basaltic composition*, V. 2: New York and London, Interscience Publishers, p. 623–688.
- Kushiro, Ikuo, 1968, Compositions of magmas formed by partial zone melting of the earth's upper mantle: *Jour. Geophys. Research*, v. 73, no. 2, p. 619–634.
- Larsen, E. S., Jr., and Cross, Whitman, 1956, Geology and petrology of the San Juan region, southwestern Colorado: U.S. Geol. Survey Prof. Paper 258, 303 p.
- Larsen, E. S., Irving, John, Gonyer, F. A., and Larsen, E. S., 3d, 1938, Petrologic results of a study of the minerals from the Tertiary volcanic rocks of the San Juan region, Colorado: *Am. Mineralogist*, v. 23, no. 7, p. 417–429.
- Laughlin, A. W., Brookins, D. G., and Carden, J. R., 1972, Variations in the initial strontium ratios of a single basalt flow: *Earth and Planetary Sci. Letters*, v. 14, p. 79–82.
- Laughlin, A. W., Brookins, D. G., Kudo, A. M., and Causey, J. D., 1971, Chemical and strontium isotopic investigations of ultramafic inclusions and basalt, Bandera Crater, New Mexico: *Geochim. et Cosmochim. Acta*, v. 35, no. 1, p. 107–113.
- Lee, W. T., 1922, Description of the Raton, Brilliant, and Koehler quadrangles [New Mexico]: U.S. Geol. Survey Geol. Atlas Folio 214.
- Leeman, W. P., and Rogers, J. W. J., 1970, Late Cenozoic alkali-olivine basalts of the basin-range province, USA: *Contr. Mineralogy and Petrology*, v. 25, p. 1–24.
- Lipman, P. W., 1969, Alkalic and tholeiitic basaltic volcanism related to the Rio Grande depression, southern Colorado and northern New Mexico: *Geol. Soc. America Bull.*, v. 80, no. 7, p. 1343–1353.
- Lipman, P. W., and Moench, R. H., 1972, Basalts of the Mount Taylor volcanic field, New Mexico: *Geol. Soc. America Bull.*, v. 83, no. 5, p. 1335–1344.
- Lipman, P. W., Steven, T. A., and Mehnert, H. H., 1970, Volcanic history of the San Juan Mountains, Colorado, as indicated by potassium-argon dating: *Geol. Soc. America Bull.*, v. 81, no. 8, p. 2329–2352.
- Macdonald, G. A., and Katsura, T., 1964, Chemical composition of Hawaiian lavas: *Jour. Petrology*, v. 5, pt. 1, p. 82–133.
- Nicholls, J., Carmichael, I. S. E., and Stormer, J. C., Jr., 1971, Silica activity and P_{total} in igneous rocks: *Contr. Mineralogy and Petrology*, v. 33, no. 1, p. 1–20.
- O'Hara, M. J., and Yoder, H. S., Jr., 1967, Formation and fractionation of basic magmas at high pressures: *Scottish Jour. Geology*, v. 3, pt. 1, p. 67–117.
- Ozima, M., Kono, M., Kaneoka, I., Kinoshita, H., Kobayashi, Kazuo, Nagata, T., Larson, E. E., and Strangway, D. W., 1967, Paleomagnetism and potassium-argon ages of some volcanic rocks from the Rio Grande gorge, New Mexico: *Jour. Geophys. Research*, v. 72, no. 10, p. 2615–2622.
- Patterson, Claire, and Tatsumoto, M., 1964, The significance of lead isotopes in detrital feldspar with respect to chemical differentiation within the earth's mantle: *Geochim. et Cosmochim. Acta*, v. 28, no. 1, p. 1–22.
- Powers, H. A., 1935, Differentiation of Hawaiian lavas: *Am. Jour. Sci.*, 5th ser., v. 30, no. 175, p. 57–71.
- Renault, Jacques, 1970, Major-element variations in the Potrillo, Carrizozo, and McCartys basalt fields, New Mexico: *New Mexico Bur. Mines and Mineral Resources Circ.* 113, 22 p.
- Russell, R. D., and Farquhar, R. M., 1960, Dating galenas by means of their isotopic constitutions—II: *Geochim. et Cosmochim. Acta*, v. 19, no. 1, p. 41–52.
- Schonfeld, Ernest, 1966, Alpha M—An improved computer program for determining radioisotopes by least-squares resolution of the gamma-ray spectra: U.S. Natl. Lab. Oak Ridge ORNL-3975, 42 p.
- Steven, T. A., and Epis, R. C., 1968, Oligocene volcanism in south-central Colorado, in *Cenozoic volcanism in the southern Rocky Mountains*: *Colorado School Mines Quart.*, v. 63, no. 3, p. 241–258.
- Stobbe, H. R., 1949, Petrology of volcanic rocks of northeastern New Mexico: *Geol. Soc. America Bull.*, v. 60, no. 6, p. 1041–1095.
- Stormer, J. C., Jr., 1972, Ages and nature of volcanic activity on the southern High Plains, New Mexico and Colorado: *Geol. Soc. America Bull.*, v. 83, no. 8, p. 2443–2448.
- Strangway, D. W., Larson, E. E., and York D., 1969, A middle Tertiary magnetic transition in northwestern Colorado [abs.]: *EOS (Am. Geophys. Union Trans.)*, v. 50, no. 4, p. 131.
- Sugimura, Arata, 1960, Zonal arrangement of some geophysical and petrological features in Japan and its environs: *Tokyo Univ. Fac. Sci. Jour.*, sec. 2, v. 12, pt. 2 p. 133–153.
- Tatsumoto, M., 1966a, Genetic relations of oceanic basalts as indicated by lead isotopes: *Science*, v. 153, no. 3740, p. 1094–1101.
- 1966b, Isotopic composition of lead in volcanic rocks from Hawaii, Iwo-Jima and Japan: *Jour. Geophys. Research*, v. 71, no. 6, p. 1721–1733.
- Tilling, R. I., and Gottfried, David, 1969, Distribution of thorium, uranium, and potassium in igneous rocks of the Boulder batholith region, Montana, and its bearing on radiogenic heat production and heat flow: U.S. Geol. Survey Prof. Paper 614-E, 29 p.
- Watkins, N. D., and Haggerty, S. E., 1967, Primary oxidation variation and petrogenesis in a single lava: *Contr. Mineralogy and Petrology*, v. 15, p. 251–271.
- Watkins, N. D., Holmes, C. W., and Haggerty, S. E., 1967, Primary oxidation variation and distribution of uranium and thorium in a lava flow: *Science*, v. 155, no. 3762, p. 579–581.
- Williams, Howel, 1936, Pliocene volcanoes of the Navajo-Hopi country: *Geol. Soc. America Bull.*, v. 47, no. 1, p. 111–172.
- Wise, W. S., 1969, Origin of basaltic magmas in the Mojave desert area, California: *Contr. Mineralogy and Petrology*, v. 23, p. 53–64.
- Yoder, H. S., Jr., and Tilley, C. E., 1962, Origin of basalt magmas—An experimental study of natural and synthetic rock systems: *Jour. Petrology*, v. 3, pt. 3, p. 342–532.



A PRECAMBRIAN DIAMICTITE BELOW THE BASE OF THE STILLWATER COMPLEX, SOUTHWESTERN MONTANA

By NORMAN J PAGE and RANDOLPH A. KOSKI, Menlo Park, Calif.

Abstract.—The metasedimentary rocks of Precambrian age below the base of the Stillwater Complex, southwestern Montana, contain a metamorphosed diamictite similar to diamictite in strata of late Precambrian and Early Cambrian age in Canada and the Western United States. The diamictite consists of a quartz-cordierite matrix containing an average 10–15 percent of rock fragments diverse in shape, size, angularity, lithologic types, and textures. The diamictite unit is poorly sorted, crops out discontinuously for 14 miles, and locally has a crude layering containing dropstones. Its origin is debatable, but the rock is suggestive of glacial marine deposition. The minimum age of the diamictite of the complex is 2,750 m.y. from U-Pb determination on zircon of intrusive quartz monzonite, the maximum 3,140 m.y. as determined on zircon from metasedimentary rocks interbedded with the diamictite.

Recently Gabrielse in Canada (1967, 1972) and Crittenden and others in the Western United States (1971) have called attention to a widespread but discontinuous diamictite in strata of late Precambrian and Early Cambrian age. This diamictite is commonly interpreted as glacial in origin (Aalto, 1971; Crittenden and others, 1971; Troxel, 1967) and is used as a synchronous unit for correlation in Western North America (Stewart, 1972). Similar diamictites occur in the hornfelsed metasedimentary rocks that form the basement below the Stillwater Complex of Precambrian age in southwestern Montana. As the age of the diamictite-bearing metasediments by U-Pb determinations of Nunes and Tilton (1971) on zircon is between 2,750 and 3,140 m.y., these pre-Stillwater diamictites are not correlative with those in the upper Precambrian, although they may be similar in aspect and origin. Because the aspect of the diamictites below the Stillwater Complex is distinctive, this report presents a detailed description of the rocks for comparison with other diamictites. Such rocks might furnish a lithologic basis for correlation in the older Precambrian strata.

The fragmental rocks, though now hornfelsed, will be referred to in this paper as diamictite, a term used to describe a nonsorted rock of sedimentary origin consisting of sand-size and (or) larger particles in a mud matrix (modified from Flint and others, 1960). Diamictites crop out discontinuously along a northwest trend for 14 or 15 miles, some immediately

adjacent to the Basal zone of the Stillwater, others almost a mile from the Basal zone (fig. 1). Owing to the complexity of the geology and the sparsity of outcrops (Page and Nokleberg, 1970), continuity of the diamictite over the extent of the trend cannot be proved, but within areas of continuous outcrop and simple structure, diamictite units 100–200 feet thick can be traced in the hornfelsed metasedimentary rocks.

Although the stratigraphic sequence within the hornfelsed metasedimentary rocks is not well established because of the structural complexity, the rocks contain a magnetite-silicate mineral iron-formation; a blue-gray metaquartzite; a sequence of layered rocks that contain relict small-scale crossbedding, graded bedding, and cut-and-fill structures; and sequences of finely banded rocks. But most of the exposed hornfelses are massive, structureless rocks. The position of the diamictites in the sequence is difficult to establish except on a local scale, but their known occurrences appear to be at the same stratigraphic horizon.

The metasedimentary rocks have had a long, complicated geologic history that includes the following sequence of events: (1) at least two generations of folding (Page and Nokleberg, 1972), (2) intrusion and hornfelsing by the basaltic magma that formed the Stillwater Complex (Jones and others, 1960), (3) local intrusion by quartz-monzonites and aplites (Page and Nokleberg, 1970), (4) possible low-grade regional metamorphism, deformation, faulting, and intrusion of diabase dikes (Page and Nokleberg, 1972), and (5) normal and thrust faulting (Jones and others, 1960). Events 1 to 4 occurred in the Precambrian, event 5 during Laramide time (Jones and others, 1960). The geologic complexity introduced by these events must be borne in mind throughout the discussion of the diamictite rocks.

GEOLOGIC OCCURRENCE AND METHODOLOGY

Two of the better exposed and more accessible areas of diamictite were chosen for study, one near the Mountain View area, the other at the head of Bobcat Creek (fig. 1). The Mountain View area was studied by mapping the fragmental rocks exposed in five roadcuts across a cliff face in Verdigris Creek on a geologic base map at a scale of 1 inch to 100 feet

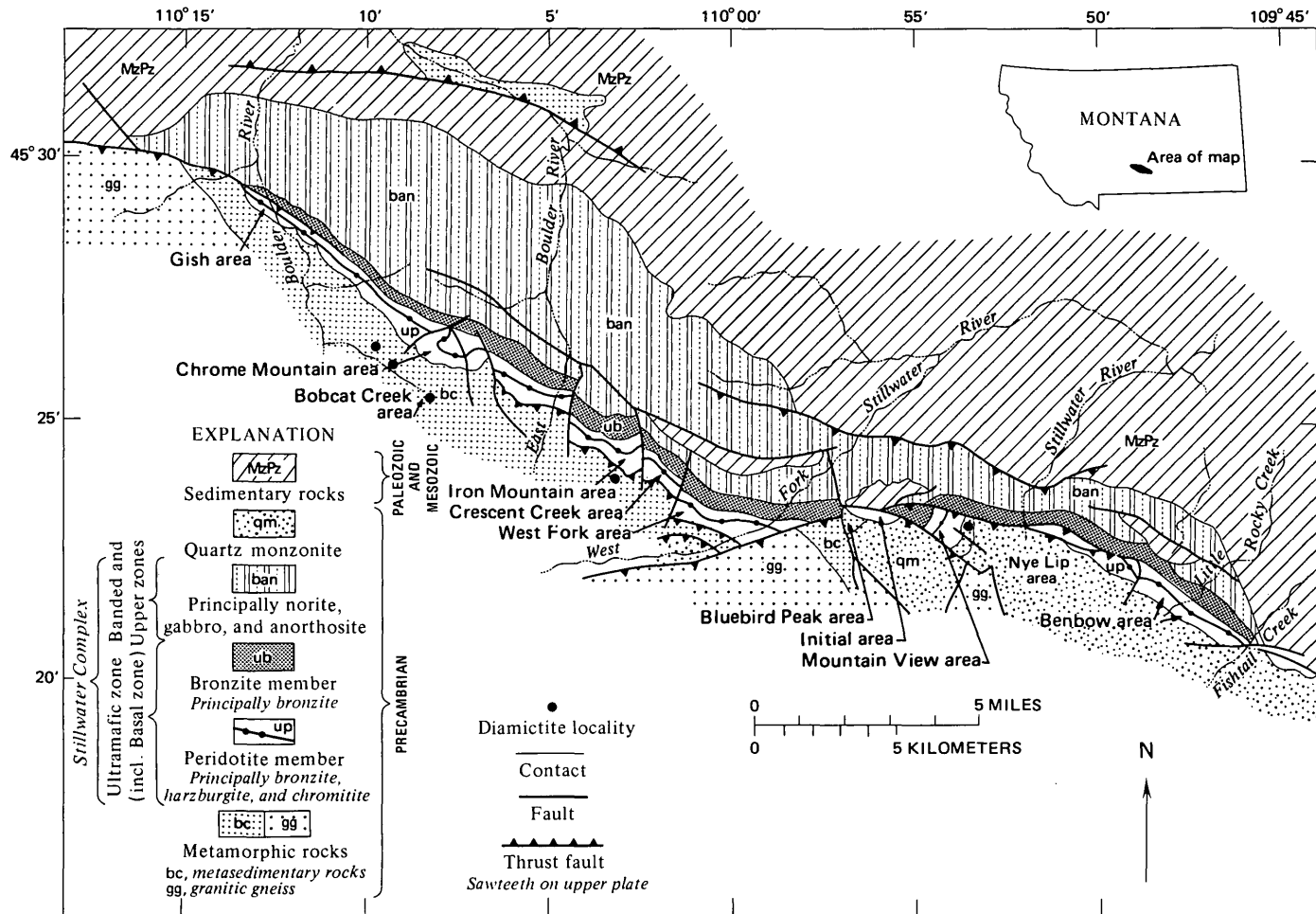


Figure 1.—Geologic sketch map of the Stillwater Complex, Montana, showing occurrences of diamictite. After Page and Nokleberg (1970).

(Peoples and others, 1954) and in greater detail at a scale of 1 inch to 20 feet. This area (fig. 2) was selected for study partly because it is intruded by noritic rocks of the Basal zone of the Stillwater Complex. The diamictite forms a layer 100–150 feet wide between finely layered hornfelses and massive structureless hornfelses that probably form a limb of a complex fold. No interfingering between the different rock types was observed.

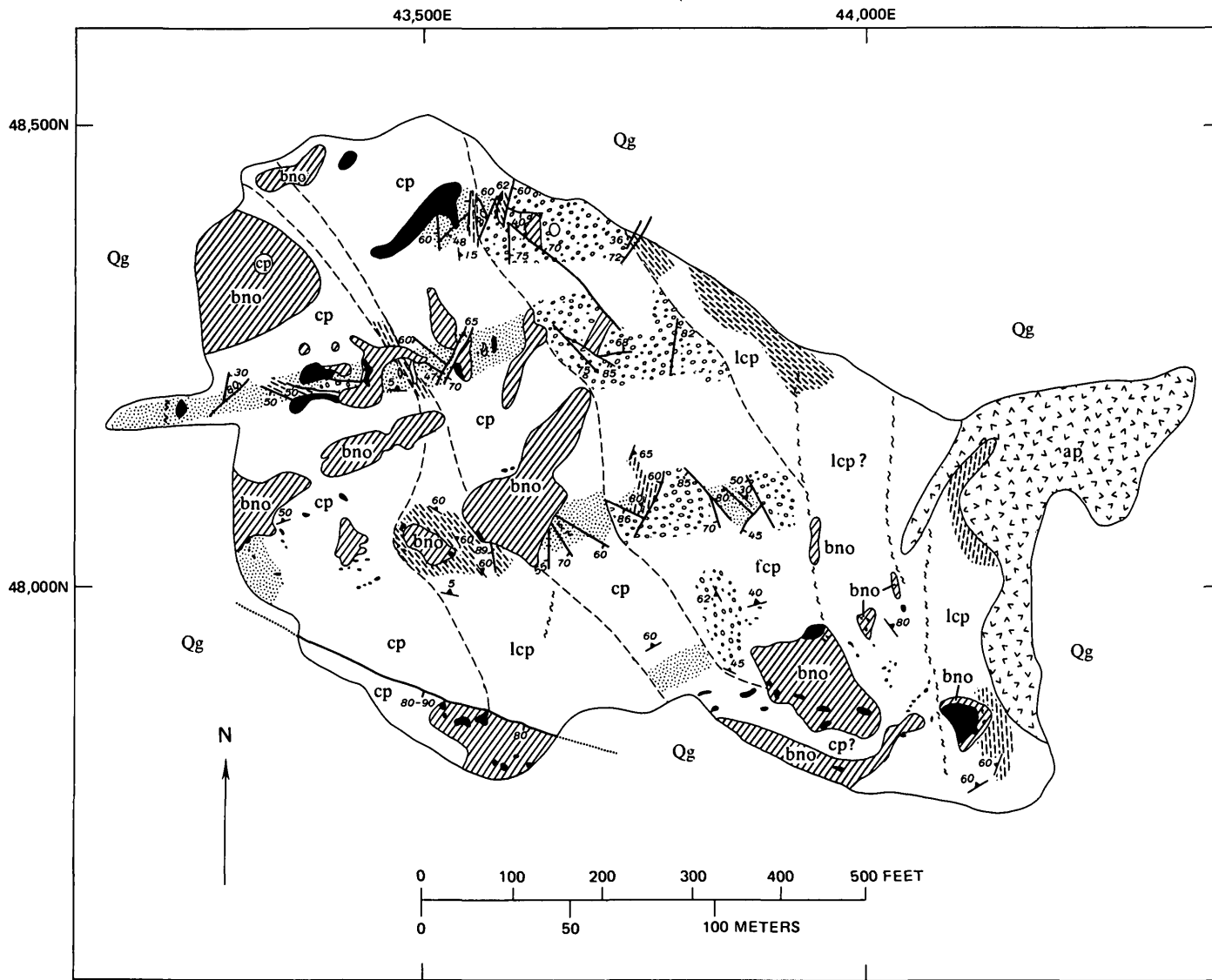
Exposures at the Bobcat Creek locality (fig. 1) are in cliffs at the head of the creek about three-fifths of a mile south of the Basal zone of the Stillwater Complex. The locality is between two faults and apparently is part of a continuous unfaulted section from the Basal zone to the diamictite. A reconstructed geologic column based on Page and Nokleberg's map (1970) indicates that the diamictite is separated from the Stillwater Complex (fig. 3) by about 2,860 feet of diabase massive cordierite-orthopyroxene-biotite-quartz-plagioclase hornfels, blue metaquartzite, and iron-formation. At this locality the diamictite, matrix and megaclasts, was examined in nine subareas totalling more than 1,200 sq ft; all visible fragments were cataloged.

Other localities shown on the geologic sketch map (fig. 1) were not studied in detail but were briefly examined during mapping.

At both localities all visible megaclasts, about an eighth of an inch to tens of feet in diameter, were described and cataloged according to texture, size (maximum and minimum dimensions), shape, angularity, and probable original rock type before metamorphism. Examination of the megaclasts in three dimensions in the field was hindered because the outcrops were in cliffs and roadcuts, where most exposures were two-dimensional, and because there is little differential weathering between the matrix and the megaclasts. Where possible, megaclast attitudes were estimated in order to determine structural orientation (long dimension or planar feature) within the diamictite. Samples were collected for thin-section and analytical studies.

DESCRIPTION OF THE DIAMICTITE

The general aspect presented by outcrops of the diamictite is one of a minor proportion of megaclasts with diverse shapes,



EXPLANATION

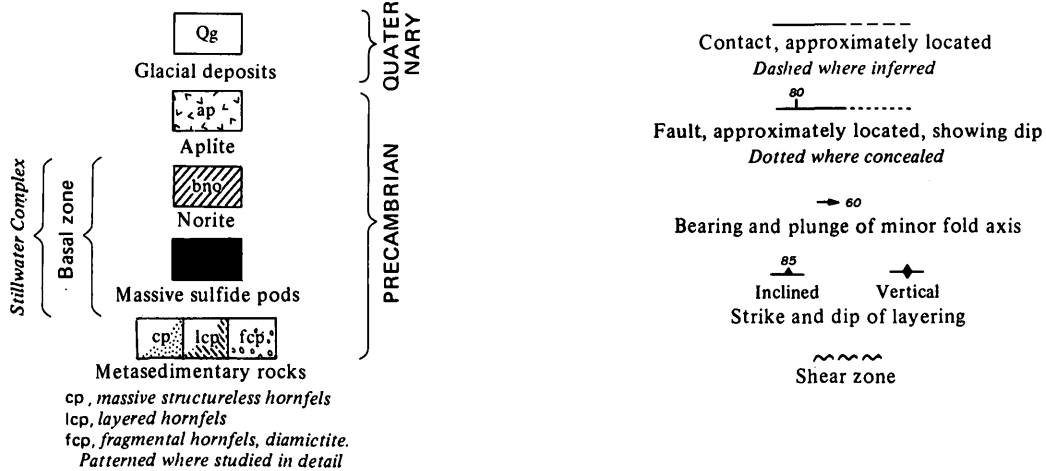


Figure 2.—Geologic map of the Mountain View area, showing outcrop north of Verdigris Creek (modified from Peoples and others, 1954; coordinates refer to coordinates on their map).

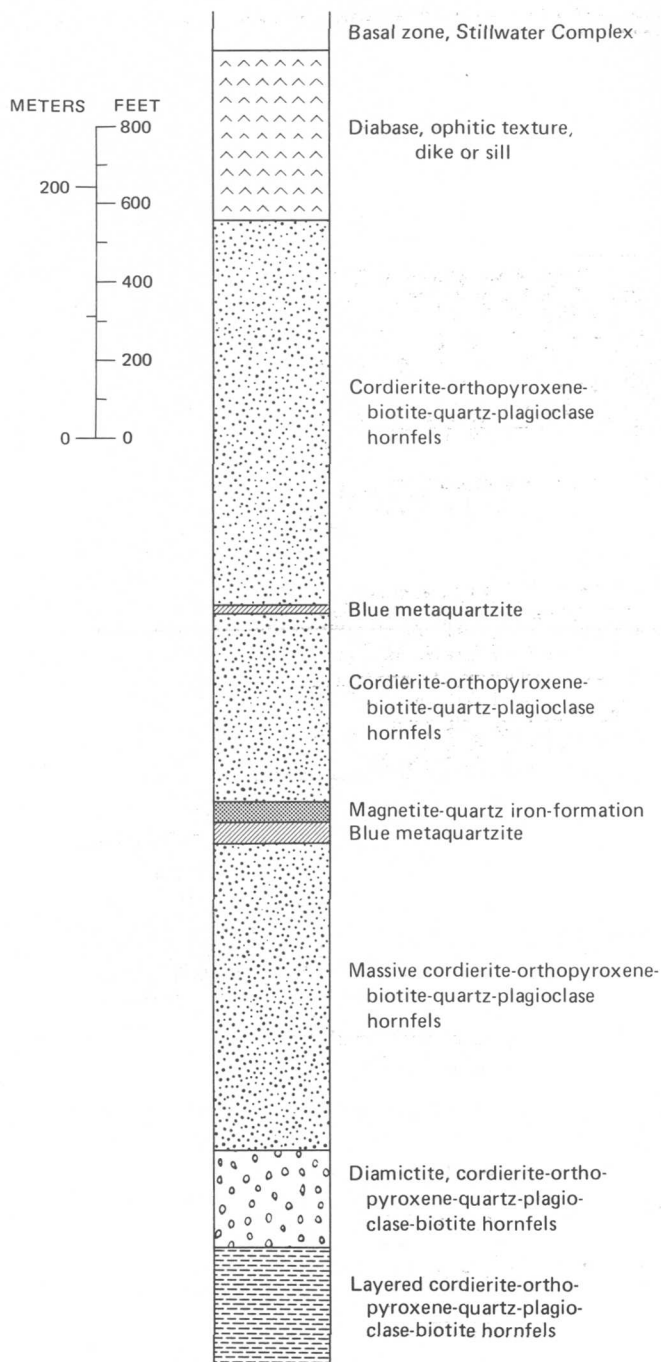


Figure 3.—Reconstructed geologic column for the Bobcat Creek locality, based on an approximate north-south section drawn from Page and Nokleberg (1970).

sizes, and angularity floating in a dark, fine-grained matrix (fig. 4). Some zones contain more megaclasts than others, suggesting weak stratification. Estimates of the volume of megaclasts in the matrix from subareas at the two localities range from less than 1 percent to 65 percent (table 1) but average 10 to 15 percent. Two methods were used to make these estimates: one was to measure the surface area of rock, sum the area



Figure 4.—Diamictite outcrop in the Mountain View area. Maximum length of visible megaclasts 30 cm.

Table 1.—Estimated volume percentages of megaclasts in matrix at the Mountain View and Bobcat Creek localities

Subarea	Volume of megaclasts	
	Measured by areas	Visual estimate
Mountain View locality		
Traverse 1	1.4
2	55.4
3	6.4
4	2.3
Area 2	30.0
3	<1-65
4a	<5
4c	25
5	50
Bobcat Creek locality		
Area 1	3.8
2	8.1
3	13.5
4	.3
5	.3
6	14.1
7	11
8	12.8

covered by megaclasts, and derive a volume percentage; the other was to estimate the megaclasts visually.

Properties of Megaclasts

Textural varieties

The abundance of visible megaclasts in the diamictite, cataloged by texture recognized in the field, is given in table 2 for the Mountain View and Bobcat Creek localities. All of the textures are relict, and all megaclasts except the metaquartzites are composed of varying proportions of cordierite, orthopyroxene, plagioclase, biotite, and quartz. It should be emphasized that classification based on texture is by necessity rather crude. One of our main objectives, however, is to point

Table 2.—Abundance of rock megaclasts classified by textural categories at the Mountain View and Bobcat Creek localities

[Based on megaclast counts in the outcrops]

Textural category	Mountain View		Bobcat Creek	
	Number	Percentage	Number	Percentage
Layered, banded, or foliated.	101	35.2	40	36.4
Massive, homogeneous.	60	20.9	48	43.6
Blue or gray metaquartzite.	50	17.4	11	10
Gneissic	45	15.7	2	1.8
Schistose	8	2.8	0	0
Granitoid, equigranular.	13	4.5	4	3.6
Volcanic	0	0	5	4.5
Not classified	10	3.5	0	0
Total	287	100	110	99.9

out the heterogeneity of megaclasts found in the diamictite, a diversity that has survived several periods of intense deformation and metamorphism. The textures and mineralogy cannot be used directly to imply the source of the megaclasts as in sedimentary rocks.

Banded, layered, or foliated megaclasts are most easily recognized and one of the more abundant types. The layering consists of two types: (1) alternating dark and light laminations reflecting varying percentages of plagioclase, cordierite, and orthopyroxene; and (2) layering formed by abrupt changes in grain size. The layers are typically undeformed and display no sedimentary structures; a few banded megaclasts appear to contain folds or slump structures. Figure 5 shows several examples. Layered megaclasts showing effects of deformation are uncommon, but a number of clasts at Bobcat Creek (fig. 5E) display a peculiar convolute (disharmonic?) folding of alternating light and dark layers with attenuated fold limbs. Some of these distorted layers are finely laminated or massive and somewhat coarser than intervening thicker massive layers of very fine grained material. Septa of light massive material often terminate or penetrate darker seams. Whether this irregular deformation occurred before, during, or after emplacement of the diamictite is not known.

Layers within megaclasts range in thickness from less than 1 mm to greater than 15 cm, a single megaclast containing two layers or more. Some of the more finely layered megaclasts are suggestive of varves formed in lacustrine environments; other, coarsely layered megaclasts resemble interlayered sandstones and siltstones.

Of the samples examined, the rock exhibiting the most spectacular layering in a megaclast at the Mountain View locality is the block shown as figure 5F, which contains a near-linear contact between two contrasting fabrics, one fine-grained, massive, and cordierite-rich, the other medium-grained and granitoid, with prismatic, euhedral pyroxenes interlocked with plagioclase. The coarse segment of the megaclast appears to be devoid of cordierite. Closer examination of the contact reveals several tongue-like protuberances of

coarser grained material penetrating approximately 0.5 cm into the massive portion of the fragment. Neither segment of this clast resembles the matrix texturally, and the megaclast boundaries are clearly marked. Other binary fragments were observed in the outcrop.

Massive megaclasts, the other most abundant category, are fine grained, dense, rich in cordierite and plagioclase or combinations of these minerals, and have a texture closely resembling that of the granofels matrix. These blocks are commonly somewhat bleached, especially near their perimeters, owing to surface weathering of cordierite and plagioclase and to a decrease of quartz in the megaclast. Some staining of megaclasts results from oxidation of sulfides and iron-bearing silicates. Microscopic examination of massive megaclasts reveals a relict texture with plagioclase and rounded or sub-rounded grains of quartz surrounded by orthopyroxene and cordierite. Locally the orthopyroxene exhibits sieve texture (fig. 5H). Where pyroxene is less common, quartz and cordierite have a distinct arrangement of isolated, round to subround grains of quartz being surrounded by clots or patches in which individual cordierite grains form a mosaic. The massive nature of these megaclasts at the outcrop is less apparent in thin section.

Megaclasts with a metamorphic fabric distinct from the granofels matrix are the third most abundant group at both localities. Most conspicuous are the blue and gray metaquartzite clasts that are easily spotted in the field and occur in slightly greater abundance at the Mountain View locality. Although common throughout the localities, generally they are so thoroughly dispersed that rarely do several metaquartzite megaclasts occur in 4 or 5 sq ft of outcrop. Textures are typically coarse grained with intergrown crystals of granular quartz and a few accessory minerals.

Megaclasts with a gneissic texture have a unique color banding resulting from differing proportions of quartz, cordierite, and orthopyroxene. The bands usually parallel the longest particle axes. In some megaclasts the variation in thickness of individual bands is slight, in others the bands are discontinuous and form lenses and "eyes" suggestive of augen gneisses. Light bands tend to have greater thickness, producing a pronounced color contrast between clast and matrix.

More difficult to distinguish at the outcrop are schistose megaclasts, so termed because planar orientation of fine-grained biotite results in the development of a pronounced cleavage or fracture.

The fourth group of megaclasts have textures that resemble those in igneous rocks. The majority of igneouslike megaclasts are granitoid or coarse-grained equigranular; the equant grains are easily observed without a hand lens and show interlocking and penetrating relations. No foliation or banding was seen in those megaclasts roughly classed as igneous. Megaclasts unique to Bobcat Creek have a blastoporphyrict texture consisting of sparse fine- to medium-grained phenocrysts of plagioclase set in a fine-grained massive matrix of plagioclase, cordierite,

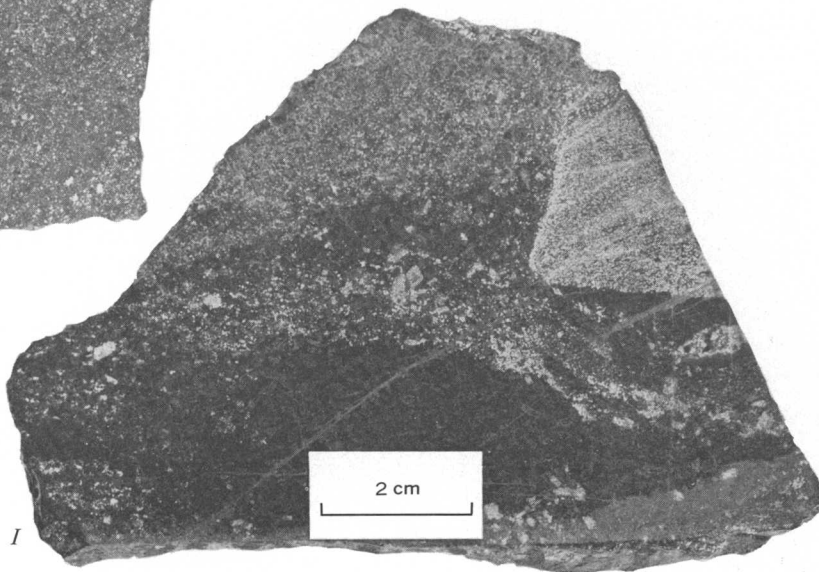
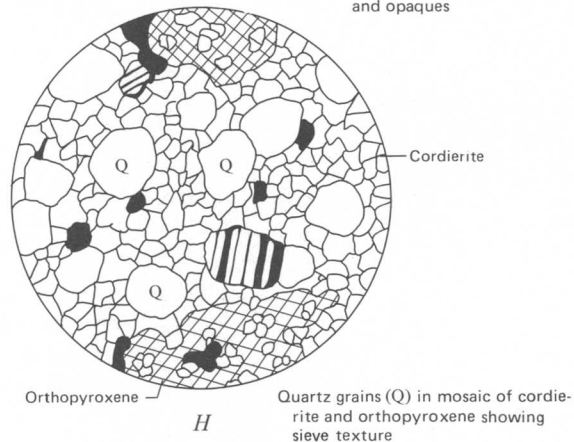
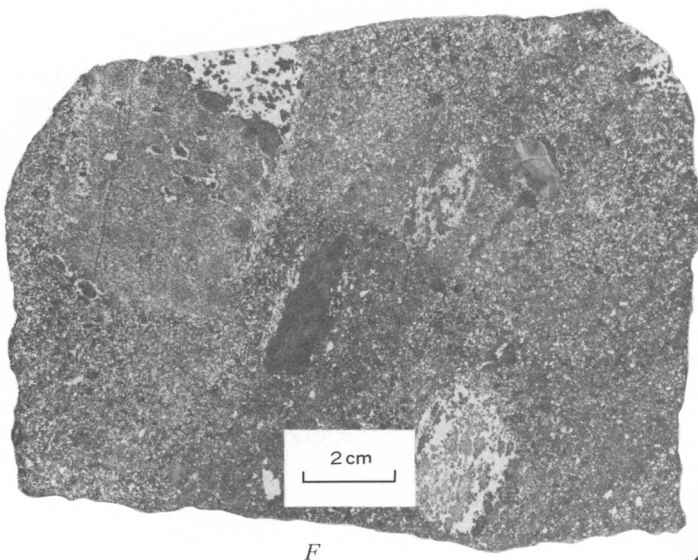
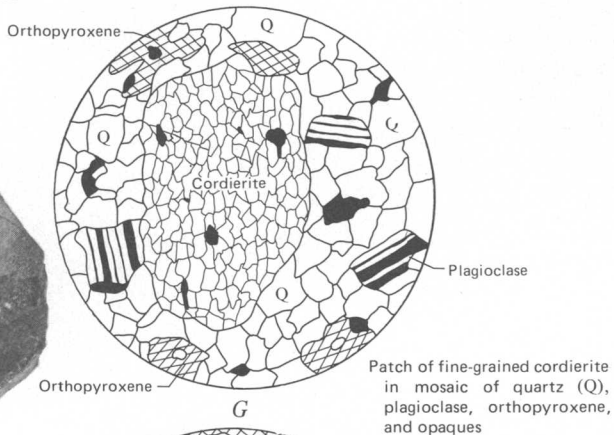
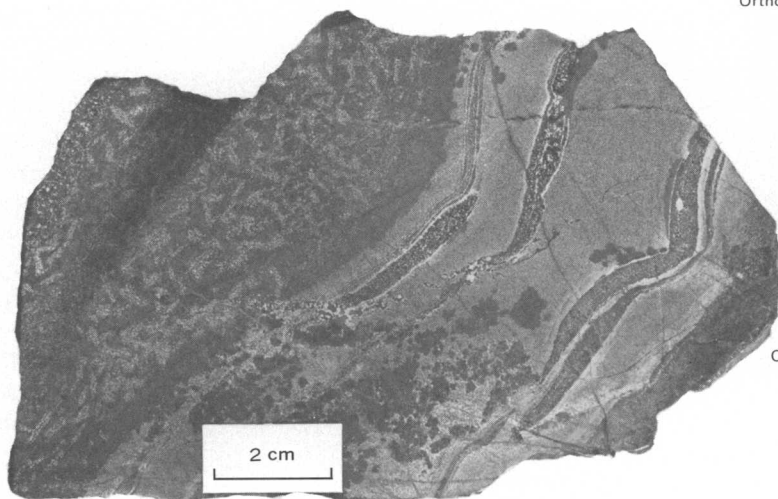
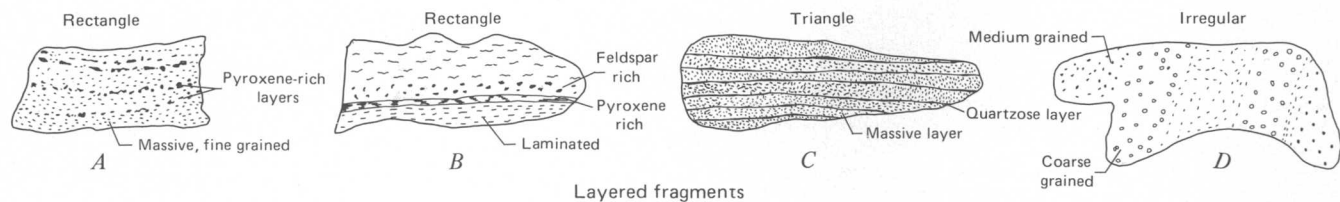


Figure 5.

pyroxene, and quartz; such clasts are considered to represent relict textures of volcanic rocks.

The layered and massive megaclasts that predominate at both the Mountain View and Bobcat Creek localities may be fragments of sedimentary rocks. The blue or gray metaquartzites could have been sedimentary rocks before they were hornfelsed but may also represent a contribution from an older metamorphic terrane, as do the gneissic and schistose megaclasts. Layered, massive, and metaquartzite megaclasts all have lithologic counterparts within a few miles of the exposed diamictite and within the same extensive metasedimentary unit. The blue-gray metaquartzite megaclasts, in particular, are suggestive of blue metaquartzite units in the hornfels unit adjacent to the base of the complex. Layered megaclasts closely resemble finely laminated metasediments that crop out elsewhere in the Mountain View area. Local provenances for the megaclasts of suspected metamorphic and igneous origins are not known.

Size characteristics

The diamictite at the Mountain View locality is marked by an extremely large range in particle size, from microscopic single grains of quartz to room-sized heterogeneous boulders. This millionfold size range is found along the entire strike of the diamictite horizon. At Bobcat Creek, a wide distribution of particle sizes exists, but unlike the Mountain View area, no megaclasts with an average diameter greater than 1 m were observed. The cumulative size-frequency curves based on the average of the apparent maximum and minimum diameters of megaclasts observed in only two dimensions at the Mountain View and Bobcat Creek localities are compared in figure 6, along with their statistical parameters. Since these curves represent field data, which omit microscopic particles, they do not represent a true size distribution for the diamictite. If microscopic fragments less than 8 mm in size were included, the dispersion, or coefficient of sorting, would be increased by several units and probably would make the size distribution curves bimodal. The size distributions of megaclasts at Mountain View and Bobcat Creek differ slightly. The median size is between 15 and 18 cm; distribution for both localities shows moderate to poor sorting characteristics and some skewness.

An accumulation of points relating apparent long and short dimensions of megaclasts at the Mountain View and Bobcat

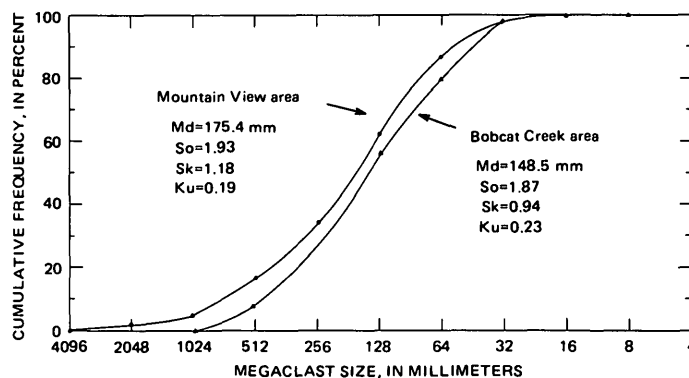


Figure 6.—Diagram showing cumulative frequency curves of megaclasts observed on outcrops. Md, median; So, sorting coefficient; Sk, skewness coefficient; Ku, kurtosis coefficient.

Creek localities (fig. 7) shows that the average of length-to-width ratios can be roughly represented by a straight line having a positive slope of about one-half. Megaclasts tend to be elongate rather than equant in two dimensions. Three-dimensional data from the few megaclasts so observed yield a range of ratios of 1:1.13:1.13 to 1:9.6:1.6.

The extremely large size variation common to all megaclasts regardless of texture is readily seen from the median and range by category (table 3). Massive, gneissic, and layered megaclasts tend to have the largest median diameters, greater than that of metaquartzites; granitoid and volcanic megaclasts, the smallest. Megaclasts of diameter less than 8 mm certainly exist but were not readily observed in the field. Several boulder-sized chunks of diamictite were brought back to the laboratory for more detailed examination. By etching slabbed sections of diamictite in hydrofluoric acid, several suspicions held in the field were confirmed: (1) all particle sizes are present down to a few tenths of a millimeter in diameter; (2) fragment density is much greater than suggested by weathered surfaces; and (3) no textural type can be placed within a restricted class size.

Shape characteristics

The shape of megaclasts at Bobcat Creek and Mountain View can be determined in only two dimensions on the face formed by the intersection of the clast and the weathered surface. Rarely can the three-dimensional form be ascertained at the outcrop, but where observed, megaclasts tend to be prismatic. The heterogeneous shape characteristics of megaclasts of various textures at Bobcat Creek and Mountain View are apparent in the diagram of shape abundance (fig. 8) and the samples shown in figure 5. Nonetheless, a numerical preference for rectangular or elliptical shapes consistent with the length-width plots (given in fig. 7) prevails at the Mountain View and Bobcat Creek localities. Elongate megaclasts displaying one or both ends tapering to a blunt or broad tip (ellipses, triangles, pears, cigars) are more than twice as abundant at Bobcat Creek than at Mountain View.

Figure 5.—Sketches and photographs of megaclasts. A, layered rectangular megaclast, length 25 cm; B, layered rectangular megaclast, length 23 cm; C, layered triangular megaclast, length 61 cm; D, layered irregular megaclast, length 15 cm; E, etched slab of layered megaclast containing folds (?); F, etched slab of megaclasts in matrix; fragment in upper left consists of two rock types in contact; G and H, microscopic texture of megaclast, diameter of circles about 2 cm; I, megaclast in matrix—possible dropstone.

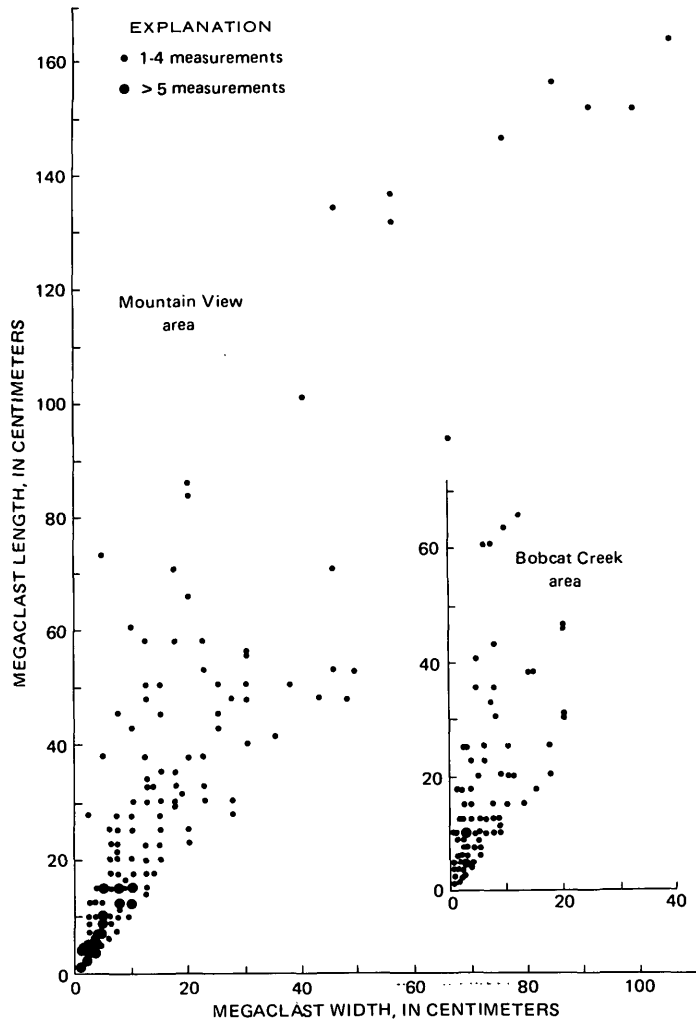


Figure 7.—Diagram showing length-to-width ratios of megaclasts at the Mountain View and Bobcat Creek localities.

Table 3.—Median diameters and ranges of the megaclasts of the different textural categories at the Mountain View and Bobcat Creek localities

Textural category	[In millimeters]			
	Mountain View		Bobcat Creek	
	Median	Range	Median	Range
Layered, banded, or foliated.	179.2	>2,048–16	243.20	512–16
Massive, homogeneous	208	>2,048–16	88	512–32
Blue or gray metaquartzite	136.3	>2,048–16	198.40	256–8
Gneissic	221.4	>2,048–16	128–32
Schistose
Granitoid, equigranular	128–32
Volcanic	198.40	512–64

When particle shape is compared with texture (fig. 8), several affinities become apparent. Rectangular megaclasts are most commonly layered or banded, whereas elliptical megaclasts tend to be massive or metaquartzite. These associations probably reflect not only the agent of transportation but also the mechanism by which the megaclasts were formed.

Comparison of particle shape to particle size shows that at both the Mountain View and Bobcat Creek localities rectangular and elliptical shapes make up 55 to 80 percent of the megaclasts with average diameters between 1,024 and 16 mm. There are few differences in shape-size correlations between the two areas except for the apparent greater abundance of elongate megaclasts at Bobcat Creek.

Roundness characteristics

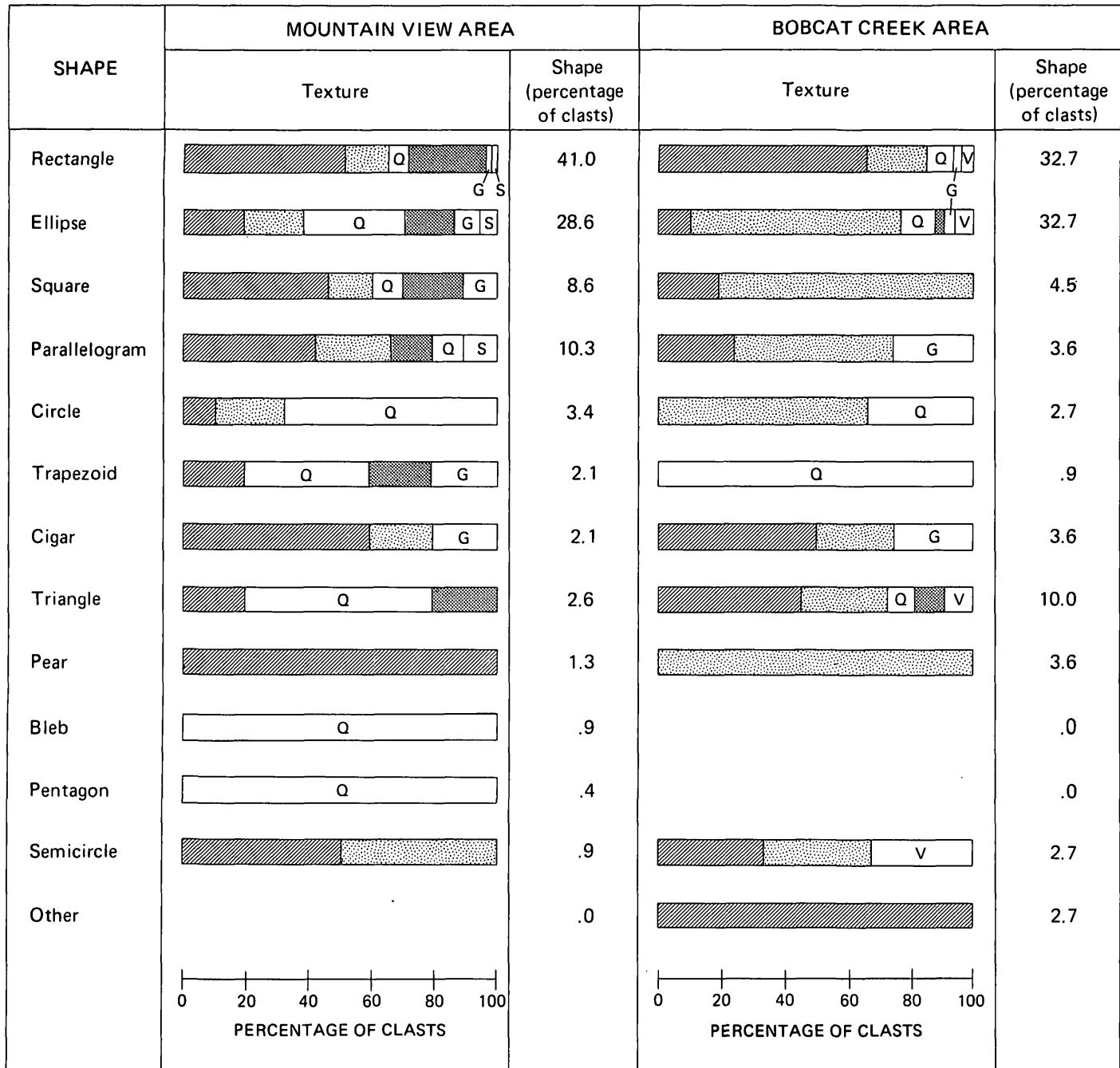
Each megaclast observed in the diamictite at the Mountain View and Bobcat Creek localities was placed in a roundness classification consisting of four categories: angular, subangular, subrounded, and rounded. Assignment to a particular category is based mainly on primary corners and edges as seen in outcrop; secondary corners are obscured by metamorphic effects and fuzzy boundaries on smaller clasts; thin sections show that recrystallization has greatly changed original clast edges. At Mountain View, about 19.5 percent are round, 27.1 percent subround, 30.1 percent subangular, and 23.3 percent angular, whereas at Bobcat Creek, 14.6 percent are round, 29.1 percent subround, 20 percent subangular, and 36.3 percent angular. As a group the megaclasts are predominantly subround to subangular.

Degree of rounding varies according to megaclast texture, size, and shape. In general, layered megaclasts tend to be subround to angular, quartzite megaclasts rounded, massive megaclasts round to subangular, gneissic megaclasts subround to angular, granitic megaclasts round, and schistose round to angular. In general, coarse clasts tend to be more angular, finer clasts more rounded, with some convergence in the intermediate size range of 256–128 mm.

Orientation

Wherever possible, megaclast attitudes were measured according to fabric or structural elements within each megaclast. Features used for megaclast orientation include foliation or schistosity, coarse banding, and fine lamination. In many places, a rough parallelism exists between planar elements in elongate megaclasts and their long dimensional surfaces. This direction of elongation of the megaclast and a rough estimation of plunge were recorded as a lineation.

Contoured fabric diagrams representing poles to megaclast foliations and lineations (plunge) are shown in figure 9. Foliation within megaclasts (fig. 9A) is represented by a weakly developed girdle that trends approximately east-west and dips 40° S. This pattern probably indicates deformation by folding after formation of the diamictite and is similar to the pattern obtained from layering in folded hornfelses within the same fault block (fig. 9B). An expanded discussion of the complexities of folding is given in Page and Nokleberg (1970, 1972) and other work of Page (unpub. data, 1972). Megaclast



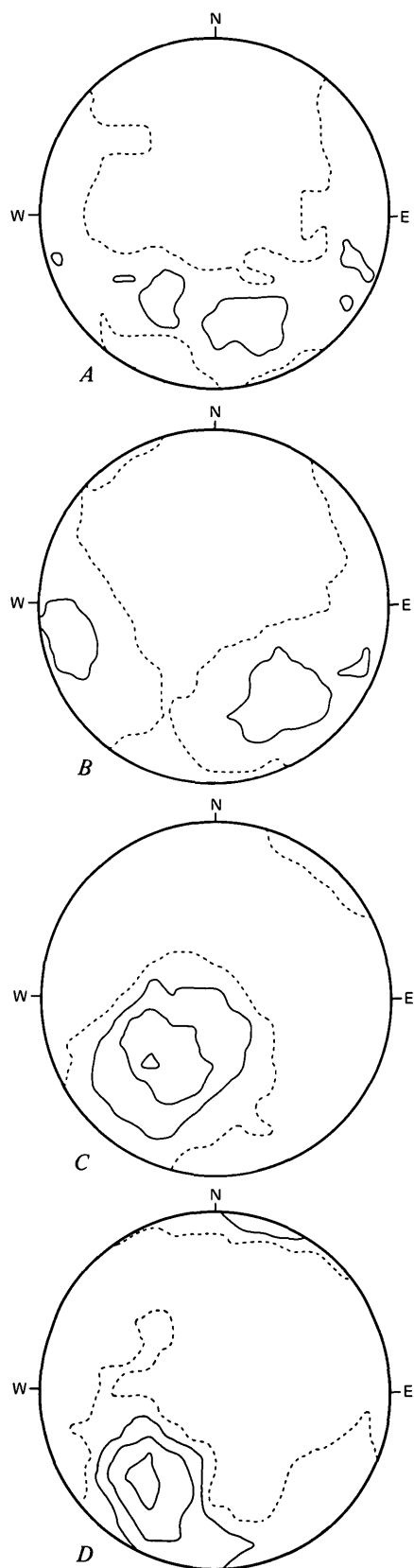
EXPLANATION



Figure 8.—Diagram showing shape abundance correlated with textural categories at Mountain View and Bobcat Creek.

elongations (maximum diameter) (fig. 9C) form a maximum plunging N. 226° E. at 47° SW., nearly in the plane of the megaclast foliation girdle. Some caution is necessary in interpreting lineation data, because bias may have been introduced in securing these "lineations" from nearly vertical cliff faces striking east-west to N. 70° E. If the elongation

represented an original prefolding lineation, one would expect it to be distributed as a small circle around the fold axis or as a great circle with respect to the fold axes. Therefore, it would appear that the orientation of the maximum diameter of the megaclasts is a function of the nature of tectonism, as is the present orientation of foliation in the megaclast.



A fabric diagram of 51 recorded megaclast foliations at Bobcat Creek, figure 9D, shows a single maximum with minor girdling indicating a preferred orientation of planar elements striking northwest-southeast and dipping to the northeast. This orientation is roughly similar to the general attitude of layering in the adjacent hornfels and is probably a result of tectonism.

From examining foliations within megaclasts and comparing these with layering and its tectonic history in adjacent rocks, it appears that the megaclasts with preexisting structures and the layering in adjacent rocks behaved in a similar fashion. The correspondence between elongate, flattened megaclast shape and foliation suggests that these blocks were deposited in an equilibrium position, that is, with the largest surface parallel with sedimentary layering. From the study of the orientation of maximum diameters, it is probable that the long axes were oriented randomly in the bedding plane.

Matrix Material

The dark matrix containing the megaclasts consists by volume of 20–40 percent quartz, 30–40 percent cordierite, 15–20 percent orthopyroxene, 5–10 percent plagioclase, 0.5–3 percent biotite, less than 3 percent sulfide and oxide minerals, and minor amounts of zircon, garnet, chlorite, and sericite. The subrounded to subangular quartz grains (fig. 5H), averaging less than a millimeter in diameter (0.2–3.5 mm) and locally composed of more than one quartz crystal, appear to represent remnants of a clastic texture. The quartz grains are enclosed by sieve-textured orthopyroxene and anhedral masses of twinned and untwinned cordierite that could be metamorphic equivalents of various combinations of chlorite and clay minerals.

Comparison of chemical analyses of the matrix material with analyses of sedimentary rocks (Pettijohn, 1963) suggests that the matrix material has a composition similar to subgraywackes and graywackes but with higher MgO, FeO, Ni, and Cr contents than an average graywacke.

Although most field observations indicate a complete absence of bedding in the matrix material, laboratory studies suggest that some may be present. Crude layering can be recognized in the matrix upon etched surfaces and at places in megaclast-layering relations. At one locality we found what is interpreted to be bedding containing a dropstone (fig. 5I), a

Figure 9.—Contoured fabric diagrams showing orientation of fragments. Contoured at 1E intervals where E is the expected number of points within the counting area for a random pattern using a method developed by Kamb (1959) and computerized by C. E. Corbato (written commun., 1970). Dashed contour is the 1E contour, solid contours are contours greater than 1E. A, poles to foliation in fragments, Mountain View area, 55 points, E = 3.73. B, poles to layering in hornfels from the Mountain View area, 22 points, E = 3.38. C, elongate orientation of fragment axes, Mountain View area, 21 points, E = 3.36. D, poles to foliation in fragments, Bobcat Creek area, 51 points, E = 3.71.

megaclast that has disturbed the underlying bedding and has been buried by later deposits.

AGE

Some of the recent age dating by Nunes and Tilton (1971) using U-Pb zircon methods on various rocks from the Stillwater Complex area can be used to establish limits on the age of the diamictite. The metasedimentary rocks intruded by the Stillwater Complex contain detrital zircons approximately 3,140 m.y. old, which establishes that these rocks are at least that old. Quartz monzonites intrude both the Stillwater Complex and the metasedimentary rocks (Page and Nokleberg, 1970, 1972). These siliceous igneous rocks yield an age of about 2,750 m.y. (Nunes and Tilton, 1971), which represents a minimum age for the metasedimentary rocks. The diamictite forms a layer or lenses within the metasedimentary rocks and has been involved in the same complex folding and faulting as the metasedimentary rocks. The age of the diamictite must be between the above two dates.

POSSIBLE ORIGINS

The composition, shape, and provenance of the megaclasts and the thickness, areal extent, and stratigraphic relations of the diamictite suggest that it is not a volcanic, fault, intrusive, or collapse breccia. The volume, abundant matrix, and bimodal texture of the diamictite imply that the megaclasts and matrix were transported by a viscous medium, either subaerially or subaqueously, which did little sorting, or that the megaclasts and matrix were separately transported to the areas of deposition. Flint (1961, p. 148-149) lists several depositional mechanisms that fit these qualifications, and Harland, Herod, and Krinsley (1966) review and reassess the criteria for the recognition of the products of these processes. Another possible origin of the diamictite is by meteoritic impact, as has been suggested for similar breccias associated with the Sudbury irruptive (French, 1968). Characteristics not supporting this origin are the appearance of megaclasts with no local provenance and the folded nature of the diamictite. In addition, the matrix fabric shows no evidence of flowage but does retain crude layering which at places contains dropstones. The most likely processes remain transport by a viscous medium or separate deposition of megaclasts and matrix.

The lack of evidence for channels, weathered zones, lag gravels, and alluvial sand and gravel deposits with channeling and current structures (Blackwelder, 1928) suggests that the diamictite did not originate as a subaerial mudflow, landslide, alluvial fan, or slumped debris. It is difficult to envision five or six drainage channels perpendicular to the general strike of the diamictite that would contribute megaclasts and matrix of a very similar nature, including clasts for which no local provenance is known.

Triangular and pentagonal clasts and dropstones could be taken as evidence of rafting, possibly by ice. All of the other described features of the diamictite are consistent with such an origin in a glacial marine environment, including deposits of drift and ice-rafted material, possibly reworked by slumping and sliding. Crowell (1964) and others have emphasized the difficulty of distinguishing such glacial marine deposits without a study of paleotectonics, paleogeography, and sediment sources, all of which are difficult, if not impossible, to evaluate in this diamictite. Although a glacial marine origin seems possible, the origin of the diamictite cannot be resolved with the available data and may be similar to the origin of the nonglacial pebbly mudstones in California described by Crowell (1957).

REFERENCES CITED

- Aalto, K. R., 1971, Glacial marine sedimentation and stratigraphy of the Toby Conglomerate (upper Proterozoic), southeastern British Columbia, northwestern Idaho and northeastern Washington: *Canadian Jour. Earth Sci.*, v. 8, no. 7, p. 753-787.
- Blackwelder, Eliot, 1928, Mudflow as a geologic agent in semiarid mountains: *Geol. Soc. America Bull.*, v. 39, p. 465-483.
- Crittenden, M. D., Jr., Schaeffer, F. E., Trimble, D. E., and Woodward, L. A., 1971, Nomenclature and correlation of some upper Precambrian and basal Cambrian sequences in western Utah and southeastern Idaho: *Geol. Soc. America Bull.*, v. 82, p. 581-602.
- Crowell, J. C., 1957, Origin of pebbly mudstones: *Geol. Soc. America Bull.*, v. 68, p. 993-1010.
- 1964, Climatic significance of sedimentary deposits containing dispersed megaclasts, in Nairn, A. E. M., ed., *Problems in palaeoclimatology*: New York, Interscience Publishers, Inc., p. 86-99.
- Flint, R. F., 1961, Geological evidence of cold climate, in Nairn, A. E. M., ed., *Descriptive palaeoclimatology*: New York, Interscience Publishers, Inc., p. 140-155.
- Flint, R. F., Sanders, J. F., and Rodgers, John, 1960, Diamictite, a substitute term for symmictite: *Geol. Soc. America Bull.*, v. 71, p. 1809.
- French, B. M., 1968, Sudbury structure, Ontario—some petrographic evidence for an origin by meteorite impact, in French, B. M., and Short, N. M., eds., *Shock metamorphism of natural materials*: Baltimore, Md., Mono Book Corp., p. 383-412.
- Gabrielse, Hubert, 1967, Tectonic evolution of northern Canadian Cordillera: *Canadian Jour. Earth Sci.*, v. 4, p. 271-298.
- 1972, Younger Precambrian of the Canadian Cordillera: *Am. Jour. Sci.*, v. 272, p. 521-536.
- Harland, W. B., Herod, K. N., and Krinsley, D. H., 1966, The definition and identification of tills and tillites: *Earth-Sci. Rev.*, v. 2, p. 225-256.
- Jones, W. R., Peoples, J. W., and Howland, A. L., 1960, Igneous and tectonic structures of the Stillwater Complex, Montana: *U.S. Geol. Survey Bull.* 1071-H, p. 281-340.
- Kamb, W. B., 1959, Petrofabric observations from Blue Glacier, Washington, in relation to theory and experiment: *Jour. Geophys. Research*, v. 64, p. 1908-1909.
- Nunes, P. D., and Tilton, G. R., 1971, Uranium-lead ages of minerals from the Stillwater Igneous Complex and associated rocks, Montana: *Geol. Soc. America Bull.*, v. 82, p. 2231-2250.
- Page, N. J., and Nokleberg, W. J., 1970, Preliminary geologic map of the Stillwater Complex, Montana: U.S. Geol. Survey open-file map, scale 1:12,000.

- Page, N. J., and Nokleberg, W. J., 1972, Genesis of mesozonal granitic rocks below the base of the Stillwater Complex in the Beartooth Mountains, Montana, in *Geological Survey Research 1972*: U.S. Geol. Survey Prof. Paper 800-D, p. D127-D141.
- Peoples, J. W., Howland, A. L., Jones, W. R., and Flint, Delos, 1954, Geologic map, sections, and map of underground workings of the Mountain View Lake area, Stillwater County, Montana: U.S. Geol. Survey open-file report, 2 maps, 8 sections.
- Pettijohn, F. J., 1963, Chemical composition of sandstones—excluding carbonate and volcanic sands—Chapter S, in *Fleischer, Michael, ed., Data of geochemistry*, 6th ed.: U.S. Geol. Survey Prof. Paper 440-S, p. S1-S21.
- Stewart, J. H., 1972, Initial deposits in the Cordilleran geosyncline—Evidence of a late Precambrian (<850 m.y.) continental separation: *Geol. Soc. America Bull.*, v. 83, p. 1345-1360.
- Troxel, B. W., 1967, Sedimentary rocks of late Precambrian and Cambrian age in the southern Salt Spring Hills, southeastern Death Valley, California: *California Div. Mines and Geology Spec. Rept.* 92, p. 33-41.



IDENTIFICATION OF A LITHIUM-BEARING SMECTITE FROM SPOR MOUNTAIN, UTAH

By HARRY C. STARKEY and WAYNE MOUNTJOY, Denver, Colo.

Abstract.—Chemical analyses, X-ray diffraction data, and cation exchange determinations are given for a lithium-bearing smectite. The X-ray data and Greene-Kelly's lithium test indicate the presence of both dioctahedral and trioctahedral phases. The exchange determinations indicate that the lithium is in the structure of the clay, and the chemical data are intermediate between those for hectorite and montmorillonite. All data indicate that the clay is a mixture of hectorite and montmorillonite.

Lithium was reported to be present, probably in montmorillonite, in the clay-size fractions of samples from a bedded rhyolite tuff at the Roadside claims in the NE $\frac{1}{4}$ sec. 8, T. 13 S., R. 12 W., Spor Mountain, in western Juab County, Utah (Shawe and others, 1964). Hectorite, which is trioctahedral, is the lithium-bearing magnesium-rich end member of the smectites, whereas montmorillonite is the dioctahedral smectite that contains virtually no lithium. It appeared likely that the Spor Mountain mineral might also be trioctahedral, and an investigation was initiated to more accurately identify the clay.

Acknowledgments.—The authors express their gratitude to Daniel R. Shawe for supplying the samples used in this study. They also appreciate the various chemical determinations furnished by J. P. Cahill, I. C. Frost, (Mrs.) Johnnie Gardner, and Violet Merritt.

METHODS AND RESULTS

The samples were fractionated by disaggregating them in water, removing the sand-size fraction by wet sieving through a 230-mesh sieve, and then separating the clay and silt by centrifugation.

X-ray diffraction analyses which were made of a randomly oriented sample of each fraction showed that the disaggregation was not complete and that some of the clay minerals remained in the sand and silt fractions as aggregates. Oriented mounts of the clay fractions were air-dried and, after being given various diagnostic treatments, were also examined by X-ray diffraction.

The X-ray diffraction patterns of the randomly oriented clay-size fraction are presented in figure 1. The impurities seen in these patterns are traces of sanidine, which is present in all samples; calcite, whose presence is seen in only three patterns; and fluorite, which is present in all samples in small amounts, but which gives very strong diffraction peaks. The differences between the dioctahedral and trioctahedral minerals are indicated by the position of the 060 peak at approximately 61–62°2 θ . This part of each pattern was rerun at a slower scanning speed ($\frac{1}{2}$ °2 θ /min as compared to 2°2 θ /min for the complete scan). A comparison of the patterns obtained by slow scanning with patterns of hectorite and montmorillonite similarly obtained shows (fig. 2) that the more intense 060 spacings of patterns a and b are closer to the 1.50-A (62°2 θ) spacing of the dioctahedral mineral montmorillonite and those of patterns e and f are closer to the 1.52-A (61°2 θ) spacing of the trioctahedral mineral hectorite. The patterns for samples c and d are intermediate with slight indications of two peaks.

The value (about 1.518 A) of the 060 spacing of the hectorite sample shown in figure 2 is lower than some of the values reported in the literature. Kerr and others (1950), who reported a value of 1.527 A, and MacEwan (1961), who reported 1.53 A, were quoting, in different ways, the value of 1.527 A reported by Nagelschmidt (1938). The hectorite used in this study is A.P.I. standard H-34. Another pattern obtained from an unnumbered hectorite sample from Hector, Calif., produced a spacing of 1.515 A. Both these values agree with the 1.52 A reported by Faust, Hathaway, and Millot (1959).

The samples were treated with Greene-Kelly's lithium test. In this treatment the oriented sample is saturated with lithium chloride, washed, and then heated overnight at 300°C and X-rayed. Then it is saturated overnight with glycerol and X-rayed again. Trioctahedral minerals will expand to a spacing of about 17.7 A with the glycerol treatment, whereas dioctahedral minerals will remain collapsed with a spacing of about 9.6 A. In each of the samples, part of the clay expanded and part did not, indicating that both dioctahedral and trioctahedral phases were present. Visual estimations of the amounts of expansible, or trioctahedral, mineral give the following sequence: b<a<c<e<d<f.

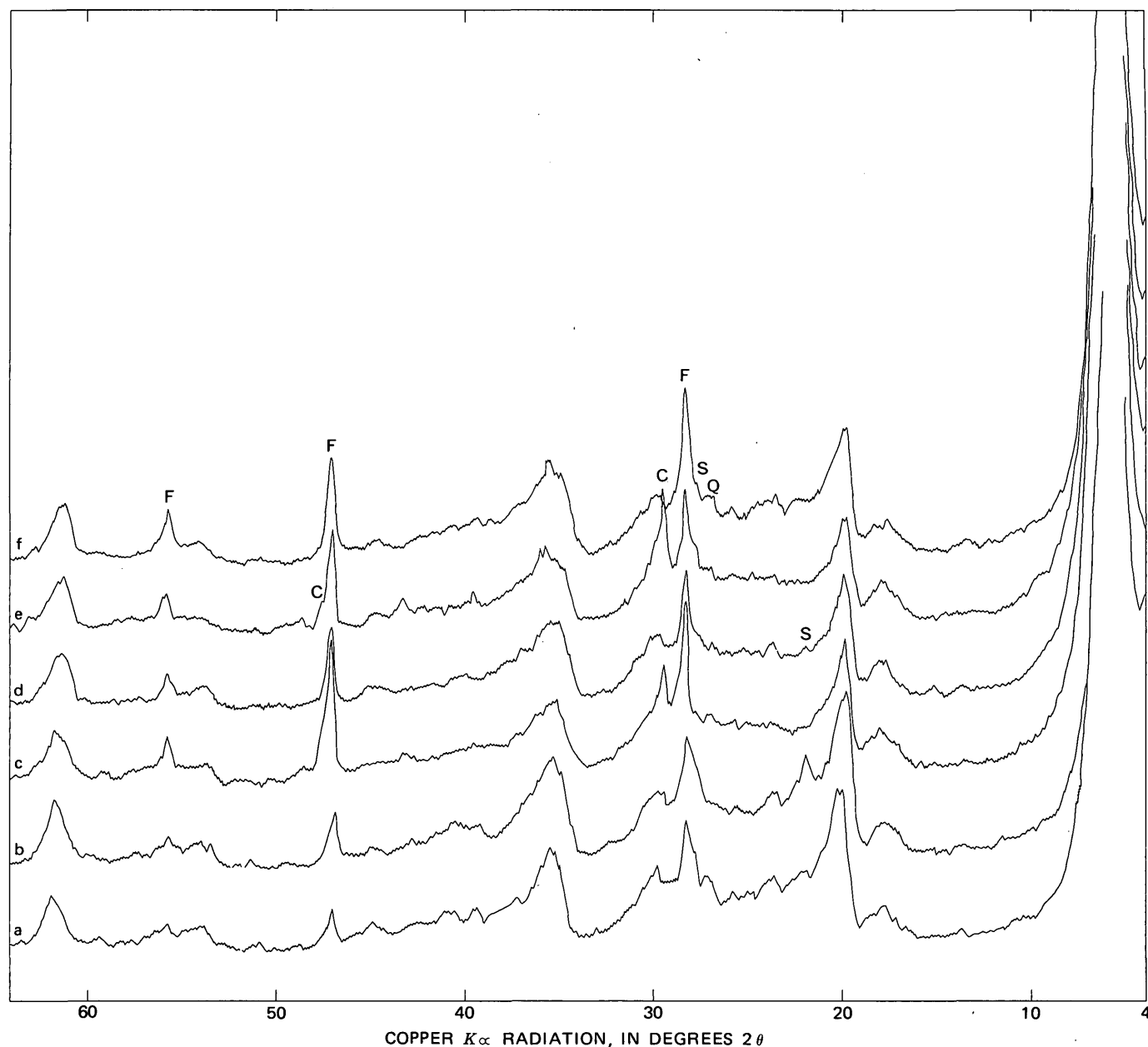


Figure 1.—X-ray diffraction patterns of randomly oriented clay-size fractions (scanning speed $2^{\circ}2\theta/\text{min}$). Impurities: C, calcite; F, fluorite; Q, quartz; S, sanidine.

Splits of the clay fraction were chemically analyzed and the results tabulated in table 1. Adsorbed water probably accounts for the totals which are more than 100 percent because the portions for the chemical analyses and those for the water determinations were not weighed at the same time. The CO_2 determined was assumed to be in calcite and the TiO_2 in anatase or some polymorph, and these amounts together with the CaO necessary to combine with the CO_2 were subtracted from the chemical analyses. Water was also subtracted, and the analyses were recalculated to 100 percent. The values are compared to previously published analyses of hectorite and

montmorillonite, also with the amounts of water subtracted (table 2). The amounts of Al_2O_3 in the samples are less than for montmorillonite but more than for hectorite. The amounts of MgO are between the two extremes, also. Lithium is not found in the standard montmorillonite; the amounts of lithium found in the samples are less than those found in the standard hectorite. These values are plotted in figure 3 to show their relationships to each other and to the standards. Fluorine is found in all the samples, but fluorine is not shown as being present in either the standard montmorillonite or the standard hectorite, although it is shown in the hectorite structural

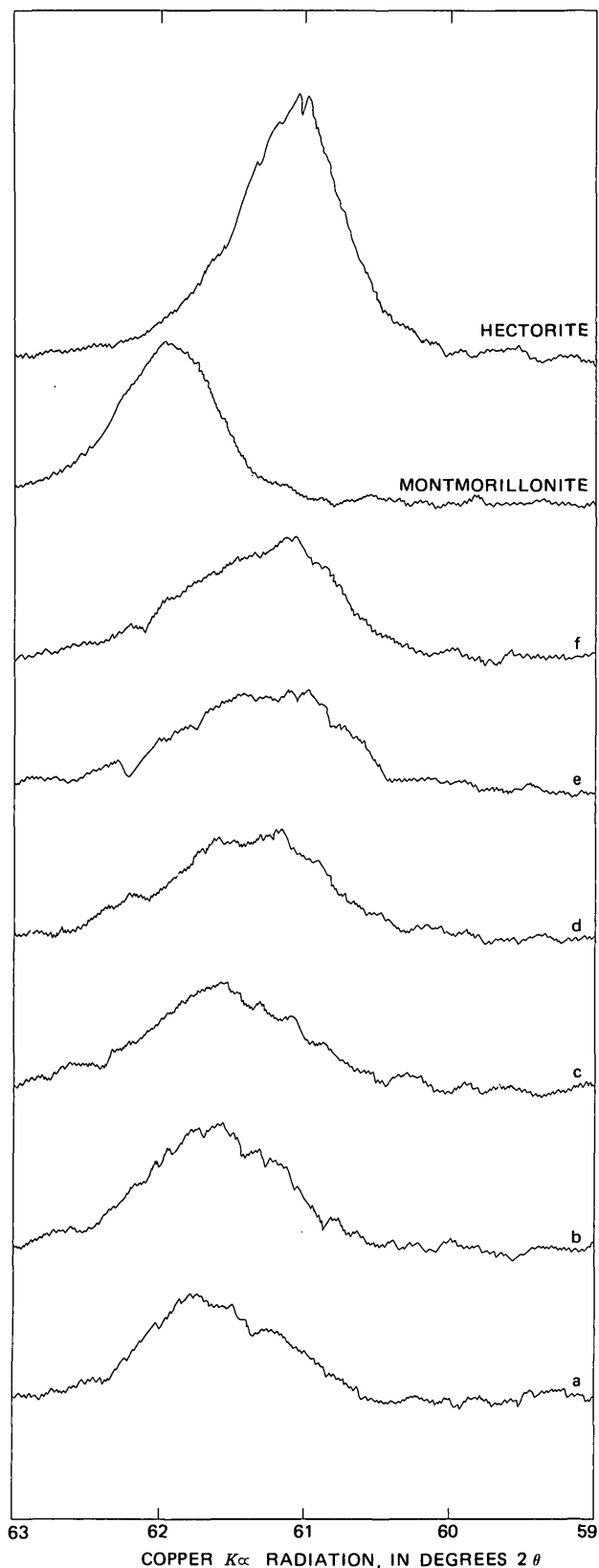


Figure 2.—X-ray diffraction pattern of the 060 region of randomly oriented clay-size fractions (scanning speed $\frac{1}{2}^{\circ}2\theta/\text{min}$).

Table 1.—Chemical data, in percent, for the clay-size fractions

[SiO₂ determined colorimetrically by Wayne Mountjoy. Al₂O₃, total Fe, MgO, CaO, MnO, Be, Cs, Li, and Rb determined by atomic absorption by Wayne Mountjoy. FeO determined volumetrically by Violet Merritt. Na₂O and K₂O determined by I. L. flame photometer by Wayne Mountjoy. TiO₂ determined colorimetrically by J. P. Cahill. CO₂ determined gasometrically by I. C. Frost. F determined by specific ion electrode by (Mrs.) Johnnie Gardner.]

Sample	a	b	c	d	e	f
Field No. . .	DRS-30-63	DRS-28-63	DRS-92-63	DRS-94-63	DRS-93-63	DRS-84-63
SiO ₂	56.5	57.8	53.4	55.3	53.1	52.5
Al ₂ O ₃	10.8	11.0	10.6	8.95	8.54	7.32
Fe ₂ O ₃	2.10	1.55	1.58	1.72	1.50	1.50
FeO1715	.14
MgO	9.8	9.9	12.8	14.3	13.4	15.3
CaO	2.63	2.75	6.42	4.61	7.29	5.77
MnO041	.019	.064	.057	.047	.019
BeO	3.77	2.28	.02	.49	.01	2.16
Na ₂ O37	.57	.21	.46	.72	.27
K ₂ O93	.80	.53	1.04	1.25	.75
Cs ₂ O01	.01	.01	.01	.01	.01
Li ₂ O42	.44	.50	.58	.57	.57
Rb ₂ O03	.03	.02	.03	.03	.02
TiO ₂04	<.03	.04	.04	.03	<.03
F	2.38	2.52	4.02	3.84	4.04	4.06
CO ₂	<.05	.32	.97	.75	2.10	.36
H ₂ O-	5.16	7.37	3.69	4.67	5.02	6.01
H ₂ O+	6.91	4.24	9.64	6.71	6.05	5.19
Subtotal	101.94	101.80	104.51	103.71	103.85	101.84
O=F	-1.00	-1.06	-1.69	-1.62	-1.70	-1.71
Total	100.94	100.74	102.82	102.09	102.15	100.13

formula (Kerr and others, 1950) and is shown as 5.96 percent in the hectorite analysis given by Ross and Hendricks (1945). Some of the fluorine found in the clays under investigation is undoubtedly present as fluorite, but if we assume that the remainder of the calcium was in the fluorite, then some fluorine would still be available for the hectorite. Beryllium has been reported to be present as bertrandite crystals less than 1μ in diameter in the Spor Mountain area (Staatz, 1963). The clay fraction of sample b was split, and an X-ray pattern of the $<0.5\mu$ fraction revealed the presence of bertrandite. If it were assumed that the beryllium shown by the chemical data (table 2) was present in the form of bertrandite and if deductions were made on the basis of this assumption, only small changes would be made in the data for samples a, b, and f, and practically no change at all for samples c, d, and e.

Other splits of the clay fraction were leached with 1 N NH₄Cl, and the leachates were analyzed for exchangeable cations. Exchange capacities were determined by distillation of the ammonium-saturated clays. The results of the determinations of both the exchangeable cations and the exchange capacities are listed in table 3. The sum of the exchangeable cations is greater than the determined capacity because of the solubility of calcite in NH₄Cl. Determinations for aluminum,

Table 2.—Chemical data, in percent, for the clay-size fractions compared with published hectorite and montmorillonite analyses¹

Sample	a	b	c	d	e	f	Hectorite ²	Montmorillonite ³
Field No.	DRS-30-63	DRS-28-63	DRS-92-63	DRS-94-63	DRS-93-63	DRS-84-63		
SiO ₂	63.7	65.5	61.5	62.4	62.1	59.7	63.72	65.66
Al ₂ O ₃	12.2	12.4	12.2	10.1	9.98	8.32	.16	22.63
Fe ₂ O ₃	2.36	1.75	1.82	1.94	1.75	1.70	.04	2.85
FeO		.19		.17	.16			.34
MgO	11.0	11.2	14.8	16.1	15.7	17.4	30.57	4.54
CaO	2.87	2.51	5.52	3.80	4.47	5.88	.19	3.04
MnO	.05	.02	.07	.07	.06	.02		.05
BeO	4.25	2.58	.02	.55	.01	2.46		
Na ₂ O	.42	.64	.24	.52	.85	.30	3.57	.18
K ₂ O	1.05	.91	.61	1.17	1.46	.86	.27	.37
Cs ₂ O	.01	.01	.01	.01	.01	.01		
Li ₂ O	.48	.48	.58	.65	.67	.64	1.45	
Rb ₂ O	.03	.03	.02	.03	.03	.02		
F	2.70	2.85	4.62	4.33	4.72	4.61		
Subtotal	101.12	101.07	102.01	101.84	101.97	101.92		
O=F	-1.12	-1.20	-1.95	-1.83	-1.99	-1.94		
Total	100.00	99.87	100.06	100.01	99.98	99.98	99.97	99.66

¹ CaCO₃, TiO₂, and H₂O amounts subtracted from samples, and H₂O amounts subtracted from standard clays.

² A.P.I. standard 34a (Kerr and others, 1950).

³ A.P.I. standard 23 (Kerr and others, 1950).

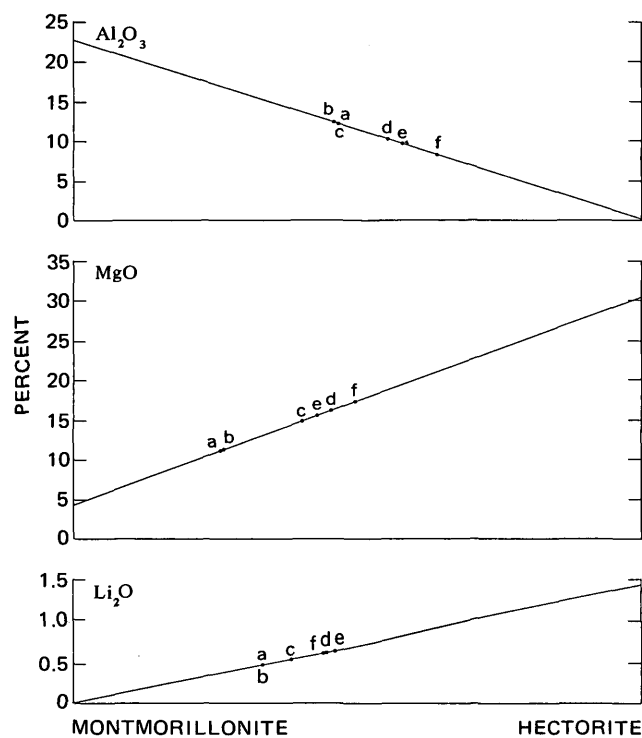


Figure 3.—Comparison of Al₂O₃, MgO, and Li₂O contents in samples a-f with those contents in hectorite and a typical montmorillonite (data from table 2).

iron, lithium, and rubidium were made on the leachates, but none of these elements was found. The values for the determined exchange capacities are within the normal ranges for hectorite and montmorillonite.

Table 3.—Exchange determinations of the clay-size fractions

		[me/100 g clay (dried at 110°C)]					Determined capacity
Sample	Field No.	Na	K	Ca	Mg	Sum	
a	DRS-30-63	3.5	1.9	41.7	38.7	85.8	78.4
b	DRS-28-63	6.9	2.0	40.8	39.4	89.1	80.8
c	DRS-92-63	3.3	1.9	85.7	40.4	131.3	84.9
d	DRS-94-63	7.7	3.4	52.6	34.5	98.2	79.6
e	DRS-93-63	17.0	4.6	99.7	33.7	155.0	78.2
f	DRS-84-63	7.5	1.5	44.6	37.5	91.1	76.8

CONCLUSIONS

Examination of the X-ray and chemical data demonstrates clearly the presence of a mixture of the two types of smectites. The X-ray patterns suggest two phases, dioctahedral and trioctahedral. Greene-Kelly's lithium test shows the two phases more clearly. The chemical data show that lithium and fluorine, which are found in hectorite but not in montmorillonite, are present but not in the amounts found in pure hectorite. The amounts of magnesium found in the samples are also intermediate between those reported for hectorite and montmorillonite. The exchange determinations indicate that the lithium is in the structure because it is not exchangeable; the exchange capacities are within the ranges expected for hectorite and montmorillonite. The samples whose more intense diffraction peaks are near 1.50 Å have less fluorine, lithium, and magnesium than those whose more intense peaks are near 1.52 Å. A mixture of montmorillonite and hectorite would satisfy these data.

No attempt was made to establish percentages for the clay minerals present. These clay minerals were not divided into hectorite and montmorillonite because a physical separation would have been impossible and a division based on chemical data and structural formulas would be meaningless because of the impurities present. However, estimations based on visual examinations of the X-ray diffraction patterns, the results of the Greene-Kelly treatment, and the chemical data indicate that samples a and b are high in montmorillonite content, sample f is highest in hectorite, and samples c, d, and e have intermediate amounts of the two minerals.

Other naturally occurring mixtures of hectorite and montmorillonite may exist but may be unrecognized because of the similarities of the two minerals, especially if the amount of hectorite is small. To be reasonably certain of the X-ray identification of lithium-bearing smectites, it may be necessary to employ supplementary procedures such as chemical analysis and the Greene-Kelly lithium saturation procedure in addition to the customary heating and glycolation X-ray diffraction treatments.

REFERENCES CITED

- Faust, G. T., Hathaway, J. C., and Millot, Georges, 1959, A restudy of stevensite and allied minerals: *Am. Mineralogist*, v. 44, nos. 3-4, p. 342-370.
- Kerr, P. F., and others, 1950, Analytical data on reference clay minerals: *Am. Petroleum Inst. Proj. 49, Prelim. Rept. 7*, 160 p.
- MacEwan, D. M. C., 1961, Montmorillonite minerals, Chap. 4 of Brown, George, ed., *The X-ray identification and crystal structures of clay minerals* [2d ed.]: London, Mineralog. Soc., Clay Minerals Group, p. 143-207.
- Nagelschmidt, G., 1938, On the atomic arrangement and variability of the members of the montmorillonite group: *Mineralog. Mag.*, v. 25, no. 162, p. 140-155.
- Ross, C. S., and Hendricks, S. B., 1945, Minerals of the montmorillonite group, their origin and relation to soils and clays: *U.S. Geol. Survey Prof. Paper 205-B*, p. 23-79 [1946].
- Shawe, D. R., Mountjoy, Wayne, and Duke, Walter, 1964, Lithium associated with beryllium in rhyolitic tuff at Spor Mountain, western Juab County, Utah, in *Geological Survey Research 1964: U.S. Geol. Survey Prof. Paper 501-C*, p. C86-C87.
- Statz, M. H., 1963, Geology of the beryllium deposits in the Thomas Range, Juab County, Utah: *U.S. Geol. Survey Bull. 1142-M*, 36 p.



STREAM-PROFILE ANALYSIS AND STREAM-GRADIENT INDEX

By JOHN T. HACK, Washington, D.C.

Abstract.—The generally regular three-dimensional geometry of drainage networks is the basis for a simple method of terrain analysis providing clues to bedrock conditions and other factors that determine topographic forms. On a reach of any stream, a gradient-index value can be obtained which allows meaningful comparisons of channel slope on streams of different sizes. The index is believed to reflect stream power or competence and is simply the product of the channel slope at a point and channel length measured along the longest stream above the point where the calculation is made. In an adjusted topography, changes in gradient-index values along a stream generally correspond to differences in bedrock or introduced load. In any landscape the gradient index of a stream is related to total relief and stream regimen. Thus, climate, tectonic events, and geomorphic history must be considered in using the gradient index. Gradient-index values can be obtained quickly by simple measurements on topographic maps, or they can be obtained by more sophisticated photogrammetric measurements that involve simple computer calculations from x , y , z coordinates.

Stream networks have regular geometric properties that can be quantitatively described. In an erosionally graded landscape (Hack, 1960, p. 89), the longitudinal profile of a stream is a property of stream geometry that can provide clues to underlying materials as well as insights into geologic processes and the geomorphic history of an area. This paper deals with a method of analyzing the longitudinal profile and develops a new unit of measurement, here called the stream-gradient index. This index relates the slope of a stream at a locality to its length at the locality and provides a basis for comparing stream reaches of different sizes.

During a study of stream profiles and streambed material in the Shenandoah Valley, Va., (Hack, 1957a, p. 87–90), it was found that a simple logarithmic graph of the stream profile provides the basis for a useful system of analysis. In this graph, the origin of the profile is at the drainage divide, which forms the source of the stream. The vertical coordinate is an arithmetic scale and represents the altitude or height above a datum. The horizontal coordinate is a logarithmic scale and represents the stream length or distance from the source. Where the stream profile is a straight line on such a plot, the profile equation is

$$H = C - k \log_e L \quad (1)$$

where H is altitude at a point on the profile and L is stream length (horizontal distance from the drainage divide to the same point on the principal stream measured along the channel). C and k are constants. The tangent to the profile or slope, S , of the stream at a point is the derivative of equation 1,

$$\frac{dH}{dL} = kL^{-1}, \text{ or } S = \frac{k}{L}. \quad (2)$$

The slope equation can be put in the form $SL = k$.

Most natural streams do not have a logarithmic profile such as the above throughout their length, but their profiles are made up of connected series of segments of various lengths, each logarithmic in form. The value of k (equivalent to the product SL) thus differs along the stream as a whole but is constant for any particular logarithmic segment. Because the value of k defines the steepness of the logarithmic profile for such a segment, it can be considered as an index of the relative steepness of the actual profile at a point. The product SL (equivalent to the constant k in equation 1) is here called the gradient index. As will be shown, this index is useful for streams as much as several hundred miles long, regardless of the overall form of the profile.

The gradient index is a significant quantity because it is crudely related to the power of a stream to transport material of a given size and to the characteristics of the channel that resist flow. This conclusion is supported by empirical evidence. It was found, for example, that streams in the Potomac basin on the average have the following relation between particle size on the bed, channel length, and channel slope:

$$S = 25 \frac{M^{0.6}}{L}, \quad (3)$$

where S is slope, M is mean particle size on the bed (in millimeters) and L is length (in miles). Where M is constant in the equation above for a given reach of a stream, the product SL (gradient index) remains constant. An increase in particle size (M) is reflected in an increase in the product SL (see Hack, 1957a, p. 71). Several streams with nearly constant SL values over long reaches were found to have bed material that showed

no systematic change in size within these reaches. The North Fork of the Shenandoah River (Hack and Young, 1959, p. 4) is an example. It has a narrow range of SL values and of particle sizes on the bed for a distance of about 100 miles (Hack and Young, 1959, p. 4). The Calfpasture River is another example and is discussed below. Thus, particle size clearly has a functional relation to gradient index.

The relation of the gradient index to the hydraulic geometry of stream systems is not understood. The fact that the product of slope and length has a relation to stream competence or power must be explainable in terms of the complex interrelations in the hydraulic geometry that characterize the conditions of dynamic equilibrium in streams. The theoretical aspects of channel equilibrium as related to the profile were discussed by Leopold, Wolman, and Miller (1964, p. 248–281). They stated (1964, table 7-7) that when power is equally distributed along a stream the product of slope and discharge is equal in all the reaches. Thus, if equal gradient indices are equatable with equal power, discharge must be proportional to length. Leopold, Wolman, and Miller's data show that, on the average, stream length is proportional to the 0.64 power of the drainage area. Also, bankfull discharge (which is thought to be the discharge that performs the significant work) is, on the average, proportional to the 0.75 power of the drainage area. Using these values, it is clear that bankfull discharge is proportional to the 1.17 power of the channel length in the average stream. However, the data from which these figures are derived include streams that have varied flow resistance and varied power along their course and that on the average probably show a decrease in flow resistance downstream. If the data were available, one might possibly be able to show that where flow energy remains the same in a downstream direction, length and bankfull discharge would be found to be nearly directly proportional.

CALCULATION OF GRADIENT INDEX

The gradient index can be measured on topographic maps, on aerial photographs using photogrammetric methods, or by ground surveys. The parameters measured are shown in figure 1. The quantity L is the stream length measured from the

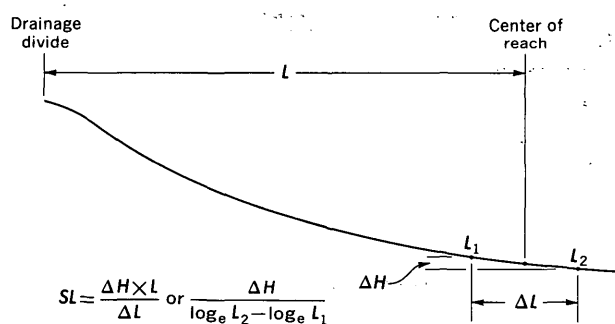


Figure 1.—Measured parameters used in calculation of gradient index. Symbols are defined in text.

drainage divide at the source of the longest stream in the drainage basin above a locality on a reach. ΔH is the difference in elevation between the ends of the reach, and ΔL is the length of the reach. The reach must be long enough so that sharp local changes in slope such as those between riffles and pools are averaged out. This distance is, of course, much longer on large streams than on small ones.

The formula for the gradient index (SL) is $SL = \frac{\Delta H \times L}{\Delta L}$.

Inasmuch as $L/\Delta L$ is a dimensionless ratio, the measurements of horizontal distance can be in any unit of measure. The measurements are generally made on a map with a map measure, so it is convenient to use inches. It is not necessary to make the conversion to ground scale. As the contours on United States maps are generally in feet, the quantity ΔH will be calculated in feet. The gradient index is the product of a ratio and a distance, so it is conveniently expressed as gradient-feet.

When measured in this way, the gradient index is equivalent to the product of the natural tangent to the channel slope at a locality and the distance in feet from the head of the stream to that locality. To find the value of the tangent expressed as a decimal, at any point, simply divide the index in gradient-feet by the distance in feet. The slope in feet per mile can be found by dividing the gradient index by the distance in miles. Thus, if the gradient index is 200 gradient-feet at 1 mile from the source, the slope will be 200 feet per mile; at 2 miles it will be 100 feet per mile. In the metric system, the gradient-index values would be different, as they would depend on measuring the difference in elevation at the ends of the reach in metric units rather than in feet.

Figure 2 is from an actual contour map and shows the measurements needed to find the gradient index at locality D in a reach extending from points A to B. ΔH is 40 feet, the value of the contour interval. ΔL is the distance from A to B, and L is the distance from C to D, including the bends in the stream. The distances can be measured on the map in any units desired, as long as the two measurements are in the same units.

As the validity of the gradient index depends on the general consistency of the relation between drainage area and channel length that exists in most natural stream systems, it is important that the distance L be measured along the principal (or longest) stream above the locality. The longest stream in the watershed must be followed continuously from its head to the terminating point at the locality. The operator must always proceed downstream from the head and never continue past a stream junction with a longer stream than the one being measured. A typical sequence of measurements is shown in figure 3.

Caution must be observed in calculating the SL value by the method above. The channel slope in the product SL is really a tangent to the profile at a particular point. In estimating the slope by measuring difference in height and length between the two ends of a reach, however, one is really measuring a

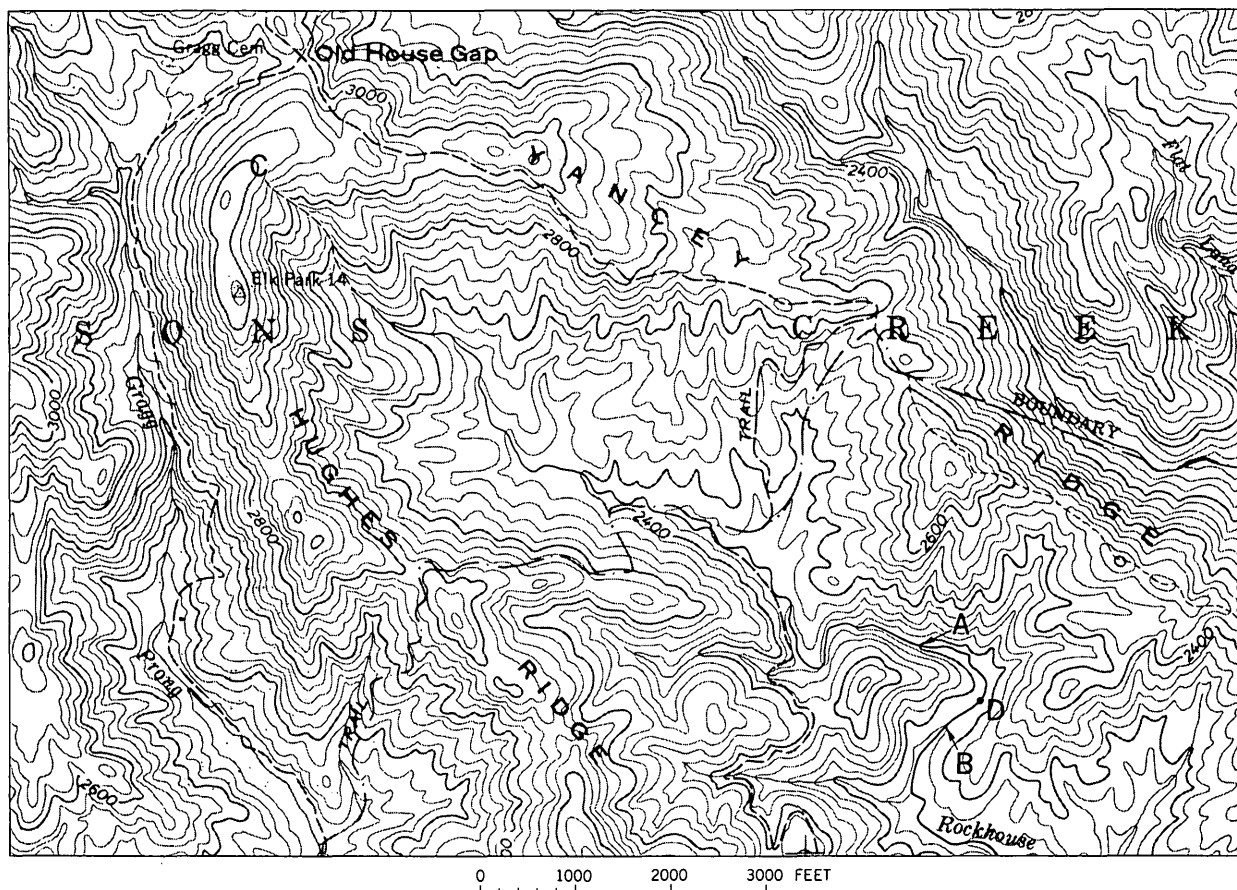


Figure 2.—Part of a topographic map used in making measurements for gradient index. From U.S. Geological Survey 7½-minute topographic map of the Grandfather Mountain quadrangle, North Carolina, 1960, 1:24,000 scale, 40-foot contour interval. See text for explanation of method.

secant of a curve. If the reach is long, this secant will not be parallel to the tangent, and the error will increase as the length of the reach increases. The error is a function of the dimensionless ratio $L/\Delta L$ and becomes larger as this ratio becomes smaller. Significant error is probably not introduced until this ratio approaches 2.0 or even 1.0. At a stream length of 100 miles, for example, the use of a secant from length 50 miles to length 150 miles would introduce an error of only about 10 percent. On the other hand, one must be careful about obtaining average SL values near the head of a stream where the curvature is high. ΔL must be kept smaller than L .

The gradient index can also be found in terms of the profile equation 1, $H = C - k \log_e L$. The gradient index is equal to the constant, k , and can be found by the formula

$$k = \frac{H_1 - H_2}{\log_e L_2 - \log_e L_1}, \quad (4)$$

where H_1 and H_2 are map elevations at each end of the reach measured, and L_1 and L_2 are distances from the source to each end of the reach.

GRADIENT-INDEX CHANGES ALONG INDIVIDUAL STREAMS

Individual profiles can be studied graphically by simple plotting on semilogarithmic graph paper or by converting the length measurements to logarithms and plotting on arithmetic scales. In practice, this is easily done by running down the map or mosaic of maps with a map measure and recording the contour elevations and their distances from the head of the stream. The data are then plotted. On such a logarithmic graph the gradient index is proportional to the slope of the plotted profile. Its numerical value can be calculated from the tabulated data at any point. Examples of several logarithmic profiles are shown and interpreted below.

Calfpasture River.—The Calfpasture River in Virginia, a headwater tributary of the James River, is, like the North Fork of the Shenandoah River (see page 422), an example of a stream whose logarithmic profile is close to a straight line (fig. 4). The average gradient index is 260 gradient-feet but it ranges from 210 to 300. The river valley is anticlinal, floored by Devonian shale, and surrounded by mountain ridges of

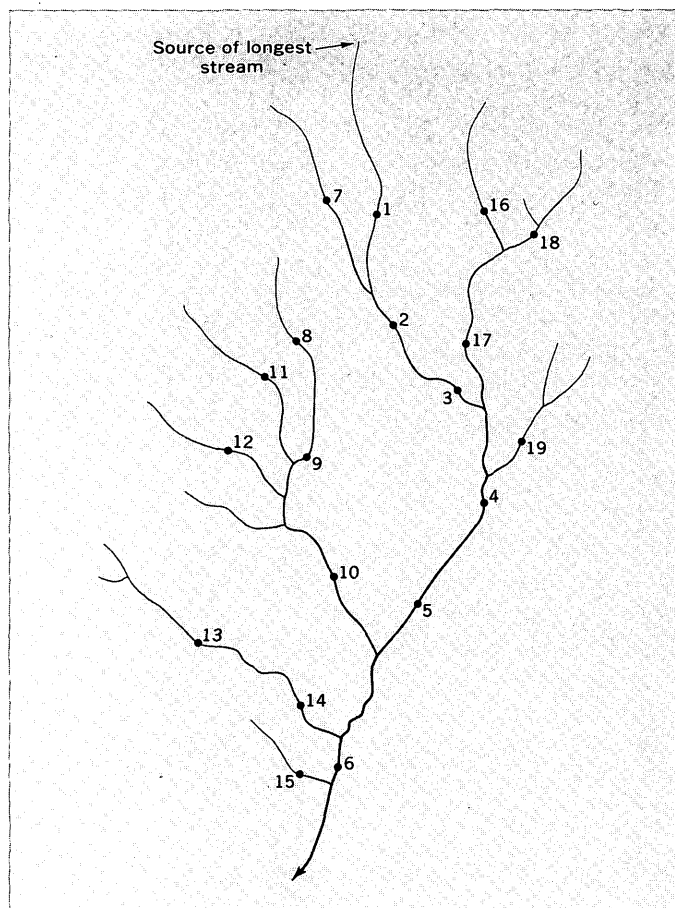


Figure 3.—A small drainage basin. Numbers represent sequence in which gradient-index values might be calculated.

sandstone of Devonian and Mississippian age. Throughout the course, cobbles of sandstone are brought in by tributaries to make up the bed material, and the stream is bordered by low alluvial terraces of rounded sandstone cobbles. Shale crops out at only a few places in the stream and makes up only a very small proportion of the bed material, presumably because it breaks up into sizes too small to remain with sandstone cobbles in this part of the channel. Samples of the bed material at 10 localities along the stream range in size from 42 to 75 mm. The average size of the 10 samples is 61 mm.

The uniformity in size of the bed material suggests that the stream has uniform competence along its course because of the bedrock geology of the basin. Data on sizes of bed material are from Hack (1957a, table 8).

North River.—The North River in Virginia, the principal headwater of the South Fork, Shenandoah River, heads on Shenandoah Mountain and drains about 50 sq mi of country underlain largely by Devonian and Mississippian sandstone beds (fig. 4). It enters the limestone and shale lowland of the Shenandoah Valley about 18 miles from its source. At this point the bed material is more than 100 mm in median size. As the North River enters the Shenandoah Valley, its flood plain

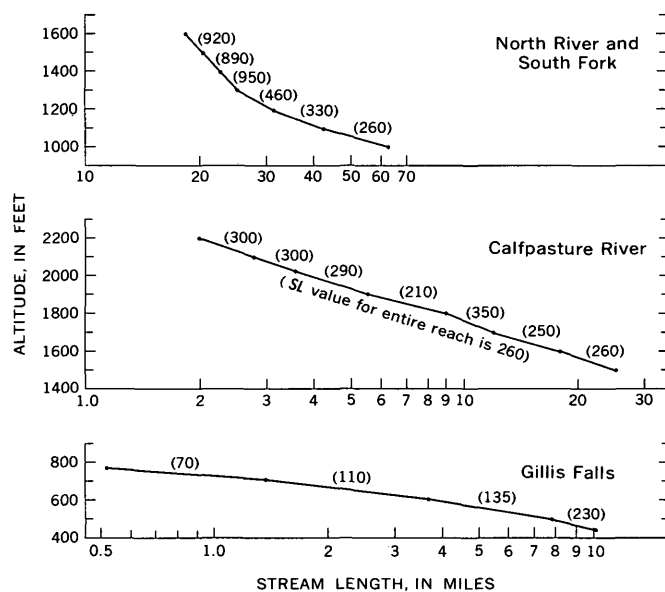


Figure 4.—Profiles of three stream reaches having (1) decreasing size of bed material downstream (North River and South Fork), (2) no systematic downstream change in size (Calfpasture River), and (3) increasing size downstream (Gillis Falls). Numbers in parentheses are SL values between data points. Data from topographic maps.

and terraces widen out to form a conspicuous lowland alluvial plain 2 miles wide which gradually narrows again downstream. At mile 36 the stream becomes entrenched in the limestone valley floor, and its flood plain is narrow. The size of the bed material systematically decreases from 110 mm to 42 mm (Hack, 1957a, table 8). As shown in figure 4, the profile is sharply curved on a logarithmic graph, and the values of the gradient index decrease from 1,000 to 250 as the gradient flattens. The bed material decreases in size with distance from the sandstone beds that are the source of the resistant material. Thus, the geology of the drainage basin controls the profile, as the competence and the slope are adjusted to handle the load.

Gillis Falls.—This stream, a headwater of the Patapsco River on the Maryland Piedmont, is an example of a stream with a profile of low concavity that shows an increase in the gradient index downstream (fig. 4). Size of bed material also increases downstream. This is because the watershed is underlain by soft, weathered phyllite laced by stringers and veins of resistant quartz. Though widespread in the watershed, the total volume of the quartz veins is very small in comparison with phyllite and weathered phyllite. The phyllite breaks up into small chips averaging less than 5 mm in size, whereas the quartz fragments average 80 to 100 mm. In the upstream reaches, vein quartz makes up only a small part of the bedload but forms a lag deposit on the bed and becomes more and more concentrated downstream where it constitutes the major part of the bedload. The fine-grained phyllite particles are

carried out of the channel in the lower reaches. The increase in size of the bed material from 7.0 mm to 80 mm is fairly systematic. The banks of the stream are loamy clay rather than sand, and the high depth-width ratio decreases from a maximum of 0.52 at 1.7 mile to 0.05 at 11.6 miles. The high depth-width ratio probably accounts in part for the low gradient of this stream in comparison with the others just described. As shown in figure 4, the logarithmic profile graph curves downward. This does not mean that the profile is in reality convex upward but rather that the natural profile is less concave upward than the others. Note that calculated values of the product SL increase downstream as the competence increases.

Cranberry River.—Major differences in the materials along the course of a stream commonly cause abrupt changes in the profile, as exemplified by the Cranberry River, Ontonagon County, Mich. (fig. 5; Hack, 1965, fig. 12, and p. B22–B28). In its upper reaches this river flows through an area of till and lake deposits. At 11.5 miles it enters a buried bedrock high, and the profile abruptly changes character. The SL or k value changes from 240 to 550. At mile 16 the river again enters till, and again the profile abruptly changes.

Lower Potomac River.—The streams discussed on the preceding pages are small, and their profiles appear to be adjusted to the geology of the terrain drained by them. In contrast, the Potomac is a very large river, and its lower course has apparently been affected by changes in base level during the late geologic history of the river. A logarithmic profile of the river below the junction with the South Branch is shown in

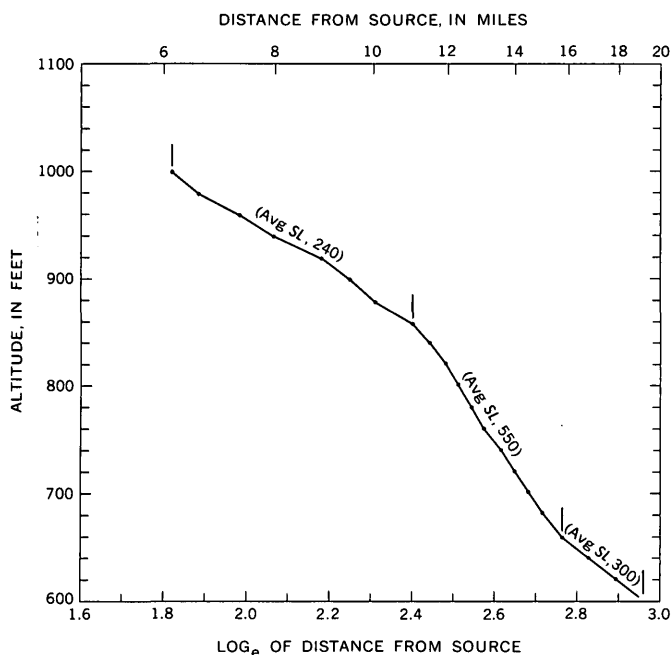


Figure 5.—Profile of the Cranberry River, Ontonagon County, Mich. The upper and lower reaches are in till; the middle reach is in sandstone.

figure 6. The data for this profile are from a survey by the U.S. Engineer Office,¹ but distances are measured from the head of the South Branch, the longest headwater, in West Virginia. Because this profile is of the lower reaches of a long river, the logarithmic profile does not show much distortion as compared with a natural profile. The amount of distortion can be judged by comparing the logarithmic and true horizontal distance scales.

In the upper part of the profile, above the Shenandoah River, SL values are comparable with the values of smaller Appalachian streams adjusted to similar rocks. Within the Valley and Ridge province below the South Branch, the river meanders through a sandstone and shale lowland. The most resistant rocks having an appreciable outcrop area along this stretch are in the Hampshire Formation, thinly interbedded shale and sandstone. Very resistant rock formations such as the Tuscarora and Pocono Sandstones also occur in the section, but they do not crop out near the channel. SL values average 480 gradient-feet, a figure similar to values for those streams in the Appalachian Valley that drain large areas of sandstone and shale and where most of the bed material consists of sandstone.

In the carbonate-rock area of the Appalachian Valley, the average SL value in the Potomac River is 429, which is higher than might be expected in carbonate rocks. However, it drops to 210 near Williamsport, Md., where the river crosses the Martinsburg Shale and to 220 in the Cambrian limestone below Shepherdstown, W. Va. An anomalously high value in the intervening reach near Dam No. 4 between Williamsport and Shepherdstown corresponds to the outcrop of the Beekmantown Dolomite, which in many places contains abundant chert.

The bed material is not readily sampled in the Potomac River because of the deep water. A random sample of part of the streambed was obtained, however, at a riffle near Shepherdstown, at the site of a onetime ford. Eighty-one fragments were measured and classified. The median size was 180 mm. The sample had the following lithologic composition: sandstone, 57 percent; limestone, 23 percent; chert, 12 percent; and not identified, 8 percent. The nearest source of sandstone is in the Valley and Ridge province, 30 to 40 miles upstream. This composition suggests that most of the bed material consists of resistant Devonian and Silurian sandstones and that they are largely responsible for the unusually steep channel slopes of the Appalachian Valley part of the stream. The average SL values obtained in other streams in carbonate rocks of the Shenandoah Valley are 180 in small streams and 245 in large streams. Large streams generally carry some resistant cobbles derived from headwater tributaries.

¹ Somervell, Brehon, 1929, Report to the Chief of Engineers, United States Army on investigation and survey of the Potomac River for navigation-power-flood control and irrigation: Typewritten report of U.S. Engineer Office, 167 p.

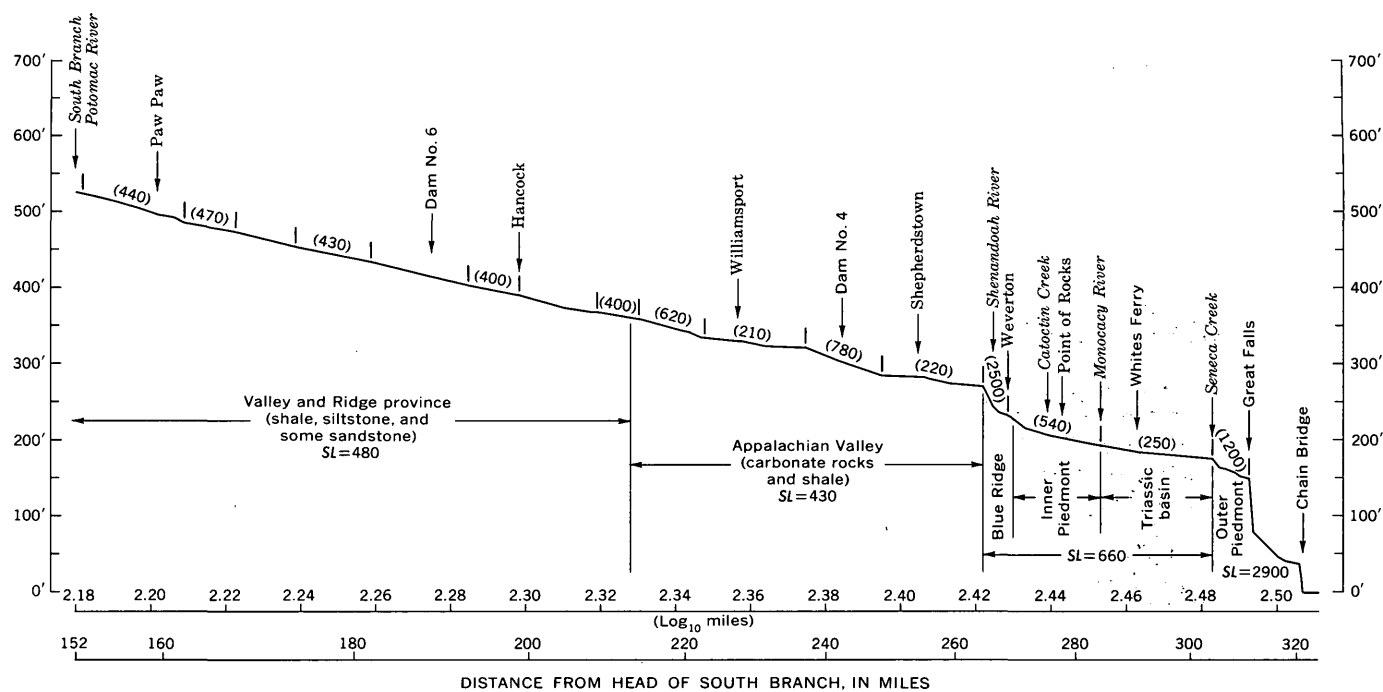


Figure 6.—Profile of the Potomac River from its junction with the South Branch to Washington, D.C. Data from Somervell, 1929 (see footnote 1). Gradient index in parentheses.

The Potomac profile steepens markedly at the water gap in the Blue Ridge. Here the river passes through the resistant quartzites and other clastic rocks of the Chilhowee Group, the metabasalt of the Catoctin Formation, and other crystalline rocks. An *SL* value of 2,500 seems high compared with *SL* values found in smaller streams in the same rocks in other places. However, this high value may simply reflect adjustment of the slope to high flow resistance encountered at the crossings of tough rock formations. In the Triassic basin between the Monocacy River and Seneca Creek, *SL* values drop again to 250, a value comparable with small streams in predominantly shale areas.

At Seneca Creek, Md., the channel slope steepens abruptly and becomes a series of rapids and falls. In this reach the average *SL* is 2,900, far higher than in the smaller streams of the adjacent Piedmont where *SL* values average less than 300. Great Falls itself corresponds to an outcrop of resistant quartz-rich gneiss (U.S. Dept. Interior, 1970, p. 11–15), so there has been some adjustment by the river to the relative resistance of the rocks. However, the anomalously high *SL* values suggest that in this reach the river is also adjusted to a lower base level than are the reaches upstream. In this connection, marine deposits of Miocene age at Ward Circle in Washington, D.C., are at 370 feet above sea level (Darton, 1950, p. 6). Marine deposits of supposed Pliocene age at Good Hope Hill in east Washington, D.C., are at 280 feet (Hack, 1955). The Pleistocene channel of the Potomac River dropped

90 feet below sea level at Alexandria, Va., approximately 12 miles downstream from Chain Bridge (Hack, 1957b, p. 823) indicating a change in base level of more than 370 feet in the last million years. Thus, the lowest part of the Potomac River gorge is probably partly adjusted to low sea level of late Wisconsin time corresponding to the -90-foot channel at Alexandria.

Two conclusions can be drawn from the profile of the Potomac River: (1) That part of the profile above the Shenandoah River is adjusted to the geology of the basin and to the profiles of other streams in the upper basin. This adjustment may extend as far as Seneca. The reaches below Seneca, however, reflect accelerated erosion related to a drop in sea level in Pliocene and post-Pliocene time. (2) The general conformity of the gradient-index values above the Shenandoah River to those of tributary streams indicates that there is probably little, if any, tendency for *SL* values to change systematically because of geometric factors related simply to the size of a stream. This conclusion is important to the usefulness of the gradient index as an analytical tool. Still larger streams, however, such as the Mississippi, may have anomalously high *SL* values. The Mississippi River is so large that the overall geometry of its basin is probably determined by factors such as the configuration of the continent and the location of mountain ranges, rather than by the evolutionary development of drainage that normally proceeds with down-wasting.

REGIONAL PLOTTING OF GRADIENT-INDEX VALUES ON MAPS

Gradient indices of streams can be studied on a regional basis by plotting regularly spaced index values on maps; contour lines can then be drawn. Several such maps have been constructed.

The procedure is to run down with a map measure all the streams in the area studied, systematically calculating *SL* values at regular intervals. It is important in doing this that stream length always be measured along the longest channel in a given basin. That is, the measurements must be ordered as shown in figure 3. The spacing of measurement points is limited by the scale and detail of the topographic maps used in the calculations as well as by the actual spacing of the streams. In the Piedmont and Appalachian regions, for example, stream channels range on the average from 0.2 to 1.0 mile apart, depending on drainage density in a region, a factor generally related to the kind of rock. Measurement localities cannot be closer to the source of a stream than about ½ mile, because close to the divide the channel is not sculptured primarily by the kinetic energy of flowing water.

Figure 7 is an example of a gradient-index map. It is based on about 400 localities measured on four 7½-minute quadrangles with 20- to 40-foot contour intervals at 1:24,000 scale. The map covers the Lenoir 15-minute quadrangle, North Carolina. It was made as part of a geomorphic study of the Blue Ridge escarpment in the Grandfather Mountain area. The problem of the Blue Ridge escarpment is not discussed here, but a few features shown on this map are pointed out as examples of interpretations that can be made.

First of all, the base of the Blue Ridge escarpment in this area corresponds closely to the trace of the Brevard zone which extends from A on the left margin of the map to A' at the top. The Piedmont province is south and east of that zone (A-A') and is underlain by lower Paleozoic metamorphic rock covered by saprolite. Northwest of the Brevard zone, the relief increases sharply, and rock outcrops are more numerous. In this area the rocks are gneisses of the Grandfather Mountain window.

Note the anomalously high values at B north of the Johns River. These correspond to several lenses of extremely resistant quartz-rich gneiss (Bryant and Reed, 1970, p. 66). The anomalously high *SL* values led the writer to them. The lenses were poorly exposed, generally along the bottoms of deep valleys often difficult to reach because they were covered by slash from logging operations, but they were associated with steep places in the streams.

At C, a large tributary of the Johns River almost as long as the Johns River itself, the values are anomalously high. This area corresponds to the outcrop of the Brown Mountain Granite (Bryant and Reed, 1970). The granite is a particularly massive rock with widely spaced joints. The river cuts through it in a deep picturesque gorge with many cascades.

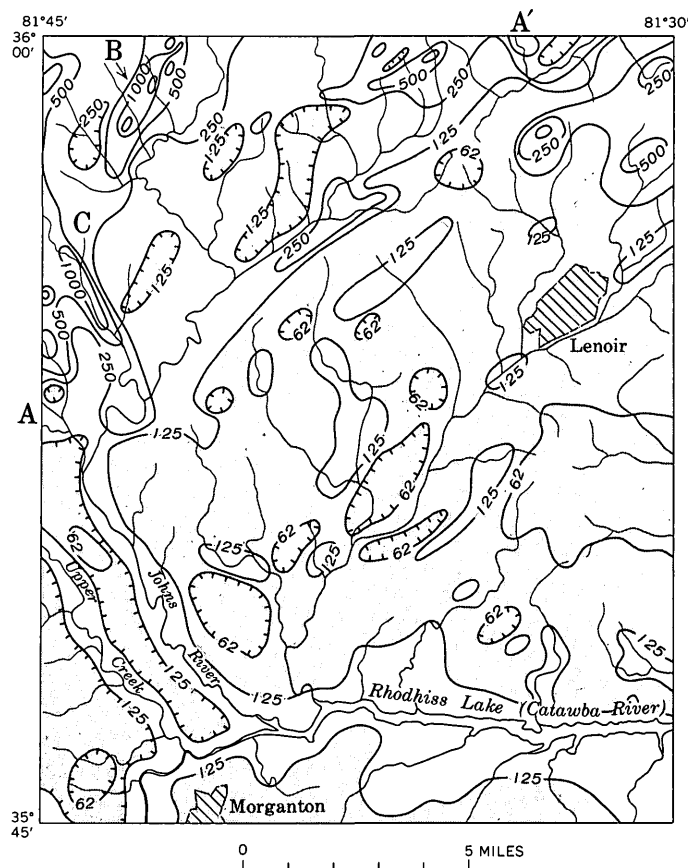


Figure 7.—Lenoir-Morganton area, North Carolina. Gradient-index values on streams are shown by contours; approximately 400 stream localities were used in making the map. Contours represent equal gradient-index values in gradient-feet; interval proportional to 2^n (62, 125, 250, 500, 1000, 2000). Areas with values less than 125 are patterned. Original data from U.S. Geological Survey Colletsville, Lenoir, Morganton North, and Drexel 7½-minute topographic quadrangles, scale 1:24,000. Letter symbols are explained in text.

SL values drop sharply in the Piedmont southeast of A-A'. An interesting feature of this region is that the large streams have higher index values than their tributaries, though the index values of the tributaries increase as they approach the large streams. The probable explanation is that the larger streams are adjusted to transport resistant material derived from resistant rocks upstream. They, therefore, require steeper slopes for a given length. The smaller streams originate in saprolite on uplands of low relief and therefore are competent to transport only fine material. The situation is analogous to that described on page 424, with reference to Gillis Falls, Md. It is a common phenomenon in the Piedmont region where the rocks are complex mineralogically. They thus have several components of varying resistance. The more resistant components, such as fragments of quartz veins or aplite dikes, concentrate downstream. As these components wear more slowly than others, the size of the bed material tends to be

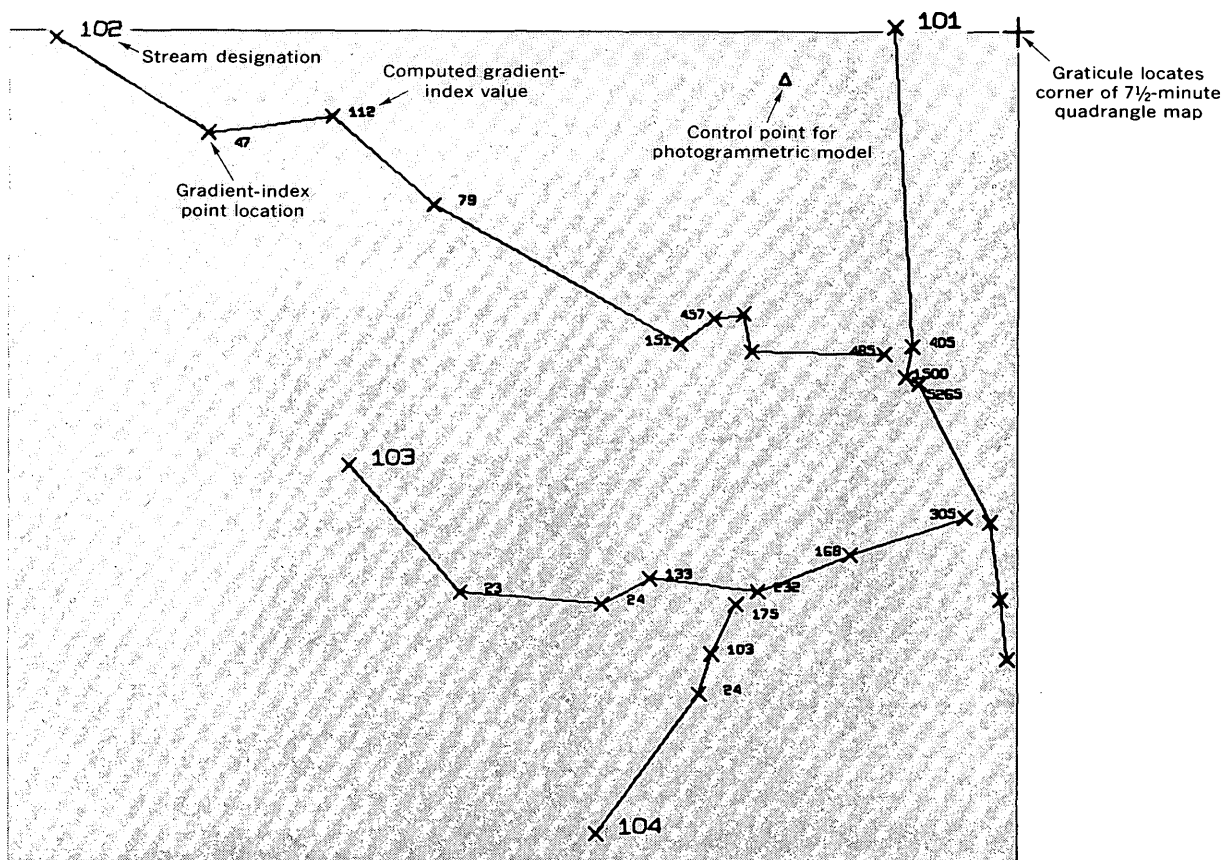


Figure 8.—Sample of a gradient-index plot of part of the Rockville quadrangle, Maryland, prepared on Cal-Comp plotter. *SL* values of some points were not computed because altitudes could not be determined accurately.

larger in the larger streams because the resistant components survive a greater distance of transport as large fragments and become relatively more abundant.

Maps similar to figure 7 can be constructed by photogrammetric measurements. By this method the spacing of points on streams is not limited by the contour interval but only by the spacing of the streams themselves and the resolution of the photogrammetric model. By use of photogrammetric equipment it is possible to plot and calculate gradient-index values automatically. A test on a model of an area in Montgomery County, Md., was made by using a Halcon stereoplotter, an optical projection instrument similar to the Kelsh plotter. The plotter was equipped with a digital readout system that provided punched cards with the *x*, *y*, and *z* coordinates of each measured point at model scale. A Haag-Streit coordinate plotter equipped with digital output in card form was used to measure points on the topographic map to be used as control for absolute orientation of the model. Data reduction and stream-gradient computations were made on an IBM 1130 computer. Graphic presentations of the results were plotted on a Cal-Comp plotter operated on line with the 1130 computer. Part of the graphic presentation is shown in figure 8.

GRADIENT INDEX IN DIFFERENT CLIMATIC AND GEOMORPHIC REGIONS

The examples of the gradient index cited are all in the Eastern United States, a humid region in which the density of perennial streams is high. The writer has had little experience with the index in arid regions, but it is questionable whether it would have the same meaning as it does in humid regions.

Although the index defines the slope of the channel relative to the length in arid regions, it would not necessarily correlate directly with stream power and flow resistance because the hydraulic geometry of the channel is different. For example, channel width may increase downstream in arid regions at different rates from those of humid regions because of the sparse vegetation on the banks. Presumably this is a factor influencing slope. Another factor is the relation of discharge to drainage area and length. In arid regions average discharge, as well as flood discharge, increases downstream at a regular rate only in small drainage areas a few square miles in size. Small areas are affected by individual storm cells. Although few data are available, in some larger drainage basins average discharge may actually decrease downstream.

Interpretation of the gradient index must differ to some extent in different geomorphic provinces. In the Eastern United States, most of the area is drained by converging streams with an average length proportional to the 0.64 power of the drainage area, a relation probably common to most stream-eroded landscapes in which tributaries converge downstream (Hack, 1957a, p. 63; Leopold, Wolman, and Miller, 1964, p. 144). In the Basin and Range province, however, and in other parts of the Western United States, long reaches of streams cross pediment surfaces, alluvial fans, and bahadas in which the geometric relations are different. Though the gradient index may be useful for analysis of such regions, it cannot be used in the same way as in most areas of the Eastern United States because the rates of increase in discharge downstream and the relation of the profile to stream power will not be similar.

CONCLUSION

The gradient index is useful in terrain analysis because it permits comparisons to be made of streams of different sizes. It is a sort of rule of thumb index of stream power and flow resistance. Because it is so simple to calculate from a topographic map, one of its most valuable uses may be to discover anomalously steep or gentle reaches of streams that are related to particularly resistant or soft rocks. The index may thus serve as an aid to geologic mapping, analogous to data on magnetic intensities.

Regional analysis of stream profiles can help in interpreting the geomorphology of large regions. Playfair (1802, p. 102–114) first enunciated the ideas that streams sculpture the valleys in which they flow, that their slopes are adjusted to carry away the debris in their watersheds, and that the whole

river network is an adjusted system. The gradient index, when used in the general context of these ideas, can provide insights into the causes of the diversity of the landscape, including the nature of the adjustments that streams have made as well as the nature of diastrophic forces opposed to them.

REFERENCES CITED

- Bryant, Bruce, and Reed, J. C., Jr., 1970, *Geology of the Grandfather Mountain window and vicinity, North Carolina and Tennessee*: U.S. Geol. Survey Prof. Paper 615, 190 p.
- Darton, N. H., 1950, *Configuration of the bedrock surface of the District of Columbia and vicinity*: U.S. Geol. Survey Prof. Paper 217, 42 p. [1952]
- Hack, J. T., 1955, *Geology of the Brandywine area and origin of the upland of southern Maryland*: U.S. Geol. Survey Prof. Paper 267-A, 43 p.
- 1957a, *Studies of longitudinal stream profiles in Virginia and Maryland*: U.S. Geol. Survey Prof. Paper 294-B, p. 45–97 [1958].
- 1957b, *Submerged river system of Chesapeake Bay*: *Geol. Soc. America Bull.*, v. 68, no. 7, p. 817–830.
- 1960, *Interpretation of erosional topography in humid temperate regions*: *Am. Jour. Sci.*, v. 258-A (Bradley Volume), p. 80–97.
- 1965, *Postglacial drainage evolution and stream geometry in the Ontonagon area, Michigan*: U.S. Geol. Survey Prof. Paper 504-B, p. B1–B40.
- Hack, J. T., and Young, R. S., 1959, *Intrrenched meanders of the North Fork of the Shenandoah River, Virginia*: U.S. Geol. Survey Prof. Paper 354-A, 10 p.
- Leopold, L. B., Wolman, M. G., and Miller, J. P., 1964, *Fluvial processes in geomorphology*: San Francisco, W. H. Freeman and Co., 522 p.
- Playfair, John, 1802, *Illustrations of the Huttonian theory of the earth*: Edinburgh, 528 p. (Reprinted by Dover Publications, Inc., New York, 1964)
- U.S. Department of the Interior, 1970, *The river and the rocks*: Washington, D.C., U.S. Govt. Printing Office, 46 p.



CURRENT SLOPE-STABILITY STUDIES IN THE SAN FRANCISCO BAY REGION

By TOR H. NILSEN and EARL E. BRABB, Menlo Park, Calif.

*Study done cooperatively with Department of Housing
and Urban Development and San Mateo County*

Abstract.—An extensive program of slope-stability studies is presently underway in the San Francisco Bay region, California. Work to date has resulted in the publication of estimates of landslide damage, an estimated-landslide-abundance map of the region, new slope maps prepared by photomechanical processes, photointerpretive maps of landslide, colluvial, and other surficial deposits, and maps of relative slope stability. These studies indicate that landsliding is a major slope-erosion process in the region, that the damage resulting from landsliding is very great, and that additional development in the upland parts of the region should not be undertaken without careful evaluation of slope stability.

The U.S. Geological Survey is presently studying the slope-stability characteristics of the San Francisco Bay region. This work is part of a larger, more broadly based study of the region that is being done in cooperation with the U.S. Department of Housing and Urban Development. In addition, San Mateo County has provided some additional funding. The larger study, entitled "The San Francisco Bay Region Environment and Resources Planning Study," was initiated in the spring of 1970 and will last for at least 3 years. Elements of the study include new topographic mapping, geologic and geophysical studies, hydrologic studies, and regional planning studies. The overall coverage of the larger study has been outlined in the Program Design (U.S. Geological Survey and U.S. Dept. Housing and Urban Development, 1971). The purpose of the present paper is to outline the types of slope-stability studies that have been undertaken in this project and the status of the studies, and to list the publications presently available.

The San Francisco Bay region includes the nine counties that border San Francisco Bay, a total land area of about 18,000 km² (7,000 sq mi), with a population exceeding 5 million (fig. 1). It lies primarily within the Coast Ranges but includes part of the western Sacramento Valley. The great variety of climatic conditions, vegetation, topographic situations, and geologic conditions makes the area attractive for future growth. Population growth has historically been con-

finied primarily to the flatlands surrounding San Francisco Bay and its adjacent waterways, the city of San Francisco, and some of the larger inland valleys. At present, however, development is spreading rapidly into adjacent hillside areas, where landsliding is becoming an increasing problem.

The geology of the region is very complex. Many different types of rocks (Schlocker, 1968, 1971) and numerous active faults (Brown, 1970; Brown and Lee, 1971) are present, and the structural and tectonic history has been complicated. Virtually all the conditions responsible for landslides are present in the San Francisco Bay region, including (1) steep, irregular slopes; (2) abundant and seasonally intense rainfall; (3) extensive human activity, including logging and the grading and cutting of slopes; (4) an abundance of rock types that are very susceptible to sliding, including extensively crushed and fractured Franciscan *mélange* complexes and poorly consolidated upper Tertiary to recent sediments; (5) thick unconsolidated colluvial deposits and thick weathered zones on steep slopes; (6) abundant expansible clay soils; and (7) frequent high-level seismic activity.

Several geologic studies have been conducted in the region, but they have focused primarily on mapping bedrock units, rather than on slope stability. Private engineering geology consultants have examined the slope-stability characteristics of many small parcels of land in detail, but little of this work has been published, and few regional studies have been undertaken. Some of the earlier studies that have been concerned with landslide features and slope-stability characteristics in the region, and which have provided much necessary data and insight for the current studies, include those by Kachadoorian (1956), Schlocker, Bonilla, and Radbruch (1958), Bonilla (1960a, 1960b, 1971), Radbruch (1957, 1969), Radbruch and Weiler (1963), Kojan (1968), Harding (1969), Clague (1969), Pampeyan (1970), Rogers (1971), and Waltz (1971). Within most of the region, however, information regarding the distribution of landslide deposits was very meager at the time that this slope-stability study began. New work has been directed toward the preparation of slope-stability maps at a

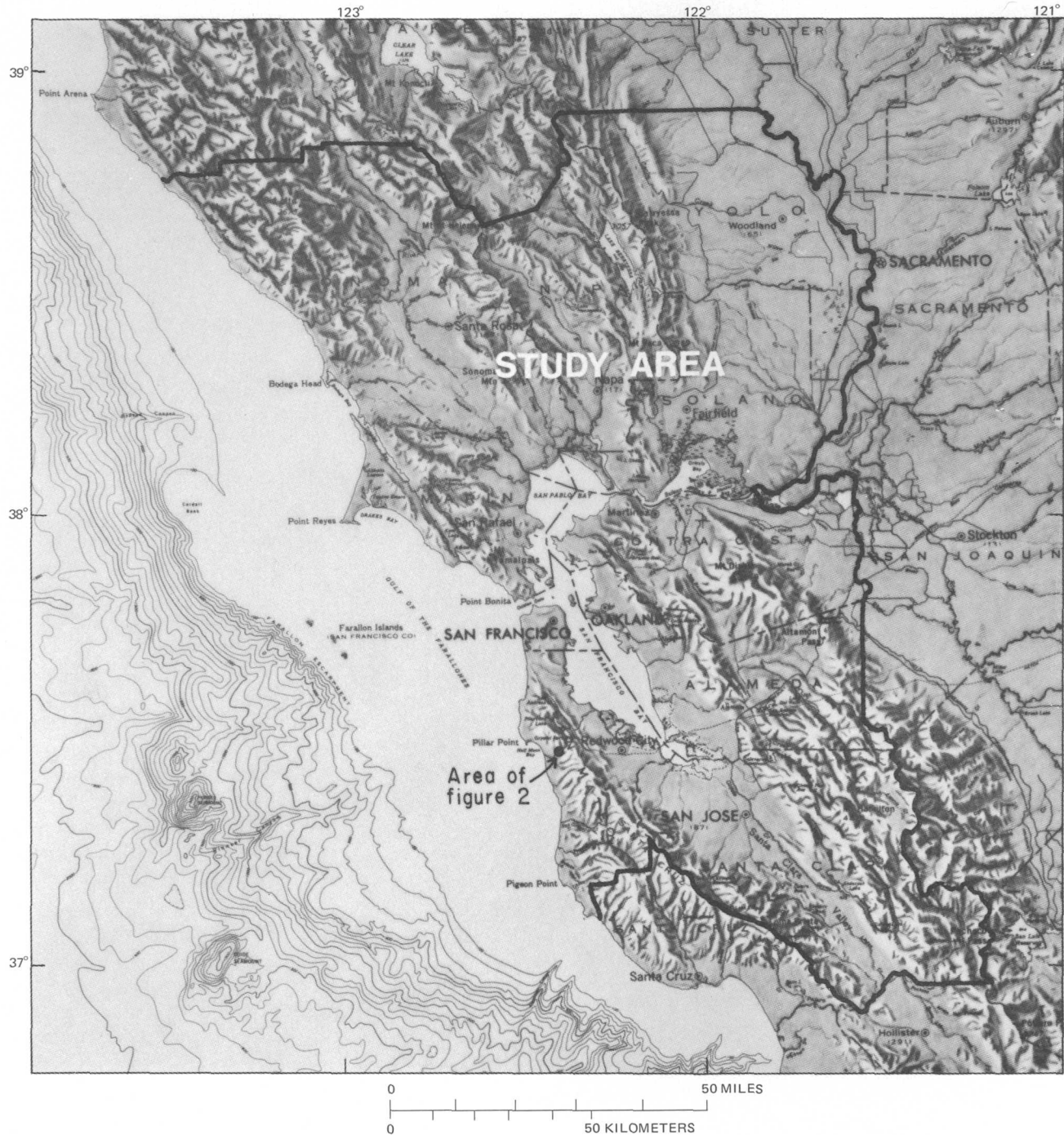


Figure 1.—Index map of the San Francisco Bay region, showing area of figure 2. Depth contour interval 100 fathoms.

regional scale (1:125,000) for the entire bay region. To attain this goal, the acquisition of much new data and much new mapping have been necessary, including the mapping of landslide deposits, bedrock geology, active faults, slopes, recent landslides, other surficial deposits, and engineering properties of bedrock and soil units.

The maps and reports from the study are being published in a three-part series: (1) Basic Data Contributions, which are

based on the initial data-gathering phase of the study; (2) Technical Reports, which are derived from the basic data; and (3) Interpretive Reports, which are nontechnical and will be addressed primarily to governmental policy makers and the non-technically-oriented private sector. To date, about 40 Basic Data Contributions and a few Technical Reports have been released. Those that relate to slope-stability studies are noted separately in the list of references at the end of this

paper. All of the publications and a current list of publications from the study can be obtained from the Public Inquiries Office, U.S. Geological Survey, 555 Battery Street, San Francisco, Calif. 94111.

ESTIMATED COSTS OF LANDSLIDE DAMAGE

Before the present study began, it was known that the yearly cost of landslides in the bay region was great, but no reliable figures were available. As part of the overall study of slope stability, we have attempted to estimate in several ways the costs to the community. This type of information was useful not only in pointing out the necessity of slope-stability studies prior to construction but also in informing various local governmental agencies of the costs involved in developments that did not consider geological factors.

Costs related to landsliding are generally very difficult to ascertain. Data on the costs of damage to structures, reevaluation of land or housing for tax purposes, and expenditures for road, sidewalk, sewer, and railroad repairs are available from some public agencies, but much damage goes unreported and many other costs are impossible to determine; and many public agencies do not carefully record information about landslide damage. Indeterminable costs include those for litigation, salaries of firemen and policemen, detours, and a host of others, many of them intangible.

Taylor and Brabb (1972) compiled data on landslide costs from governmental and private agencies in the San Francisco Bay region for the rainy season of 1968–69, dividing the costs into public, private, and miscellaneous categories, and enumerating costs to each county separately. They found that public and private costs totalled more than \$25 million, and this figure is probably minimal.

Nilsen and Brabb (1972) investigated a group of landslides in the northeastern part of the city of San Jose that had damaged public and private facilities during a 10-year period. Their report shows the locations of landslide deposits and damaged buildings and streets and also summarizes some of the costs of the landslides to the city. During a 5-year period, San Jose spent more than \$750,000 to study one of the landslides, to attempt to control its movement, and to maintain roads across it.

ESTIMATES OF LANDSLIDE ABUNDANCE

Radbruch and Wentworth (1971) made preliminary estimates of the relative abundance of landslides in the bay region by comparing types of earth materials in the region, amount of rainfall, and degree of slope. They divided the region into six categories, ranging from least abundant to most abundant landslides. Their map is an approximation, because when it was made, little information about the distribution of landslides was available. Nevertheless, it provides a reasonably good overview of the distribution of landslides in the region.

Taylor and Brabb (1972) included in their report a map

(scale 1:500,000) showing all landslides that they investigated for the 1968–69 season. The map gives an impression of the distribution of structurally damaging landslides in the region, and of how many new ones might be expected from development of some hilly regions where Radbruch and Wentworth's (1971) map shows landslides to be abundant.

INVENTORY OF LANDSLIDE DEPOSITS

Maps showing the distribution of landslide deposits in the entire bay region (scale 1:62,500) are now being prepared, primarily by interpretation of aerial photographs, with minimal field checking. This technique is necessary because of the size of the area, inaccessibility of much of it, and time limitations. The inventory of landslide deposits provided by these maps will be used in conjunction with other data to prepare derivative maps showing relative slope stability.

Seven preliminary photointerpretation maps of landslide deposits have been released (Brabb and Pampeyan, 1972b; Nilsen, 1971, 1972a,b,c,d; Sims and Nilsen, 1972), and many more are being prepared. They show where landslide deposits were recognized at the time the aerial photographs were taken. Although the type of movement, date of most recent activity, and nature of the landslide materials are not indicated, the maps are nevertheless useful. Most landslide activity consists of renewed movement of older landslide deposits. The maps can therefore be used as a general guide to problem areas, and as they provide a regional picture of the past history of landslide activity, they are also useful for site investigations by consulting engineering geologists. Construction activities can alter the marginally stable character of older landslide deposits and induce renewed movement.

The photointerpretive techniques used have enabled recognition of a large number of landslide deposits in most areas and have shown that landsliding is one of the major erosional processes in the bay region. The techniques depend upon recognition of scarps, anomalous bulges and lumps, hummocky topography, ridgetop trenches and fissures, terraced slopes, abrupt slope changes, altered stream courses, discontinuous drainage patterns, closed depressions, springs, and anomalous color, texture, shade, vegetation, and bedrock patterns.

SLOPE MAPS

Slope maps of selected areas within the San Francisco Bay region have been prepared by a new, experimental technique utilizing contour negatives of the Geological Survey's 1:24,000 topographic map series. The contour lines are diffused photomechanically in measured increments to produce the desired slope intervals (in percent): 0–5, 5–15, 15–30, 30–50, 50–70, and greater than 70. These six intervals are currently being used for many other studies and were selected after discussions with project geologists and city, county, and regional planners and engineers. Complete coverage of the nine

San Francisco Bay counties with slope maps at scales of 1:62,500 and 1:125,000 is planned.

Color transparencies as well as black-and-white prints have been combined several different ways to determine the best way to show slope intervals. For San Mateo County, a color transparency at a scale of 1:62,500 was superimposed on geologic and landslide maps to make a landslide-susceptibility analysis (see discussions under "Slope stability"). Inexpensive diazo prints were also prepared from positives of the color-separation negatives and were used to provide slope information for a coastline study by regional planners. Black-and-white composites as well as transparencies with dark shades of color have so far proved unsatisfactory for slope-stability studies because the contour base or other information needed for the study, such as the identification of the rock unit, cannot easily be seen.

Minor errors are introduced by the photomechanical process, especially along narrow ridge crests and valley floors, where slope categories tend to be too high. The errors can be taken into account when the contour base is examined in conjunction with the slope data.

SLOPE STABILITY

Geologic maps emphasizing engineering properties of rock units, including slope stability and shear strength, have been published for only a few parts of the bay region. Maps showing only slope stability, however, are rare. Johnson and Ellen (1968) and Johnson and Lobo-Guerrero (1968) made slope-stability maps of small areas in the town of Portola Valley. These maps were the first in the San Francisco Bay region to depict slope stability in a cartographic format that could be readily understood by urban planners. Unfortunately, neither map has been published.

A report by Blanc and Cleveland (1968) firmly established a methodology for preparing slope-stability maps in a small area of southern California. Brabb, Pampeyan, and Bonilla (1972) prepared a landslide-susceptibility map of San Mateo County based in part on the methodology of Blanc and Cleveland (1968) and in part on data provided by Bonilla (1960a,b). They (Brabb and others) avoided using the term "slope stability" because the stability of an individual slope was not analyzed. Instead, they expressed the average susceptibility of slope-material units over the region. Their map differs from others in that the landslide failure record for each rock unit in six different slope categories was systematically measured and used in the analysis. Slope and strength of the rock unit seem to be the principal factors controlling slope stability in San Mateo County—other factors, such as structural control, soil type, rainfall, climate, and vegetation, appear to be averaged through time and space so that their relative influence, at least on a regional basis, is minimal.

Brabb, Pampeyan, and Bonilla (1972) used a geologic map, landslide map, and slope map (fig. 2) to prepare the

landslide-susceptibility map of San Mateo County. All three maps are at a scale of 1:62,500. Part of the geologic map, compiled by Brabb and Pampeyan (1972a), is shown on figure 2A. The landslide map, figure 2B, was prepared by Brabb and Pampeyan (1972b), largely by photointerpretation. The slope map, figure 2C, was prepared experimentally by the Geological Survey specifically for the slope-stability studies.

The landslide-susceptibility map, figure 2D, was prepared from the three aforementioned maps by the following method: the percentages of area within 35 geologic map units in San Mateo County that are covered by landslide deposits were estimated by use of a grid overlay with a grid size of 0.01 sq mi at the map scale. The geologic map units were then arbitrarily grouped in six classes, from class I with 0–1 percent area covered by landslide deposits to class VI with 54–70 percent. The class numbers express, therefore, the relative susceptibility of the geologic map units to landsliding, from I, very low, to VI, very high. The landslide deposits themselves are shown as a separate class, L. Each geologic map unit was then further evaluated to determine which slope categories were critical for the formation of landslides. If few or no landslide deposits formed on low slopes, the class number for the geologic map unit was reduced. Thus, a geologic map unit might be assigned III in comparison with the landslide susceptibility of other geologic map units, and II or I in low-slope categories where few failures occurred.

One advantage of this method is that it provides the regional planner with a way of evaluating the area between landslide deposits on the basis of the average failure record of the geologic map unit throughout a county. The method also compensates for stable formations on steep slopes and unstable formations on low slopes. The principal disadvantages are that the landslide susceptibility of flat areas adjacent to unstable slopes is underestimated, and the map does not express in absolute terms the likelihood that any given slope will fail in any given period of time. Field studies by engineering geologists are, of course, still necessary for evaluating any particular site.

The publication status of and area covered by the slope-stability and landslide maps are shown on figure 3.

CONCLUSIONS

Slope-stability studies provide basic information needed by land-use planners in the bay region. Much additional work will be required before the dynamics of downslope movements are completely understood, but the preliminary compilations (like the landslide inventory) are necessary for a broader understanding of regional slope stability. Also currently being studied are the relationships between recent landslide activity and rainfall cycles, and between landsliding and urban development, as well as the mechanics of coastal landsliding and the clay mineralogy of soils and bedrock units susceptible to sliding.

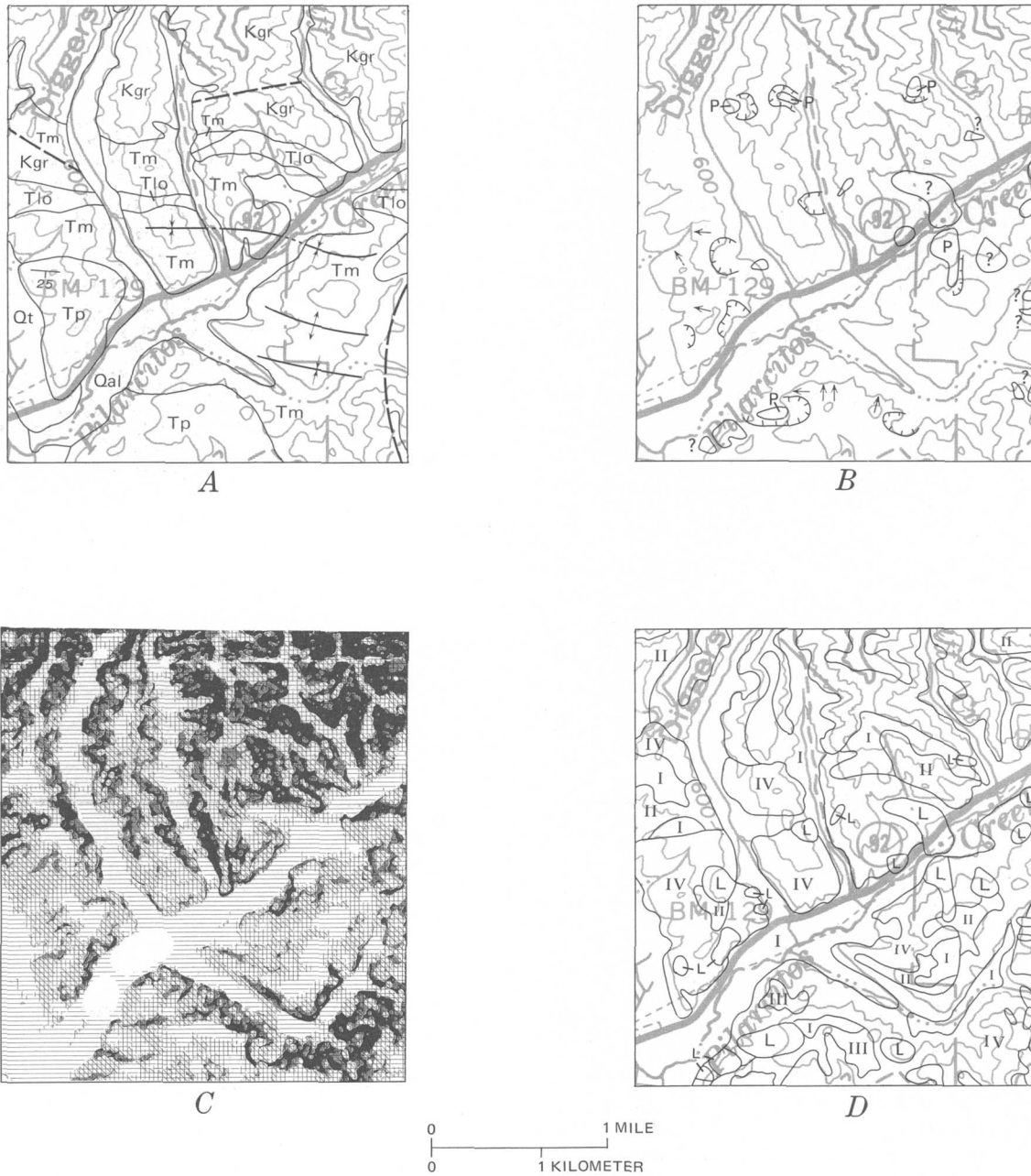


Figure 2.—Materials used for a landslide susceptibility map of San Mateo County, Calif. The area shown is near the town of Half Moon Bay about 25 km south of San Francisco (see fig. 1).

- A, geologic map; includes granitic rocks of Cretaceous age (Kgr), shale and sandstone of Miocene and Pliocene age (Tp, Tm, Tlo), terrace deposits (Qt), and alluvium (Oal). Heavy dashed lines are faults; thinner lines with arrows are fold axes.
- B, landslide map; the small arrows show landslide deposits 15 to 150 m in size, and the other lines show landslides larger than 150 m. The hachured lines show landslide scarps. P, probable landslide deposit; ?, questionable landslide deposit.
- C, slope map; the darker the tone, the greater the slope.
- D, landslide susceptibility map; the higher the roman numeral, the greater the susceptibility to landsliding. Landslide deposits (L) are shown as a separate category (the highest).

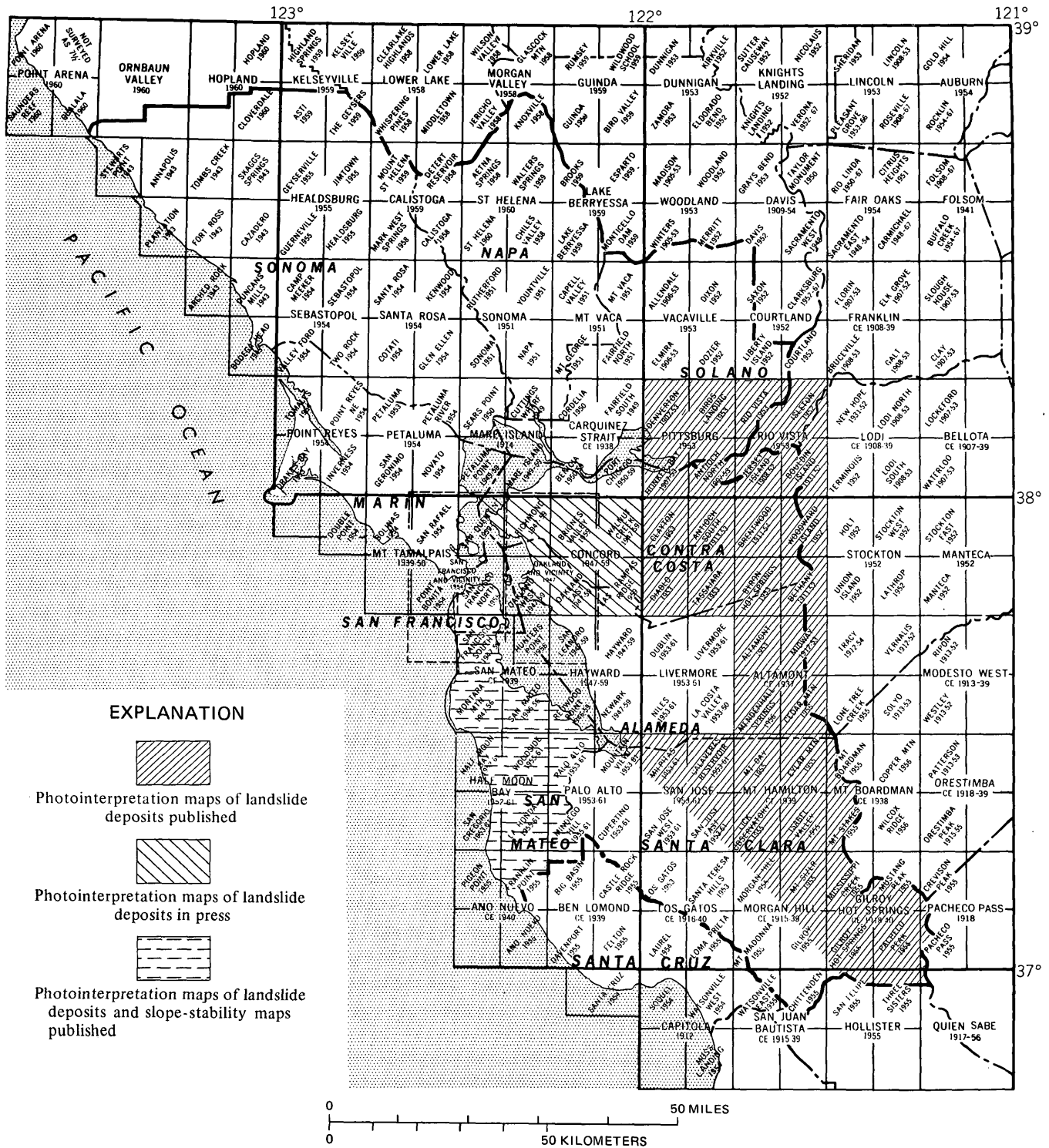


Figure 3.—Status of slope-stability studies in the San Francisco Bay region.

REFERENCES CITED

[Reports that have been released as Basic Data Contributions of the San Francisco Bay Region Environment and Resources Planning Study are noted in brackets after the formal reference citation as "BDC," with the number of the publication following]

Blanc, R. P., and Cleveland, G. B., 1968, Natural slope stability as related to geology, San Clemente area, Orange and San Diego Counties, California: California Div. Mines and Geology Spec. Rept. 98, 19 p.
 Bonilla, M. G., 1960a, Landslides in the San Francisco South quadrant, California: U.S. Geol. Survey open-file report, 44 p.

- 1960b, A sample of California Coast Range landslides: Art. 66 in U.S. Geol. Survey Prof. Paper 400-B, p. B149.
- 1971, Preliminary geologic map of the San Francisco South and part of the Hunters Point quadrangles: U.S. Geol. Survey Misc. Field Studies Map MF-311, scale 1:24,000 [BDC 29].
- Brabb, E. E., and Pampeyan, E. H., compilers, 1972a, Preliminary geologic map of San Mateo County, California: U.S. Geol. Survey Misc. Field Studies Map MF-328, scale 1:62,500 [BDC 41].
- 1972b, Preliminary map of landslides in San Mateo County, California: U.S. Geol. Survey Misc. Field Studies Map MF-344, scale 1:62,500 [BDC 42].
- Brabb, E. E., Pampeyan, E. H., and Bonilla, M. G., 1972, Landslide susceptibility in San Mateo County, California: U.S. Geol. Survey Misc. Field Studies Map MF-360 [BDC 43].
- Brown, R. D., Jr., 1970, Faults that are historically active or that show evidence of geologically young surface displacements, San Francisco Bay region; a progress report, October 1970: U.S. Geol. Survey Misc. Field Studies Map MF-331, scale 1:250,000 [BDC 7].
- Brown, R. D., Jr., and Lee, W. H. K., 1971, Active faults and preliminary earthquake epicenters (1969–1970) in the southern part of the San Francisco Bay region: U.S. Geol. Survey Misc. Field Studies Map MF-307, scale 1:250,000 [BDC 30].
- Clague, J. J., 1969, Landslides of southern Point Reyes National Seashore: California Div. Mines and Geology Mineral Inf. Service, v. 22, no. 7, p. 107–110, 116–118.
- Harding, R. C., 1969, Landslides—a continuing problem for Bay area development, in Danehy, E. A., ed., Urban environmental geology in the San Francisco Bay region, p. 65–74: Assoc. Eng. Geologists, San Francisco Section, Spec. Pub., 162 p.
- Johnson, A. M., and Ellen, S. D., 1968, Preliminary evaluation of the interaction between engineering development and natural geologic processes on the Bovet property, Town of Portola Valley, California, with a section on the San Andreas fault by William R. Dickinson: Report prepared for Town of Portola Valley, Calif., map scale about 1:2,400.
- Johnson, A. M., and Lobo-Guerrero, A. U., 1968, Preliminary evaluation of the relative stability of ground, Marianni property, Town of Portola Valley, California, with a section on the San Andreas fault by W. R. Dickinson: Report prepared for Town of Portola Valley, California, 22 p.
- Kachadoorian, R., 1956, Engineering geology of the Warford Mesa Subdivision, Orinda, California: U.S. Geol. Survey open-file report, 13 p.
- Kojan, E., 1968, Mechanics and rates of natural soil creep: Eng. Geologists and Soil Engineers Symposium, 5th Ann., Pocatello, Idaho, April 1967, Proc., p. 233–253.
- Nilsen, T. H., 1971, Preliminary photointerpretation map of landslide and other surficial deposits of the Mount Diablo area, Contra Costa and Alameda Counties, California: U.S. Geol. Survey Misc. Field Studies Map MF-310, scale 1:62,500 [BDC 31].
- 1972a, Preliminary photointerpretation map of landslide and other surficial deposits of parts of the Altamont and Carbona 15-minute quadrangles, Alameda County, California: U.S. Geol. Survey Misc. Field Studies Map MF-321, scale 1:62,500 [BDC 34].
- 1972b, Preliminary photointerpretation map of landslide and other surficial deposits of the Byron area, Contra Costa and Alameda Counties, California: U.S. Geol. Survey Misc. Field Studies Map MF-338, scale 1:62,500 [BDC 38].
- 1972c, Preliminary photointerpretation map of landslide and other surficial deposits of the Mount Hamilton quadrangle and parts of the Mount Boardman and San Jose quadrangles, Alameda and Santa Clara Counties, California: U.S. Geol. Survey Misc. Field Studies Map MF-339, scale 1:62,500 [BDC 40].
- 1972d, Preliminary photointerpretation map of landslide and other surficial deposits of parts of the Los Gatos, Morgan Hill, Gilroy Hot Springs, Pacheco Pass, Quien Sabe, and Hollister 15-minute quadrangles, Santa Clara County, California: U.S. Geol. Survey Misc. Field Studies Map MF-416, scale 1:62,500 [BDC 46].
- Nilsen, T. H., and Brabb, E. E., 1972, Preliminary photointerpretation and damage maps of landslide and other surficial deposits in northeastern San Jose, California: U.S. Geol. Survey Misc. Field Studies Map MF-361, scales 1:12,000 and 1:24,000 [BDC 45].
- Pampeyan, E. H., 1970, Geologic map of the Palo Alto 7½-minute quadrangle, San Mateo and Santa Clara Counties, California: U.S. Geol. Survey open-file map, scale 1:24,000 [BDC 2].
- Radbruch, D. H., 1957, Areal and engineering geology of the Oakland West quadrangle, California: U.S. Geol. Survey Misc. Geol. Inv. Map I-239, scale 1:24,000.
- 1969, Areal and engineering geology of the Oakland East quadrangle, California: U.S. Geol. Survey Geol. Quad. Map GQ-769, scale 1:24,000.
- Radbruch, D. H., and Weiler, L. M., 1963, Preliminary report on landslides in a part of the Orinda Formation, Contra Costa County, California: U.S. Geol. Survey open-file report, 35 p.
- Radbruch, D. H., and Wentworth, C. M., 1971, Estimated relative abundance of landslides in the San Francisco Bay region, California: U.S. Geol. Survey open-file map, scale 1:500,000 [BDC 11].
- Rogers, T. H., 1971, Environmental geologic analysis of the Santa Cruz Mountain study area, Santa Clara County, California: Sacramento, California Div. Mines and Geology, 64 p.
- Schlocker, Julius, 1968, The geology of the San Francisco Bay area and its significance in land use planning: Berkeley, Calif., Assoc. Bay Area Govts., Supp. Rept. IS-3, 47 p.
- 1971, Generalized geologic map of the San Francisco Bay region, California: U.S. Geol. Survey open-file map, scale 1:500,000 [BDC 8].
- Schlocker, Julius, Bonilla, M. G., and Radbruch, D. H., 1958, Geology of the San Francisco North quadrangle, California: U.S. Geol. Survey Misc. Geol. Inv. Map I-272, scale 1:24,000.
- Sims, J. D., and Nilsen, T. H., 1972, Preliminary photointerpretation map of landslide and other surficial deposits of parts of the Pittsburg and Rio Vista 15-minute quadrangles, Contra Costa and Solano Counties, California: U.S. Geol. Survey Misc. Field Studies Map MF-322, scale 1:62,500 [BDC 35].
- Taylor, F. A., and Brabb, E. E., 1972, Map showing distribution and cost by counties of structurally damaging landslides in the San Francisco Bay region, California, winter of 1968–69: U.S. Geol. Survey Misc. Field Studies Map MF-327, scale 1:1,000,000 [BDC 37].
- U.S. Geological Survey and U.S. Department of Housing and Urban Development, 1971, Program design 1971, San Francisco Bay region environment and resources planning study, PB2-06826: Available only from U.S. Dept. Commerce Natl. Tech. Inf. Service, Springfield, Va., 123 p.
- Waltz, J. P., 1971, An analysis of selected landslides in Alameda and Contra Costa Counties, California: Assoc. Eng. Geologists Bull., v. 8, no. 2, p. 153–163.



DEEP-SEA FAN PALEOCURRENT PATTERNS OF THE EOCENE BUTANO SANDSTONE, SANTA CRUZ MOUNTAINS, CALIFORNIA

By TOR H. NILSEN and T. R. SIMONI, JR., Menlo Park, Calif.

Abstract.—The Butano Sandstone is an Eocene continental borderland deep-sea fan deposit located in the Santa Cruz Mountains, Calif. Paleoslope measurements from contorted strata within it yield a regional northward paleoslope for the fan. Detailed paleocurrent measurements from conglomerate clast orientations, flute casts, groove casts, current-ripple markings, small-scale cross-strata, convolute laminations, and flame structures yield a sediment-dispersal pattern characterized by northward transport of coarser grained sediments downfan along major channels and transport of finer grained sediments outward and away from channels by overspilling. The overall paleocurrent pattern is oriented radially outward from the fan apex and indicates that the growth, development, and dispersal of sediments on this ancient deep-sea fan resembled that on modern deep-sea fans.

Sedimentological studies by the writers indicate that the Butano Sandstone of the Santa Cruz Mountains was deposited as a deep-sea fan in a continental borderland setting (Nilsen, 1970, 1971). Among the attributes of the Butano that strongly suggest this depositional setting are the paleocurrent patterns derived from various sedimentary structures within it. Documentations of such patterns from ancient deep-sea fan deposits are generally lacking in geologic literature; the paleocurrent patterns and the associated sediment-dispersal model presented herein will provide an example for geologists working on other ancient fan deposits and will permit sedimentological comparisons with modern fan systems.

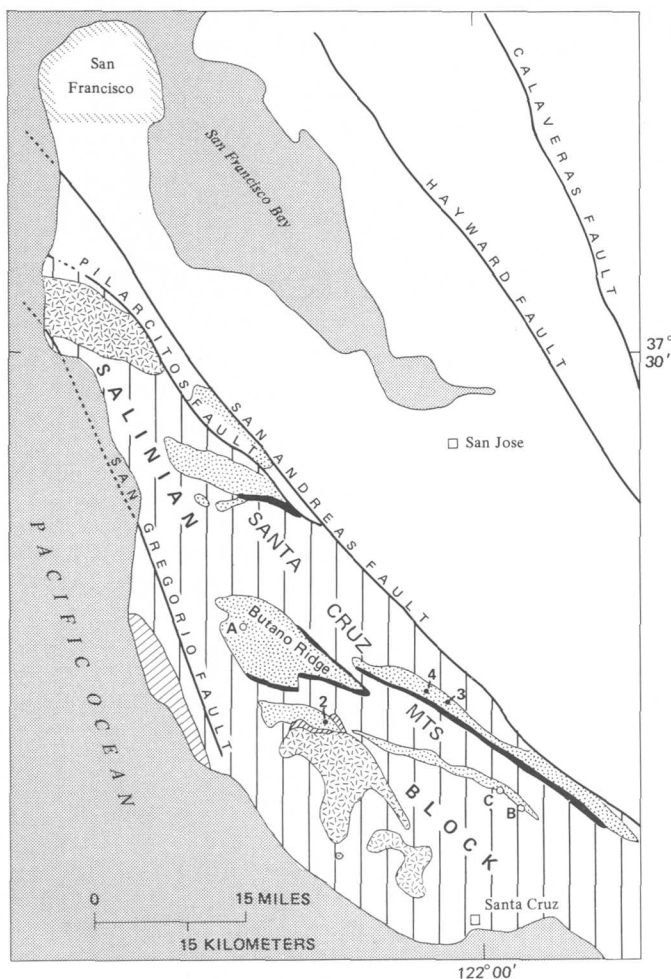
The Butano crops out discontinuously in the Santa Cruz Mountains over a northwest-southeast distance of about 40 miles (fig. 1). Its thickness and areal extent make it a major rock unit in the region, and it is an oil reservoir in the La Honda and Costa oil fields. The northeastern edge of its outcrop area is abruptly terminated by the Pilarcitos and San Andreas faults. Regional paleogeographic reconstructions and sedimentologic studies suggest that the missing eastern part of the ancient Butano fan is the Point of Rocks Sandstone in the Temblor Range, located approximately 190–200 miles to the southeast (Clarke and Nilsen, 1972). Because the rocks on opposite sides of the San Andreas fault have undergone considerable right-lateral offset (Dibblee, 1966a), rocks mapped by Dibblee (1966b) and Brabb (1970) as Butano(?)

Sandstone in the part of the Santa Cruz Mountains east of the Pilarcitos and San Andreas faults should not be considered Butano. These rocks were originally deposited in a separate basin at least 200 miles distant from the true Butano located west of these faults (Beaulieu, 1970).

The Butano Sandstone was named by Branner, Newsom, and Arnold (1909) for massive brown and buff sandstone and minor conglomerate over 2,000 feet thick on Butano Ridge. It was later mapped and studied in greater detail in Stanford University Ph. D. theses by Touring (1959), Brabb (1960a), Cummings (1960), and Clark (1966); it was also mapped and described in several Stanford University M.S. theses and student projects during approximately the same period of time. Cummings, Touring, and Brabb (1962) have summarized the lithologic characteristics and stratigraphic relations of the Butano; Brabb (1970) and Brabb and Pampeyan (1972) have compiled recent geologic maps showing the distribution of the Butano Sandstone. The type section for its uppermost part was designated by Cummings, Touring, and Brabb (1962, p. 184) as along Little Boulder Creek in SW¼ sec. 22, SE¼ sec. 21, and N½ sec. 28, T. 8 S., R. 3 W.

The Butano ranges in age from early Eocene (Penutian) to late Eocene (Narizian) on the basis of foraminiferal studies, although most of it was deposited during the Narizian Stage of Mallory (1959). The foraminiferal studies also indicate that deposition took place in a bathyal to abyssal marine environment in a basin with unrestricted access to the ocean (Sullivan, 1962; Clark, 1966; Fairchild and others, 1969).

The Butano unconformably overlies the marine Paleocene Locatelli Formation of Brabb (1960b) and is overlain conformably by the Twobar Shale Member of Brabb (1964), a deep-sea hemipelagic shale deposit forming the lowest member of the San Lorenzo Formation. The minimum thickness of the Butano is 4,000 feet; the maximum, possibly as much as 10,000 feet. However, because it crops out as a series of isolated folded and faulted blocks, a complete section is nowhere exposed (fig. 1). Outcrops of the Butano are generally poor because of deep weathering, thick soil horizons, and extensive vegetative cover, and beds cannot generally be traced for more than 50–100 feet.



EXPLANATION

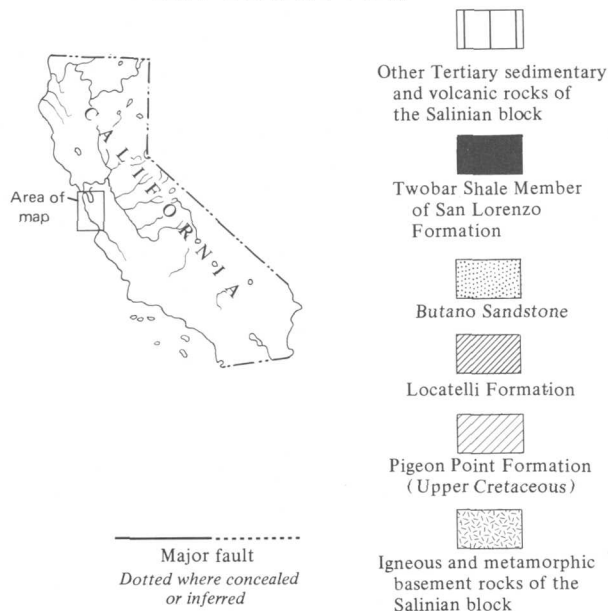


Figure 1.—Generalized geologic map of the Santa Cruz Mountains, showing the distribution of Butano Sandstone. Numbers 2, 3, and 4 are locations of figures 2, 3, and 4, respectively; A, B, and C, are locations of conglomerate fabric measurements of figure 7. Geology from Brabb (1970) and Brabb and Pampeyan (1972).

Acknowledgments.—We thank Earl E. Brabb for suggesting the study and providing much assistance during it.

SEDIMENTOLOGY

Sedimentary facies

The Butano Sandstone contains a great variety of sedimentary structures characteristic of deposition by grain-flow or other mass flow processes, turbidity currents, and downslope slumping. Sandstone, conglomerate, and shale are the major rock types. Coarser and thicker bedded deposits are most common in the southern part of the outcrop area, where thickly bedded sandstone and conglomerate that resemble fluxoturbidite and grain-flow deposits are found (Dzulynski and others, 1959; Stauffer, 1967; Stanley and Unrug, 1972).

The conglomerate, which is abundant to the south, is locally very coarse, is typically irregularly bedded, and commonly shows abrupt lateral changes in bedding thickness and coarseness (fig. 2). The sandstone typically consists of repetitively alternating deposits of thick ungraded medium- or coarse-grained Bouma *a* sandstone overlain by thin, discontinuous Bouma *e* shale (Bouma, 1962); the sandstone is commonly channeled into the underlying deposits, with considerable lateral thickening and thinning (fig. 3). These deposits are thought to represent channel deposits of the upper part (toward the south) of the Butano deep-sea fan. These channel deposits grade laterally northward into finer grained and thinner bedded channel deposits characterized by Bouma *ae* and Bouma *abe* sequences; further north, these deposits become even more thinly bedded and finer grained and are characterized by Bouma *abcde* and *bcde* sequences.

Interbedded vertically with the channel deposits and grading laterally into them are various types of interchannel deposits.

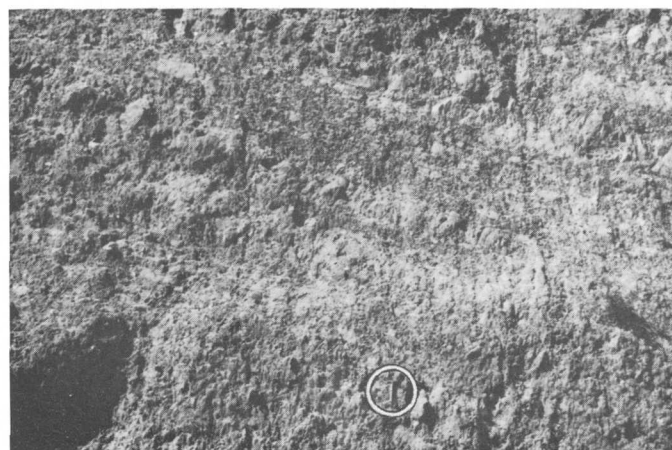


Figure 2.—Irregularly bedded, coarse-grained conglomerate from upper fan-channel deposit in the Butano Sandstone. Rock hammer (circled) located in lower center for scale. Location of photograph shown on figure 1.

In the southern part of the outcrop area, these interchannel deposits consist of repetitively alternating thin beds of fine-grained sandstone and shale, forming Bouma *cde* sequences; further north, these deposits consist of Bouma *bcde*, *cde* and *de* sequences (fig. 4). In the northernmost outcrops thick sequences of mudstone containing thinly interbedded fine-grained sandstone or siltstone with current-ripple laminae and irregular small-scale cross-laminae are conspicuous.

The various sedimentary facies show abrupt lateral changes throughout the outcrop extent of the Butano Sandstone. In

fact, nearby measured sections covering the same stratigraphic intervals differ markedly, making correlation of individual beds or groups of beds virtually impossible. In vertical sequence, the facies also change abruptly, with sequences of thinly bedded, finer grained interchannel deposits irregularly alternating with sequences of thickly bedded, coarser grained channel deposits. These relations indicate continued migration of channels and changing patterns of deposition during growth of the fan.

Sedimentary structures

Sedimentary structures in the Butano are found typically within Bouma sequences, which consist of regularly interbedded cycles of coarser grained sediments that grade upward into finer grained sediments (Bouma, 1962). Sedimentary structures found include flute casts, groove casts, cross-stratification, current-ripple markings, planar bedding, convolute laminations, flame structures, dish structures, load casts, extensive bioturbation, channeling, graded bedding, shale rip-ups, diapirs, possible antidune features, amalgamated sandstone beds, mass-flow features, small-scale structures formed by the escape of gas or water, and various types of synsedimentary slumped and contorted strata. Conglomerate fabrics are variable, but some are markedly anisotropic and contain well-oriented and imbricated clasts.

Conglomerate clast size distribution

The longest dimensions of the 10 largest conglomerate clasts were measured at each conglomerate-bearing outcrop of Butano Sandstone (fig. 5). The largest clasts are concentrated into two distinct groups along the southwestern and southeastern edges of the outcrop area. These boulder accumulations probably represent deposits in major channels of the upper fan region. The maximum clast size decreases very rapidly northward from these areas, as well as between them; only scattered occurrences of very fine pebbles are found in the northern outcrops.

PALEOSLOPES AND PALEOCURRENTS

Method of study

Synsedimentary contorted strata and slumps were used to determine probable paleoslope orientations; paleocurrents were determined from conglomerate clast orientations and measurements of flute casts, groove casts, current-ripple markings, small-scale cross-strata, trough cross-strata, convolute laminations, and flame structures. A total of 565 paleocurrent indicators and 105 paleoslope indicators were measured in the field. Separate maps were prepared for each type of sedimentary structure or group of genetically related



Figure 3.—Thickly bedded, medium- to coarse-grained sandstone from upper to middle fan-channel deposit in the Butano Sandstone. Notebook in lower left is approximately 8 inches long. Location of photograph shown on figure 1.



Figure 4.—Rhythmically interbedded fine-grained sandstone and mudstone from upper to middle fan interchannel deposit in the Butano Sandstone. Location of photograph shown on figure 1.

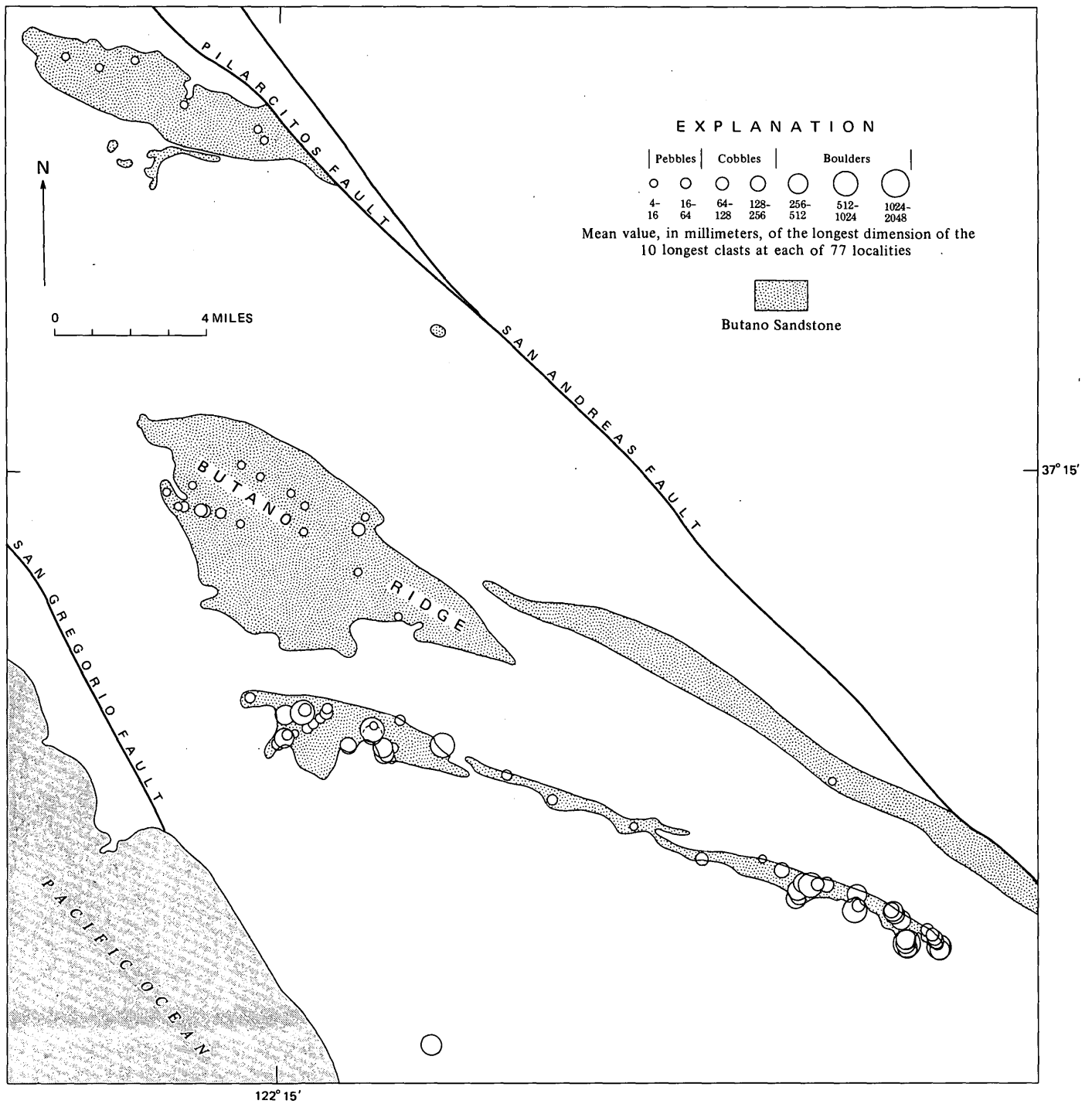


Figure 5.—Distribution of longest clasts in conglomerate beds in the Butano Sandstone.

structures so that paleocurrent and paleoslope patterns resulting from various depositional processes could be clearly differentiated.

The term paleoslope or paleocurrent "direction" is applied in this paper to derived orientations that have only one

possible solution, such as from cross-strata, flute casts, and asymmetrical current-ripple markings. Paleoslope or paleocurrent "sense" is applied to derived orientations that do not have single solutions that may be in one of two directions 180° apart, such as from groove casts and symmetrical ripple

markings. Some sedimentary structures that ordinarily yield paleocurrent directions were so poorly exposed or developed that only paleocurrent senses could be derived from them.

All paleoslope and paleocurrent measurements were made in the field; subsequent stereographic two-tilt restorations were made by use of computer programs developed by Parks (1970). As many as four directions from a single locality are plotted individually on the paleoslope and paleocurrent maps; where more than four direction measurements were taken at a single locality, the vector mean and standard deviation for the group of directions are plotted. The vector means have been derived according to Curray's method (1956), and standard deviations have been derived mathematically. The standard deviations have been used even where larger than about 60° , their normal useful limit for circular distributions. Paleocurrent or paleoslope directions are plotted separately from senses on all maps.

The locations of paleoslope and paleocurrent orientations are plotted without regard to their stratigraphic position within the Butano Sandstone. Thus, the patterns presented herein are composites taken from all outcrops and the entire stratigraphic range of the Butano. We have, however, separately determined that the paleoslope and paleocurrent orientations from individual measured sections have approximately as wide a spread as a similar number of orientations from a larger area. This indicates great variability in paleoslope and paleocurrent orientations over the entire surface of the fan as well as in any portion of the fan through time.

Paleoslope orientations

The Butano Sandstone contains abundant evidence for downslope subaqueous slumping and sliding. Both low-angle rotational slumps of the type described by Laird (1968) and contorted, folded strata are common. Within the proposed fan environment, downslope movements took place mainly toward the north down the probable regional paleoslope, but also more randomly into local topographic lows such as channels or interchannel areas adjacent to channel levees. The slumping and sliding probably occurred on relatively low slopes under the influence of gravity, as suggested by Dott (1963).

Paleoslope measurements were made on 105 contorted beds. In 62 places, the contorted or folded beds had a preferred orientation of asymmetry, yielding a paleoslope direction; in the remainder, the folds were either symmetrical or so complexly folded that only paleoslope senses could be determined. The mean paleoslope direction for the asymmetric contorted strata is $8^\circ \pm 63^\circ$, and mean paleoslope sense for the symmetric or complexly contorted strata is $32^\circ \pm 57^\circ$ (fig. 6).

Almost all of the contorted beds range in thickness from 7 to 70 cm. Overlying and underlying beds are usually flat and undisturbed. The contorted beds most commonly consist of thinly interbedded fine-grained sandstone and mudstone of Bouma *cde* sequences; these are particularly common in

interchannel and lower fan-channel deposits. As such, they are found scattered throughout much of the outcrop area. Some contorted beds may have resulted from the shearing stress applied by currents passing over flat beds, similar to the way that convolute laminations are developed (Sanders, 1960, 1965). However, most do not appear related to current movements, but to downslope sliding and slumping along bedding planes while the sediments were still unconsolidated and characterized by high pore fluid pressures.

The predominant orientation of the paleoslope directions toward the north suggests that the regional northward paleoslope of the ancient Butano fan provided the major control over the direction of movement of folded and contorted beds. Some contorted strata slumped southward, however, which suggests that variably oriented features with small-scale relief were present on the fan surface. No reliable measurements were made of the orientation of surfaces along which rotational slumping took place; most of the paleoslope data are based on measurements of contorted strata.

Paleocurrent orientations

Conglomerate fabric.—Some conglomerates in the Butano Sandstone have well-defined fabrics, with the long axes of elongate clasts oriented parallel to one another on bedding surfaces, and a strongly preferred imbrication. Unfortunately, extensive studies of clast orientations were not possible because of the high degree of induration and the lack of good exposures of conglomerate containing well-defined bedding. The conglomerate fabric orientation was, however, measured at the three localities noted on figure 1; these localities were the only suitable sites found for fabric measurements. The conglomerates at these localities undoubtedly are fan-channel deposits.

The orientations of long axes of clasts on bedding surfaces at two locations (A and B, fig. 1) are shown in figure 7; the vector means and standard deviations are $294^\circ \pm 51^\circ$ and $324^\circ \pm 45^\circ$ for 65 and 95 observations, respectively. The conglomerate at locality A is finer grained and has a smaller percentage of elongate clasts than the one at locality B. The conglomerates are not, however, from the same stratigraphic horizon or sedimentation unit. The poles to the maximum projection areas of 69 randomly selected flat-shaped clasts from locality C, were plotted on the lower hemisphere of an equal-area stereonet projection (fig. 7); most poles plot in the north-central part of the stereonet, indicating a northward-directed imbrication that would be produced by northerly flowing currents.

These limited fabric data suggest sediment transport to the north in channels of the southeastern area (localities B and C) and to the northwest in the northwestern area (locality A); however, many more measurements are required to define the channel orientations and current directions from the conglomeratic fabric.

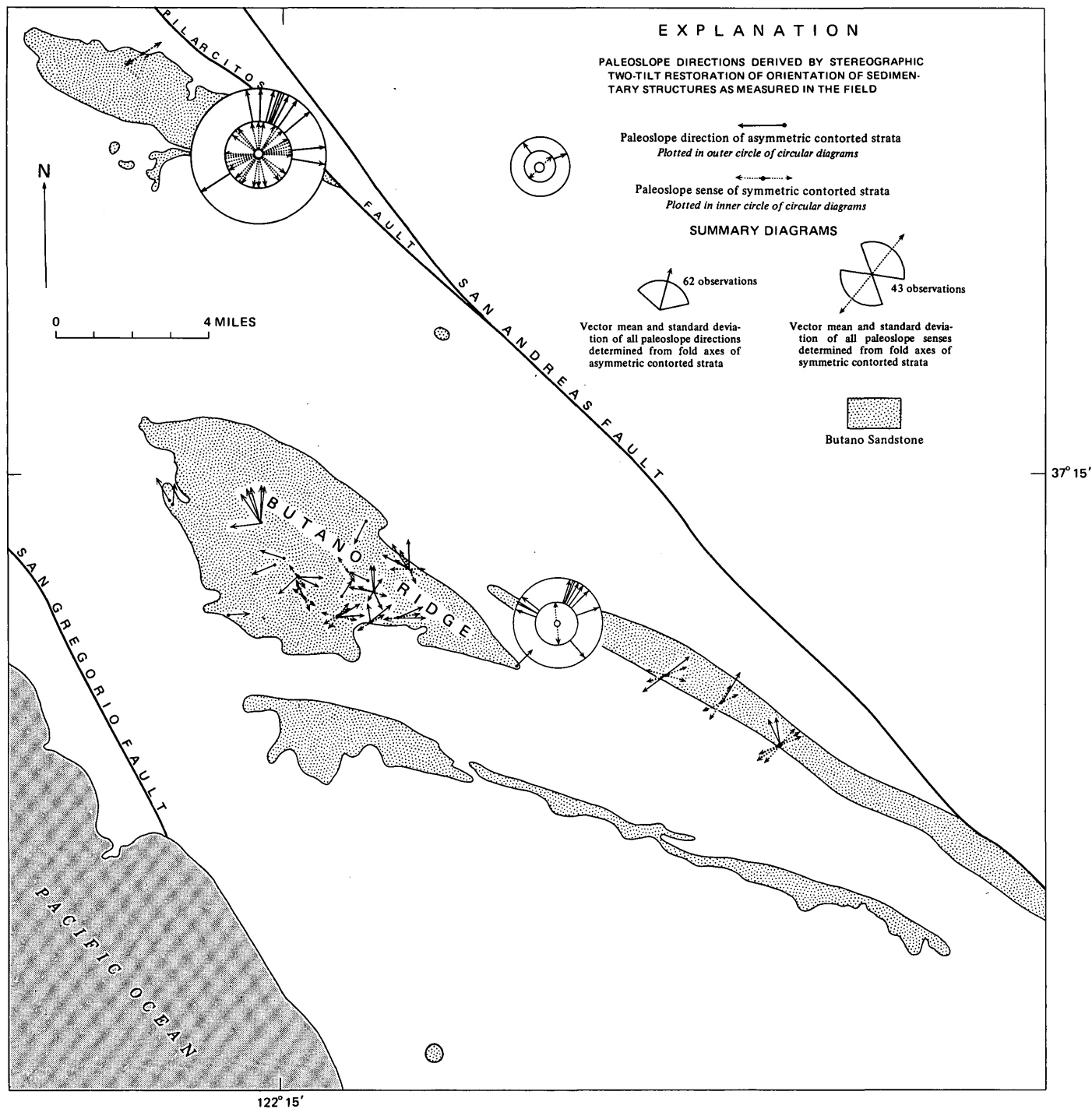
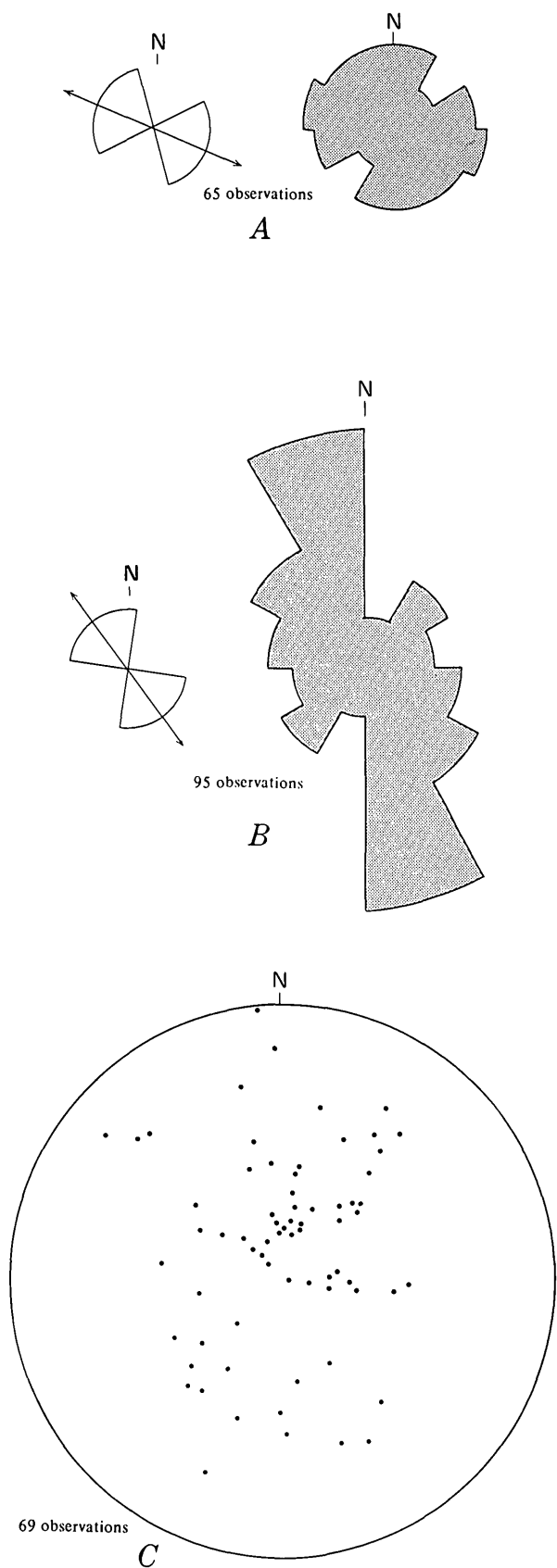


Figure 6.—Paleoslope pattern from contorted stratification in the Butano Sandstone.

Flute casts and groove casts.—Ten paleocurrent directions determined from flute casts in the Butano Sandstone yield a mean paleocurrent direction of $335^{\circ} \pm 20^{\circ}$ (fig. 8). Nineteen additional measurements from groove casts and poorly developed flute casts with uncertain asymmetry yield northerly

paleocurrent senses. Most of the flute casts and groove casts are irregularly shaped, similar to the type described by Stauffer (1967) from grain-flow deposits in the Santa Ynez Mountains, Calif. Most are sole markings at the base of thick Bouma *ae* sequences and presumably formed in main channels



of the upper to lower fan area. The relatively narrow range in their orientation suggests that the main channels primarily had northerly trends.

Ripple markings.—The orientations of 44 ripple markings were measured in the Butano Sandstone. All the ripple markings visible in cross section are of the current-ripple type. On bedding surfaces, however, many are symmetrical in shape, so that only current senses could be determined from them. The mean current direction of the 25 asymmetrical current-ripple markings is $50^{\circ} \pm 62^{\circ}$; the mean current sense of the 19 symmetrical ripple markings is $15^{\circ} \pm 53^{\circ}$ (fig. 9). Thus, the ripple markings show a wide range of current orientations, many at approximately right angles to the general northern paleoslope direction. The ripple markings are all small scale and are typically from Bouma *c* horizons. They are found in interchannel deposits as well as in middle and lower fan-channel and fan-fringe deposits. Thus, their variable orientations probably reflect downchannel current transport as well as overbank spilling perpendicular to the channels.

Cross-strata.—The largest number of paleocurrent measurements were from small-scale cross-strata; these are plotted in figure 10 and yield a vector mean of $8^{\circ} \pm 61^{\circ}$. All of the 453 inclined cross-strata are small scale, with amplitudes ranging from 2 to 10 cm; nearly all were formed by migrating current ripples and dunes. Only two trough cross-strata were noted and measured in the field; these are of larger scale than the inclined cross-strata, having amplitudes of about 20 cm. They were found at the top of thick, massive Bouma *a* deposits and may have developed when movement of entrained water from a grain-flow scoured the top of the bed after the flow had ceased (Middleton, 1969, p. GM-B-11).

The distribution of the small-scale cross-strata is similar to that of the ripple markings. However, the larger number of measurements of these structures reveals far more details of the overall paleocurrent pattern. Many paleocurrent directions are clearly at right angles to the general northern direction of transport, particularly along the eastern and western edges of the outcrop area. The northernmost outcrops yield paleocurrents that are generally directed northward. The summary rose diagram yields a radial distribution of paleocurrent directions for the postulated Butano deep-sea fan.

Convolute laminations and flame structures.—Paleocurrent measurements were made from 38 convolute laminations, three of which were so irregularly shaped that only paleocurrent senses could be determined from them (fig. 11). Four flame structures yielded scattered paleocurrent directions. The

Figure 7.—Long-axis orientation of elongate clasts and imbrication of flat clasts in conglomerate of the Butano Sandstone. *A* and *B*, direction of long axes of elongate clasts on bedding surfaces; vector means and standard deviations on left, rose diagrams on right. *C*, imbrication measurements; poles to maximum projection area of flat clasts projected onto lower hemisphere of equal-area stereonet. See figure 1 for locations of measurements.

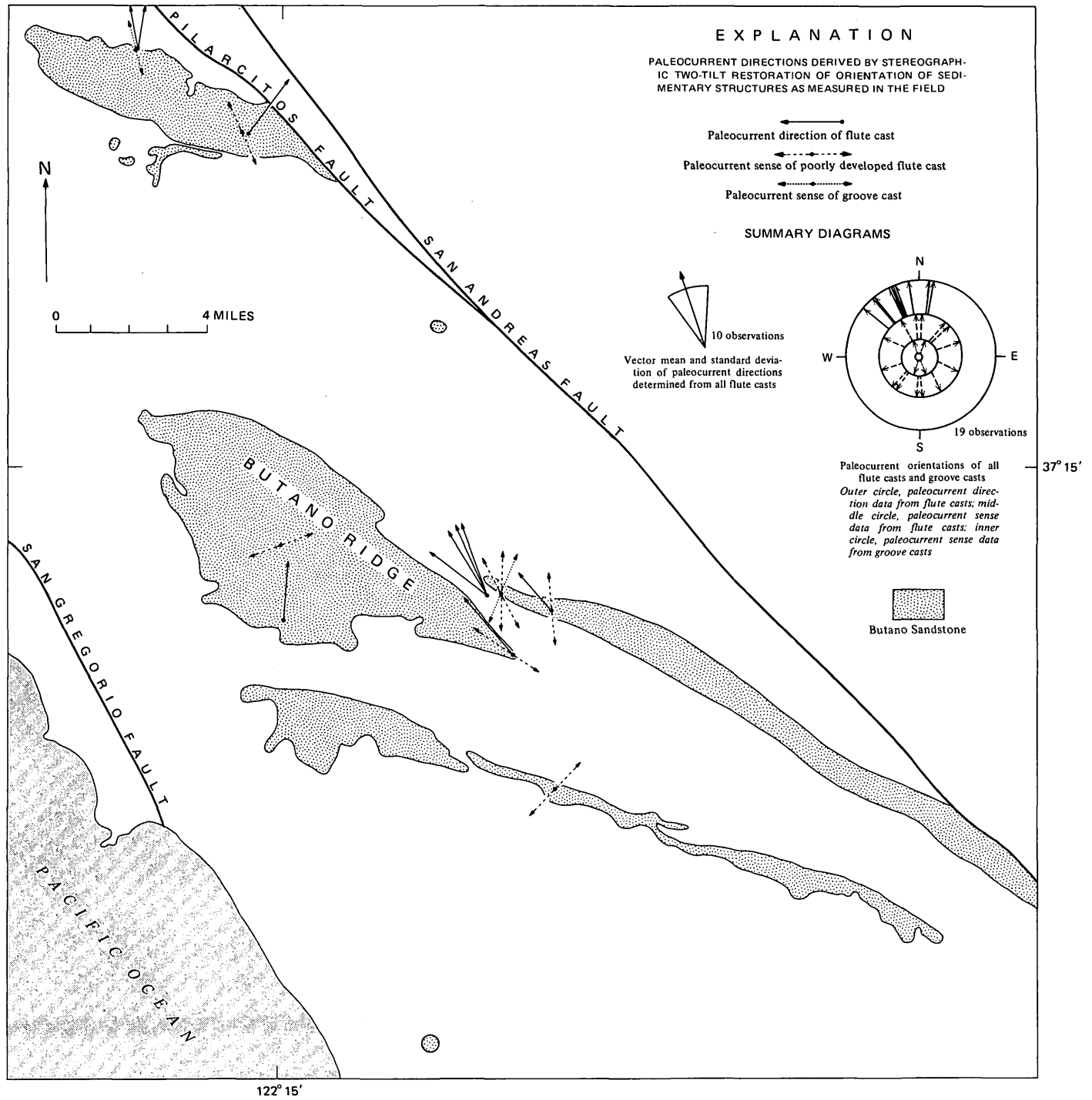


Figure 8.—Paleocurrent pattern from flute casts and groove casts in the Butano Sandstone.

convolute laminations have a wide range of paleocurrent orientations, with a vector mean of $16^{\circ} \pm 62^{\circ}$. These structures are characteristic of Bouma *c* deposits and are found in the same types of deposits as small-scale cross-strata and ripple markings.

Summary

The paleocurrent and paleoslope data are summarized in table 1. Flute casts and groove casts have the narrowest spread of paleocurrent orientations, probably reflecting the fact that

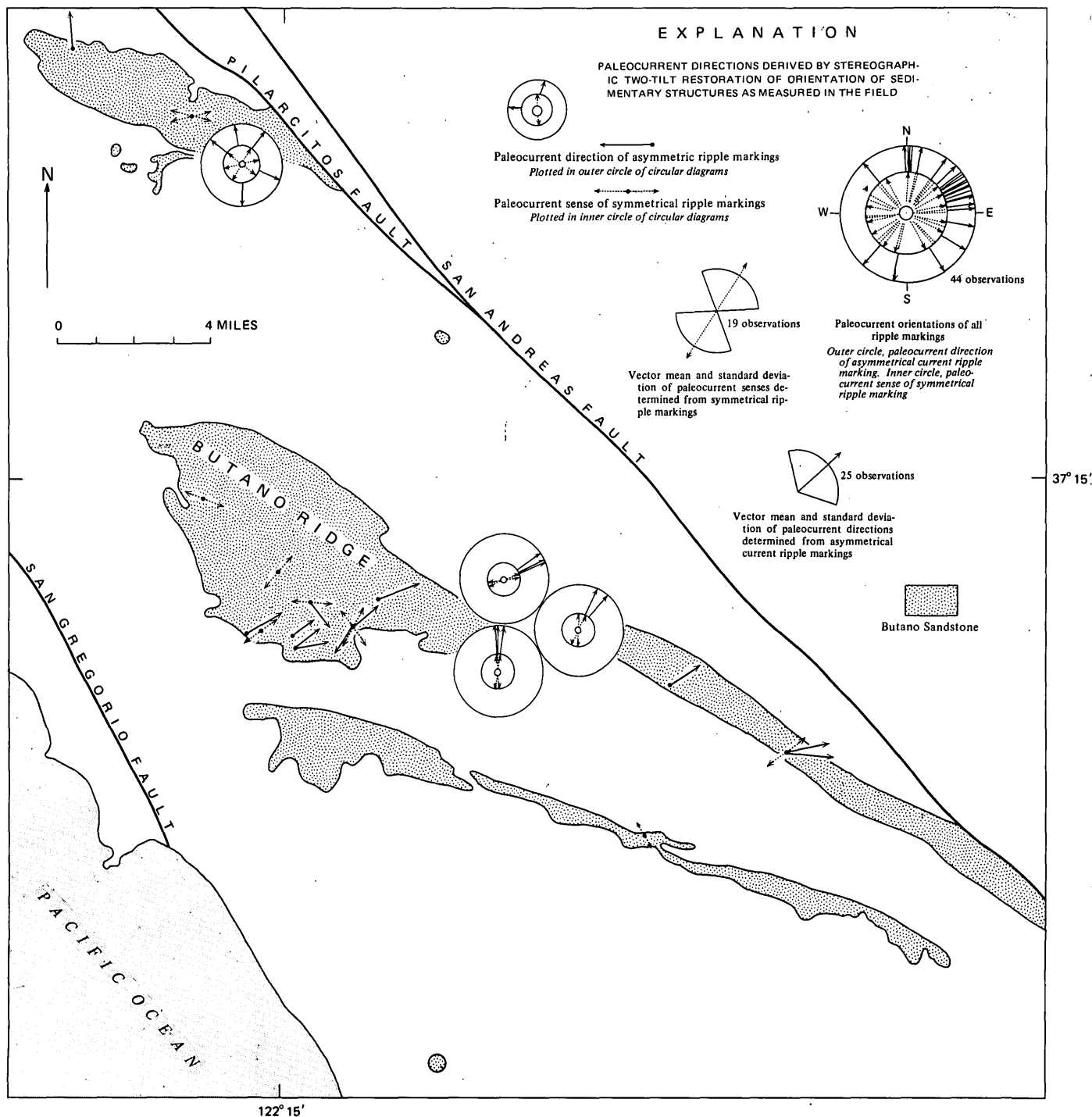


Figure 9.—Paleocurrent pattern from ripple markings in the Butano Sandstone.

they formed in channels in which sediment transport was primarily downfan. Other sedimentary structures, including ripple markings, cross-strata, and convolute laminations, have higher standard deviations because of more variable directions of sediment transport, especially out of and away from channels.

SEDIMENT DISPERSAL ON MODERN DEEP-SEA FANS

Modern deep-sea fans are generally characterized by (1) a submarine canyon which acts as a conduit for the transport of sediment from the shallow marine or nearshore environments

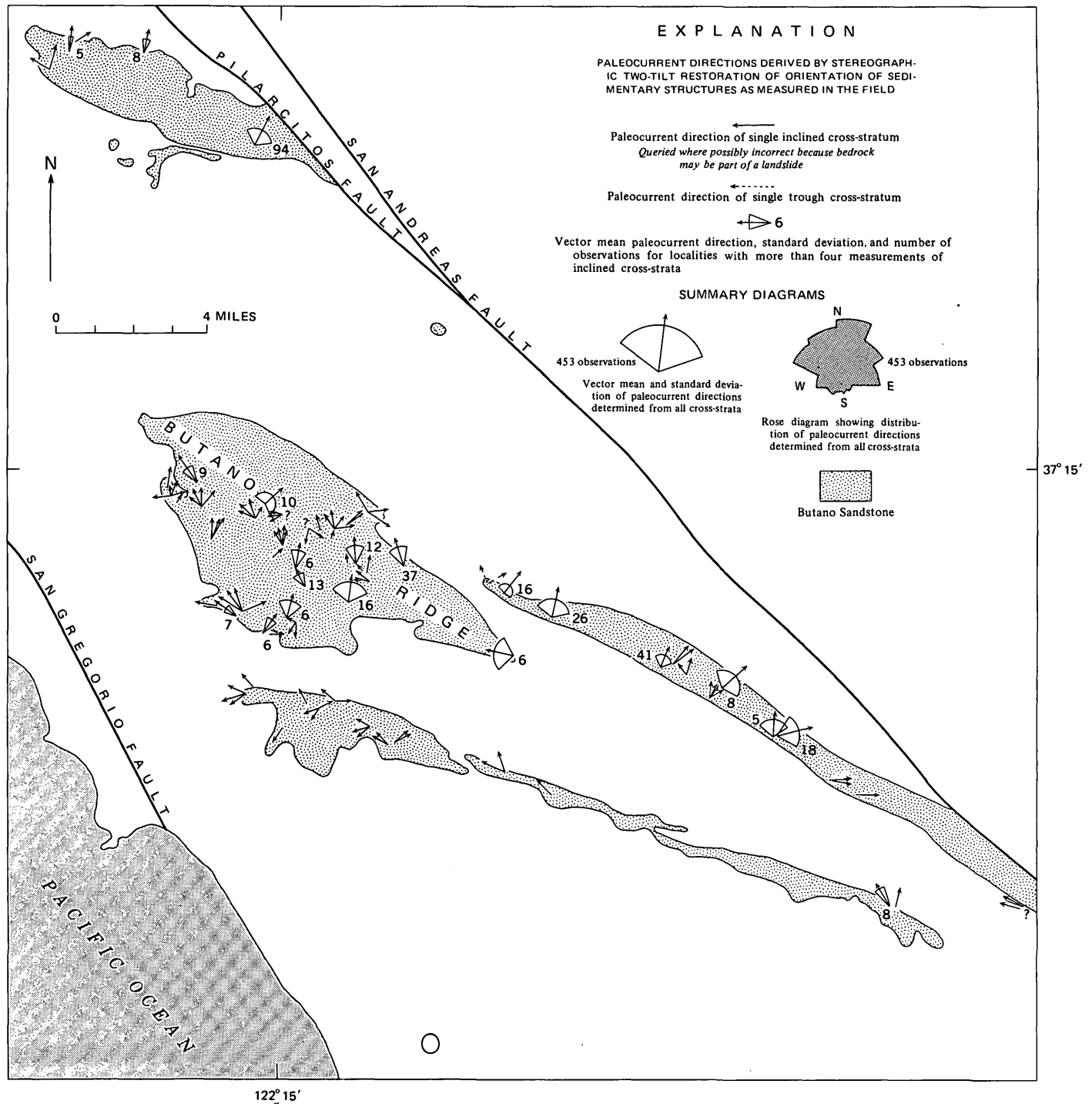


Figure 10.—Paleocurrent pattern from cross-strata in the Butano Sandstone.

to deeper water; (2) a leveed, incised upper fan valley which extends out onto the fan surface from the canyon; (3) a midfan bulge, or suprafan, formed where the leveed upper fan valley divides downfan into two or more major fan channels; (4) a distal fan area where the suprafan channels divide downfan into many smaller and shallower distributary chan-

nels; and (5) a fan-fringe area, where the sands and silts deposited on the fan grade laterally outward into hemipelagic sediments of the open ocean (Normark, 1970a; Piper, 1970; Haner, 1971; Nelson and others, 1970; Normark and Piper, 1969, 1972). Deposits are thickest and sedimentation rates highest on the suprafan area. Fan shapes are influenced by

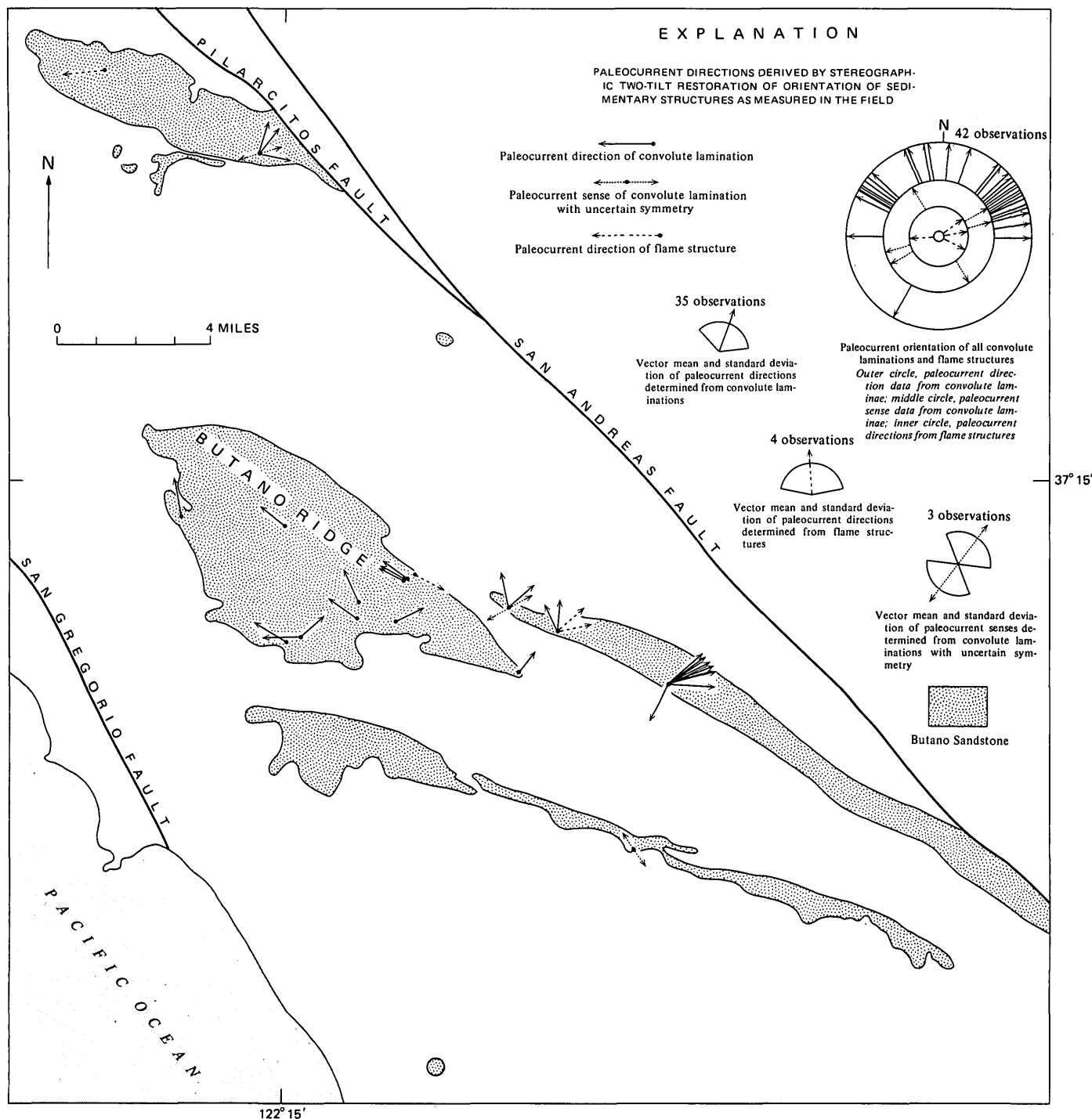


Figure 11.—Paleocurrent pattern from convolute laminations and flame structures in the Butano Sandstone.

local submarine geography, penecontemporaneous tectonism, sediment supply, and climatic factors.

The general direction of sediment transport on modern deep-sea fans is oriented radially outward from the fan apex, similar to that of alluvial fans (Bull, 1972). However, control of the depositional process by major channels yields two major

components of sediment transport: (1) downfan transport along channels, and (2) overflow transport out from and commonly perpendicular to the channels. This relatively simple pattern of sediment transport is modified, however, by several other factors which may yield very complex paleocurrent patterns for ancient fan deposits.

Table 1.—Summary of paleoslope and paleocurrent indicators

Indicator	No. of observations	Vector mean direction or sense \pm standard deviation	Type of deposit
Paleocurrent indicators			
Conglomerate long-axis orientation.	Two localities, 65 and 95 observations.	294° \pm 51° and 324° \pm 45°	Channel deposits, upper fan.
Conglomerate imbrication.	One locality, 60 observations.	Northerly	Do.
Flute casts	17	335° \pm 20°	Channel deposits Do.
Groove casts . . .	2	Northerly	
Asymmetrical ripple markings.	25	50° \pm 62°	Interchannel deposits and middle to lower fan-channel deposits.
Symmetrical ripple markings.	19	15° \pm 53°	
Small-scale inclined cross-strata.	453	8° \pm 61°	
Trough cross-strata.	2	Northerly	
Convolute laminations.	35	16° \pm 62°	
Convolute laminations of uncertain asymmetry.	3	38° \pm 60°	
Flame structures	4	343° \pm 81°	
Paleoslope indicators			
Asymmetrical contorted strata.	62	8° \pm 63°	Primarily inter-channel deposits and middle to lower fan-channel deposits.
Symmetrical contorted strata.	43	32° \pm 57°	

First, complex orientations of paleocurrent directions that are measured from channel deposits will result from the meandering and braided character, particularly in midfan areas, of the fan channels. Fan channels can meander considerably, may have irregular trends, and can even be oriented perpendicular to the regional slope of the fan (Shepard, 1966; Nelson and others, 1970; Haner, 1971; Normark, 1970b). Thus, the fan channels may have orientations that are widely divergent from the general slope of the fan, and paleocurrents measured from fan-channel deposits can yield diverse paleocurrent orientations. Second, overflow deposits in the interchannel areas will have paleocurrents directed not only away from adjacent channels but also downslope from them. This additional component of flow results from the adjustment of the overflow current to the local interchannel slope orientation. Finally, contour or bottom currents are common on modern fans (Stanley and Kelling, 1969; Zimmerman, 1971). These currents commonly flow perpendicular to the general slope of the fan and rework unconsolidated surficial fan deposits. Thus, the preserved sedimentary structures and their orientations on some fan

deposits may reflect these currents rather than the original depositing currents, thus yielding anomalous paleocurrent patterns.

Fan valley systems of many modern fans, particularly along the Pacific margin of North America, appear to shift toward the left through time (Menard, 1955); as the fans grow, the major deposition tends to shift periodically to the left, presumably under the influence of the Coriolis effect. The Coriolis effect deflects currents to the right in the Northern Hemisphere, so that levees on the right side of channels are generally higher than levees on the left side, because more sediment is deposited on the right. This buildup of levees on the right side may make it easier for channels to migrate leftward, thus shifting the locus of sedimentation in that direction. Consequently, the youngest or active channels are commonly located along the left side of the fan (looking downfan from the apex). As a result of this growth pattern, paleocurrent patterns from ancient fan deposits may be strongly oriented toward the left.

SEDIMENT-DISPERSAL MODEL FOR THE BUTANO SANDSTONE

The paleoslope and paleocurrent patterns of the Butano Sandstone indicate a complex system of sediment dispersal on the fan, comparable to that just outlined for modern deep-sea fans. Studies of maximum clast size, grain-size distributions, petrography, lithofacies, micropaleontology, and sedimentology of the formation indicate that deposition occurred in deep water within a tectonic basin formed on continental crust of the Salinian block (Cummings and others, 1962; Nilsen, 1971), which is an elongate fault-bounded tectonic block in the California Coast Ranges underlain by a granitic basement complex (Compton, 1966). Regional paleogeographic studies indicate that the Salinian block formed a continental borderland off the Pacific margin of California during Eocene time, perhaps similar to the present borderland off the coast of southern California (Clarke and Nilsen, 1972). Tectonic activity in this ancient borderland region created isolated uplands and intervening submarine basins in which submarine fans were deposited.

Sediments of the Butano fan were probably derived from a southern provenance area located adjacent to Monterey Bay. However, because some modern fan-channel systems diverge as much as 90° from the orientation of their adjoining submarine canyons, the location and orientation of the submarine canyon or canyons feeding the Butano fan system cannot be determined from the paleocurrent data alone. Petrographic studies of sandstone and conglomerate of the Butano Sandstone, however, indicate that granitic basement rocks and overlying sedimentary rocks of the Salinian block to the south were the major source.

Synthesis of the paleocurrent patterns from figures 7–11 permits formation of a model for sediment dispersal of the Butano Sandstone (fig. 12). Two major channels of the upper

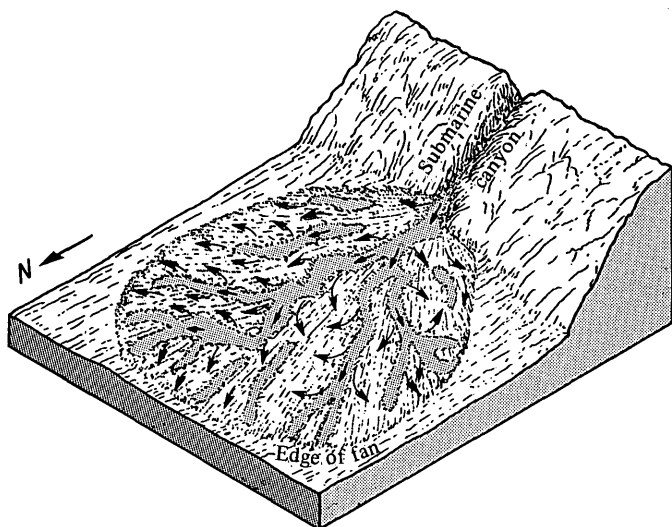


Figure 12.—Sediment-dispersal model for the Butano Sandstone, a deep-sea fan deposit. Arrows represent direction of sediment transport; shaded areas represent major channels.

fan are delineated by the distribution of maximum conglomerate clast sizes (fig. 5). These two channels may have been active at the same time, but limited fossil data indicate that deposits in the eastern channel may be older (Clark, 1966); in fact, the older channel may have been permanently replaced by the younger during growth of the fan. The sediment-dispersal model shows a clearly defined northward transport of sediments down the channels accompanied by transport outward and away from the major channels. The lower fan and fan-fringe areas contain radially oriented small distributary channels. In the lowest parts of the fan and in the fan-fringe areas, fine-grained sediments are deposited, a mixture of pelagic sediments and terrigenous detritus slowly settling out of suspension. Bottom currents may be particularly effective in redistributing these fine-grained sediments.

This type of sediment-dispersal pattern has been suggested by others for modern deep-sea fans and can now be demonstrated for an ancient deep-sea fan as well. Paleocurrent studies of ancient deep-sea fan deposits must be based on measurements of all available sedimentary structures because (1) many different subenvironments are present, (2) many different processes of deposition are active, and (3) rapid changes and growth of the fan yield complex lithofacies relations. Analysis of selected structures only does not yield sufficient data for determination of sediment-dispersal patterns.

REFERENCES CITED

Beaulieu, J. O., 1970, Cenozoic stratigraphy of the Santa Cruz Mountains, California, and inferred displacement along the San Andreas fault: Stanford, Calif., Stanford Univ. Ph. D. thesis, 202 p.
 Bouma, A. H., 1962, Sedimentology of some flysch deposits, a graphic approach to facies interpretation: Amsterdam, Elsevier, 168 p.

- Brabb, E. E., 1960a, Geology of the Big Basin area, Santa Cruz Mountains, California: Stanford, Calif., Stanford Univ. Ph. D. thesis, 191 p.
 — 1960b, Geology of the Big Basin area, Santa Cruz Mountains, California: Dissert. Abs., v. 21, no. 5, p. 1163.
 — 1964, Subdivision of San Lorenzo Formation (Eocene-Oligocene), west-central California: Am. Assoc. Petroleum Geologists Bull., v. 48, no. 5, p. 670–679.
 — compiler, 1970, Preliminary geologic map of the central Santa Cruz Mountains, California: U.S. Geol. Survey open-file map, scale 1:62,500.
 Brabb, E. E., and Pampeyan, E. H., compilers, 1972, Preliminary geologic map of San Mateo County, California: U.S. Geol. Survey Misc. Field Studies Map MF-328, scale 1:62,500.
 Branner, J. C., Newsom, J. F., and Arnold, Ralph, 1909, Description of the Santa Cruz quadrangle, California: U.S. Geol. Survey Geol. Atlas, Folio 163, 12 p.
 Bull, W. B., 1972, Recognition of alluvial-fan deposits in the stratigraphic record, in Rigby, J. K., and Hamblin, W. K., eds., Recognition of ancient sedimentary environments: Soc. Econ. Paleontologists and Mineralogists Spec. Pub. 16, p. 63–83.
 Clark, J. C., 1966, Tertiary stratigraphy of the Felton-Santa Cruz area, Santa Cruz Mountains, California: Stanford, Calif., Stanford Univ. Ph. D. thesis, 179 p.
 Clarke, Samuel, and Nilsen, T. H., 1972, Postulated offsets of Eocene strata along the San Andreas fault zone, central California: Geol. Soc. America Abs. with Programs, v. 4, no. 3, p. 137–138.
 Compton, R. R., 1966, Granitic and metamorphic rocks of the Salinian block, California Coast Ranges, in Bailey, E. H., ed., Geology of northern California: California Div. Mines and Geology Bull. 190, p. 277–288.
 Cummings, J. C., 1960, Geology of the Langley Hill-Waterman Gap area, Santa Cruz Mountains, California: Stanford, Calif., Stanford Univ. Ph. D. thesis, 233 p.
 Cummings, J. C., Touring, R. M., and Brabb, E. E., 1962, Geology of the northern Santa Cruz Mountains, California, in Bowen, O. E., ed., Geologic guide to the gas and oil fields of northern California: California Div. Mines and Geology Bull. 181, p. 179–220.
 Curray, J. R., 1956, The analysis of two-dimensional orientation data: Jour. Geology, v. 64, p. 117–131.
 Dibblee, T. W., Jr., 1966a, Evidence for cumulative offset on the San Andreas fault in central and northern California, in Bailey, E. H., ed., Geology of northern California: California Div. Mines and Geology Bull. 190, p. 375–384.
 — 1966b, Geologic map of the Palo Alto 15-minute quadrangle, California: California Div. Mines and Geology Map Sheet 8, scale 1:62,500.
 Dott, R. H., Jr., 1963, Dynamics of subaqueous gravity depositional structures: Am. Assoc. Petroleum Geologists Bull. 47, p. 104–128.
 Dzulynski, S., Ksiazkiewicz, M., and Kuenen, Ph. H., 1959, Turbidites in flysch of the Polish Carpathian Mountains: Geol. Soc. America Bull., v. 70, p. 1089–1118.
 Fairchild, W. W., Wesendunk, P. R., and Weaver, D. W., 1969, Eocene and Oligocene Foraminifera from the Santa Cruz Mountains, California: California Univ. Pubs. Geol. Sci., v. 81, 93 p.
 Haner, B. E., 1971, Morphology and sediments of Redondo Submarine Fan, southern California: Geol. Soc. America Bull., v. 82, p. 2413–2432.
 Laird, M. G., 1968, Rotational slumps and slump scars in Silurian rocks, western Ireland: Sedimentology, v. 10, p. 111–120.
 Mallory, V. S., 1959, Lower Tertiary biostratigraphy of the California Coast Ranges: Tulsa, Okla., Am. Assoc. Petroleum Geologists, 416 p.
 Menard, H. W., 1955, Deep-sea channels, topography, and sedimentation: Am. Assoc. Petroleum Geologists Bull., v. 39, p. 236–255.

- Middleton, G. M., 1969, Grain flows and other mass movements down slopes, in Stanley, D. J., ed., *The new concepts of continental margin sedimentation*: Am. Geol. Inst., Washington, D.C., p. GM-B-1 to GM-B-14.
- Nelson, C. H., Carlson, P. R., Byrne, J. V., and Alpha, T. R., 1970, Physiography of the Astoria Canyon Fan System: *Marine Geology*, v. 8, p. 259–291.
- Nilsen, T. H., 1970, Paleocurrent analysis of the flysch-like Butano Sandstone (Eocene), Santa Cruz Mountains, California: *Geol. Soc. America Abs. with Programs*, v. 2, no. 7, p. 636.
- 1971, Sedimentology of the Eocene Butano Sandstone, a continental borderland submarine fan deposit, Santa Cruz Mountains, California: *Geol. Soc. America Abs. with Programs*, v. 3, no. 7, p. 660.
- Normark, W. R., 1970a, Growth patterns of deep-sea fans: *Am. Assoc. Petroleum Geologists Bull.*, v. 54, p. 2170–2195.
- 1970b, Channel piracy on Monterey deep-sea fan: *Deep-Sea Research*, v. 17, p. 837–846.
- Normark, W. R., and Piper, D. J. W., 1969, Deep-sea fan valleys, past and present: *Geol. Soc. America Bull.*, v. 70, p. 1859–1866.
- 1972, Sediments and growth pattern of Navy deep-sea fan, San Clemente Basin, California borderland: *Jour. Geology*, v. 80, p. 198–223.
- Parks, J. M., 1970, Computerized trigonometric method for rotation of structurally tilted sedimentary directional features: *Geol. Soc. America Bull.*, v. 81, p. 537–540.
- Piper, D. J. W., 1970, Transportation and deposition of Holocene sediment on La Jolla deep sea fan, California: *Marine Geology*, v. 8, p. 211–228.
- Sanders, J. E., 1960, Origin of convolute laminae: *Geol. Mag.*, v. 97, p. 409–421.
- 1965, Primary sedimentary structures formed by turbidity currents and related resedimentation mechanisms, in Middleton, G. M., ed., *Primary sedimentary structures and their hydrodynamic interpretation*: Soc. Econ. Paleontologists and Mineralogists Spec. Pub. 12, p. 192–219.
- Shepard, F. P., 1966, Meander in valley crossing a deep-ocean fan: *Science*, v. 154, p. 385–386.
- Stanley, D. J., and Kelling, G., 1969, Photographic investigation of sediment texture, bottom current activity, and benthonic organisms in the Wilmington submarine canyon: U.S. Coast Guard Oceanog. Rept. 22, 95 p.
- Stanley, D. J., and Unrug, Rafael, 1972, Submarine channel deposits, fluxoturbidites and other indicators of slope and base-of-slope environments in modern and ancient marine basins, in Rigby, J. F., and Hamblin, W. K., eds., *Recognition of ancient sedimentary environments*: Soc. Econ. Paleontologists and Mineralogists Spec. Pub. 16, p. 287–340.
- Stauffer, P. H., 1967, Grain-flow deposits and their implications, Santa Ynez Mountains, California: *Jour. Sed. Petrology*, v. 37, p. 487–508.
- Sullivan, F. R., 1962, Foraminifera from the type section of the San Lorenzo Formation, Santa Cruz County, California: *California Univ. Pubs. Geol. Sci.*, v. 37, no. 4, p. 233–352.
- Touring, R. M., 1959, Structure and stratigraphy of the La Honda and San Gregorio quadrangles, San Mateo County, California: Stanford, Calif., Stanford Univ. Ph. D. thesis, 288 p.
- Zimmerman, H. B., 1971, Bottom currents on the New England continental rise: *Jour. Geophys. Res.*, v. 76, no. 24, p. 5865–5876.



LOWER JURASSIC AMMONITE FROM THE SOUTH-CENTRAL SIERRA NEVADA, CALIFORNIA

By DAVID L. JONES and JAMES G. MOORE, Menlo Park, Calif.

Abstract.—A Lower Jurassic ammonite has been found in metasilstone of the Boyden Cave roof pendant, south-central Sierra Nevada, Calif. Although too poorly preserved to permit positive generic and specific identification, its general shape, coiling, and ornamentation are characteristic of Early Jurassic forms. Strata associated with the fossiliferous rocks in the pendant include quartzite, andalusite hornfels, and marble. This assemblage differs strikingly from nearby volcanic rocks to the east, some of which in the Ritter Range pendant also contain Lower Jurassic fossils. The presence of nonvolcanic Lower Jurassic rocks of the Boyden Cave pendant lying west of coeval volcanic rocks of the Ritter Range pendant is anomalous and may be the result of large-scale tectonic dislocations.

Fossils indicative of age are rare in the pregranitic metamorphic remnants of the Sierra Nevada. A Lower Jurassic ammonite discovered in the south-central part of the Sierra Nevada in the summer of 1971 is therefore of regional significance. The fossil was found in a metasilstone unit within the Boyden Cave roof pendant near the confluence of the Middle and South Forks of the Kings River (fig. 1) in the Tehipite Dome 15-minute quadrangle. Fossils of apparent Jurassic or Triassic age were found earlier in the same stratigraphic unit (Moore and Dodge, 1962), but none are as definitive as this new find.

CHARACTER AND PROBABLE AGE OF THE AMMONITE

The ammonite from the Boyden Cave roof pendant was found on a steep hillside east of Boulder Creek about 200 feet above creek level (USGS Mesozoic loc. 30196) very close to the *Pentacrinus* locality described in an earlier paper (Moore and Dodge, 1962, loc. 2). The internal mold and the external impression were found as loose blocks lying about 20 feet apart. The matrix is black siliceous metasilstone. The proximity of the two halves indicates that they had not been transported far from their original bedrock source.

The ammonite (fig. 2) is badly deformed and eroded, and many diagnostic features, including the sutures, have been obliterated. From an individual having an original diameter of about 4 inches, it has been stretched to more than 6 inches in

maximum dimension. Five whorls are clearly visible; two or three early whorls are smashed. Coiling is highly evolute. Ornamentation consists of regular, narrow, widely spaced, radial ribs that are most prominent near the umbilical shoulder and fade out high on the flanks. Most of the venter is smashed, but a suggestion of a ventral keel is discernible in the external impression.

According to R. W. Imlay (written commun., 1972), this ammonite, in ribbing and coiling, more closely resembles such Lower Jurassic (Sinemurian and Pliensbachian) genera as *Paracoriceras* or *Metophioceras* than ammonites of either Triassic or later Jurassic age, although its poor state of preservation precludes a positive identification of even its family affinities. According to N. J. Silberling (oral commun., 1971), this ammonite is not similar to Triassic forms and is almost certainly of Early Jurassic age.

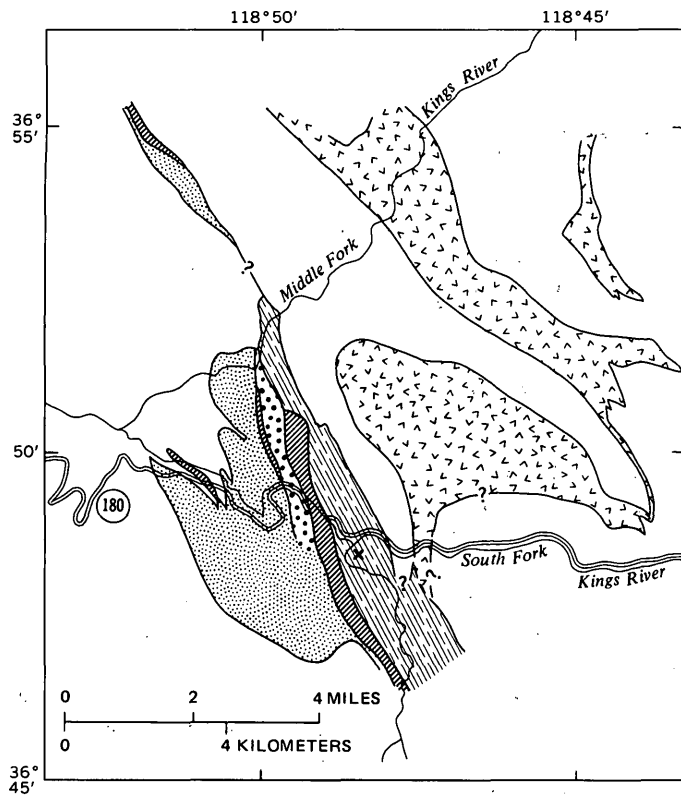
BOYDEN CAVE PENDANT

The Boyden Cave pendant (fig. 1), about 7 miles long and 3 miles wide, is composed of metamorphosed sedimentary rocks surrounded by younger granitic rocks of the Sierra Nevada batholith.

Bedding within the metasedimentary rocks is steep and locally intensely folded. The finer grained rocks have developed a cleavage, particularly in the eastern part of the pendant. Four general rock units have been recognized, from west to east: quartzitic sandstone, andalusite hornfels, marble, and metasilstone. Directions of tops in the quartzitic sandstone are predominantly toward the west, suggesting that the sandstone is the youngest unit and that the other units are progressively older eastward, but the pendant has not been mapped in detail, and folding and faulting may have disturbed this apparent stratigraphic relation. Only the metasilstone unit has yielded fossils, and its partial age been established.

Quartzitic sandstone unit

The westernmost and presumed youngest unit in the pendant forms a band about 9,000 feet wide composed of



EXPLANATION

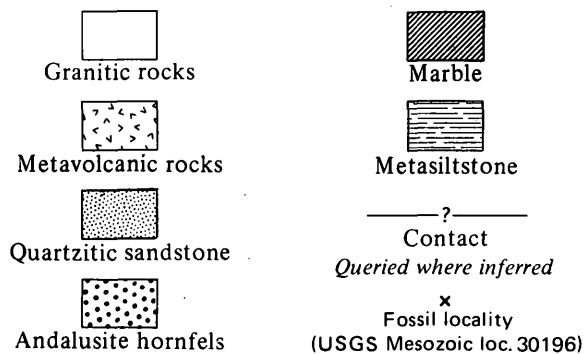


Figure 1.—Map of Boyden Cave pendant, showing lithologic units and Lower Jurassic ammonite locality.

white to gray, thick-bedded metamorphosed sandstone which is commonly crossbedded. The crossbeds average half an inch in thickness; the main beds are half a foot to several feet thick.

The rock is composed predominantly of quartz; K-feldspar is locally rather common and may make up 10–15 percent of the rock. A small amount of muscovite is present in nearly all specimens; biotite, chlorite, and epidote are rare constituents. Grains smaller than a few millimeters have recrystallized and exhibit a metamorphic texture of ragged, interlocking grains. Larger grains still preserve rounded shapes. In some places, beds are coarser grained, containing pebbles as large as 1 cm in size. Most of the pebbles are quartz; some are K-feldspar; a few are aggregates of quartz, K-feldspar, and muscovite.

Andalusite hornfels

Andalusite hornfels, formed by metamorphism of a clay-rich shaly rock, crops out in a band about 1,000 feet wide between the quartzitic sandstone and the largest marble layer. The rock weathers to a brownish color but has a faint bluish cast on fresh surfaces. It is generally mica rich and commonly schistose. In addition to quartz and spongy andalusite crystals as much as several millimeters in size, biotite and muscovite are common and magnetite is locally abundant.

Marble

The most resistant unit in the Boyden Cave pendant is a layer of massive marble about 1,000 feet thick that forms a prominent rib on both walls of the South Fork canyon. This unit is composed of calcite and dolomite containing grains as much as several millimeters in diameter. Bedding in the massive marble is weakly defined by darker layers a quarter of an inch to a foot thick. The strike of these layers wraps around the blunt northern termination of the main marble mass on the crest of the Monarch Divide. The significance of this structure is difficult to evaluate, but it does indicate that major folding and perhaps thrust faulting may have grossly modified the structure of the metasedimentary sequence.

Metasiltstone

Thin-bedded metamorphic rocks of diverse composition occur in a belt 2,000–4,000 feet wide on the east side of the Boyden Cave pendant. The ammonite described here was found near the center of this unit (fig. 1) in a siliceous metasiltstone that has been only slightly recrystallized. Associated with the ammonite are crinoid columnals and pelecypods that have been reported previously (Moore and Dodge, 1962). Thin-bedded calc-hornfels and fine-grained black carbonaceous hornfels are interbedded with the siliceous metasiltstone.

Sedimentary breccia is common in western exposures near the contact with the marble unit. In the breccia, fragments of beds of siltstone and fine-grained sandstone are included in a dark to black shaly to silty matrix; they range in size from less than 1 mm to fragments several tens of centimeters long. The breccia probably was formed by submarine slumps or turbidity flows.

In its eastern exposures, the unit consists of thin-bedded shale and siltstone interbedded with limy layers several millimeters to 20–40 cm thick.

COMPARISON WITH THE RITTER RANGE PENDANT

Lower Jurassic rocks occur about 65 miles to the north in the Ritter Range roof pendant (fig. 3), where they have been studied by Rinehart, Ross, and Huber (1959). These rocks are

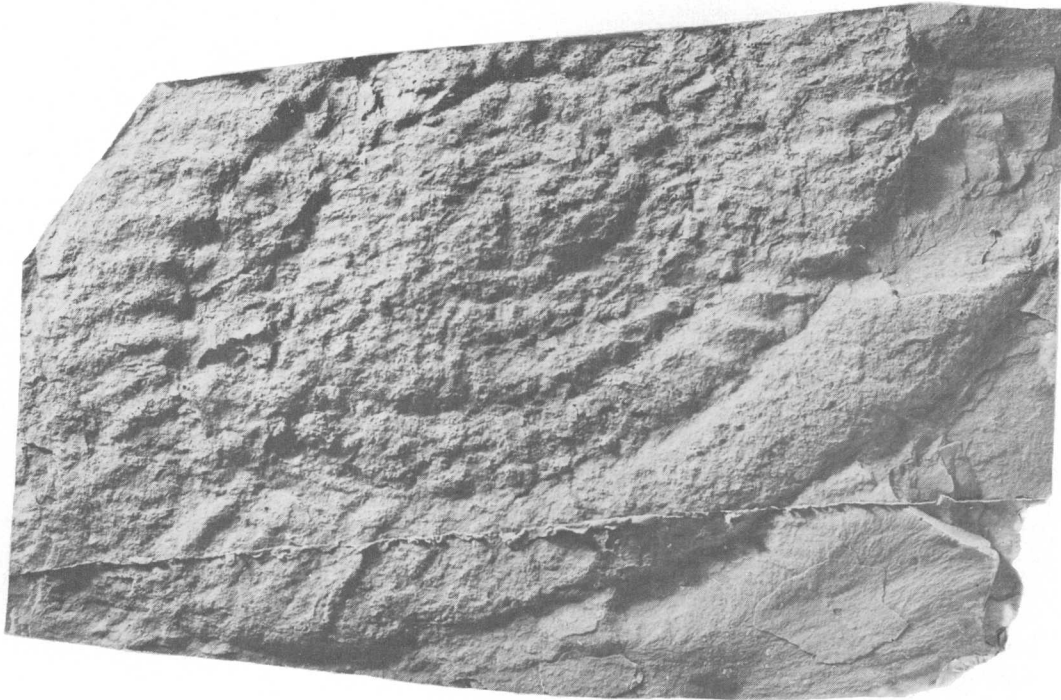
*A**B*

Figure 2.—Lower Jurassic ammonite from Boyden Cave pendant. Natural size. USGS Mesozoic loc. 30196. USNM 185744. *A*, Rubber cast of exterior mold. *B*, Internal mold.

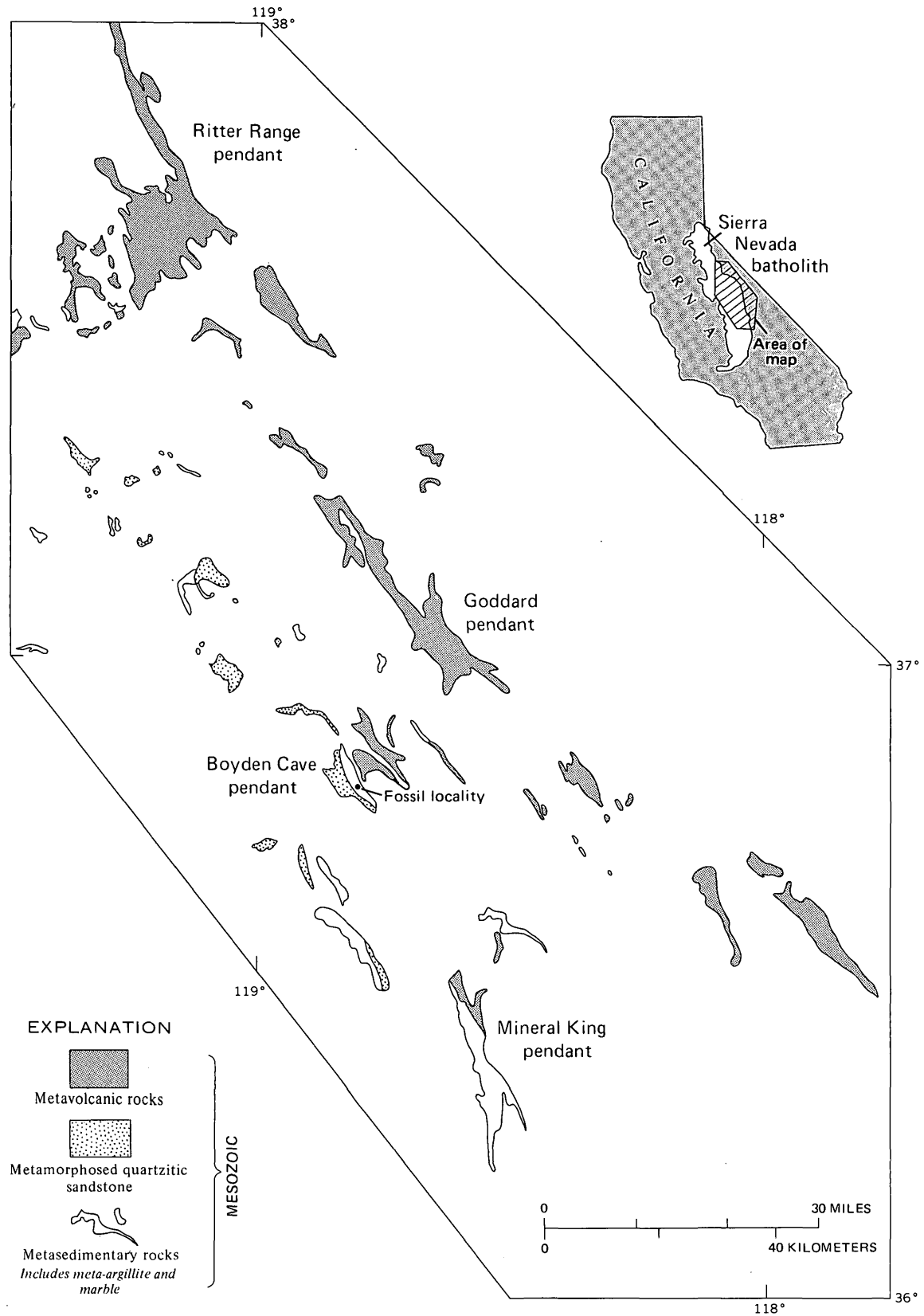


Figure 3.—Map showing location of fossil locality and general lithology of roof pendants of a part of the central Sierra Nevada batholith. Paleozoic metasedimentary roof pendants east of the Mesozoic metavolcanic rocks are not shown.

part of a volcanic sequence more than 30,000 feet thick that overlies upper Paleozoic pelitic hornfels and marble (fig. 4). They are composed chiefly of felsic metavolcanic tuffs and flows with minor interbedded calcareous and tuffaceous metasedimentary rocks. The Early Jurassic age is based mainly on fairly abundant specimens of the pelecypod *Weyla* that occur in a narrow belt of calcareous metasedimentary rock about 10,000 feet above the base of the volcanic sequence (Rinehart and others, 1959, p. 944). These fossils are poorly preserved and generally so crushed that positive specific determinations are impossible. As the genus *Weyla* is restricted mainly to strata of Sinemurian and Pliensbachian age (S. W. Muller, written commun., 1961), these specimens are grossly comparable in age to the Boyden Cave ammonite. A more definitive correlation between the two places is not possible with the poor specimens we have, but considering the great thickness of strata exposed at both places, it is reasonable to suppose at least partial age equivalency.

The columnar sections (fig. 4) show that the overall lithologic sequences of the Ritter Range pendant and the Boyden Cave pendant are totally different. Of particular significance is the absence of volcanic rocks and the presence of abundant quartz-rich sedimentary rocks in the Boyden Cave sequence.

REGIONAL SETTING

Metasedimentary rocks similar to those within the Boyden Cave pendant occur as remnants within a zone more than 70 miles long. This belt extends from the San Joaquin River

drainage (Huber, 1968) on the northwest, through the Dinkey Creek area (Kistler and Bateman, 1966) and North Fork of the Kings River (Krauskopf, 1953) to the Boyden Cave pendant in the Kings River drainage, and south to the Kaweah River area (Ross, 1958). These metasedimentary remnants are characterized by relatively clean, crossbedded quartzitic sandstone interbedded with limestone and argillite and form a remarkably coherent lithologic zone (fig. 3).

The zone of pendants that includes the Boyden Cave pendant lies parallel to, and about 15 miles west of, an even more extensive zone of roof pendants composed mainly of silicic metavolcanic rocks (Bateman and others, 1963). This zone extends 130 miles from the Ritter Range pendant to a belt of similar volcanic rocks in the Inyo Mountains which overlie fossiliferous marine limestone and shale of Early and Middle Triassic age.

It has long been recognized that Lower Jurassic deposits of the Western United States comprise two distinctly different assemblages: an eastern belt characterized by quartz-rich sedimentary rocks that were deposited in shallow marine and nonmarine environments; and a western belt characterized by (1) abundant andesitic volcanic and volcanoclastic sedimentary rocks with subordinate limestone, (2) interbedded limestone and mudstone, and (3) orogenic conglomerate (Stanley and others, 1971, p. 15). The part of the western belt that is rich in volcanic material is mainly in eastern California, westernmost Nevada, northern California, and central Oregon. Stanley and his coworkers (1971, p. 12) include the volcanic rocks of the Ritter Range pendant in this volcanic belt, which they (1971, p. 17) believe represents a volcanic island arc. They postulate that a deep oceanic trench in which subduction of an oceanic plate was occurring lay on the west side of this arc.

The lack of volcanic flows and pyroclastic rocks and the quartz-rich nature of the sedimentary rocks in the Boyden Cave pendant suggest that they might have an affinity with Lower Jurassic rocks of the eastern belt, assuming that the undated lithologic units of the Boyden Cave sequence are also of Early Jurassic age. Their present position west of the westernmost known Lower Jurassic volcanic rocks is anomalous, as is the absence or sparsity of volcanic detritus despite proximity to volcanic terranes. These anomalies suggest that large-scale tectonic dislocations may have occurred and that once-distant deposits are now juxtaposed. Right-lateral faulting along northwest-trending wrench faults might be responsible for this juxtaposition, although any direct evidence for large-scale slip has been destroyed by batholithic intrusion. Alternatively, if the quartz-rich belt were originally deposited west of the volcanic belt, perhaps in an arc-trench gap, complex paleogeographic problems are introduced, as there is no obvious source terrane for these rocks in the narrow tract that intervenes between the volcanic belt and the quartzite belt. Juxtaposition by major thrusting is a possibility that should be considered along with the hypothesis for strike-slip faulting.

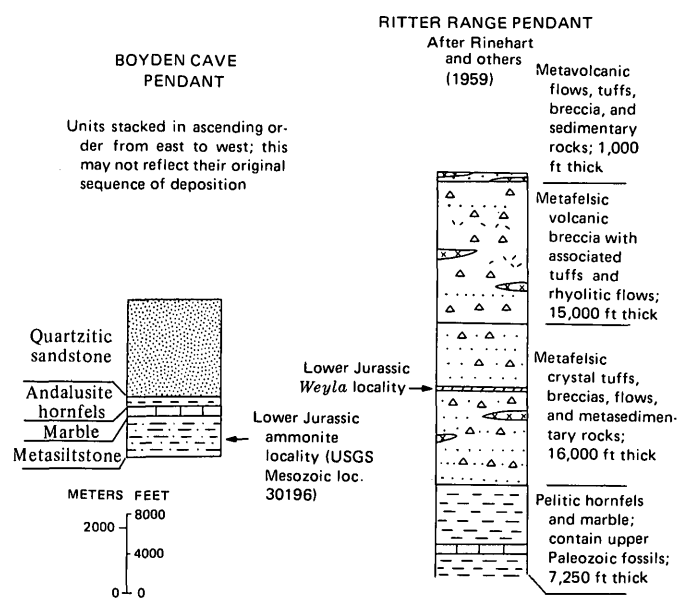


Figure 4.—Schematic columnar sections of Boyden Cave pendant and Ritter Range pendant.

In summary, the presence of nonvolcanic, quartz-rich apparent Lower Jurassic sedimentary rocks close to, but west of, presumed coeval volcanic terranes suggests that the prebatholithic depositional and tectonic history of the south-central Sierra Nevada is more complex than hitherto suspected. Large-scale tectonic dislocations may be invoked to explain this anomalous relation, but data are insufficient to permit a clear understanding of this complex area.

REFERENCES CITED

- Bateman, P. C., Clark, L. D., Huber, N. K., Moore, J. G., and Rinehart, C. D., 1963, The Sierra Nevada batholith—a synthesis of recent work across the central part: U.S. Geol. Survey Prof. Paper 414-D, 46 p.
- Huber, N. K., 1968, Geologic map of the Shuteye Peak quadrangle, Sierra Nevada, California: U.S. Geol. Survey Geol. Quad. Map GQ-728.
- Kistler, R. W., and Bateman, P. C., 1966, Stratigraphy and structure of the Dinkey Creek roof pendant in the central Sierra Nevada, California: U.S. Geol. Survey Prof. Paper 524-B, 14 p.
- Krauskopf, K. B., 1953, Tungsten deposits of Madera, Fresno, and Tulare Counties, California: California Div. Mines Spec. Rept. 35, 83 p.
- Moore, J. G., and Dodge, F. C., 1962, Mesozoic age of metamorphic rocks in the Kings River area, southern Sierra Nevada, California: Art. 7 in U.S. Geol. Survey Prof. Paper 450-B, p. B19–B21.
- Rinehart, C. D., Ross, D. C., and Huber, N. K., 1959, Paleozoic and Mesozoic fossils in a thick stratigraphic section in the eastern Sierra Nevada, California: Geol. Soc. America Bull., v. 70, p. 941–946.
- Ross, D. C., 1958, Igneous and metamorphic rocks of parts of Sequoia and Kings Canyon National Parks, California: California Div. Mines Spec. Rept. 53, 24 p.
- Stanley, K. O., Jordan, W. M., and Dott, R. H., Jr., 1971, New hypothesis of early Jurassic paleogeography and sediment dispersal for western United States: Am. Assoc. Petroleum Geologists Bull., v. 55, no. 1, p. 10–19.



THE LATE CRETACEOUS AMMONITE BACULITES UNDATUS STEPHENSON IN COLORADO AND NEW MEXICO

By W. A. COBBAN, Denver, Colo.

Abstract.—*Baculites undatus* Stephenson, originally described from the Nacatoch Sand of northeastern Texas, has been found in the Pierre Shale at 25 localities in Colorado and two in New Mexico. An early form of the species occurs in the zone of *Didymoceras cheyennense* (Meek and Hayden), and the typical form occurs in the overlying zones of *Baculites compressus* Say, *B. cuneatus* Cobban, and *B. reesidei* Elias. The species is characterized by its stout cross section, broad venter, conspicuous lateral and ventral ribs, and suture of about average complexity for the genus.

Baculites undatus Stephenson (1941, p. 405, pl. 79, figs. 5-10) is characterized by its very stout cross section, unusually broad venter, rather widely spaced conspicuous lateral ribs, and long ventral ribs. The species was originally described from the Nacatoch Sand of Navarro County in northeastern Texas. Stephenson recorded it from this formation at 10 localities in Navarro and Kaufman Counties as well as from the slightly older Neylandville Marl at one locality. The species has been recorded from Tennessee, Mississippi, Delaware, and New Jersey (Owens and others, 1970, p. 32). In recent years, specimens that seem referable to *B. undatus* have been discovered in the Pierre Shale in Colorado and New Mexico (fig. 1).

GEOGRAPHIC DISTRIBUTION IN COLORADO AND NEW MEXICO

Ammonites referable to *Baculites undatus* have been collected from the Pierre Shale at 25 localities in Colorado and two localities in New Mexico. These localities are shown on figure 1, and the descriptions of the localities are given in table 1.

Baculites undatus Stephenson

Figures 2-5

1941. *Baculites undatus* Stephenson, Texas Univ. Bull. 4101, p. 405, pl. 79, figs. 5-10.

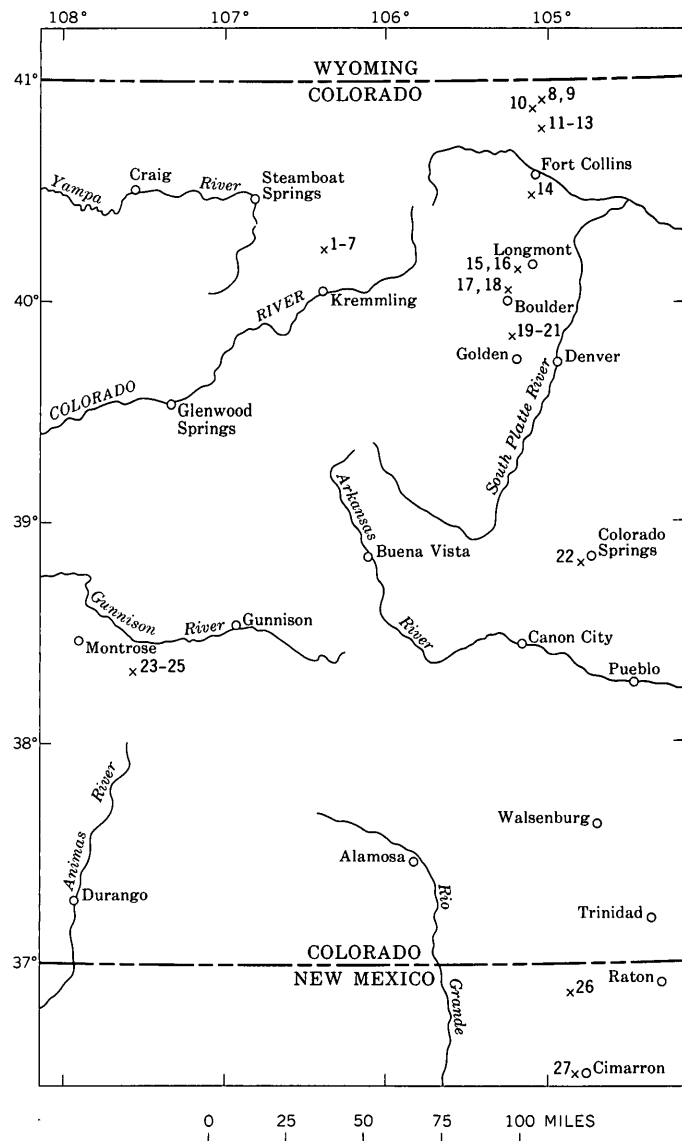


Figure 1.—Localities of *Baculites undatus* Stephenson in Colorado and New Mexico. Numbers refer to the detailed descriptions of localities in table 1.

Table 1.—Localities at which fossils were collected

Locality No. (fig. 1)	U.S. Geol. Survey Mesozoic locality No.	Collector, year of collection, description of locality, and stratigraphic assignment
1.....	D5991.....	G. A. Izett and W. A. Cobban, 1967. Center of the N½ sec. 12, T. 3 N., R. 81 W., Grand County, Colo. Pierre Shale, from limestone concretions about 380 ft above the Carter Sandstone Member.
2.....	D8060.....	G. A. Izett and W. A. Cobban, 1971. NW¼NW¼SE¼ sec. 12, T. 3 N., R. 81 W., Grand County, Colo. Pierre Shale, from limestone concretions about 380 ft above the Carter Sandstone Member.
3.....	D5972.....	G. A. Izett, 1967. E½SW¼SE¼ sec. 7; T. 3 N., R. 80 W., Grand County, Colo. Pierre Shale, from limestone concretions about 380 ft above the top of the Carter Sandstone Member.
4.....	D6566.....	G. A. Izett, 1968. SW¼NE¼NE¼ sec. 18, T. 3 N., R. 80 W., Grand County, Colo. Pierre Shale, from limestone concretions about 400 ft above the Carter Sandstone Member.
5.....	D1353.....	G. R. Scott and W. A. Cobban, 1957. NW¼SW¼ sec. 17, T. 3 N., R. 80 W., Grand County, Colo. Pierre Shale, from brown- and gray-weathering sandy limestone concretions about 420 ft above the top of the Carter Sandstone Member.
6.....	D1354.....	G. R. Scott and W. A. Cobban, 1957. W½NW¼NW¼ sec. 17, T. 3 N., R. 80 W., Grand County, Colo. Pierre Shale, from sandy limestone concretions in the interval 490–660 ft above the top of the Carter Sandstone Member.
7.....	D5864.....	G. A. Izett, 1967. SW¼SW¼NE¼ sec. 20, T. 3 N., R. 80 W., Grand County, Colo. Pierre Shale, about 400 ft above the top of the Carter Sandstone Member.
8.....	D370.....	G. R. Scott, 1955. Half a mile south of Round Butte, in the SE¼NW¼ sec. 19, T. 11 N., R. 68 W., Larimer County, Colo. Pierre Shale, Larimer Sandstone Member.
9.....	D372.....	G. R. Scott and W. A. Cobban, 1955. South of Round Butte, in the E½NW¼ sec. 19, T. 11 N., R. 68 W., Larimer County, Colo. Pierre Shale, Larimer Sandstone Member.
10.....	D2825.....	G. R. Scott, 1960. SW¼NE¼ sec. 2, T. 10 N., R. 69 W., Larimer County, Colo. Pierre Shale.
11.....	D2719.....	G. R. Scott, 1960. NW¼SE¼SW¼ sec. 12, T. 9 N., R. 69 W., Larimer County, Colo. Pierre Shale, Larimer Sandstone Member.
12.....	D1567.....	G. R. Scott and W. A. Cobban, 1971. South of Bubbles Lake, near center of the S½NW¼ sec. 7, T. 9 N., R. 68 W., Larimer County, Colo. Pierre Shale, Larimer Sandstone Member.
13.....	16213.....	R. G. Coffin, 1932. South of Bubbles Lake, in the NW¼ sec. 7, T. 9 N., R. 68 W., Larimer County, Colo. Pierre Shale, Larimer Sandstone Member.
14.....	D2849.....	G. R. Scott, 1960. NW¼NE¼NW¼ sec. 23, T. 6 N., R. 69 W., Larimer County, Colo. Pierre Shale, Rocky Ridge Sandstone Member.
15.....	D727.....	G. R. Scott, 1955. NW¼SE¼SE¼ sec. 9, T. 2 N., R. 70 W., Boulder County, Colo. Pierre Shale, from sandy limestone concretions in a sandstone unit.

Table 1.—Localities at which fossils were collected—Continued

Locality No. (fig. 1)	U.S. Geol. Survey Mesozoic locality No.	Collector, year of collection, description of locality, and stratigraphic assignment
16.....	D730.....	G. R. Scott, 1955. SE¼NW¼SE¼ sec. 9, T. 2 N., R. 70 W., Boulder County, Colo. Pierre Shale, from limestone concretions in a dark-gray shale unit.
17.....	D2740.....	G. R. Scott and W. A. Cobban, 1960. NW¼NW¼ sec. 3, T. 1 N., R. 70 W., Boulder County, Colo. Pierre Shale.
18.....	D293.....	G. R. Scott, 1955. Two miles north of Boulder, in the NE¼SE¼SW¼ sec. 8, T. 1 N., R. 70 W., Boulder County, Colo. Pierre Shale, from a sandy shale unit.
19.....	D700.....	G. R. Scott and W. A. Cobban, 1956. Six miles north of Golden, in the SE¼SE¼ sec. 20, T. 2 S., R. 70 W., Jefferson County, Colo. Pierre Shale, from iron-stained limestone concretions.
20.....	D704.....	G. R. Scott, R. Van Horn, and W. A. Cobban, 1956. Six miles north of Golden, in the SE¼NW¼SE¼ sec. 20, T. 2 S., R. 70 W., Jefferson County, Colo. Pierre Shale, from brown-weathering sandy concretions.
21.....	D705.....	G. R. Scott, 1956. About 6 miles north of Golden, in the SE¼NE¼ sec. 29, T. 2 S., R. 70 W., Jefferson County, Colo. Pierre Shale, from brown-weathering sandy concretions.
22.....	D1710.....	G. R. Scott, 1958. SE¼NE¼NW¼ sec. 14, T. 14 S., R. 67 W., El Paso County, Colo. Pierre Shale, from small ferruginous concretions in a bentonite-bearing gray shale unit.
23.....	D4311.....	R. G. Dickinson, 1963. Twenty-one miles southeast of Montrose in the SE¼SW¼ sec. 16, T. 47 N., R. 6 W., Montrose County, Colo. Mancos Shale, near top.
24.....	D4312.....	R. G. Dickinson, 1963. NE¼SW¼ sec. 10, T. 47 N., R. 6 W., Montrose County, Colo. Mancos Shale, near top.
25.....	D5435.....	R. G. Dickinson, 1966. SE¼NE¼ sec. 33, T. 47 N., R. 6 W., Gunnison County, Colo. Mancos Shale, about 100–200 ft below top.
26.....	D7484.....	Karen Pillmore, 1970. Casa Grande in Vermejo Park, Colfax County, N. Mex. Pierre Shale, 150–200 ft below top.
27.....	D4826.....	J. R. Gill, 1964. Two miles west of Cimarron in the NW¼NW¼NW¼ sec. 5, T. 26 N., R. 19 E., Colfax County, N. Mex. Pierre Shale, from limestone concretions 260–290 ft below top.

The holotype is a well-preserved undistorted specimen 38.5 mm in diameter at the larger end. Most of the shell material is retained; a piece missing at the larger end of the specimen reveals that the specimen is a phragmocone having a moderately simple suture. The cross section is elliptical and stout (fig. 2). At a diameter of 35.5 mm the ratio of the width to the diameter is 71 percent for the intercostal width and 85 percent for the costal width. The flanks are ornamented by strong broad arcuate nodelike ribs that have an average spacing of 1.4 for the shell diameter (diameter of shell ÷ distance between crest of ribs). Ribs of irregular height and spacing

DESCRIPTION OF COLLECTIONS

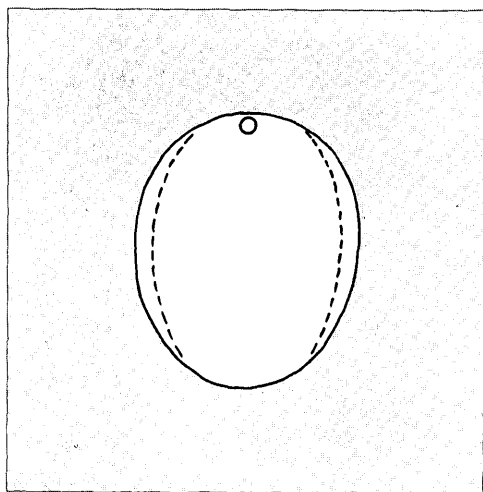


Figure 2.—Cross section, natural size, of the holotype of *Baculites undatus* Stephenson at a diameter of 36 mm. Drawn from a plaster cast. USNM 77245.

cross the very broad venter and extend well up onto the flanks. Two paratypes figured by Stephenson (1941, pl. 79, figs. 9, 10) are more strongly sculptured than the holotype. They are smaller than the holotype and have 1–2 lateral ribs per shell diameter. The paratypes and the holotype taper 5° . The holotype and one paratype (Stephenson, 1941, pl. 79, figs. 5–9) came from a locality just west of Chatfield, Tex. One of two topotypes from this locality is illustrated on figure 3, *p–r*. The other paratype came from the Nacatoch Sand near a small cemetery 1.1 miles northwest of Chatfield. A suite of 23 specimens from this locality collected by Mr. James P. Conlin, Fort Worth, Tex., presents an interesting sample of a population of *B. undatus*. These specimens range in diameter from 4 to 42 mm. Lateral ribs, which are present on all specimens (13) larger than 14 mm in diameter, may appear on some individuals as small as 7 mm. These ribs resemble those on the types and are spaced from 1 to 3 for the shell diameter with most spaced at 1.5. The specimens have angles of taper from 1° to 7° , and all have very broad venters and moderately stout to very stout subelliptical sections. A few of the specimens are illustrated on figure 3, *a–j*, and sutures of two are shown on figure 4, *c, d*.

According to a locality map of Stephenson (1941, loc. 762 on fig. 6), the holotype of *B. undatus* came from the upper part of the Nacatoch Sand. The specimen was associated with the type specimens of Stephenson's *Scaphites rugosus*, *S. pumilus*, and *Solenoceras multicostatum* as well as with specimens identified by Stephenson as *Solenoceras texanum* (Shumard), *Nostoceras stantoni* Hyatt, *N. helicinum* (Shumard), *Turrilites splendidus* Shumard, *Helicoceras navarroense* Shumard, and *Parapachydiscus arkansanus* Stephenson.

Specimens referable to *Baculites undatus* have been found in the following zones, from oldest to youngest: *Didymoceras cheyennense* (Meek and Hayden), *Baculites compressus* Say, *B. cuneatus* Cobban, and *B. reesidei* Elias.

Zone of *Didymoceras cheyennense* (Meek and Hayden).—Eight specimens from six localities (fig. 1, locs. 17, 20, 21, 23–25) are interpreted as representing an early form of *B. undatus*. All have conspicuous lateral and ventral ribs, but none has a venter as broad as that of the typical form of the species. A septate specimen is shown on figure 5, *a, b*.

Zone of *Baculites compressus* Say.—Specimens that have the very broad venter and distinctive sculpture of *B. undatus* have been collected in association with *B. compressus* at three localities in Colorado (fig. 1, locs. 2, 4, 7). In addition, two specimens from two localities in New Mexico (fig. 1, locs. 26, 27) that seem certain to be *B. undatus* were not associated with other baculites, but they are probably from the zone of *B. compressus*. Distorted specimens and fragments of baculites that may be *B. undatus* were found with *B. compressus* at two other localities in Colorado (fig. 1, locs. 1, 3).

Two of the best specimens from the Kremmling, Colo., area are uncrushed internal molds that have maximum diameters of 19.5 and 25 mm (fig. 5, *h–m*). The smaller one has a taper of 4° and a stout elliptical cross section. Its nodate lateral ribs number 1–2 for the shell diameter. Ventral ribs are mostly weak and irregular in height. The specimen is a phragmocone, and its suture is shown on figure 4, *A*. The larger specimen is characterized by strong ventral ribs that extend half way up the flanks. The two specimens from New Mexico assigned to the zone of *B. compressus* are the largest individuals from this zone. One is a distorted septate fragment about 53 mm in diameter, and the other (fig. 5, *n, o*) is the older part of a body chamber that has a diameter of 38.7 mm at its base.

Axonoceras compressum Stephenson (1941, p. 422, pl. 89, figs. 1–5) was associated with one of the baculites from the Kremmling area (fig. 1, loc. 1) assigned to *B. undatus*. The holotype and paratypes of *A. compressum* came from the Neylandville Marl of Navarro County, Tex.

Zone of *Baculites cuneatus* Cobban.—Baculites assigned to *B. undatus* have been found in this zone at only one locality near Kremmling (fig. 1, loc. 5) in a bed of large limy sandstone concretions in the Pierre Shale about 420 feet above the top of the Carter Sandstone Member (Izett and others, 1971, p. A15). Six specimens were collected along with 150 specimens of *B. cuneatus*. The specimens of *B. undatus* are internal molds 21–37 mm in diameter. Two examples are shown on figure 5, *r–t*. A larger internal mold, about 50 mm in diameter, from this locality was collected recently by Mr. Karl Hirsh, Denver, Colo., who kindly made the specimen available for study (fig. 3, *m–o*). It has a taper of 4° and conspicuous lateral ribs that



Figure 3.

Figure 3.—Specimens of *Baculites undatus* Stephenson, natural size, from Texas and Colorado.

a–d. Dorsal, lateral, ventral, and end views of hypotype USNM 182430 from the Nacatoch Sand 1.1 miles northwest of Chatfield, Navarro County, Tex.

e. Lateral view of hypotype USNM 182429 from locality of a–d.

f. Lateral view of hypotype USNM 182428 from locality of a–d.

g–j. End, ventral, lateral, and dorsal views of hypotype USNM 182431 from locality of a–d.

k, l. Lateral and end views of hypotype USNM 182432 from the Pierre Shale (fig. 1, loc. 2).

m–o. End, lateral, and ventral views of hypotype USNM 182437 from the Pierre Shale (fig. 1, loc. 5).

p–r. End, ventral, and lateral views of hypotype USNM 182427 from the Nacatoch Sand at USGS Mesozoic locality 762 near Chatfield, Tex.

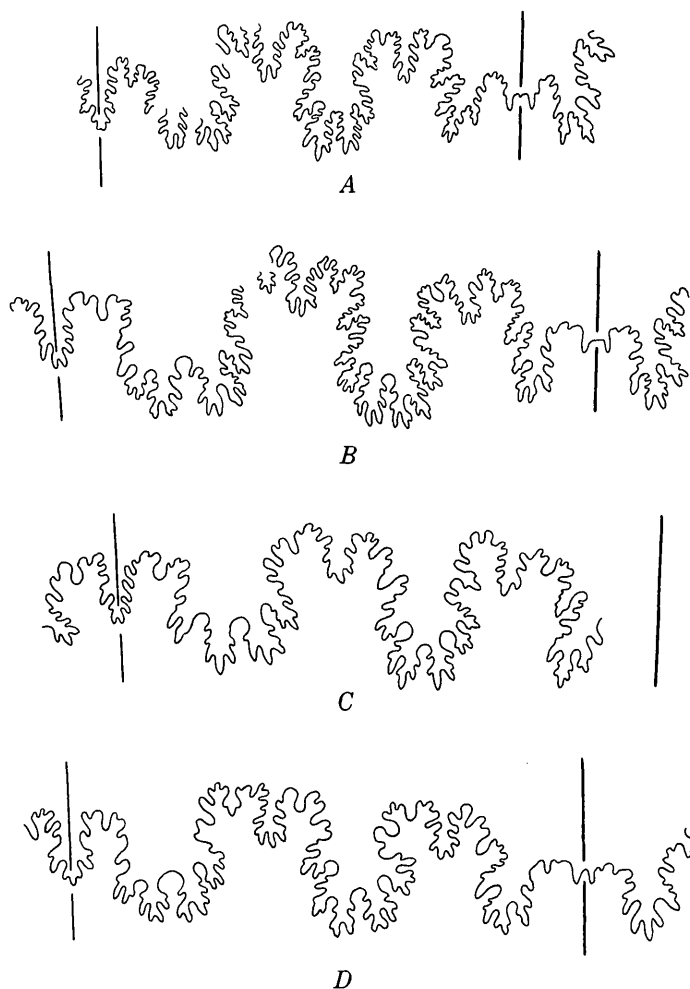


Figure 4.—Sutures of *Baculites undatus* Stephenson. A, Hypotype USNM 182433, $\times 2$, at a diameter of 17 mm (fig. 5, h–j). B, Hypotype USNM 182441, $\times 2$, at a diameter of 25.5 mm (fig. 5, e–g). C, Hypotype USNM 182430, $\times 4$, at a diameter of 11.5 mm (fig. 3, a–d). D, Hypotype USNM 182429, $\times 4$, at a diameter of 13 mm (fig. 3, e).

extend to and across the venter.

The baculites from the Kremmling locality were associated with *Nostoceras dracone* Stephenson, "*Helicoceras*" *navarroense* Shumard, and *Solenoceras texanum* (Shumard). These ammonites are known from the Neylandville Marl of northeast Texas, and "*Helicoceras*" *navarroense* and *Solenoceras texanum* also occur in the overlying Nacatoch Sand (Stephenson, 1941, p. 401, 414, 418).

Zone of *Baculites reesidei* Elias.—Eight collections of fossils from this zone have baculites that seem assignable to *B. undatus* (fig. 1, locs. 6, 8–11, 13, 15, 19), and five collections contain a single specimen each that may represent this species (fig. 1, locs. 12, 14, 16, 18, 22). Most specimens are from the Fort Collins area in northern Colorado where they occur with numerous specimens of *B. reesidei* in the Larimer Sandstone Member of the Pierre Shale. The specimens of *B. undatus* are scarce in contrast to the associated *B. reesidei*. One collection (fig. 1, loc. 9) consists of 150 specimens of *B. reesidei* and a single example of *B. undatus*. The largest collection of *B. undatus* consists of six specimens 11–27 mm in diameter (fig. 1, loc. 8), and the largest individual in this collection is shown on figure 5, e–g, and its suture on figure 4, B. The largest specimen in all collections is a somewhat crushed body chamber 78 mm in diameter (fig. 1, loc. 13). A small strongly sculptured septate individual from this locality is shown on figure 5, c, d. This specimen has a taper of 5° . Its lateral ribs are spaced at one per shell diameter, whereas the ventral ribs are spaced at three. An unusually strongly ribbed specimen from another locality (fig. 1, loc. 10) is shown on figure 5, p, q. Lateral ribs, spaced one per shell diameter, extend to the venter and cross it strongly.

In the Fort Collins area, *B. undatus* is associated with several molluscan species that occur also in the Nacatoch Sand of

northeastern Texas. The collection (fig. 1, loc. 8) that contains the most (six) specimens of *B. undatus* includes Stephenson's *Nuculana corbetensis*, *Nemodon adkinsi*, *Volsella uddeni*, *Cardium* (*Ethmocardium*) *welleri*, and *Tellina munda*. The gastropod *Capulus spangleri* Henderson and the ammonite "*Helicoceras*" *navarroense* Shumard, which have been found in the Nacatoch Sand of Texas, were associated with *B. undatus* in one of the collections (fig. 1, loc. 13).

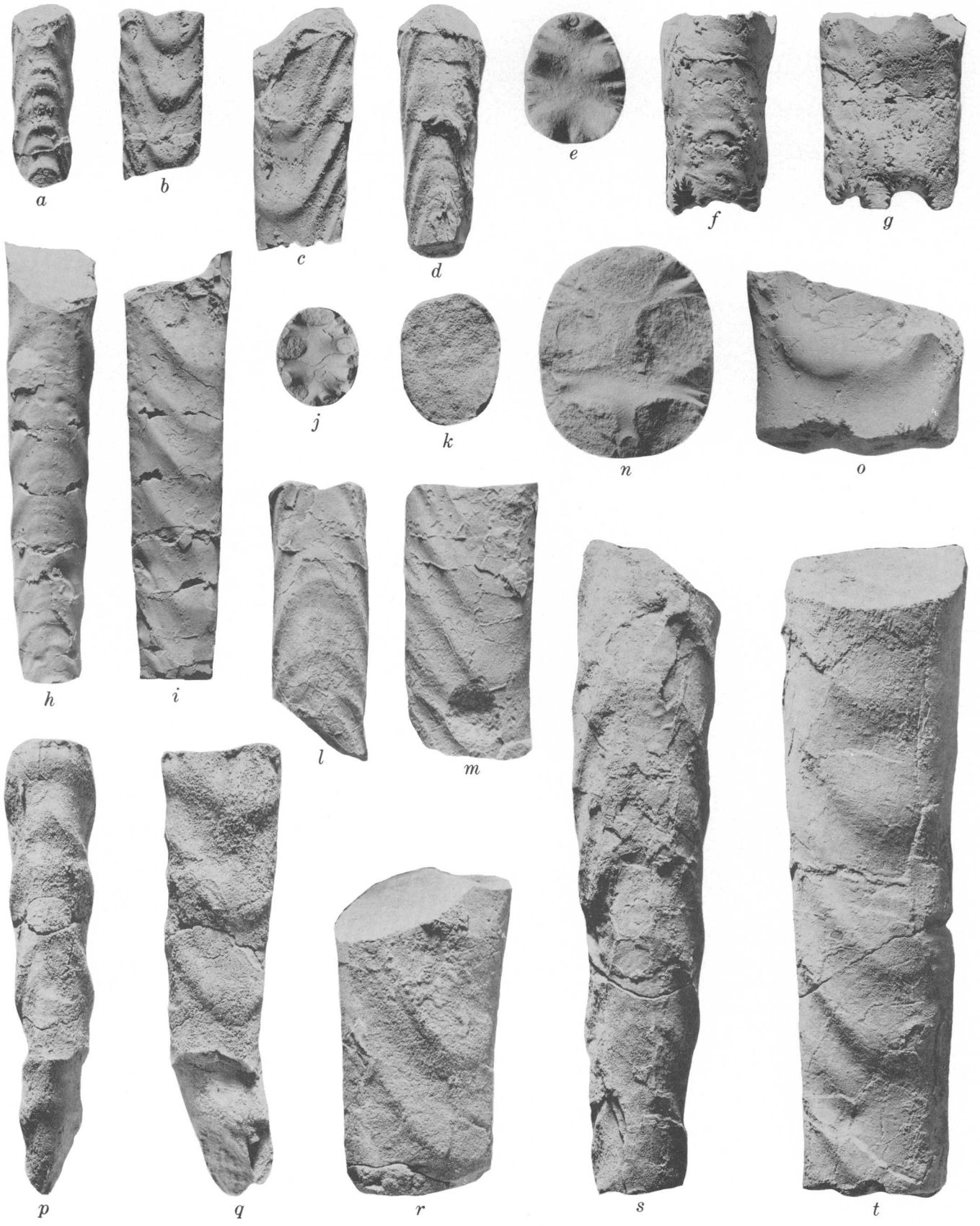


Figure 5

Figure 5.—Specimens of *Baculites undatus* Stephenson, natural size, from the Pierre Shale of Colorado and New Mexico.

- a, b. Ventral and lateral views of hypotype USNM 182440 (fig. 1, loc. 21).
 c, d. Lateral and ventral views of hypotype USNM 182438 (fig. 1, loc. 13).
 e-g. End, ventral, and lateral views of hypotype USNM 182441 (fig. 1, loc. 8).
 h-j. Ventral and lateral views and sectional view at a diameter of 18 mm of hypotype USNM 182433 (fig. 1, loc. 2).
 k-m. End, ventral, and lateral views of hypotype USNM 182435 (fig. 1, loc. 5).
 n, o. End and lateral views of hypotype USNM 182442 (fig. 1, loc. 26).
 p, q. Ventral and lateral views of hypotype USNM 182439 (fig. 1, loc. 10).
 r. Lateral view of hypotype USNM 182435 (fig. 1, loc. 5).
 s, t. Ventral and lateral views of hypotype USNM 182436 (fig. 1, loc. 5).

REFERENCES CITED

- Izett, G. A., Cobban, W. A., and Gill, J. R., 1971, The Pierre Shale near Kremmling, Colorado, and its correlation to the east and the west: U.S. Geol. Survey Prof. Paper. 684-A, 19 p., illus.
 Owens, J. P., Minard, J. P., Sohl, N. F., and Mello, J. F., 1970, Stratigraphy of the outcropping post-Magothy Upper Cretaceous formations in southern New Jersey and northern Delmarva Peninsula, Delaware and Maryland: U.S. Geol. Survey Prof. Paper 674, 60 p., illus.
 Stephenson, L. W., 1941, The larger invertebrate fossils of the Navarro group of Texas: Texas Univ. Bull. 4101, 641, p., 95 pls.



POTENTIAL SHALE-OIL RESOURCES OF A STRATIGRAPHIC SEQUENCE ABOVE THE MAHOGANY ZONE, GREEN RIVER FORMATION, PICEANCE CREEK BASIN, COLORADO

By JANET K. PITMAN and JOHN R. DONNELL, Denver, Colo.

Abstract.—In the southern part of the Piceance Creek basin the upper part of the Green River Formation above the Mahogany zone contains beds of rich oil shale which may be economically recoverable by a surface-mining operation. Four units within this sequence were evaluated for thickness, distribution, oil yield, and potential shale-oil resources. In the area appraised, total estimated resources of 128.5 billion bbl of oil are contained within the sequence. It is thickest in T. 3 S., R. 96 W., where 354 feet of oil shale yields an average of 14 gal of oil per ton, with a total resource of 9.0 billion bbl. It is richest in T. 5 S., R. 96 W., where 250 feet of oil shale yields an average of 19 gal of oil per ton, with a total resource of 6.5 billion bbl. Resources are tabulated for four units of the sequence.

age oil yield and for drawing graphs were written by George Van Trump and Margaret Roberts, of the U.S. Geological Survey.

STRATIGRAPHY

Bradley (1931) named four members of the Green River Formation in the Piceance Creek basin—Douglas Creek, Garden Gulch, Parachute Creek, and Evacuation Creek, in ascending order—and Donnell mapped and described them (Donnell, 1961; Donnell and Blair, 1970). The Douglas Creek

The decline in production of domestic crude oil and the increasing cost of imported crude oil emphasize the need for a supplementary domestic supply of oil. Extensive deposits of oil shale in the Eocene Green River Formation underlie large areas of Colorado, Utah, and Wyoming, and are potential sources of synthetic crude oil (fig. 1). The largest and richest of these deposits occur in the Piceance Creek basin, Colorado.

This report is concerned with the thickness, distribution, oil yield, and potential oil-shale resources of four units of the stratigraphic sequence above the Mahogany zone in the Piceance Creek basin, Colorado. Detailed appraisals of oil-shale resources published for the Mahogany zone and for two lower rich oil-shale zones by Donnell and Blair (1970) indicate that these three zones are of the greatest interest economically. Although the upper sequence of oil shale is not as rich as the Mahogany and lower zones, it is closer to the surface, and locally may be recoverable by surface-mining methods.

Acknowledgments.—The U.S. Bureau of Mines Oil-Shale Petroleum and Research Center at Laramie, Wyo., is the source of most of the Fischer assay data used in this report (Stanfield and others, 1954, 1957, 1960, 1967; Belser, 1951). A small amount of assay information was supplied by private companies and individuals. Computer programs for deriving aver-

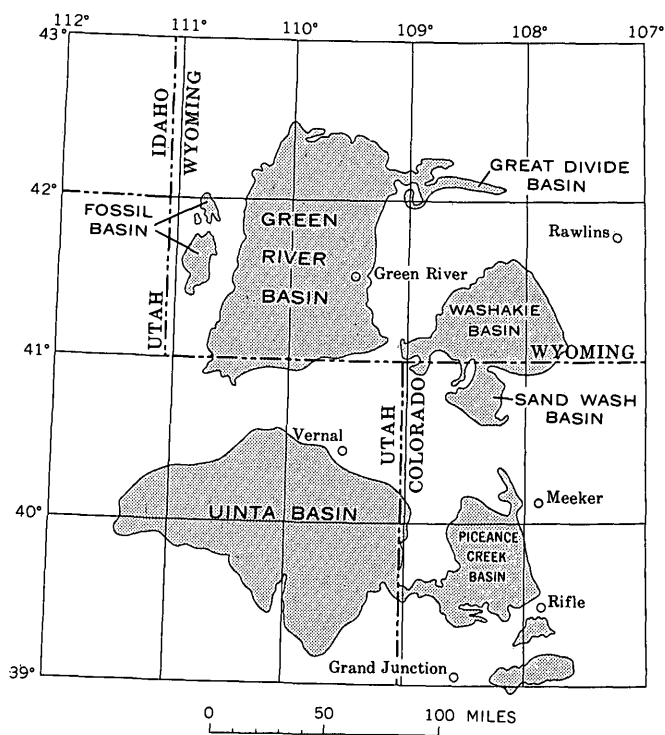


Figure 1.—Area (patterned) underlain by the Green River Formation, Colorado, Utah, and Wyoming.

consists of sandstone and minor amounts of algal and oolitic limestone; the Garden Gulch is mainly clay shale and low- to moderate-grade oil shale that grades into richer oil shale at the basin center; the Parachute Creek is almost entirely low-grade to rich oil shale that contains thin analcitized tuff beds and thin sandstone beds, finely disseminated dawsonite, pods of nahcolite, and beds of halite and nahcolite; the Evacuation Creek consists of tuffaceous siltstone and sandstone and minor amounts of low-grade oil shale and barren marlstone (Donnell and Blair, 1970).

The Parachute Creek Member has been subdivided on the basis of oil yield into zones, each of which is characterized by persistent ledges, beds, and groups of beds. Many of these have been informally named (Duncan and Denson, 1949) and are used to define the units shown on figure 2. Several groups of

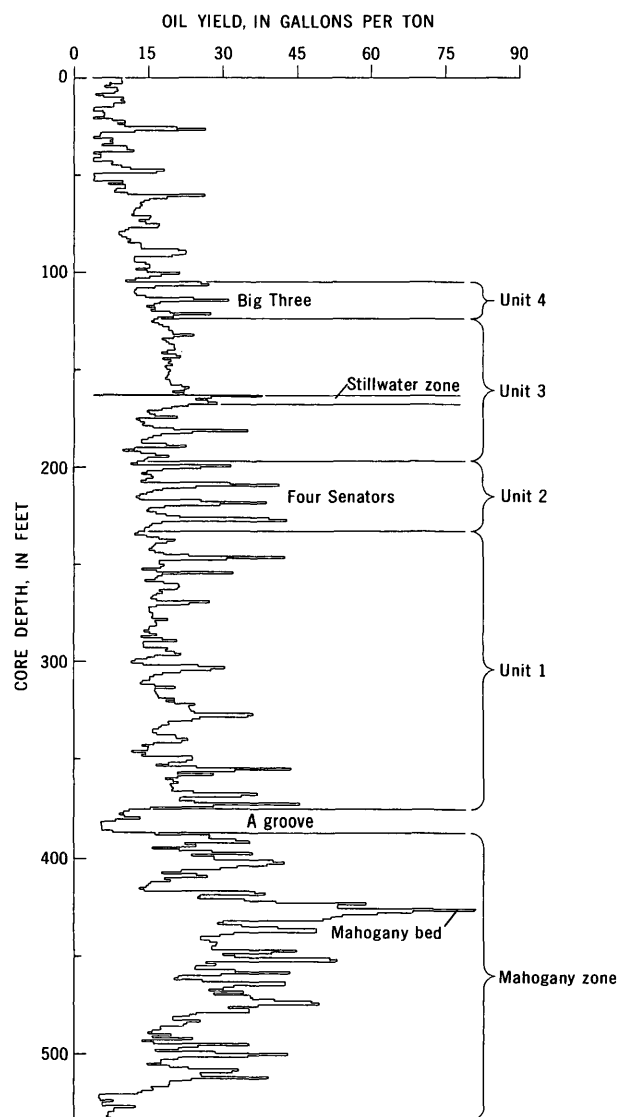


Figure 2.—Partial oil-yield graph indicating shale-oil units used in resource appraisal.

beds and oil-shale zones have been recognized in the subsurface and are traceable over a large part of the Piceance Creek basin of Colorado and the Uinta Basin of Utah (Cashion and Donnell, 1972). The most conspicuous of these is the Mahogany ledge (called Mahogany zone in the subsurface) which contains the Mahogany bed, a thin and exceedingly rich marker bed (Donnell, 1961). Another persistent marker, the A groove, is a sequence of marlstone and lean oil shale, 10–15 feet thick, that directly overlies the Mahogany zone. It is so named because it weathers to form a recess in the cliff.

About 100 feet above the top of the A groove in the southwestern part of the basin and approximately 200 feet above the A groove near the depositional center is a sequence containing four rich oil-shale beds—the Four Senators zone, which ranges in thickness from 18 to 38 feet. They yield an average of approximately 30 gal of oil per ton and are separated by tuff stringers and oil shale that yield less than 15 gal of oil per ton. Another sequence containing rich oil-shale beds, approximately 40–50 feet thick, occurs 20–30 feet above the Four Senators. The base of this sequence is marked by the Stillwater zone, a massive ledge 5–10 feet thick, which has an average oil yield of 20 gal per ton. The upper limit of the richer oil-shale sequence is marked by the Big Three. This series of three rich oil-shale beds, 1–2 feet thick, in an interval less than 25 feet, yields between 12 and 20 gal of oil per ton. In many areas as much as 200 feet of continuous oil shale has been deposited above the Big Three.

The contact between the Parachute Creek and Evacuation Creek Members is placed where the sequence of rocks changes from lean oil shale to a sequence composed predominantly of sandstone and siltstone.

PROCEDURES

Data used to construct isopach maps of oil-shale units (fig. 3) were obtained from graphs of assayed core and from electric, gamma-ray neutron, gamma-ray density, and sonic logs of other exploratory wells. Isovalue maps (figs. 4 and 5) show for each unit the variation of potential oil yield in gallons per ton and thousands of barrels per acre. Oil-yield values (gallons per ton) for each unit are based on the total thickness at each sample locality. Intervals for which no data were available were assigned the potential value of an equivalent bed in an adjacent hole. Potential resource values (yield of oil in barrels per acre) were computed from the oil yield (gallons per ton) and the thickness of the unit at each control point.

The four units were not appraised in the northern part of the basin because either the oil shale in the interval assayed yielded less than 12 gal per ton or no assay information was available.

Potential shale-oil resources for the four units are computed on a township basis and are reported in table 1.

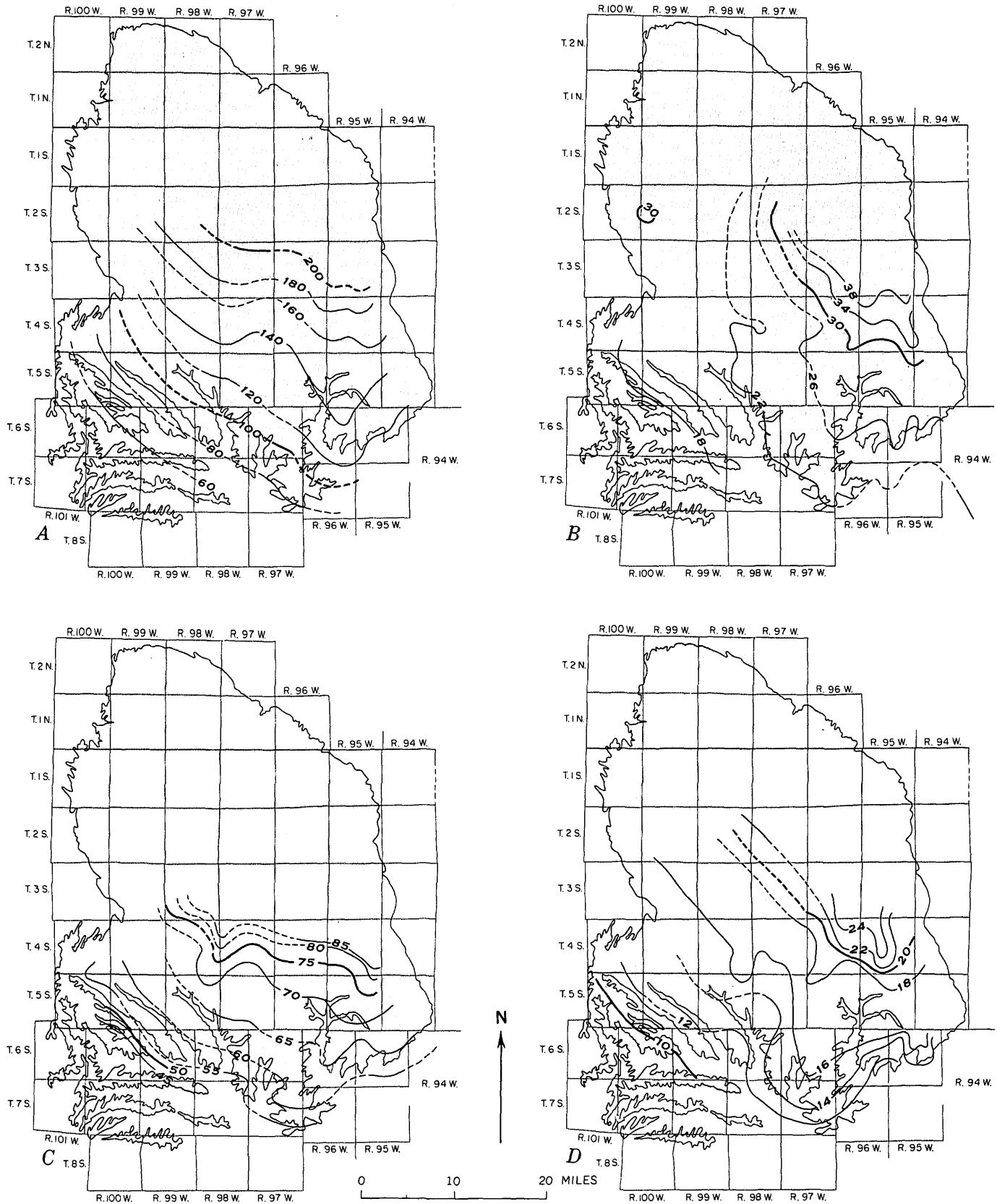


Figure 3.—Maps showing thicknesses of shale-oil units in the Piceance Creek basin. Lines are dashed where information is sparse. A, unit 1 (interval is 20 feet). B, unit 2 (4 feet). C, unit 3 (5 feet). D, unit 4 (2 feet).

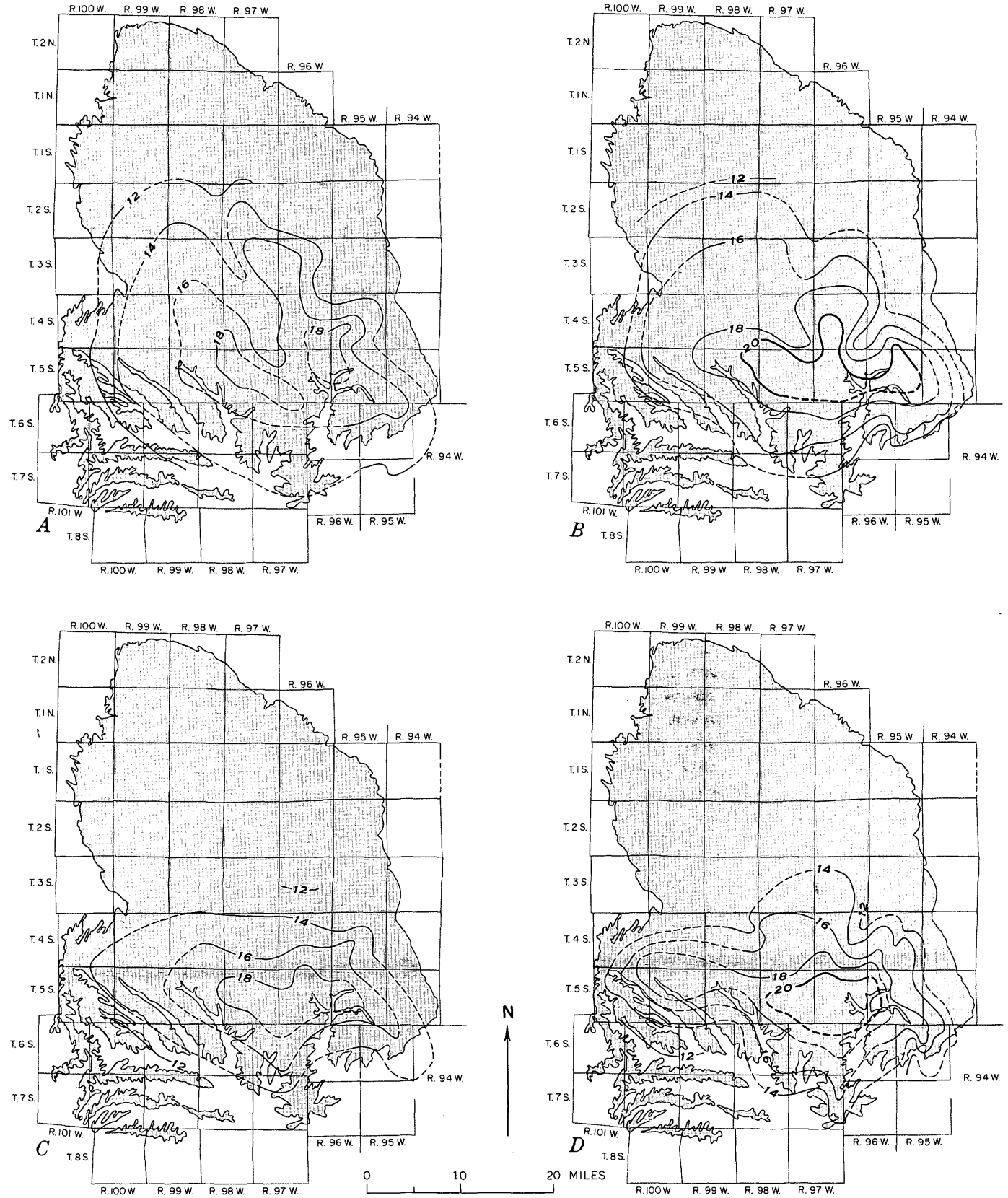


Figure 4.—Maps showing potential shale-oil yield, in gallons per ton, of A, unit 1, B, unit 2, C, unit 3, and D, unit 4, in the Piceance Creek basin. Interval is 2 gal per ton. Lines are dashed where information is sparse.

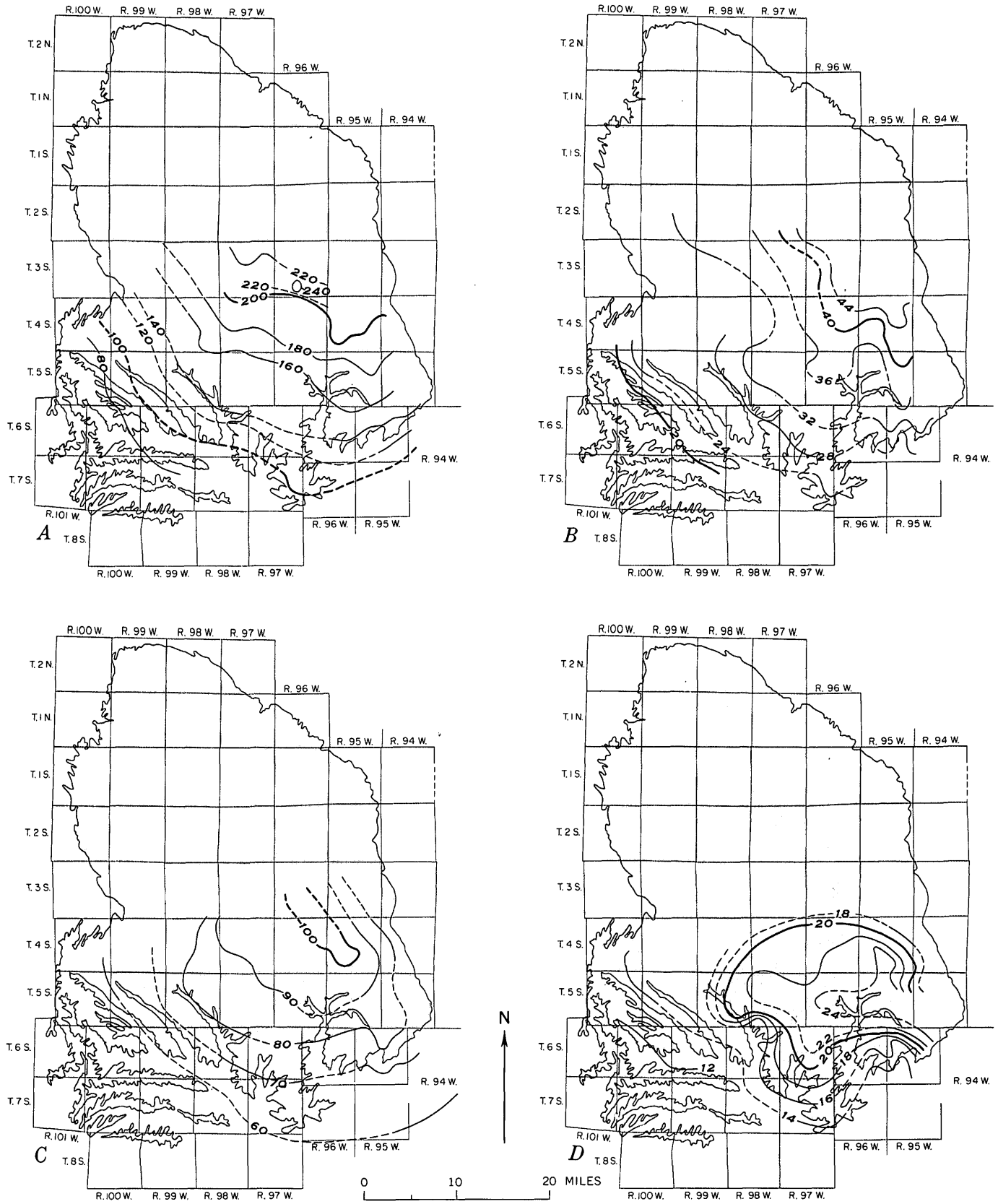


Figure 5.—Maps showing potential shale-oil yield of units in the Piceance Creek basin. Lines are dashed where information is sparse. A, unit 1 (interval is 20 thousand bbl per acre). B, unit 2 (4 thousand bbl per acre). C, unit 3 (10 thousand bbl per acre). D, unit 4 (2 thousand bbl per acre).

Table 1.—Total resources, in billions of barrels, of the oil-shale sequence overlying the Mahogany zone

[No allowances made for losses in mining or processing]

Location		Unit				Total resources
T (S.)	R (W.)	1	2	3	4	
2	97...	1.0	1.0
	98...99
	99...88
3	95...	1.9	1.9
	96...	5.4	1.1	2.5	9.0
	97...	5.2	.9	6.1
	98...	4.3	.7	5.0
4	99...	3.6	.7	4.3
	94...	1.78	0.2	2.7
	95...	5.0	1.0	2.4	.5	8.9
	96...	4.4	.9	2.3	.5	8.1
	97...	4.4	.8	2.3	.5	8.0
	98...	3.7	.7	1.9	.4	6.7
	99...	2.9	.6	1.6	.4	5.5
5	100...	1.2	.3	.8	.2	2.5
	94...	3.1	1.5	.3	4.9
	95...	3.7	.8	1.9	.5	6.9
	96...	3.3	.8	1.9	.5	6.5
	97...	3.5	.8	2.0	.5	6.8
	98...	2.8	.6	1.6	.4	5.4
	99...	2.0	.5	1.2	.3	4.0
6	100...	1.3	.3	.9	.2	2.7
	95...	1.6	.4	.9	.2	3.1
	96...	1.7	.3	.9	.2	3.1
	97...	2.6	.6	1.5	.4	5.1
	98...	1.5	.3	.9	.2	2.9
7	99...	.9	.2	.5	.1	1.7
	100...	.8	.21	1.1
	96...	.4	.11	.6
	97...	.9	.22	1.3
Total	72.6	16.7	32.2	7.0	128.5
	Area (sq mi) ..	745	815	619	588	2,767

SHALE-OIL RESOURCES

The part of the Parachute Creek Member that overlies the Mahogany zone (fig. 2) is subdivided into resource units as follows:

Unit 1. Interval between the top of the A groove and the base of the Four Senators.

Unit 2. Interval containing the Four Senators.

Unit 3. Interval between the top of the Four Senators and the base of the Big Three.

Unit 4. Interval containing the Big Three.

Unit 1 varies in thickness from 60 feet near the southwest edge of the basin to more than 200 feet in the east-central part (fig. 3A), and ranges in average oil yield from a minimum of 12 gal per ton along the western margin of the basin to 18 gal per ton in the south-central part (fig. 4A). It contains approximately 80 thousand bbl of oil per acre in the southwestern part of the basin and more than 220 thousand bbl per acre in the east-central part (fig. 5A). For an area of approximately 745 sq mi, the interval has a total resource of 72.6 billion bbl of oil (table 1).

Unit 2 ranges in thickness from 18 feet in the southwest edge of the basin to 38 feet in the east-central part (fig. 3B),

and yields an average of 12 gal per ton along the northwestern part of the basin to 20 gal per ton in the south-central part (fig. 4B). For an area of approximately 815 sq mi, unit 2 has an estimated total resource of 16.7 billion bbl of oil (table 1). The average yield per acre varies from 20 thousand bbl in the southwestern part of the basin to more than 44 thousand bbl in the east-central part (fig. 5B).

Unit 3 ranges in thickness from 45 feet to 85 feet (fig. 3C), and the oil yield varies from 12 gal per ton in the south and east-central parts of the basin to 18 gal per ton in the south-central part (fig. 4C). An oil yield of 60 thousand bbl per acre is estimated for the southern part of the basin, with a maximum of 100 thousand bbl per acre in the east-central part (fig. 5C). A total resource of 32.2 billion bbl of oil is estimated for an area of approximately 619 sq mi (table 1).

Unit 4 thickens in a northeast direction from a minimum of 10 feet in the southwestern part of the basin to more than 24 feet in the southeastern part (fig. 3D). The oil yield of the sequence averages 12 gal per ton along the south, west, and southeast margins of the basin and is as much as 20 gal per ton in the south-central part (fig. 4D). A minimum of 12 thousand bbl per acre is present in the southwestern part of the basin and a maximum of 24 thousand bbl per acre is estimated for the southeastern part (fig. 5D). A total resource of 7.0 billion bbl of oil is estimated for an area of approximately 588 sq mi.

In the area appraised, the four units have total estimated resources of 128.5 billion bbl of oil. The thickness and potential oil yield of the oil-shale sequence above the Mahogany zone in general increase from a minimum along the southwest basin margin to a maximum parallel to the depositional axis. Northeastward from the axis the sequence thickens and loses oil yield because of dilution by clastic material which occurs as bedded deposits or as contaminants of oil shale.

The sequence of oil shale overlying the Mahogany zone (units 1–4) is thickest in T. 3 S., R. 96 W. The total interval between the top of the A groove and the top of the Big Three is about 354 feet thick, averaging approximately 14 gal of oil per ton with a total resource of 9.0 billion bbl of oil. The sequence is richest in T. 5 S., R. 96 W., where 250 feet of oil shale yields an average of 19 gal of oil per ton, with a total resource of 6.5 billion bbl. In this area, however, the overburden above the Mahogany bed is more than 500 feet thick.

The area most favorable for a surface-mining operation is along the western margin of the basin in T. 4 S., R. 99 W. Approximately 190 feet of oil shale with an average yield of 15 gal per ton occurs within 400 feet of the surface. Some sequences as thick as 25 feet will yield an average of about 20 gal per ton.

In a surface-mining operation, perhaps low grade to moderately rich oil shales above the Mahogany zone could be saved and blended with rich oil shales from the Mahogany zone and underlying rich zones that average more than 30 gal per ton to produce a retort feed of 25 gal per ton.

REFERENCES CITED

- Belser, Carl, 1951, Green River oil-shale reserves of northwestern Colorado: U.S. Bur. Mines Rept. Inv. 4769, 13 p.
- Bradley, W. H., 1931, Origin and microfossils of the oil shale of the Green River formation of Colorado and Utah: U.S. Geol. Survey Prof. Paper 168, 58 p.
- Cashion, W. B., and Donnell, J. R., 1972, Chart showing correlations of selected key units in the organic-rich sequence of the Green River Formation, Piceance Creek basin, Colorado, and Uinta Basin, Utah: U.S. Geol. Survey Oil and Gas Inv. Chart OC-65.
- Donnell, J. R., 1961, Tertiary geology and oil-shale resources of the Piceance Creek basin between the Colorado and White Rivers, northwestern Colorado: U.S. Geol. Survey Bull. 1082-L, p. 835-891.
- Donnell, J. R., and Blair, R. W., 1970, Resource appraisal of three rich oil-shale zones in the Green River Formation, Piceance Creek basin, Colorado: Colorado School Mines Quart., v. 65, no. 4, p. 73-87.
- Duncan, D. C., and Denson, N. M., 1949, Geology of Naval Oil Shale Reserves 1 and 3, Garfield County, Colorado: U.S. Geol. Survey Oil and Gas Inv. Prelim. Map 94.
- Stanfield, K. E., and others, 1954, Oil yields of sections of Green River oil shale in Colorado, Utah, and Wyoming, 1945-52: U.S. Bur. Mines Rept. Inv. 5081, 153 p.
- 1957, Oil yields of sections of Green River oil shale in Colorado, 1952-54: U.S. Bur. Mines Rept. Inv. 5321, 132 p.
- 1960, Oil yields of sections of Green River oil shale in Colorado, 1954-57: U.S. Bur. Mines Rept. Inv. 5614, 186 p.
- 1967, Oil yields of sections of Green River oil shale in Colorado, 1957-63: U.S. Bur. Mines Rept. Inv. 7051, 284 p.



SPECTROCHEMICAL COMPUTER ANALYSIS—INSTRUMENTATION

By A. W. HELZ, Washington, D.C.

Abstract.—A microphotometer is described for making magnetic tape recordings of spectra 480 mm long from 102- by 508-mm photographic plates. Transmission readings are recorded at a rate exceeding 1,300 per second for every 5.08 μm of length of the spectrum. A two-line cadmium fiducial line system and a developing tank for 102- by 508-mm plates also are described as equipment ancillary to a system of computer spectral analysis applied to the spectrochemical analysis of geologic materials.

The recording-computer system for a complete spectrochemical analytical procedure that was previously outlined (Helz and others, 1969) is now in routine service. Computer-prepared analytical reports show concentrations of 69 elements determined from a single 70-second microphotometric scan of a spectrum between 2,300 and 4,700 Å. A search is made by the computer for about 400 spectral lines from among 92,000 optical transmission readings. All the calculations are completed automatically, including conversion of transmissions to intensities, background correction, reference to analytical curve data for concentration determination, spectral interference allowance, and choice of the "best" value on the basis of a set of line-intensity rules. Among the many changes that the procedure has undergone during the last few years are the use of 102- by 508-mm (4- by 20-inch) plates, studies of many new analytical lines, and a complete change in the line-finding logic with the attendant two-cadmium-line principle. These changes have resulted from the cooperative efforts of several of my colleagues.

Automatic trace-element analysis of geologic materials was one of the goals of this program. It was anticipated that the most refined principles of metrology would be involved because of (1) the unusually high complexity of spectra for silicate rocks and (2) the very high accuracy requirements for finding very weak lines at a predetermined wavelength (as opposed to the converse of identifying by wavelength a readily apparent line). With the objective achieved it was obvious that advantage could be taken of this system in developing many new applications.

This report describes a microphotometer designed to meet the requirements of accuracy and speed. To be effective, the microphotometer recording system had to be capable of

recording a spectrum nearly 500 mm long at constant velocity from start to finish in no more than 90 seconds, making at least 1,000 transmission readings per second. Transmission readings at 5- μm intervals along the spectrum, based on known positions within the spectrum, were also required.

Acknowledgments.—C. J. Massoni not only did all the on-the-job shop work referred to in this report, but also designed a large number of mechanical refinements. Walthall (1973) devised, completed, and tested the complex computer programs in use. His work dealt with line-finding problems, line-peak definition, plate calibration, curve fitting, background treatment, element concentration calculations, report formatting, and many other details. Dorrzapf (1973) worked out details of the applied spectrochemical procedure, particularly those of the argon-oxygen shielded arc and of plate exposure and processing.

The author is particularly appreciative of help provided by A. E. Johnson and Vilmars Fimbers, of the Moore Special Tool Co., for making possible the modifications in their standard measuring machine.

RECORDING SYSTEM

The complete recording system is shown in figure 1; it includes the tape recorder, the relay rack containing most of the electronic circuits, and the microphotometer.

The recording of a single spectrum consists of first entering on the tape a 12-digit number for identification purposes. This number is determined by adjusting thumb wheel switches. Second, the memory is cleared, and third, the motor drive for the table is started. The plate containing the spectrum is moved by the motor through the scanning beam at a steady speed. A phototube constantly monitors the scanning beam, which changes in intensity as it is intercepted by the spectral lines. The photoelectric output is sampled for every 5.08 μm of travel of the spectrum plate. The reading is digitized and then stored in the memory bank. The sampling of the photoelectric output is averaged over a short but finite fraction of time between two readings in order to smooth out electronic noise fluctuations. Whenever a predetermined number of readings has accumulated in the memory bank, the entire group of readings is transferred to the tape as a single record without interruption of the constant flow of incoming

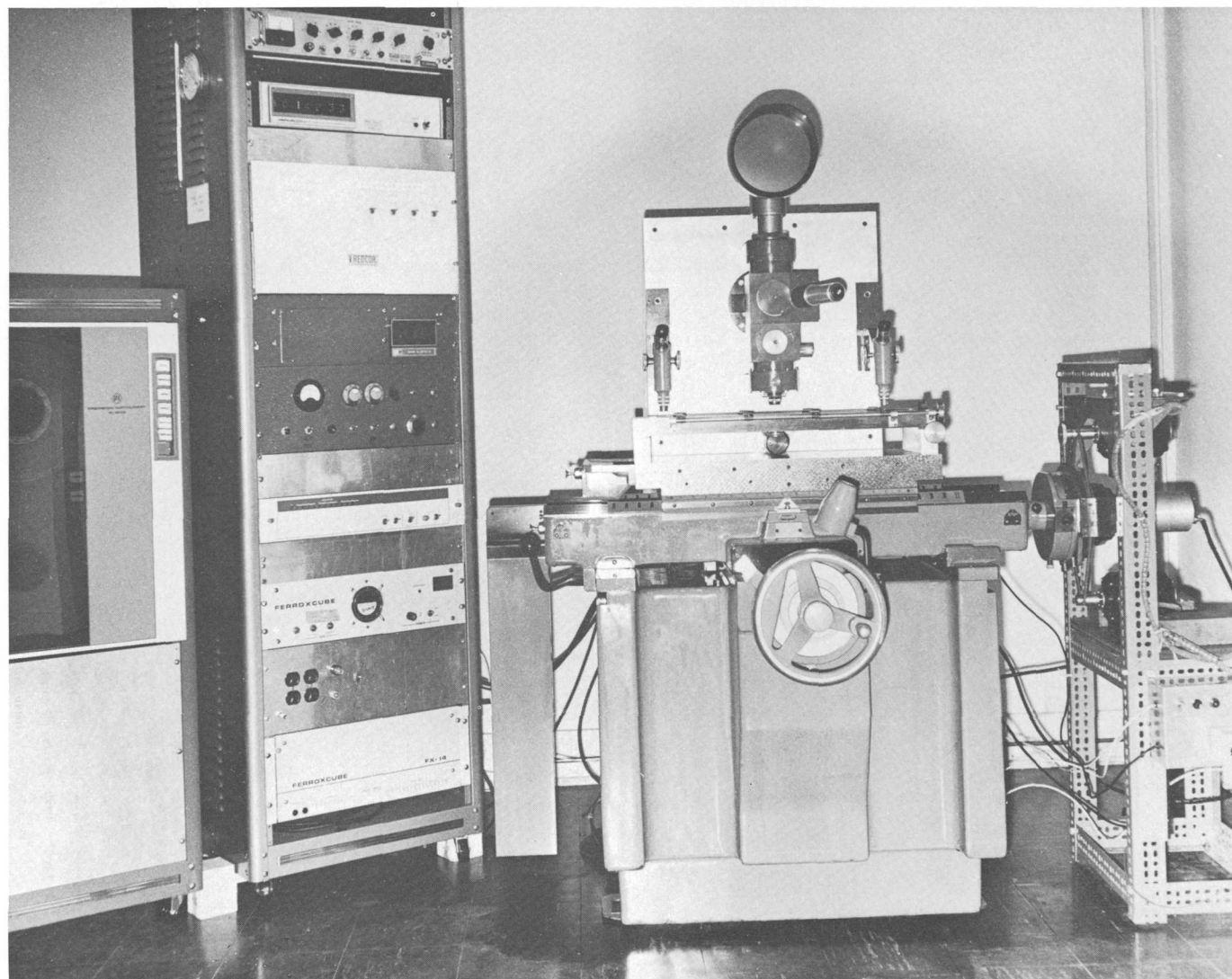


Figure 1.—Recording system. At the extreme left is the tape recorder. The tall relay rack to its right houses power supplies, counter, time devices, a-d converter, memory unit, fixed data entry, numerous control switches, and scanning lamp and phototube adjustment facilities. The microphotometer is in the center, and the power drive for the table is at the extreme right. The microphotometer is about 5½ feet tall.

readings. The tape recorder has the circuitry necessary to produce the computer-required spaces between the records. A limit switch for the table motion and a stop on the control relay rack are activated at the end of a spectrum scan.

The activated stop switch permits the one remaining incomplete record to be recorded and also produces an end-of-file mark on the tape. Thus, all the records for a single spectrum, including an identifier, are grouped into a "file." Vital to this recording process is the condition that no readings be lost. Readings made while a record is being "dumped" on tape and a gap is being formed are kept in proper order in the memory bank. The ordinal number of a reading multiplied by the reading interval determines the basic relationship between length and wavelength. The elimination of the necessity of recording explicit "length" or position data reduces the

amount of recorded data by a factor of three. This saving is made possible with the use of a memory bank of sufficient storage capacity to include all the readings of one record plus the number of readings taken during the time required for the complete dumping process.

MICROPHOTOMETER

The horizontal motion of the microphotometer is provided by the Moore No. 3 Measuring Machine.¹ This machine was obtained with a simple vertical bracket in place of the standard vertical column (fig. 2). The machine was also supplied with a modification of the longitudinal traverse to provide for 483

¹ Moore Special Tool Co., Bridgeport, Conn.

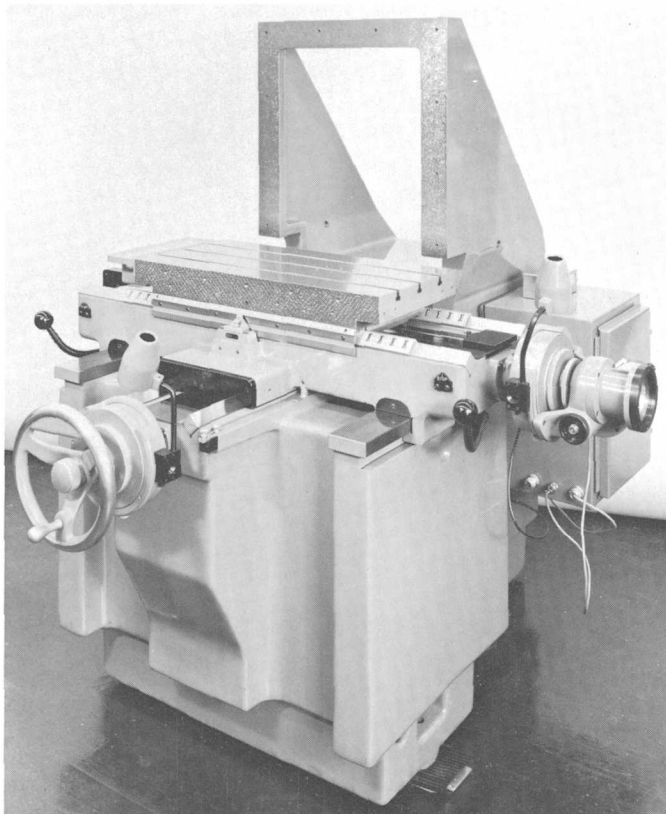


Figure 2.—Measuring machine with bracket for installing the micro-photometer optics. Height is about 5 feet.

mm rather than the standard 458 mm of travel. Although this change was made at the risk of some loss of ruggedness, it was not considered serious because of the light-duty application. Concern over the comparatively high speed requirement determined our selection of roller-bearing support, on advice of the manufacturer, for the table's longitudinal motion. The heart of this machine and the fundamental length determinant of the spectral reading system is the 533-mm-long lead screw having tolerances of +0 and $-0.9 \mu\text{m}$ overall and $0.4 \mu\text{m}$ in any 25-mm section (+0 and -35 millionths of an inch overall and within 15 millionths of an inch in any 1-inch section). The optical system is mounted on a 559- by 508- by 19-mm aluminum-alloy plate bolted to the vertical bracket of the measuring machine. A spectral plate holding-and-orienting device, cut from a single piece of normalized mild steel 610 by 152 by 38 mm, is mounted on the table of the measuring machine (fig. 4A). This plateholder is supported at the ends, 48 mm above the table, to provide the space needed for the light path below the spectral plate. A bidirectional, incremental, rotary encoder is mounted with its axis in line with the longitudinal screw and is connected to the screw with a precision bellows coupling.

The optical system follows conventional practice for good resolution, high contrast, and low scattered or diffuse light detection. The optical system is not entirely in one plane as seemingly indicated in figure 3. For the source area and for the end with the phototube the plane of the drawing is horizontal; the remainder of the drawing is in a vertical plane.

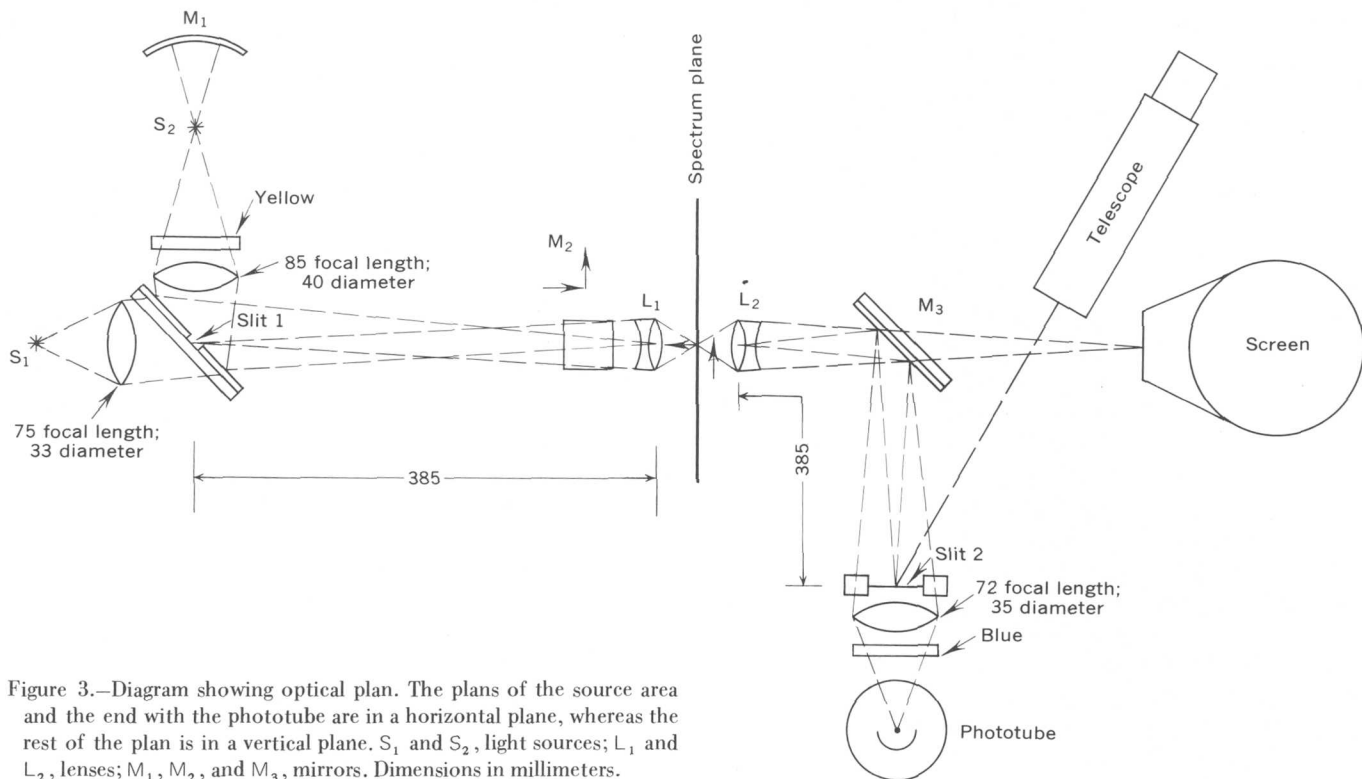


Figure 3.—Diagram showing optical plan. The plans of the source area and the end with the phototube are in a horizontal plane, whereas the rest of the plan is in a vertical plane. S_1 and S_2 , light sources; L_1 and L_2 , lenses; M_1 , M_2 , and M_3 , mirrors. Dimensions in millimeters.

Two low-power light sources are used. The reading source, S_1 , is d-c powered and illuminates entrance slit 1 (fig. 3). The source S_2 is a-c powered and illuminates the front mirror surface of the entrance slit. This source provides field illumination for the viewing screen. Both lamps are 6-volt, 3-amp, microscope illuminator type. The fixed entrance slit consists of a precision-ruled, 100- μm -wide window in a mirror. A 32-mm-focal-length Micro-Tessar lens, L_1 , focuses an image one-tenth the slit size on the plane of the spectrum. This image for the scanning light, about 7 μm wide, was selected to be about one-quarter of the width (a sizable fraction) of a spectral line and about 1 mm in length, which is as long as practical. Precision adjustments of slit 1 for translation and rotation are provided for alinement relative to the spectral lines and slit 2. The box holding the source section of the microphotometer is shown in figure 5.

The "observer" half of the optical system starts with a 32-mm Micro-Tessar lens, L_2 in figure 3, having specifications identical with those for L_1 . A blue image of the spectral area (which is illuminated through slit 1) is formed by L_2 on a second slit (slit 2) via a dichroic mirror, M_3 . The yellow field illumination of the same spectral area is transmitted through the dichroic mirror to form a viewing image on the screen. Magnification of the spectrum is about 10 times at the exit slit, and 100 times at the screen. An image of slit 1 is also visible on the screen. Slit 2 has width and height adjustments and is accurately rotatable for alinement. A blue filter in front of the phototube aids in the further elimination of the light of the field illuminator source from the phototube.

The telescope indicated in figure 3 is used to set up a run but cannot be used for accurate alinement because it is positioned off axis. This was done to permit viewing past mirror M_3 . Initial alinement and focal adjustments are facilitated by replacing the phototube-filter-lens combination with a low-power microscope focused on the rear of the slit. Focus, orientation, and position of the two slits and spectral lines may be accurately adjusted in this manner. Once this is accomplished and the viewing screen is adjusted, routine alinement may be made precisely on the viewing screen.

Location of the optical parts discussed above is illustrated in figure 4. The photopickup illustrated in figure 5A is a commercial phototube and a solid-state preamplifier. This combination has sufficient speed of response and is preferred over a multiplier phototube when the light level is adequate, because of its greater long-term stability and freedom from drift. The outboard microscopes, shown in figures 1 and 4A, are used to aline the spectra parallel to the table motion. The plateholder, visible in figures 4A and B with a spectral plate in position, has a rotational adjustment about a vertical axis for achieving this parallelism. The plate-supporting surface of the plateholder was machined and hand scraped to be parallel to the table, within 2.5 μm , throughout its entire motion.

A variable-speed d-c motor and a gear reduction drive were used at first for the scanning motion. However, spurious

spectral lines occasionally were observed when scanning at the maximum speed, and these were traced to vibration of the vertical optical train caused by the gear drive. Although the problem was eliminated by changing the power drive, strengthening of the brackets of the optical column is recommended. The revised power drive now in use, with the worm and helical gears replaced by a 165-mm-diameter pulley, is shown in figure 6. This pulley is driven with two reversible, constant-speed, a-c motors mounted diametrically opposite the screw shaft. These motors are wired in parallel. A Buna-N O-ring, 240 mm in diameter and 7 mm in cross section, transmits the power of this dual motor arrangement with very little stress (other than that of rotation) on the precision screw and bearing.

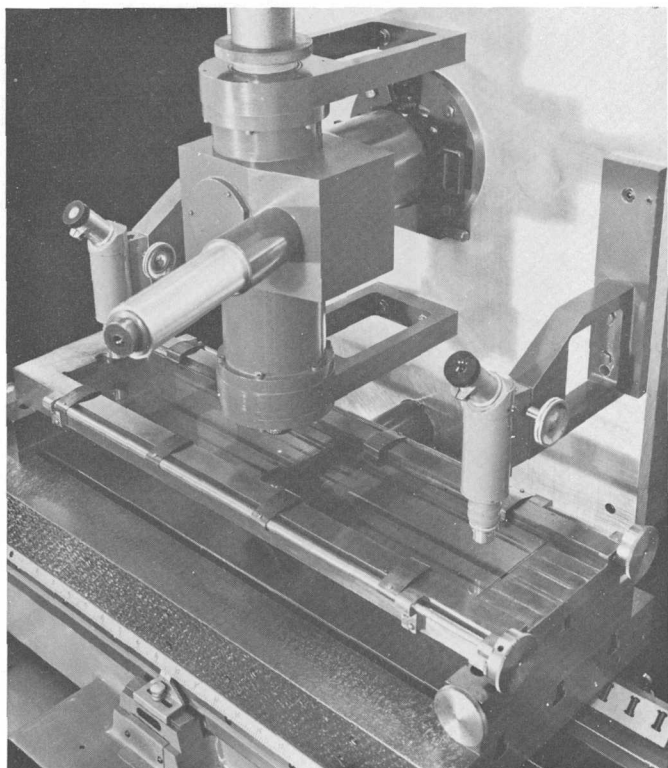
At this writing, a motor-drive speed is used that completes scanning a spectrum in 70 seconds. Thus the rate of taking transmission readings exceeds 1,300 per second. We are hesitant to go to higher speeds because of unknown thermal effects and mechanical wear effects on the precision screw. Furthermore, we are close to the limits of speed of response of the photometric system used and also limitations of the particular recording system in use.

FIDUCIAL LINES

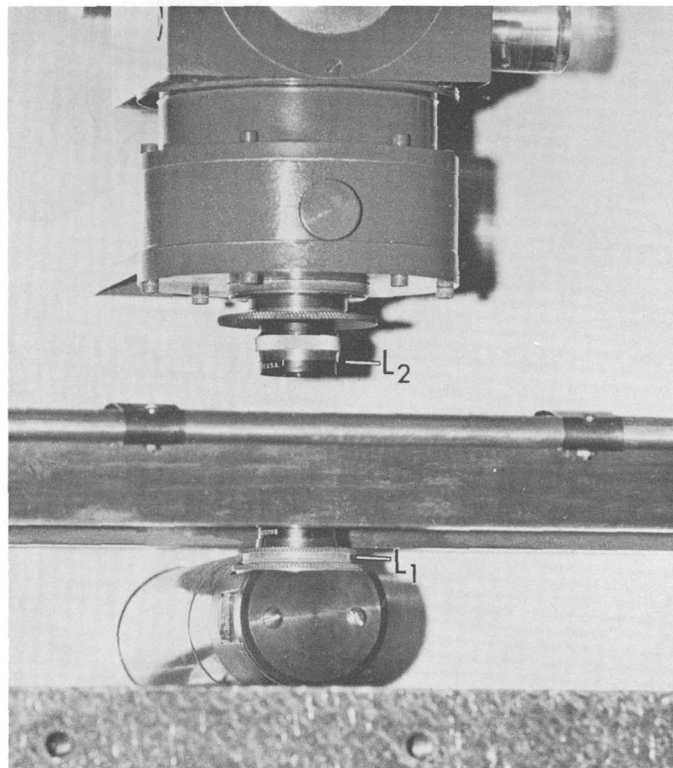
Computer line finding in our earlier work depended upon having Cd 2288.02 Å and numerous iron lines in each spectrum. The cadmium line was obtained with an Osram-type discharge lamp and selective filtering, and the others resulted from having iron at a concentration of at least 1 percent in each sample. The latter requirement represented a nuisance value and limited the determinations of iron in the analytical scheme. As work progressed, it became apparent that the reading-number differences between given lines, even from the first to last lines in a spectrum, tended to be the same. Differences that did exist showed a definite pattern rather than random scatter, suggesting that the precision of the system, including the spacing of the microphotometer measurements, was of such a high order as to make the many-iron-fiducial-line procedure superfluous.

The differences in the length of a spectrum referred to above may be thought of as a "stretching" error. Temperature changes of either the spectrograph or the microphotometer, or both, could produce errors of this kind. However, the source of this stretching error was found to be mainly mechanical, in the spectrograph, arising from a failure of the photographic plate to slide in a fixed plane as it is racked from spectrum to spectrum. Adjustment of the plateholder reduced this problem to a tolerable level. The residual mechanical error and the plate-to-plate temperature errors are effectively diminished by the use of two cadmium fiducial lines as described below.

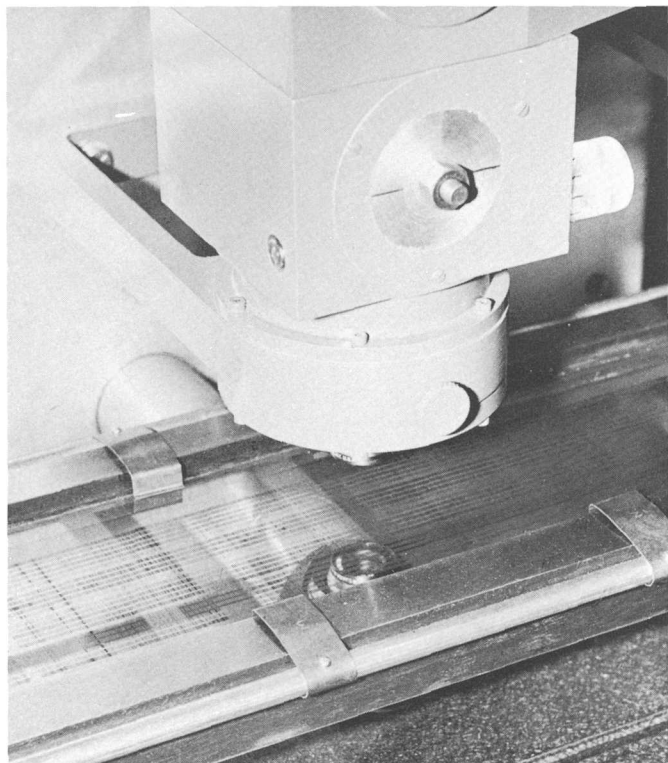
Cadmium fiducial lines are recorded in each spectrum with the use of a 19-mm-diameter cylindrical mask mounted as close as possible to the focal plane of the spectrograph. As diagramed in figure 7, there are three positions. When set in



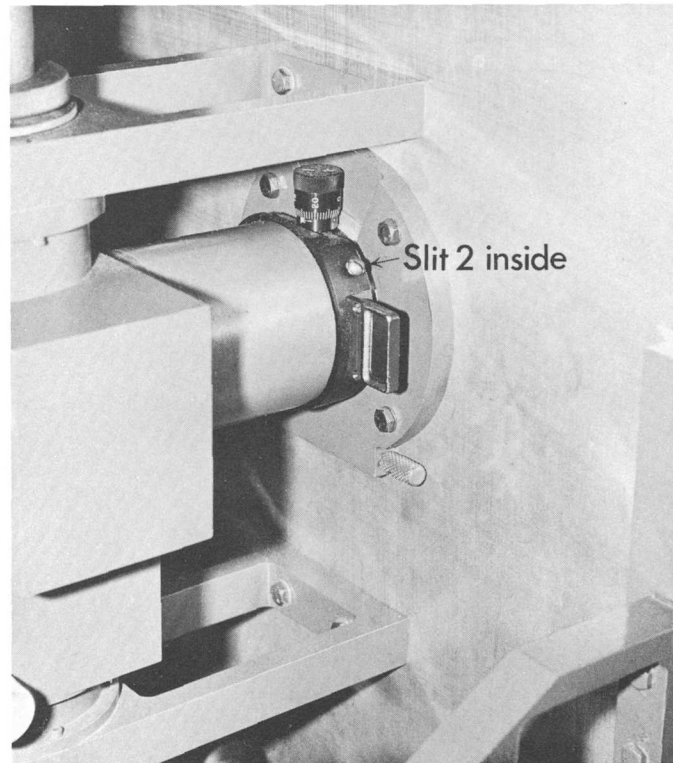
A



C



B



D

Figure 4.—Front of optical support panel of microphotometer. A, With spectrum plate in position. B, Closeup view of central part of A. C, Edge of plateholder and the two Micro-Tessar lenses. D, Exit slit.

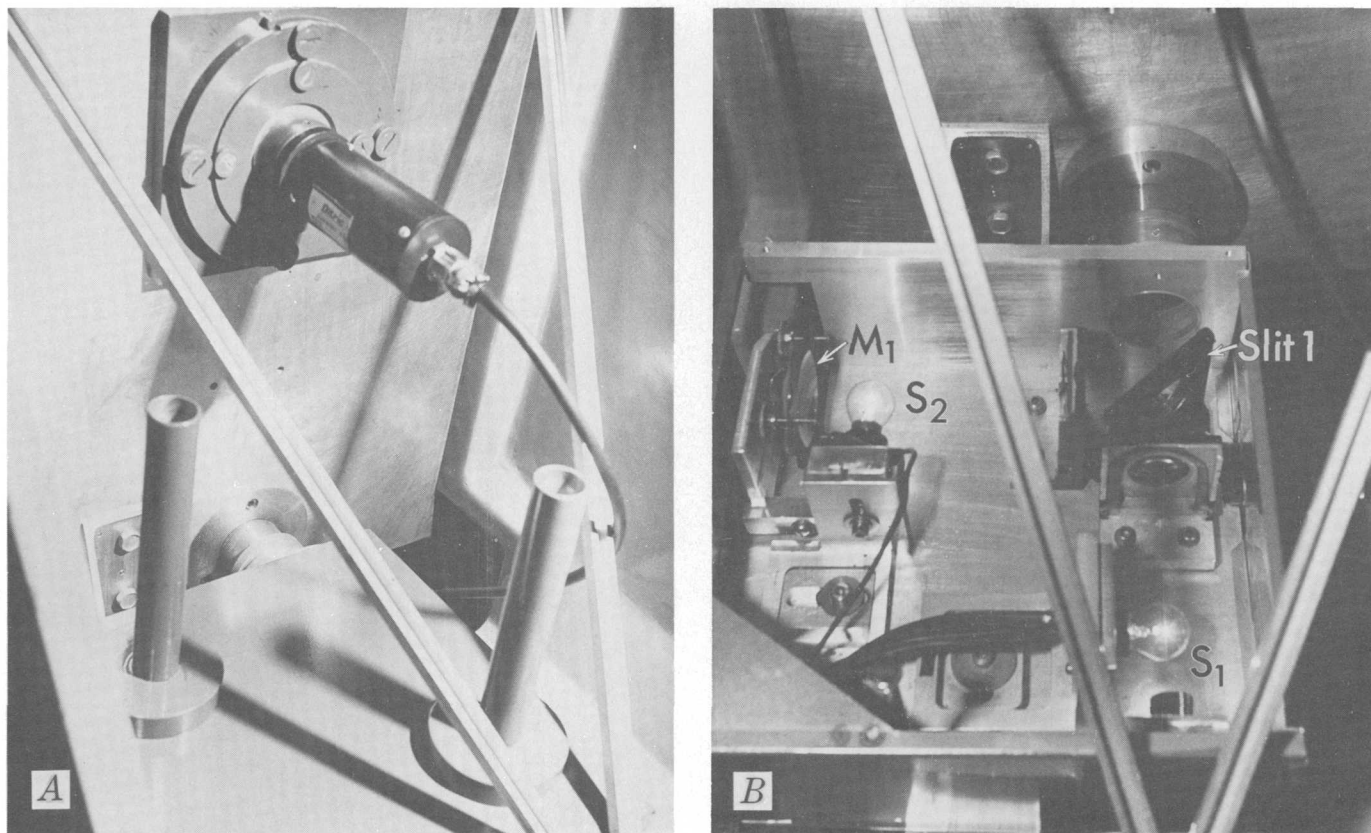


Figure 5.—Rear of optical support panel of microphotometer. *A*, The photopickup (4¼ inches long) is at the top center. The light-source section, at the bottom, is covered and has chimneys directly over the lamps for convection ventilation. *B*, A view of the box with its cover removed. The box is 10 inches square.

position 1 the entire spectral range may be exposed except for two 4-mm-wide spectral ranges, each about 20 Å. Position 2 of the mask excludes from exposure all the spectrum except the same two narrow ranges. Position 3 differs from position 1 only in height of the openings. Position 1, 4 mm high, is used for iron two-step plate-calibration exposures; position 3, 2 mm high, is used for sample exposures. With this device Cd 2748.58-Å and Cd 4415.70-Å lines may be placed in small clear areas in each sample spectrum in exact wavelength relation to the sample lines. After the plateholder has been racked to a new position, it is exposed to cadmium radiation from an Osram-type cadmium lamp for 20 seconds through position 2 of the mask, thus exposing the photographic plate through the two small windows. A solenoid, timer-operated mirror facilitates this procedure. The mask is then rotated to position 3 for exposing a sample spectrum. Special care is taken to eliminate any disturbance of the position of the spectrum and the photographic plate between the cadmium and sample exposures.

The two cadmium lines are clearly identifiable because of the elimination of spectral background in their immediate vicinity; they are easily and uniquely located by the computer. The wide wavelength spread between the two cadmium lines

assures precise data for stretching correction in the computer line-finding calculations. Using the two cadmium lines as described above has the additional advantage of maintaining precision, inasmuch as the intensities of the cadmium lines and their spectral background are under control and independent of the sample spectrum.

PHOTOGRAPHIC PLATE PROCESSING

Specially constructed plate processing, washing, and drying apparatus is required because of the 508-mm length of the spectral plates. A developing tank (fig. 8) is made of acrylic plastic sheets except for a stainless steel separator between the developer and stop-bath sections. The photographic plate is lowered into the long thin tank compartments endwise with stainless steel strips (not shown). Small volume of developing solution (450 ml), good stirring, and temperature control are basic requirements. Fixer and stop-bath solutions are circulated through heat exchangers in an external thermostatically controlled bath. The developing solution is in thermal contact with the stop bath by means of the stainless steel separator; temperature uniformity and stirring of the developer is accomplished with a gaseous burst. Nitrogen is introduced at

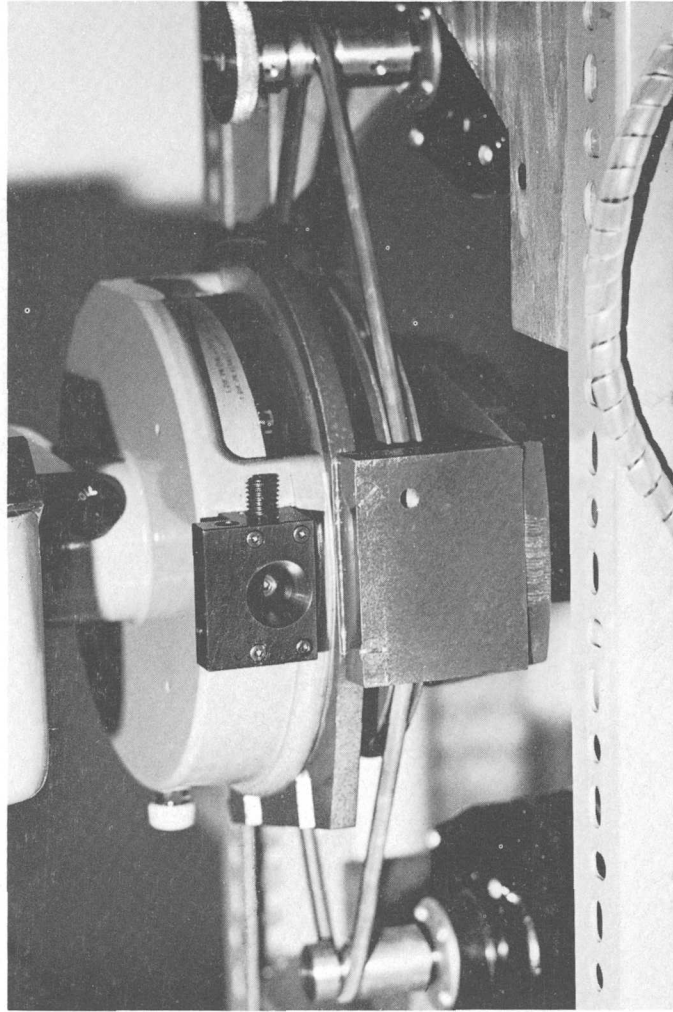


Figure 6.—Motor drive. The two a-c motors are mounted above and below the 165-mm pulley. The diameter of the central cylinder is about 6 inches.

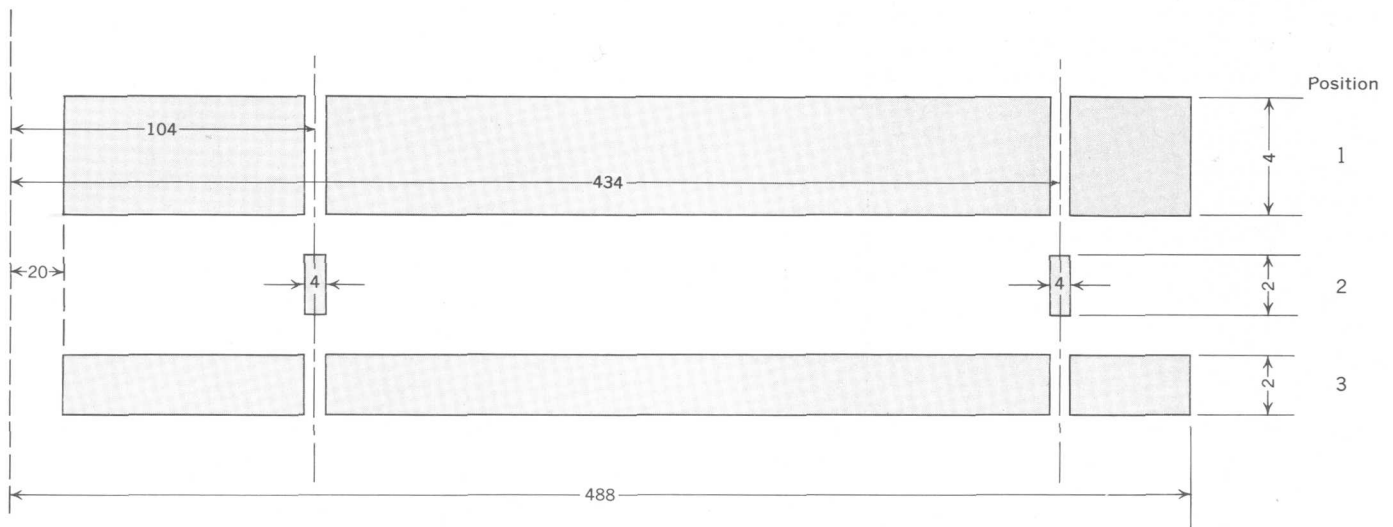


Figure 7.—Diagram showing the plan of the mask mounted on the spectrograph near the focal plane. Not drawn to scale. Dimensions in millimeters are a function of the dispersion of the particular spectrograph employed. See text for explanation.

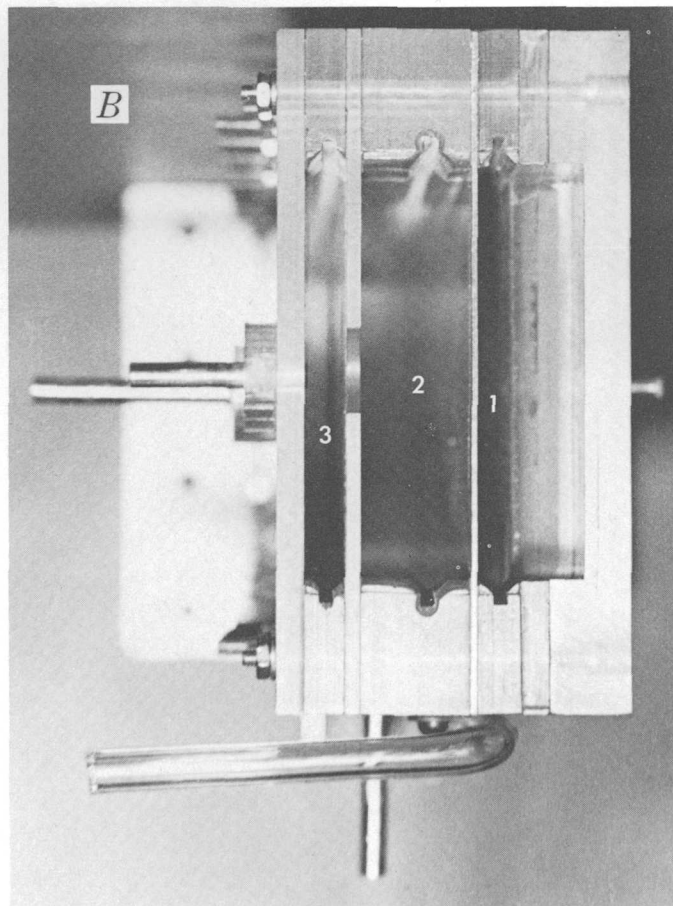
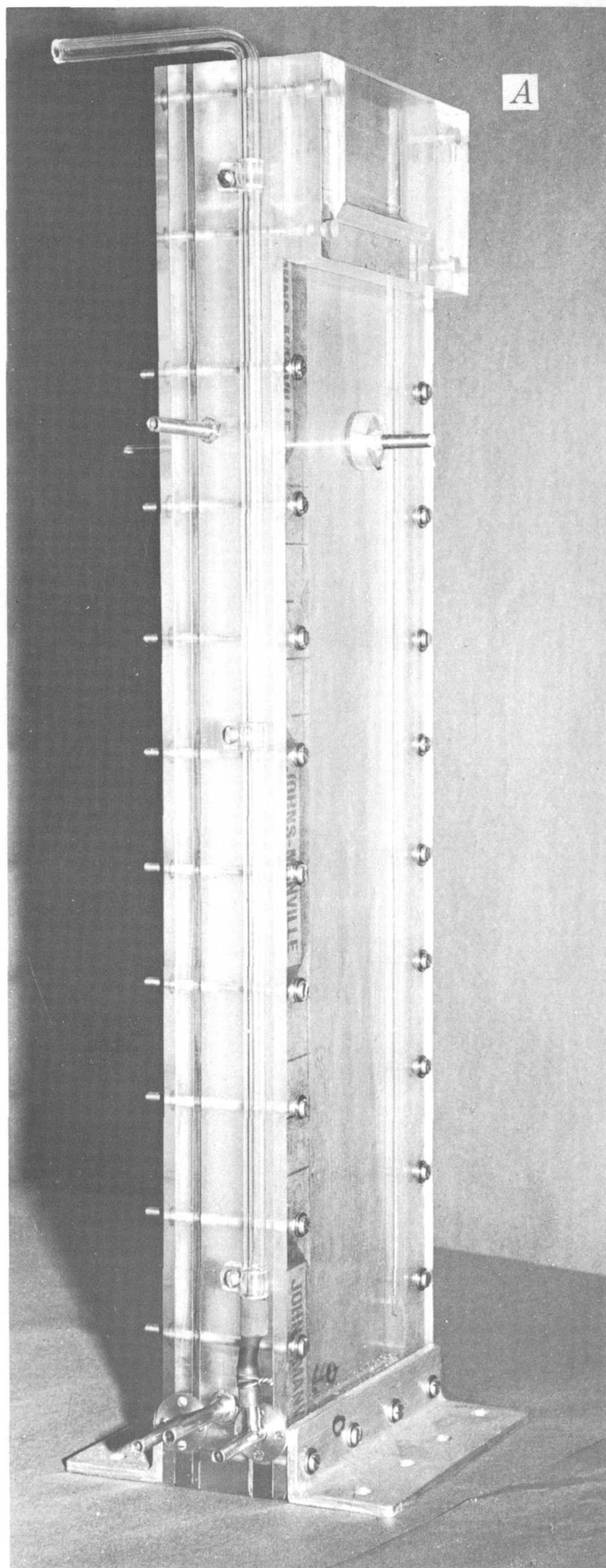


Figure 8.—Developing tank. *A*, Side view, tank is 25 inches tall. *B*, Top view. 1, Developer section; 2, stop bath; and 3, fixer. The longer dimension is 6 inches. Note in *A* and *B* that the developer section is widened near the top to prevent overflow from gaseous burst.

the top level of the tank and flows down the glass tube to the bottom where it is connected to a stainless steel "bubble" tube extending across the bottom of the tank and about 38 mm below the end of the photographic plate. Essential to proper stirring, the gas is allowed to escape to the atmosphere through an alternate vent at a constant carefully adjusted rate with enough impedance in the line to hold the liquid level in the glass tube near the bottom—just short of escaping into the developing solution. This quiet part of the cycle is timed for 8 seconds. A 2-second stirring phase obtains when a solenoid cuts off the escaping gas.

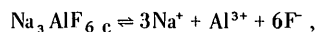
REFERENCES CITED

- Dorzapf, A. F., Jr., 1973, Spectrochemical computer analysis—argon-oxygen d-c arc method for silicate rocks: U.S. Geol. Survey Jour. Research (In press).
- Helz, A. W., Walthall, F. G., and Berman, Sol, 1969, Computer analysis of photographed optical emission spectra: *Appl. Spectroscopy*, v. 23, no. 5, p. 508–518.
- Walthall, F. G., 1973, Spectrochemical computer analysis—program description: U.S. Geol. Survey Jour. Research (In press).

SOLUBILITY OF CRYOLITE AT 25°C AND 1 ATMOSPHERE PRESSURE

By C. E. ROBERSON and J. D. HEM, Menlo Park, Calif.

Abstract.—For natural cryolite from Greenland the activity product for the reaction (in water),



was found to be $10^{-34.3 \pm 0.1}$. This is in good agreement with earlier work in which equilibrium was approached from supersaturation.

Synthetic cryolite is easily prepared at 25°C and 1 atmosphere pressure from solutions containing suitable concentrations of Na^+ , Al^{3+} , and F^- (Roberson and Hem, 1968, 1969). Equilibrium was postulated after repeated analysis of the solutions showed that the ion activity products remained constant for many months. The crystalline precipitate was identified by X-ray diffraction. It is always desirable in solubility studies, however, to approach equilibrium from both supersaturation and undersaturation. This report describes the latter approach using natural cryolite from Ivigtut, Greenland, as starting material.

Acknowledgments.—We thank our colleagues of the U.S. Geological Survey: Robert Schoen for X-ray diffraction analyses, and R. A. Gulbrandsen, C. J. Lind, and J. B. Rapp for reviewing the manuscript.

EXPERIMENTAL METHOD

The cryolite was ground by mortar and pestle and was wet sieved. The fraction between 48 and 150 mesh was washed with distilled water and dried at 110°C. After further grinding, this fraction was examined by X-ray diffraction. It consisted of well-crystallized cryolite with no impurities detected by X-ray.

Two experiments were made with weighed amounts of ground cryolite and water in polyethylene bottles. For experiment 6-19-70, 1.00 g cryolite and 500 ml distilled, deionized water were used; in experiment 3-31-71, 2.00 g cryolite and 2,000 ml distilled, deionized water were used.

The solution-solid mixtures were stored at room temperature (25±1°C) and stirred occasionally during the first few days. Periodically, pH and activities for Na^+ and F^- were

measured by use of electrodes. Total aluminum and sodium concentrations were determined by atomic absorption spectrophotometry. Total fluoride concentrations were measured by either a colorimetric method or by means of a specific-ion electrode method (Brown and others, 1970, p. 90, 93).

RESULTS AND DISCUSSION

Portions of the solutions from experimental runs 6-19-70 and 3-13-71 were filtered through plastic membranes with 0.1- μm pore diameter and were analyzed at various times for 17 months and 11 months, respectively. Analytical data and calculated values for pAl and K_{S0} are shown in table 1. The terms "pH," "pF," "pNa," and "pAl" represent $-\log [i]$ where $[i]$ represents activities of H^+ , F^- , Na^+ , or Al^{3+} . The equilibrium constant K_{S0} is for zero ionic strength. The electrodes used for measuring pH and pF were calibrated with standards of known activities. Values for pNa for all but the first entry in table 1 were calculated from activity coefficients for Na^+ obtained from the Debye-Hückel equation (Klotz, 1964, p. 419) and stoichiometric concentrations of Na^+ . For the first set of data (table 1), pNa was measured with a sodium-ion electrode. Our particular pNa electrode did not perform satisfactorily for the later measurements.

Because most of the dissolved aluminum is in the form of fluoride complexes rather than free aluminum ion Al^{3+} , the activity of Al^{3+} at 25°C and 1 atmosphere total pressure is calculated by means of the array of chemical equilibria and stoichiometric summarizations (Roberson and Hem, 1969, p. C3) given in equations 1 through 12. Values for $[\text{Al}^{3+}]$ can be calculated directly after substituting into equation 1 the expressions described by equations 4 through 12 and using the measured molal concentration of aluminum (C_{Al}) and measured pH and pF. In addition, one needs a measure of ionic strength for calculation of activity coefficients (γ_i). The ionic strength in these solutions is taken as approximately equal to the total sodium-ion concentration, C_{Na} . The calculations are readily performed by electronic computer.

The equilibrium constant K_{S0} for the thermodynamic solubility of cryolite is:

$$K_{S0} = [\text{Na}^+]^3 [\text{Al}^{3+}] [\text{F}^-]^6$$

Table 1.—Analytical data, calculated activities of aluminum, and thermodynamic solubility products of cryolite

[C _{Na} and C _{Al} , molal concentrations of Na ⁺ and Al ³⁺ , respectively]							
Age of precipitate	C _{Na} (total)	pH	pNa ^a	pF	C _{Al} (total)	pAl ^b	log K _{S0}
Experiment 6-19-70							
40 days		6.56	3.27	2.37	1.63×10 ⁻³	13.22	-37.25
8 months	5.57×10 ⁻³	5.89	2.28	2.39	1.85×10 ⁻³	13.11	-34.29
14 months	5.43×10 ⁻³	5.86	2.30	2.37	1.96×10 ⁻³	13.16	-34.28
17 months	5.57×10 ⁻³	5.55	2.28	2.38	1.78×10 ⁻³	13.17	-34.29
Experiment 3-31-71							
3.5 months	5.52×10 ⁻³	6.03	2.29	2.40	1.93×10 ⁻³	13.06	-34.33
7.5 months	5.48×10 ⁻³	5.87	2.29	2.39	1.63×10 ⁻³	13.17	-34.38
11 months	5.22×10 ⁻³	6.48	2.31	2.36	1.78×10 ⁻³	13.24	-34.33

^aValue for pNa for 40 days was measured by sodium selective-ion electrode. Other values for pNa were calculated from a measured concentration of Na⁺ (atomic absorption) and from activity coefficients obtained from Debye-Hückel equation (Klotz, 1964, p. 419), assuming that ionic strength was approximately equal to the sodium-ion concentration.

^bCalculated -log of free Al³⁺ activity (see text).

or

$$-\log K_{S0} = 3pNa + pAl + 6pF.$$

Values for log K_{S0} are seen to be nearly constant after 3.5 to 8 months of equilibration time (table 1). The mean value, considering all points except the first where equilibrium had not been reached, is -34.3±0.1.

Equations 1-12, referred to in preceding paragraphs

$$C_{Al} = \frac{[Al^{3+}]}{\gamma_{Al^{3+}}} + \frac{[AlOH^{2+}]}{\gamma_{AlOH^{2+}}} + \frac{[Al(OH)_4^-]}{\gamma_{Al(OH)_4^-}} + \frac{[AlF^{2+}]}{\gamma_{AlF^{2+}}} + \frac{[AlF_2^+]}{\gamma_{AlF_2^+}} + \frac{[AlF_3^0]}{\gamma_{AlF_3^0}} + \frac{[AlF_4^-]}{\gamma_{AlF_4^-}} + \frac{[AlF_5^{2-}]}{\gamma_{AlF_5^{2-}}} + \frac{[AlF_6^{3-}]}{\gamma_{AlF_6^{3-}}}, \text{ and} \quad (1)$$

$$C_F = \frac{[F^-]}{\gamma_{F^-}} + \frac{[HF^0]}{\gamma_{HF^0}} + \frac{[AlF^{2+}]}{\gamma_{AlF^{2+}}} + \frac{2[AlF_2^+]}{\gamma_{AlF_2^+}} + \frac{3[AlF_3^0]}{\gamma_{AlF_3^0}} + \frac{4[AlF_4^-]}{\gamma_{AlF_4^-}} + \frac{5[AlF_5^{2-}]}{\gamma_{AlF_5^{2-}}} + \frac{6[AlF_6^{3-}]}{\gamma_{AlF_6^{3-}}}, \quad (2)$$

where

$$[HF^0] = [H^+][F^-] 10^{3.17}, \quad (3)$$

$$[AlOH^{2+}] = 10^{9.23} [Al^{3+}][OH^-], \quad (4)$$

$$[Al(OH)_4^-] = 10^{33.96} [Al^{3+}][OH^-]^4, \quad (5)$$

$$[OH^-] = 10^{-14.00} [H^+]^{-1}; [H^+] = 10^{pH}, \quad (6)$$

$$[AlF^{2+}] = 10^{7.01} [Al^{3+}][F^-], \quad (7)$$

$$[AlF_2^+] = 10^{12.75} [Al^{3+}][F^-]^2, \quad (8)$$

$$[AlF_3^0] = 10^{17.02} [Al^{3+}][F^-]^3, \quad (9)$$

$$[AlF_4^-] = 10^{19.72} [Al^{3+}][F^-]^4, \quad (10)$$

$$[AlF_5^{2-}] = 10^{20.91} [Al^{3+}][F^-]^5, \text{ and} \quad (11)$$

$$[AlF_6^{3-}] = 10^{20.86} [Al^{3+}][F^-]^6. \quad (12)$$

In the present study, equilibrium was approached from undersaturation. In earlier work (Roberson and Hem, 1968, 1969), equilibrium was approached from supersaturation, including experiments where cryolite constituents Al³⁺ and F⁻ varied over considerable concentration ranges, and a value for log K_{S0} of -33.84 was obtained. Therefore we believed that equilibrium was closely approached in both series of experiments. The experimental uncertainty introduced by possible impurities in the solids, particle-size effects, and the magnification of analytical errors introduced by the large exponents in the solubility equilibrium equation is at least as great as the difference in the solubility products.

As a further test, the dissolution Na₃AlF₆ c = 3Na⁺ + Al³⁺ + 6F⁻ was reversed by adding sodium fluoride solution to a filtered portion of the solution from experiment 3-31-71. The entry in table 1 for 11 months for experiment 3-31-71 represents the composition of the solution before adding sodium fluoride. To 250 ml of solution, separated from the

cryolite by filtration through a membrane of 0.1- μ m porosity, 5.21 ml of 0.50 *m* NaF was added initially and then, because no precipitate was visually observed after 5 days, 5.00 ml more of 0.50 *m* NaF was added. After 9 days from the time the first fluoride was added, a portion of the solution was filtered and a considerable amount of solid was retained on the filter. X-ray examination revealed the precipitate to be cryolite. The fact that no precipitate was observed after the first addition was probably because the crystals were very small and the index of refraction of cryolite is so near that of water.

The analytical data for the solution phase before and after adding sodium fluoride are shown below:

	Before sodium fluoride	After sodium fluoride
pH	6.48	6.60
pNa	2.29	1.76
pF	2.36	1.77
C_{Na}	5.22×10^{-3}	Not determined.
C_{Al}	1.78×10^{-3}	See text.
C_F	Not determined.	2.08×10^{-2}

The increased activities of Na^+ and F^- , caused by adding sodium fluoride, had decreased the aluminum concentration (C_{Al}) to such a low level that it could no longer be detected by atomic absorption (detection limit about 7.4×10^{-5} mol/l). The colorimetric method (Brown and others, 1970, p. 44) was unsuitable because of fluoride interference. However, one can calculate $[Al^{3+}]$ using measured parameters pH, pF, C_F , and ionic strength with equation 2 along with equations 3 and 7 through 12. This calculation rests on the assumptions that the difference between C_F and $\frac{[F^-]}{\gamma_{F^-}}$ is the result of complexing of fluoride with hydrogen and aluminum and that no aluminum complexes other than fluoride species are significant. For solutions having the composition and pH observed here, these are valid assumptions (Hem, 1972, p. 131). The calculation gives $[Al^{3+}] = 10^{-16.39}$. The value finally obtained for log

K_{S0} for cryolite is -32.30. This is considerably larger than the value obtained in earlier precipitation experiments ($10^{-33.84}$) but such an effect is to be anticipated because of the short (9-day) aging period. A longer aging period can be expected to give a lower solubility, as the crystals increase in size.

Incidentally this experiment demonstrates the feasibility of using the fluoride electrode (together with pF, pH, C_F , and ionic strength) to determine aluminum in certain types of solutions. The accuracy of the determination is adversely affected here, however, because the amount of fluoride complexed is small compared to the total fluoride concentration. The difference between calculated K_{S0} values may be partly the result of this factor.

CONCLUSION

Data of this report are compared with earlier solubility measurements (Roberson and Hem, 1968, 1969) and show that the solubility of natural cryolite is very close to that of the synthetic product which has been aged for a few months. The activity product constant for the solubility (K_{S0}) of natural and synthetic cryolite can therefore be represented by $10^{-34.0 \pm 0.3}$.

REFERENCES CITED

- Brown, Eugene, Skougstad, M. W., and Fishman, M. J., 1970, Methods for collection and analysis of water samples for dissolved minerals and gases: U.S. Geol. Survey Techniques Water-Resources Inv., book 5, chap. A-1, 160 p.
- Hem, J. D., 1972, Graphical methods for representing form and stability of aqueous metal ions: Chem. Geology, v. 9, p. 119-132.
- Klotz, I. M., 1964, Chemical thermodynamics: New York, W. A. Benjamin, Inc., 468 p.
- Roberson, C. E., and Hem, J. D., 1968, Activity product constant of cryolite at 25°C and 1 atmosphere using selective-ion electrodes to estimate sodium and fluoride activities: Geochim. et Cosmochim. Acta, v. 32, p. 1343-1351.
- 1969, Solubility of aluminum in the presence of hydroxide, fluoride, and sulfate: U.S. Geol. Survey Water-Supply Paper 1827-C, 37 p.



HYDROLOGIC CHANGES AFTER CLEAR-CUT LOGGING IN A SMALL OREGON COASTAL WATERSHED

By. D. D. HARRIS, Portland, Oreg.

Abstract.—Preliminary graphical analysis indicates that clear-cut logging of a small Oregon watershed has significantly altered certain hydrologic characteristics. After logging, moderate increases were noted in annual runoff, but no significant changes were detected in either peak or minimum flow rates. Both the annual sediment yields and the maximum monthly water temperatures increased greatly after logging; sediment yields and temperatures in the unlogged control watershed actually decreased during the postlogging period.

In 1957 a research study was begun by the Oregon Governor's Committee on Natural Resources to examine the impact of different patterns of logging on stream environment. One aspect of the study was to investigate effects of clear-cut logging on the hydrology of small streams. The U.S. Geological Survey was asked to do this particular part of the study.

To make this preliminary evaluation of logging effects, a graphical analysis was used rather than a rigorous statistical analysis of the limited postlogging data. Data will continue to be collected through the 1973 water year. The postlogging period will then coincide in length with the 7-year prelogging period. After 1973, a thorough and detailed evaluation of changes will be made with more precise study methods than those described in this report.

A small watershed, Needle Branch, in the Alsea River basin was clear cut to evaluate the effects of this logging practice on stream hydrology. Another small watershed, Flynn Creek, was used as the control watershed for comparing prelogging and postlogging hydrologic characteristics. The study watersheds are shown on the map in figure 1. The two watersheds, both of which cover less than a square mile and have the same general orientation, provide a reasonable comparison to evaluate the effects of logging.

Needle Branch has a drainage area of 0.27 sq mi (175 acres). The forest cover was 85 percent Douglas-fir and 15 percent alder and vine maple. Thirty-two acres in the headwaters had been logged in the early 1950's. The grade of sidehill slopes averages about 37 percent.

Flynn Creek has a drainage area of 0.78 sq mi (502 acres). Forest cover is about 70 percent alder and 30 percent Douglas-fir. The grade of sidehill slopes averages about 34 percent.

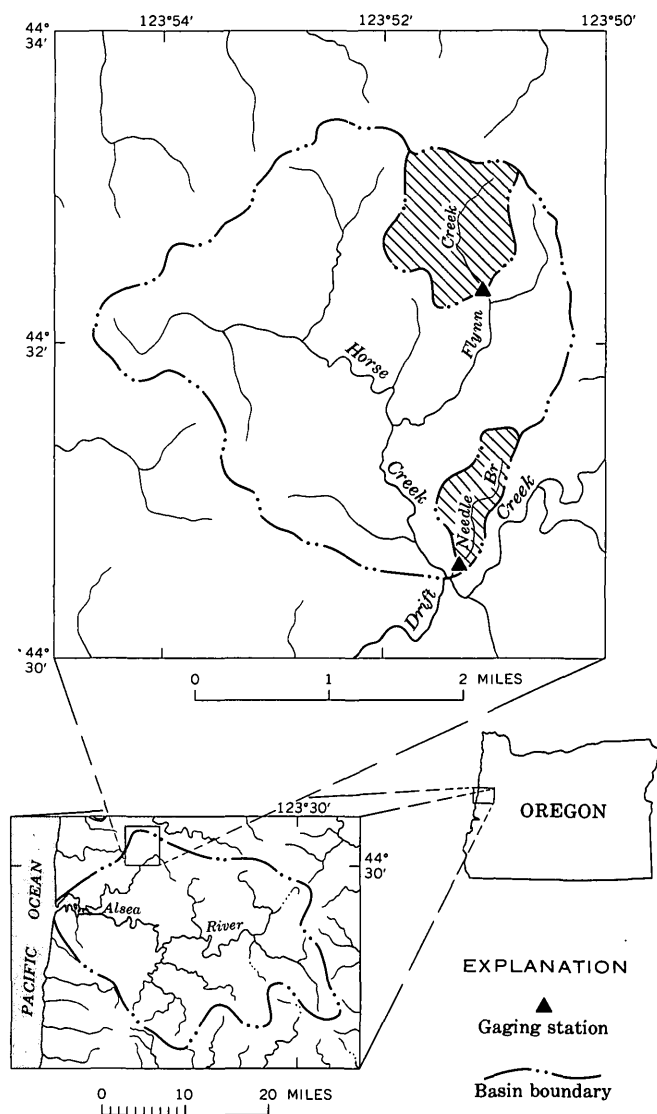


Figure 1.—Location of study watersheds (patterned) in Alsea River basin, Oregon.

DATA COLLECTED AND METHOD OF STUDY

Measurements of streamflow, sediment concentration, and water temperature near the mouths of the two study streams

provided the data needed to evaluate change in their hydrologic characteristics. The records were collected at U.S. Geological Survey gaging stations, each equipped with concrete weir controls.

The study was intended to define the hydrologic characteristics of the streams for the prelogging period, 1958-65 (Harris and Williams, 1971), to compare with those for the postlogging period. The principal study method used was to relate streamflow, sediment yield, and water temperature of Needle Branch to those of Flynn Creek, the control stream. Regression lines of prelogging relations were developed for each hydrologic characteristic evaluated. Prediction limits at the 95-percent level were computed for the regressions to assess the significance of changes. The 95-percent prediction limits show the limits outside of which there is 95 percent confidence that a change has occurred. If postlogging values plot outside the prediction limits, the change resulting from logging can be considered significant.

Data for 4 years after logging, 1967-70, were compared to the prelogging relations. Because roadbuilding and logging were done throughout most of 1966, that year was not used in the evaluation.

EVALUATION OF CHANGES IN HYDROLOGIC CHARACTERISTICS

To isolate the effects of logging on streamflow, sediment yield, and water temperature, the areal distribution of precipitation must be consistent over the two watersheds. Therefore, a relation between cumulative precipitation was prepared (fig. 2) from data collected near each of the two

stream-gaging stations to assure that no change in precipitation distribution occurred before or after logging. Precipitation data were available only into 1968, but the relation does indicate no change in general weather pattern after logging.

Changes in annual runoff, peak and low flows, sediment discharge, and water temperature were studied to provide a comparison of before- and after-logging characteristics. Annual runoff in inches from the two study basins for water years 1959-70 is shown in table 1. The table is divided into prelogging and postlogging periods. A comparison of annual runoff of Flynn Creek and Needle Branch during the prelogging and postlogging periods is shown in figure 3. A relation of

Table 1.—Annual runoff, in inches, for the prelogging and postlogging periods

Water year	Flynn Creek	Needle Branch
Prelogging period		
1959	78.60	84.04
1960	72.18	69.55
1961	93.30	85.56
1962	66.45	61.61
1963	69.17	62.83
1964	77.21	75.28
1965	87.07	80.80
Mean	77.71	74.24
Postlogging period		
1967	75.74	86.98
1968	68.01	85.55
1969	86.70	106.93
1970	61.77	80.51
Mean	73.06	89.99

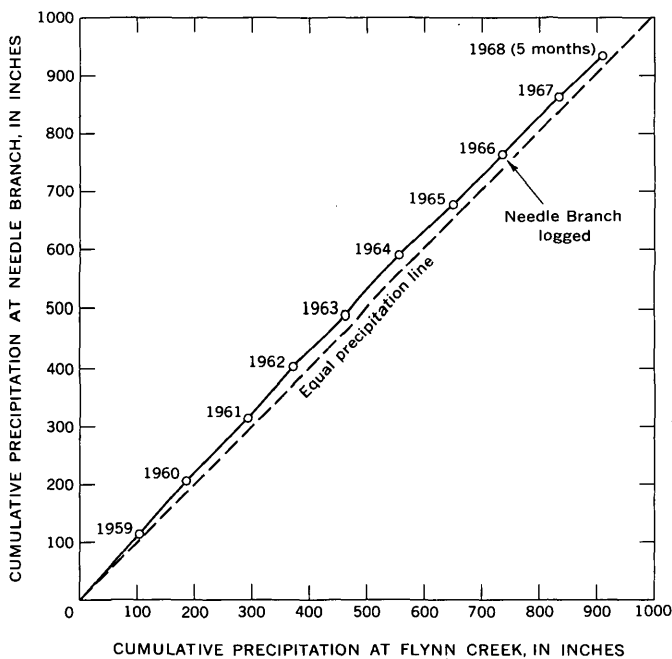


Figure 2.—Relation of cumulative annual precipitation at Needle Branch gage to that at Flynn Creek gage.

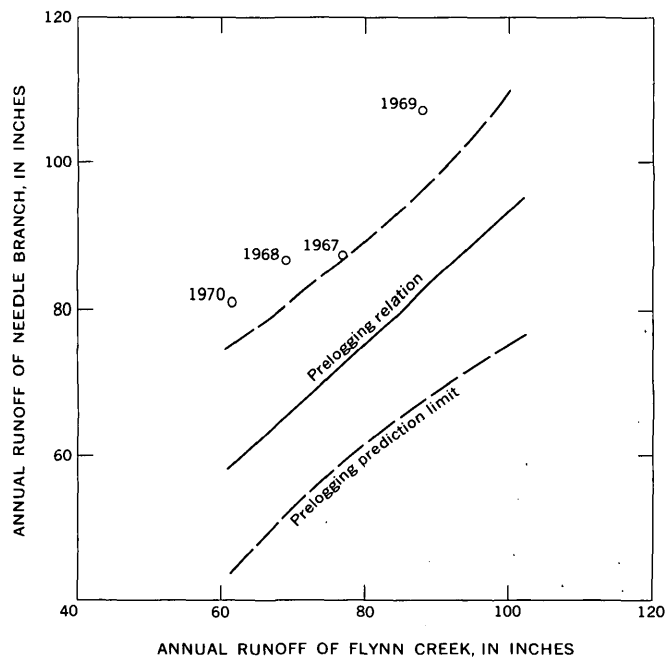


Figure 3.—Relation of annual runoff of Needle Branch to that of Flynn Creek.

cumulative runoff for the two watersheds is shown in figure 4. From table 1 and figures 3 and 4, it is evident that annual runoff in the clear-cut watershed has increased significantly since logging. The 7-year average runoff prior to logging was 3 inches less on Needle Branch than on Flynn Creek, whereas in

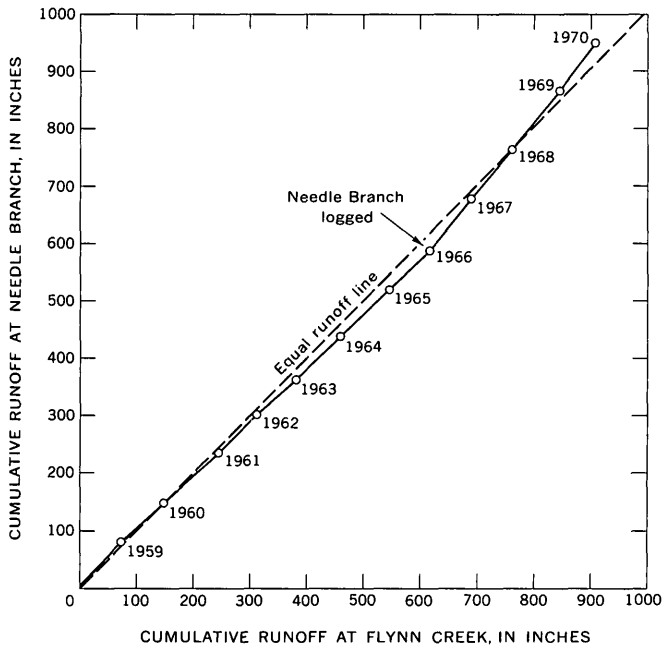


Figure 4.—Relation of cumulative annual runoff of Needle Branch to that of Flynn Creek.

the 4 years after logging Needle Branch averaged 16 inches more runoff than did Flynn Creek.

Peak flows for the prelogging and postlogging periods for the two study streams are listed in table 2. The regression of prelogging peak flows in comparison to postlogging peak flows is shown in figure 5. The peak flows show some increase after logging, but the increases may not be statistically significant.

Minimum flows for the prelogging and postlogging periods were compared by using the minimum daily flows of each September, a month with normally low flows. Minimum daily September flows on Flynn Creek and concurrent daily flows for Needle Branch are shown in table 3. No regression analysis was made for low flows because the small changes could not be detected easily by use of that method. The table does, however, indicate a small increase in low flow since logging.

Annual sediment yields for the prelogging and postlogging periods for the two study streams are listed in table 4. Figure 6 shows postlogging sediment yield compared to the prelogging regression line and the prediction limit. It is evident that sediment yields have increased significantly since logging. However, it is apparent that annual sediment yields are gradually diminishing toward prelogging conditions. The large and abrupt increase in sediment yield immediately after logging and the gradual return toward prelogging conditions

Table 2.—Concurrent peak discharge rates on Flynn Creek and Needle Branch for all Flynn Creek peaks exceeding 50 cfs per sq mi

Water year	Date	Flynn Creek		Needle Branch	
		(cfs)	(cfs per sq mi)	(cfs)	(cfs per sq mi)
Prelogging period					
1959	Jan. 9	53	67.9	22	81.5
	Jan. 27	42	53.8	19	70.4
1960	Feb. 9	43	55.1	20	74.1
1961	Nov. 24	78	100.0	33	122.2
	Feb. 10	64	82.1	28	103.7
	Feb. 13	47	60.3	18	66.7
1962	Nov. 22	46	59.0	29	107.4
	Dec. 19	41	52.6	18	66.7
	Dec. 20	43	55.1	17	63.0
1963	Nov. 26	65	83.3	28	103.7
1964	Jan. 19	63	80.8	28	103.7
	Jan. 25	40	51.3	17	63.0
1965	Dec. 1	43	55.1	17	63.0
	Dec. 22	90	115.4	32	118.5
	Jan. 28	137	175.6	50	185.2
Mean			76.5		92.9
Postlogging period					
1967	Jan. 27	70	89.7	33	122.2
1968	Feb. 19	45	57.7	25	92.6
1969	Dec. 4	45	57.7	24	88.9
	Dec. 10	43	55.1	24	88.9
	Jan. 7	41	52.6	20	74.1
1970	Jan. 18	50	64.1	25	92.6
	Jan. 23	43	55.1	22	81.5
	Jan. 27	45	57.7	19	70.4
Mean			61.2		88.9

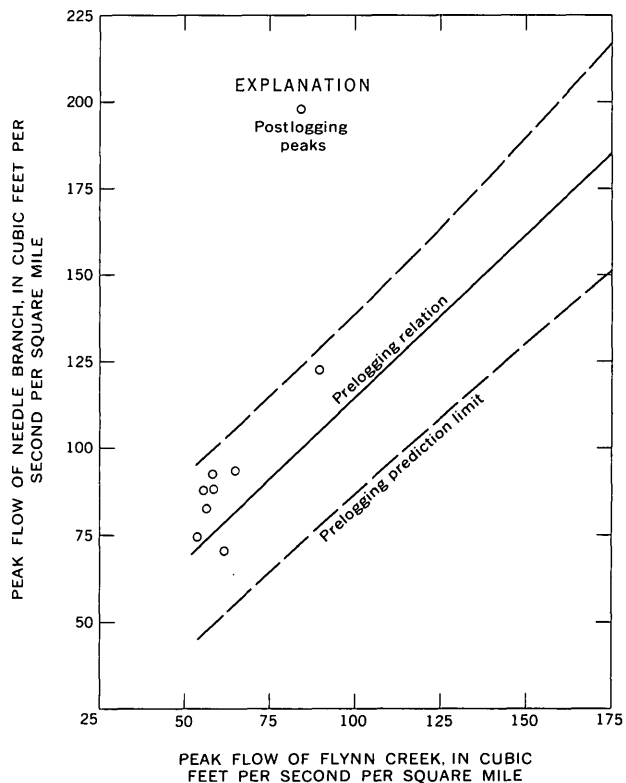


Figure 5.—Relation of peak flow of Needle Branch to that of Flynn Creek.

Table 3.—Minimum daily September flows of Flynn Creek and concurrent flows of Needle Branch, in cubic feet per second

Water year	Flynn Creek	Needle Branch
Prelogging period		
1959	0.36	0.11
196014	.02
196120	.02
196220	.02
196322	.06
196422	.03
196512	.01
Mean	¹ .21	² .04
Postlogging period		
1967	0.09	0.02
196835	.14
196918	.04
197014	.02
Mean	³ .19	⁴ .06

¹ 0.27 cfs per sq mi. ² 0.15 cfs per sq mi.
³ 0.24 cfs per sq mi. ⁴ 0.22 cfs per sq mi.

Table 4.—Annual sediment yields of the two watersheds, in tons per square mile

Water year	Flynn Creek	Needle Branch
Prelogging period		
1959	88	59
1960	65	41
1961	338	186
1962	138	141
1963	114	117
1964	226	184
1965	1,270	430
Mean	320	165
Postlogging period		
1967	131	905
1968	66	490
1969	142	515
1970	114	232
Mean	113	536

are evident in the relation of cumulative sediment yields shown in figure 7.

Figure 8 shows maximum monthly water temperatures for the postlogging period compared to the prelogging maximum temperature regression and the prediction limits. It is evident from this illustration that water temperatures have increased greatly since logging. However, during the postlogging period, water temperatures have decreased each year toward those of the prelogging period.

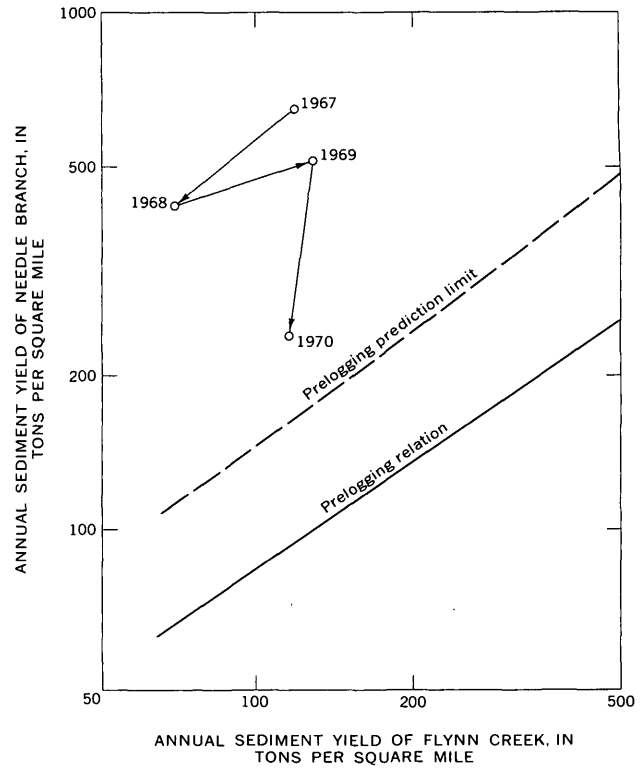


Figure 6.—Relation of annual sediment yield of Needle Branch to that of Flynn Creek.

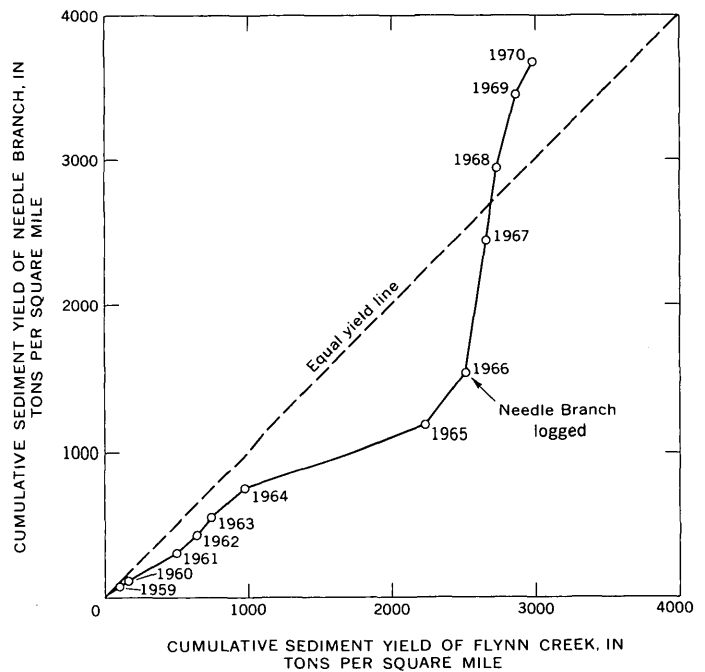


Figure 7.—Relation of cumulative annual sediment yield of Needle Branch to that of Flynn Creek.

SUMMARY

Preliminary study of the effects of clear-cut logging of a small watershed on the Oregon coast indicates that some large and some small changes have occurred in hydrologic characteristics of the stream draining the watershed. Annual runoff has increased moderately; peak flows show a small but probably not statistically significant increase, and low flows have increased only slightly, if at all. Large and significant increases appear to have occurred in sediment yields and water

temperatures. During the postlogging period, however, the sediment yields and water temperatures appear to be decreasing each year toward those for the prelogging period.

REFERENCE CITED

Harris, D. D., and Williams, R. C., 1971, Streamflow, sediment-transport, and water-temperature characteristics of three small watersheds in the Alsea River basin, Oregon: U.S. Geol. Survey Circ. 642, 21 p.

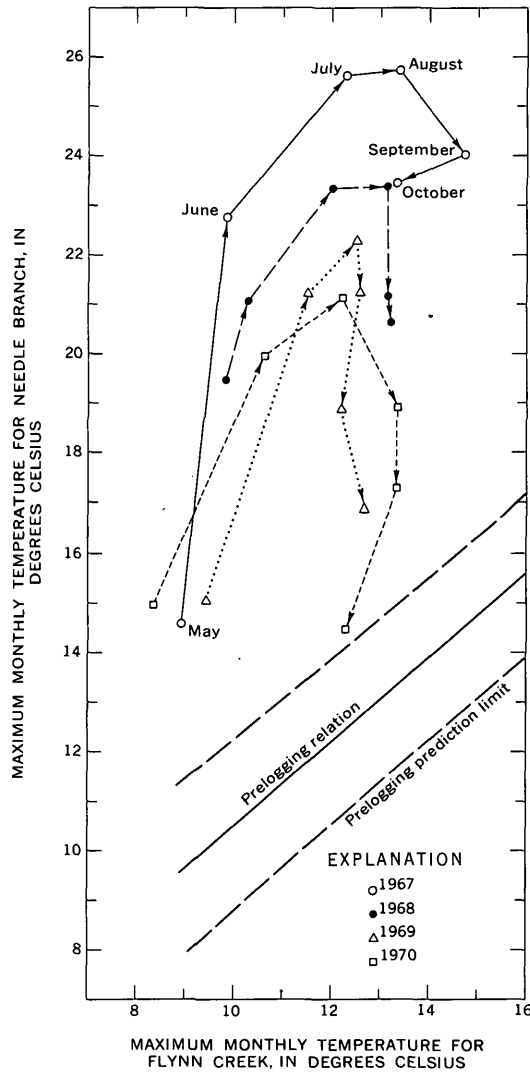


Figure 8.—Relation of maximum monthly water temperature of Needle Branch to that of Flynn Creek.



APPLICATION OF THE SOURCE-AREA CONCEPT OF STORM RUNOFF TO A SMALL ARIZONA WATERSHED

By F. E. ARTEAGA¹ and S. E. RANTZ,
Davis, Calif., Menlo Park, Calif.

Abstract.—An attempt to demonstrate the source-area concept of storm runoff by analysis of the rainfall-runoff relation for the watershed of Queen Creek tributary in south-central Arizona was moderately successful. The demonstration was somewhat marred by the necessity to make several simplifying assumptions to eliminate some of the many basin variables of unknown magnitude. The percentage of watershed contributing storm runoff was related to total rainfall received—that is, antecedent and storm rainfall—on the assumption that the availability of rainfall excess from any subarea was dependent on the saturation, or near saturation, of a permeable upper layer of soil. An average unit hydrograph was used for all computed sizes of the runoff-contributing area.

During the past decade several hydrologic studies have been reported in support of the source-area concept of storm runoff. That principle, in effect, states that even during intense basinwide storms, only certain areas in a watershed—source areas—contribute storm runoff. The remaining areas are noncontributing because they can support infiltration and subsequent percolation at rates that usually exceed the rainfall intensities that are experienced. The results reported by some investigators (for example, Ragan, 1967; Dunne and Black, 1970) provide evidence that the source area is usually constant and is confined to the vicinity of the stream channel. The results reported by others (for example, Whipkey, 1965; Hewlett and Hibbert, 1967) indicate a more variable source area that increases with total storm precipitation. The source-area concept is a reasonable one. In fact, the runoff response to storm rainfall is often difficult to explain on any other basis, as will be demonstrated in the discussion that follows on storm runoff from the watershed of Queen Creek tributary at Apache Junction in south-central Arizona.

DESCRIPTION OF WATERSHED OF QUEEN CREEK TRIBUTARY

Queen Creek tributary has a drainage area of 0.50 sq mi upstream from the site at which the stream is gaged. The

watershed, roughly rectangular in shape, is approximately 1.5 miles long, and altitudes range from 1,720 to 1,820 feet. The soil in the watershed is classed as a limy-sandy loam, and the vegetation is designated by the U.S. Soil Conservation Service as southern desert scrub. Runoff is ephemeral—there is no ground-water outflow (base flow)—and results primarily from summer convective storms of high intensity and short duration.

DISCUSSION OF AVAILABLE DATA

A recording rain gage is operated a quarter of a mile upstream from the water-stage recorder. During the years 1966–71, 11 storm-runoff events were recorded at the gages and were available for analysis. Rainfall and discharge for those events were tabulated at 5-minute intervals and are summarized in table 1. Inspection of the records showed that no runoff resulted unless rainfall occurred at a rate that exceeded 0.02 inch in a 5-minute interval. Consequently, the storm durations shown in column 4 of table 1 are for periods that started with a rainfall rate of 0.03 inch or more per 5 minutes and ended when the rainfall rate dropped below 0.03 inch per 5 minutes and rain did not resume soon after at a higher rate. It was therefore possible for a storm period to include a brief lull during which there were several 5-minute periods, each having less than 0.03 inch of recorded rainfall. Only two such storms occurred—those of August 12 and September 30, 1971.

The antecedent precipitation shown in column 3 of table 1 represents rainfall recorded prior to the beginning of runoff. For the major storm of September 30, 1971 (No. 11), the antecedent precipitation includes both the rainfall that occurred on September 30 prior to the onset of runoff-producing precipitation and the rainfall that occurred on the preceding day—there was no precipitation for weeks prior to September 29. As for the other three storms (8–10) for which antecedent precipitation is shown, there was no rainfall for many days immediately preceding the calendar dates of the storms.

All recorded runoff hydrographs were of simple shape,

¹ University of California at Davis.

Table 1.—Summary of rainfall-runoff data

Storm No.	Date of storm	Antecedent rainfall (inches)	Total storm duration (minutes)	Total storm rainfall (inches)	Observed average basinwide runoff (inches)	Average basinwide water loss (inches)	Average rainfall intensity (inches per hour)	Average rate of basinwide water loss (inches per hour)
(1)	(2)	(3)	(4)	(5)	(6)	(7)	(8)	(9)
1	Aug. 30, 1966	0	20	1.10	0.22	0.88	3.30	2.64
2	Sept. 12, 1966	0	10	.60	.15	.45	3.60	2.70
3	July 11, 1967	0	35	.77	.08	.69	1.32	1.18
4	July 3, 1968	0	40	.70	.06	.64	1.05	.96
5	Aug. 3, 1968	0	30	.91	.15	.76	1.82	1.52
6	Sept. 16, 1969	0	20	.59	.06	.53	1.77	1.59
7	Oct. 21, 1969	0	10	.46	.07	.39	2.76	2.34
8	Sept. 5, 1970	.56	50	1.26	.33	.93	1.51	1.12
9	Sept. 5, 1970	2.30	25	.64	.17	.47	1.54	1.13
10	Aug. 12, 1971	.24	65	.86	.11	.75	.79	.69
11	Sept. 30, 1971	1.28	130	2.07	.98	1.09	.96	.50

having a single peak between rising and falling limbs, except those for the storms of August 12 and September 30, 1971 (10 and 11), which had double peaks. The two storms of September 5, 1970 (8 and 9), are considered separate events because the two bursts of runoff-producing rainfall were separated by 7¼ hours, and there was no flow in the stream for more than 5 hours during the lull in precipitation. Although we will demonstrate that runoff was apparently confined to partial areas of the watershed, the inches of runoff and water loss given in table 1 and elsewhere in this report are average basinwide values, computed as though the entire watershed—0.5 sq mi—were contributing runoff. (Water loss equals rainfall minus runoff.)

ANALYSIS OF STORM-RUNOFF CHARACTERISTICS

An attempt was first made to analyze the storm data by conventional methods using, for the sake of simplicity, only storms 1–7, none of which had antecedent rainfall. In that attempt, the computation of basinwide water loss either as an average constant loss rate for all storms (average ϕ -index), or as an average time-dependent loss rate for all storms (Horton concept), gave unsatisfactory runoff results. (A description of the ϕ -index and of the Horton theory of infiltration is given in most standard hydrology texts—for example, Linsley and others, 1958, p. 164–167, 180.)

In a step preliminary to our next attempt, we averaged the values of storm rainfall and basinwide water loss (cols. 5 and 7 of table 1) over their corresponding duration periods (col. 4). The resulting average rates are given in columns 8 and 9 and are plotted in figure 1. Inspection of figure 1, again confining our attention to storms 1–7, indicates that an open-end linear relation exists between average rate of water loss and average intensity of storm rainfall, for intensities greater than 0.77 inch per hour. That lower limit of the relation is the value at which the line of relation is intersected by a 45-degree line through the origin in figure 1—water loss cannot exceed rainfall.

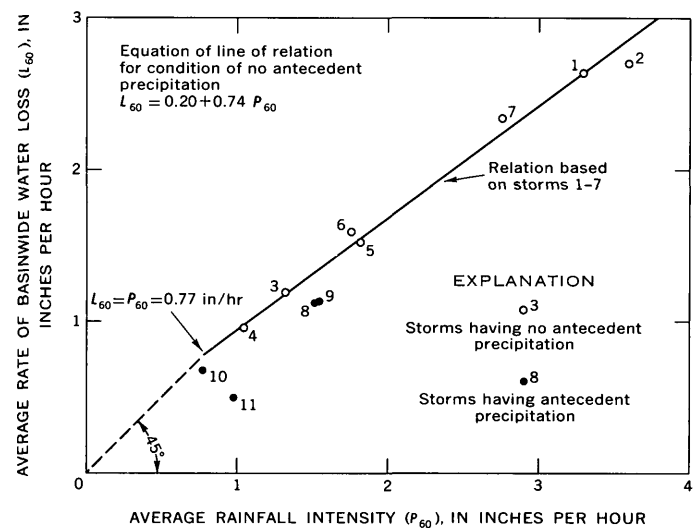


Figure 1.—Relation of average rate of basinwide water loss to average rainfall intensity for individual storms.

The direct relation (fig. 1) between average rate of water loss and average rainfall intensity is roughly consistent with the Horton infiltration theory for storms of short duration, as is the inverse relation (table 1) between average water-loss rate and storm duration. (The term “short duration” in the preceding sentence refers to durations that are too short to permit infiltration rates to reduce to their final equilibrium value.) However, as mentioned earlier, we had obtained unsatisfactory runoff results when we applied the Horton concept of a time-dependent infiltration rate to the entire watershed. It was, therefore, necessary to find some other interpretation of the line of relation in figure 1.

The equation of that relation suggests that only a part of the watershed is contributing runoff. The reasoning behind the premise of noncontributing area is as follows: The equation shown in figure 1 is

$$L_{60} = 0.20 + 0.74 P_{60} \quad (1)$$

where

L_{60} = average water-loss rate, in inches per hour, and

P_{60} = average rainfall intensity, in inches per hour. If we solve for average runoff rate in inches per hour (R_{60}), by use of the equation $R_{60} = P_{60} - L_{60}$, then

$$R_{60} = 0.26 P_{60} - 0.20, \text{ or} \quad (2)$$

$$R_{60} = 0.26 (P_{60} - 0.77). \quad (3)$$

Simplistically, we can interpret equation 3 as meaning that 74 percent of the watershed is noncontributing because its infiltration capacity exceeds the precipitation intensities experienced; the remaining 26 percent of the watershed has an infiltration capacity (ϕ -index) of 0.77 inch per hour, and all precipitation in excess of 0.77 inch per hour runs off from that partial, or source, area. If we are concerned with rainfall and runoff in 5-minute time increments, as we will be, equation 3 transforms to

$$R_5 = 0.26 (P_5 - 0.064), \quad (4)$$

where the subscript "5" refers to 5 minutes. The water loss in 5 minutes, 0.064 inch, is obtained by dividing 0.77 inch per hour (from equation 3) by 12.

Equations 3 and 4, as we have implied, are simplisms; they cannot be used in a numerical analysis of the rainfall-runoff data. Aside from the fact that some theoretical considerations with regard to infiltration are ignored in the equations, there is a practical consideration that precludes their use. We will discuss the practical shortcoming first. Points labeled 1-7 in figure 1 do not depart significantly from the line of relation for water loss in that figure. However, it is with runoff, and not water loss, that our principal concern lies. Those small departures in water loss from the relation given in equation 1 are carried through unaltered in magnitude in the relation for runoff in equation 3. Furthermore, runoff is usually small with respect to corresponding water loss, as we see from a comparison of the values in columns 6 and 7 of table 1. Consequently, although the departures from the equations represent a small percentage of water loss, they represent a large percentage of the runoff. An added complication is the fact that rainfall during many of the individual 5-minute intervals was less than the ϕ -index value of 0.064 inch in 5 minutes given in equation 4; that had the effect of further weakening the simple linear relation of storm runoff to storm rainfall.

As we have mentioned, the theoretical considerations ignored in equations 3 and 4 refer to infiltration. Infiltration capacity, and therefore rate of water loss, is not time invariant during runoff-producing storms, as the equations indicate, particularly during the first half hour of rainfall. (All but three of the storms listed had durations of 40 minutes or less.) Infiltration capacity decreases rapidly with time in the early

part of a storm, and its initial value varies inversely with the initial wetness of the soil. Furthermore, during runoff-producing storms it is not necessarily the infiltration capacity (potential rate of water movement through the soil-air interface) that limits the rate of water loss throughout the storm. Commonly it is the thickness of a permeable upper layer of soil that is underlain by a less permeable layer, that becomes the limiting factor. In other words, infiltration capacity may be the limiting factor only until the permeable upper layer becomes saturated or nearly saturated, after which time it is the percolation rate through the interface of the two dissimilar soil layers that limits the rate of water loss.

We refer again to the study watershed. Figure 1 suggests that the source-area concept of storm runoff applies to the watershed of Queen Creek tributary. The consistency with which points 1-7 define the water-loss relation in figure 1 makes it unlikely that the existence of source areas can be attributed largely to the vagaries of desert rainfall with respect to areal distribution. However, uneven rainfall distribution may be a factor even in a watershed as small as our study basin. From inspection of figure 1 we also expect the size of our source area to be variable—events having antecedent rainfall (8-11) plot below the line of relation for events having no antecedent rainfall (1-7), indicating a greater contributing area under wet antecedent conditions than under dry conditions. We undoubtedly are dealing with a heterogeneous watershed, as most watersheds are, where infiltration capacity and thickness of permeable soil horizon vary areally. Furthermore, if the source area of storm runoff varies in size and location with storm magnitude and antecedent soil moisture, for each set of conditions there will be an individual relation between rainfall excess and runoff—for example, a single unit hydrograph will not be applicable for the entire range of source-area size.

How then do we analyze storm runoff for the watershed? The only hydrologic observations available are those obtained at and near the downstream end of the watershed—the stream-gaging station provides a record of runoff from the watershed; the recording rain gage provides a record of rainfall that may or may not be completely representative of basinwide precipitation. For each storm of differing characteristics we probably have differing values of size of source area, rate of water loss, and time relation of runoff to rainfall excess. We therefore must make some simplifying assumptions that will reduce the number of variables.

The following assumptions were made for the purpose of simplifying the rainfall-runoff analysis.

1. The rainfall catch at the precipitation station is representative of rainfall over the entire watershed:

2. Infiltration capacity, at all times and at all sites, exceeds the precipitation intensity until the permeable upper soil layer reaches saturation or near saturation. The percentage of watershed contributing runoff is therefore governed by the thickness and porosity of the permeable upper soil layer. By

adopting that assumption, percentage of contributing watershed becomes a function of the total rainfall received—that is, antecedent plus storm rainfall.

3. The rate of water loss for runoff-contributing areas is equivalent to the percolation rate through the soil interface underlying the permeable upper soil layer, and that rate is a single constant value for all sites in the watershed.

4. An average unit hydrograph is applicable for all storm conditions, despite differences in size of the runoff-contributing area. As indicated earlier, the use of an average unit hydrograph is theoretically incompatible with the source-area concept of runoff, but it is used here as an expedient. The damping effect of a watershed on fluctuations in the supply of effective rainfall (rainfall excess) commonly permits the application of a linear function (unit hydrograph) to a nonlinear system (the watershed).

COMPUTATION OF VOLUME OF STORM RUNOFF

Several rates of water loss were tested, the lowest value tried being 0.02 inch per 5 minutes. A constant loss rate of 0.04 inch per 5 minutes gave best results and was selected for use. Therefore, from each 5-minute increment of storm rainfall, a water loss of 0.04 inch was subtracted. The resulting values of rainfall excess were totaled for each storm and are tabulated under the heading "Gross rainfall excess" in column 2 of table 2. Column 4 of the table shows the storm index, or rainfall associated with each runoff event, storm index being the sum of antecedent rainfall and one-half the total storm rainfall. The use of only half the total storm rainfall is explained as follows: Under our assumption that percentage of runoff-contributing area increases with the rainfall received, the contributing area during a storm will increase as the storm progresses. At the

start of a runoff-producing storm the contributing area will be relatively small, its size being governed only by the quantity of antecedent rainfall (A). Near the end of the storm the contributing area will be larger, its size now being governed by the quantity of antecedent rainfall plus the total storm rainfall (S). If we assume that an index to the average size of area contributing runoff during the storm is the average of the rainfall quantities at the beginning and end of the storm, our

storm index becomes $\frac{(A) + (A + S)}{2}$, or $A + S/2$.

To obtain the percentage of the watershed contributing runoff in each storm, the values of observed basinwide runoff (column 5 of table 2) were divided by the values of gross rainfall excess (column 2). The resulting percentages are shown in column 6. The next step was to obtain a relation between storm index and percentage of contributing area; in figure 2 a curve of relation has been fitted to values from columns 4 and 6 of table 2.

Percentages of contributing area that correspond to the tabulated values of storm index were obtained from the curve and are shown in column 7 of table 2. Multiplication of those percentages by the corresponding values of gross rainfall excess in column 2 gave the values of computed basinwide rainfall excess (basinwide storm runoff) that are shown in column 8. A graphical comparison of observed and computed volumes of runoff (column 5 versus column 8) is given in figure 3. In view of the many simplifying assumptions that were made, it is not surprising that some of the plotted points depart widely from the 45-degree line of equality in figure 3.

The widest scatter in figure 3, as in figure 2, is shown by storms 2 and 9. The wide departure of storm 2 undoubtedly

Table 2.—Computation summary

Storm No.	Gross rainfall excess ¹ (inches)	Number of minutes of rainfall excess ²	Storm index ³ (inches)	Observed average basinwide runoff ⁴ (inches)	Percentage of watershed contributing runoff		Computed basinwide rainfall excess ⁶ (inches)	Peak discharge (cfs)	
					Derived from column 2 ⁵	From curve in fig. 2		Observed	Computed from unit hydrograph
(1)	(2)	(3)	(4)	(5)	(6)	(7)	(8)	(9)	(10)
1	0.94	20	0.55	0.22	23.4	23.4	0.220	126	115
2	.52	10	.30	.15	28.8	15.2	.079	88	47
3	.50	20	.38	.08	16.0	18.0	.090	42	49
4	.39	25	.35	.06	15.4	17.0	.066	40	32
5	.68	25	.46	.15	22.1	20.7	.141	70	73
6	.43	20	.30	.06	14.0	15.2	.065	26	36
7	.38	10	.23	.07	18.4	12.6	.048	38	27
8	.86	45	1.19	.33	38.4	40.5	.348	137	129
9	.44	15	2.62	.17	38.6	66.3	.292	84	162
10	.40	45	.67	.11	27.5	27.0	.108	40	39
11	1.54	60	2.32	.98	63.6	61.5	.947	278	290

¹ Sum of rainfall quantities recorded in 5-minute increments, after first excluding increments having rainfall that did not exceed 0.04 inch, and then subtracting a loss of 0.04 inch from each remaining increment of rainfall.

² Sum of 5-minute time increments during each of which storm rainfall exceeded 0.04 inch.

³ Sum of antecedent rainfall (column 3 of table 1) and one-half of total storm rainfall (column 5 of table 1).

⁴ From column 6 of table 1.

⁵ (Column 5 ÷ column 2) × 100.

⁶ Column 7 × column 2.

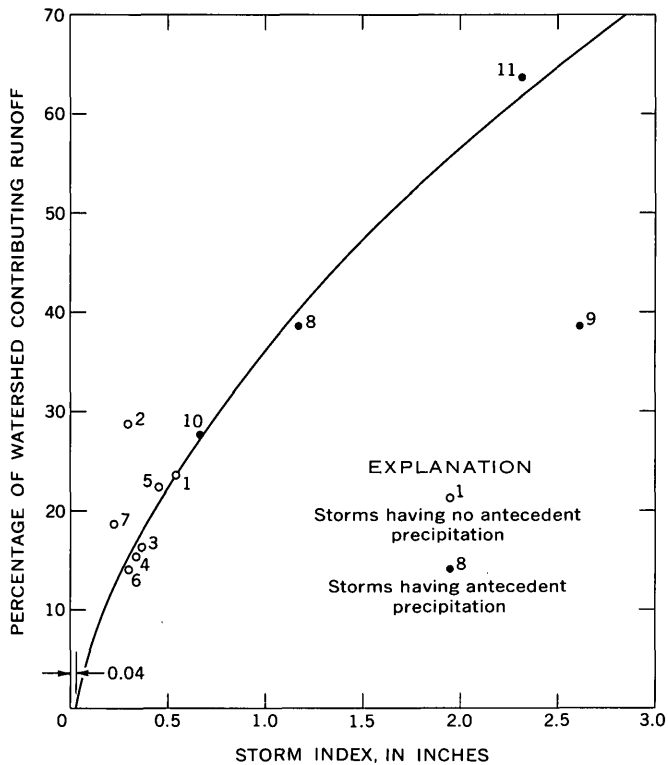


Figure 2.—Relation of percentage of watershed contributing runoff to storm index.

results from our simplifying assumption that the infiltration capacity at all sites and at all times exceeds precipitation intensity, and that, therefore, the percentage of contributing area is independent of infiltration capacity. That assumption apparently creates no serious problems except when we have an exceedingly intense storm of such short duration that the total storm rainfall is relatively small, as, for example, in storm 2, where the total storm rainfall was 0.60 inch, but 0.55 inch occurred in the first 5 minutes. Under those circumstances we expect the rainfall intensity during the first 5 minutes to exceed the infiltration capacity over a relatively large area, all of which will tend to contribute runoff. That fact is not reflected in the graph in figure 2, where the relatively small value of total rainfall indicates a small contributing area. Consequently, the use of figure 2 causes us to underestimate the total runoff of storm 2, which in turn will cause us to later underestimate its peak discharge.

We are at a loss to explain the wide departure of storm 9 in figures 2 and 3. It is possible, of course, that the storm rainfall in the vicinity of the rain gage was much heavier than that which occurred over most of the watershed. If that were true, our use of an erroneously large value of rainfall for storm 9 would explain the discrepancy. However, one derives little satisfaction from the supposition of nonrepresentative data. The excessively large computed value of total runoff for storm 9 will cause us to later overestimate its peak discharge.

COMPUTATION OF PEAK DISCHARGE

The first step in computing peak discharge was to obtain values of basinwide rainfall excess for each 5-minute increment of storm rainfall. We previously had subtracted 0.04 inch of rainfall loss from each increment in computing what we had termed "gross rainfall excess." We now multiply each 5-minute increment of gross rainfall excess by the percentage of contributing area for the particular storm, as given in column 7 of table 2. For example, all increments of gross rainfall excess in storm 1 were multiplied by 0.234, those in storm 2 were multiplied by 0.152, and so on. It was realized that for consistency with our assumption that the percentage of contributing area increases with storm index, we should have used a variable percentage of contributing area during each storm. In other words, each 5-minute increment of rainfall actually had an antecedent rainfall that exceeded that of the preceding increment by an amount equal to the rainfall in that preceding 5-minute increment. Therefore, as the storm progressed, the contributing, or source, area should have been increased in size. However, such refinement was considered unwarranted in view of the many other simplifications that had been introduced into the analysis, and a single value for percentage of contributing area was used for each storm.

The final step in the computation of peak discharge was to apply a unit hydrograph to the 5-minute increments of basinwide rainfall excess. We had decided earlier that an average unit hydrograph would be considered applicable for all

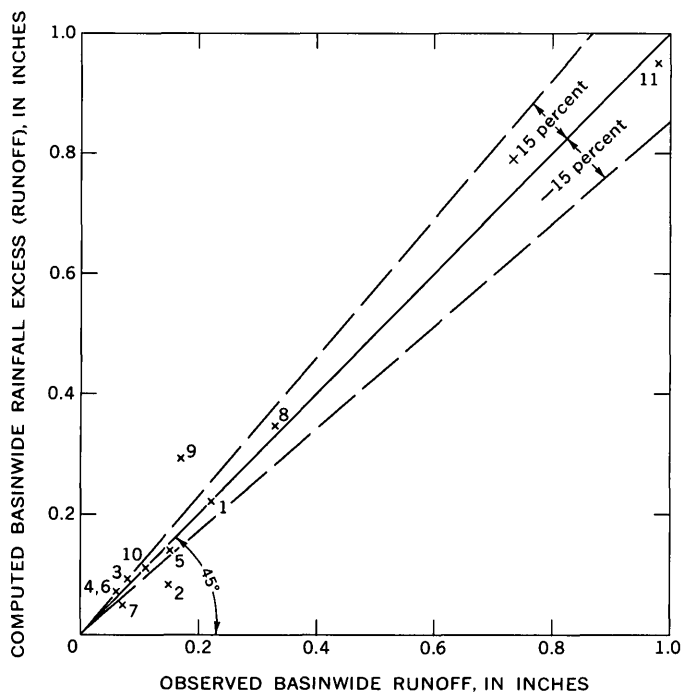


Figure 3.—Comparison of observed and computed basinwide storm runoff for all 11 storms.

storm conditions despite differences in the size of the runoff-contributing area. The ordinates of the 5-minute unit hydrograph used are given in table 3. Figure 4 shows, as an

Table 3.—Ordinates of 5-minute unit hydrograph

Time (5-minute increments)	Discharge (cfs)	Time (5-minute increments)	Discharge (cfs)
0	0	9	280
1	120	10	200
2	240	11	130
3	360	12	80
4	480	13	40
5	600	14	17
6	520	15	5
7	440	16	0
8	360		

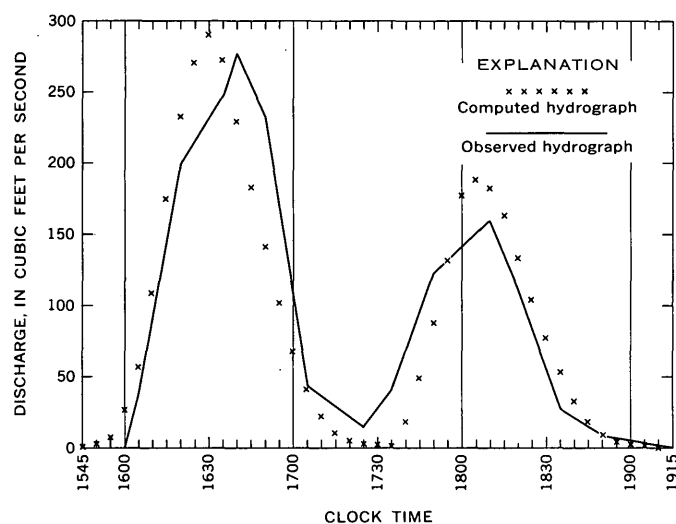


Figure 4.—Comparison of observed and computed discharge hydrographs for storm of September 30, 1971.

example, a comparison of observed and computed discharge hydrographs for the compound storm of September 30, 1971. In columns 9 and 10 of table 2, the observed and computed peak discharges for each storm are given, and figure 5 is a graphical comparison of those values.

Again, it is not surprising that some of the plotted points depart widely from the 45-degree line of equality in figure 5, in view of the many simplifying assumptions that were made, including that of uniform rainfall over the entire watershed in the amount indicated by the rain gage near the downstream end of the basin. The wide departures of computed peak discharges for storms 2 and 9 result from our failure to compute the total volume of runoff for those storms with acceptable accuracy, as explained in the preceding section of this paper.

A comparison of computed and observed time of peak discharge showed no bias in computed times. For some storms, the computed time of peak discharge was earlier than the

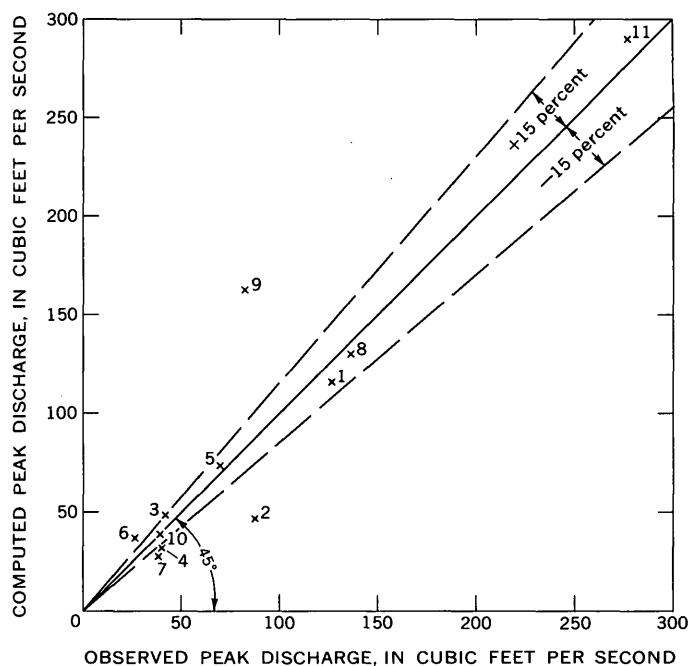


Figure 5.—Comparison of observed and computed peak discharge for all 11 storms.

observed time of peak, and for other storms the reverse was true. It was also evident from our tabulations of 5-minute increments of observed rainfall and runoff that for two storms the time synchronization of the rainfall and streamflow recording gages was poor.

SUMMARY

The relation in figure 1 of average rate of water loss to average rate of storm rainfall suggests that the concept of source areas of storm runoff is applicable to the watershed of Queen Creek tributary in south-central Arizona. The quantitative demonstration of the applicability of that concept was moderately successful, although marred by the necessity to make several simplifying assumptions to eliminate some of the many basin variables of unknown magnitude.

REFERENCES CITED

Dunne, Thomas, and Black, R. D., 1970, Partial area contributions to storm runoff in a small New England watershed: *Water Resources Research*, v. 6, no. 5, p. 1296-1311.
 Hewlett, J. D., and Hibbert, A. R., 1967, Factors affecting the response of small watersheds to precipitation in humid areas, in *International Symposium on Forest Hydrology*: New York, Pergamon Press, p. 275-290.
 Linsley, R. K., Kohler, M. A., and Paulhus, J. L. H., 1958, *Hydrology for engineers*: New York, McGraw-Hill Book Co., 340 p.
 Ragan, R. M., 1967, An experimental investigation of partial area contributions: *Internat. Assoc. Sci. Hydrology, Berne Symposium, Pub. 76*, p. 241-251 [1958].
 Whipkey, R. Z., 1965, Subsurface stormflow from forested slopes: *Internat. Assoc. Sci. Hydrology Bull.*, v. 10, no. 2, p. 74-85.



TESTS OF RHODAMINE WT DYE FOR TOXICITY TO OYSTERS AND FISH

By GARALD G. PARKER, JR., Tacoma, Wash.

Prepared in cooperation with the Lummi Indian Tribal Council

Abstract.—Because of the toxicity to oyster larvae and eggs of rhodamine B dye in concentrations greater than 1 mg/l in earlier tests, there was a concern that rhodamine WT, a similar tracer dye, would have a detrimental effect on marine life being developed under the aquaculture program of the Lummi Indian Tribe near Bellingham, Wash. Tests showed that 48-hour exposures at 24°C of 11,000 oyster eggs per liter and 6,000 12-day-old larvae per liter, in sea water with concentrations of rhodamine WT ranging from 1 µg/l to 10 mg/l, resulted in development of the eggs to normal straight-hinge larvae and no abnormalities in the larvae development. Tests made on the smolt of both silver salmon and Donaldson trout, with the fish held for 17.5 hours in a tankfull of sea water with a dye concentration of 10 mg/l at 22°C showed no mortalities or respiratory problems. With the concentration increased to 375 mg/l, and the time extended an additional 3.2 hours, still no mortalities or abnormalities were noted. The fish remained healthy in dye-free water when last checked a month after the test.

The Lummi Indian Tribe near Bellingham, Wash., is engaged in an aquaculture program that includes the propagation and sale of silver salmon, Donaldson and steelhead trout, and oysters. In cooperation with the Lummi Indian Tribal Council, the U.S. Geological Survey is conducting an evaluation of the water resources of the Lummi Indian Reservation, and part of this program required the use of rhodamine WT dye as a tracer in both the fresh- and salt-water environments.

Earlier tests using rhodamine B (Panciera, 1967) have shown that dye in concentrations greater than 1 mg/l is deleterious to oyster larvae and eggs. Marie Panciera, at the U.S. Bureau of Commercial Fisheries Biological Laboratory, Milford, Conn., found that eggs of *Crassostrea virginica* exposed to 100 mg/l dye concentrations for 48 hours did not develop and larvae that were exposed died within 2 days. In dye concentrations of 10 mg/l there was some development to the straight-hinge stage, but 27 percent of the individuals were abnormal. Development in concentrations of 1 mg/l or lower was comparable to that in control cultures.

Because of the similarity of rhodamine B to rhodamine WT, and the possibility that dye concentrations as high as 1 mg/l might reach some of the oysters and fish in the 750-acre aquaculture pond, tests were made of the effects of rhodamine WT dye on this marine life.

In cooperation with Dr. Wallace Heath, technical director of the Lummi Indian aquaculture program, and Richard L. Poole, director of oyster research, the eggs and 12-day-old larvae of the Pacific oyster (*Crassostrea gigas*) were exposed for 48 hours in water at 24°C with rhodamine WT dye concentrations that ranged from 1 µg/l to 10 mg/l. All the water used was taken from the 750-acre aquaculture pond which receives marine water directly from the Strait of Georgia. The average concentration of the eggs tested was 11,000 per liter, and the average concentration of the larvae was 6,000 per liter. The results of all the tests were comparable to those of the control cultures. All eggs tested developed to straight-hinge larvae with no abnormalities, and all the 12-day-old larvae survived with no abnormalities.

An additional test was made on smolt (4–6 inches long) of both silver salmon and Donaldson trout. Eight salmon and eight trout were held in a tank of water from the aquaculture pond with a concentration of 10 mg/l of rhodamine WT dye. The fish were held in this tank for 17.5 hours with water at 22°C. No mortalities or respiratory problems were noted, and the fish appeared similar in behavior to those in the control tank. The dye concentration in the test tank was then increased to 375 mg/l for an additional 3.2 hours. Again, no mortalities or other problems were observed. The fish tested remained healthy in dye-free water when last checked approximately 1 month after the test.

REFERENCE CITED

- Panciera, Maria, 1967, The toxicity of rhodamine-B to eggs and larvae of *Crassostrea virginica*: Natl. Shellfisheries Assoc. Proc., v. 58, p. 7–8.



RECENT PUBLICATIONS OF THE U.S. GEOLOGICAL SURVEY

(Books may be ordered from the Superintendent of Documents, Government Printing Office, Washington, D.C., 20402, to whom remittances should be sent by check or money order. Give title, series No., stock No. (shown in parentheses in this list), and catalog No. [shown in brackets])

Professional Papers

- 313-F. Geology and phosphate deposits of the Permian rocks in central western Montana, by R. W. Swanson. 1973. p. 779–833; plates in pocket. \$2.35. (2401-2201) [I 19:16:313-F]
- 386-D. Disposal of uranium-mill effluent by well injection in the Grants area, Valencia County, N. Mex., by S. W. West. 1972 (1973). p. D1–D28; plates in pocket. \$1.55. (2401-2160) [I 19:16:386-D]
- 486-J. Geohydrology of the Needles area, Arizona, California, and Nevada, by D. G. Metzger and O. J. Loeltz. 1973. p. J1–J54; plates in pocket. \$1.75. (2401-02212) [I 19:16:486-J]
- 646-C. Gravity, magnetics, and geology of the San Andreas fault area near Cholame, Calif., by W. F. Hanna, S. H. Burch, and T. W. Dibblee, Jr. 1972 (1973). p. C1–C29; plates in pocket. \$3.05. (2401-2170) [I 19:16:646-C]
- 663-B. Structural geology of the Sun River Canyon and adjacent areas, northwestern Montana, by M. R. Mudge. 1972 (1973). p. B1–B52; plates in pocket. \$4. (2401-2080) [I 19:16:663-B]
675. Landslides in the vicinity of the Fort Randall Reservoir, S. Dak., by C. F. Erskine. 1973. 64 p.; plates in pocket. \$3.75. (2401-2200) [I 19:16:675]
740. Paleozoic and Precambrian rocks of Alaska and their role in its structural evolution, by Michael Churkin, Jr. 1973. 64 p. 90¢. (2401-00272) [I 19:16:740]
- 743-B. Stratigraphic distribution of significant Eocene palynomorphs of the Mississippi embayment, by R. H. Tschudy. 1973. p. B1–B24; 4 plates showing fossils. 75¢. (2401-00271) [I 19:16:743-B]
- 754-A. Glacial and postglacial geologic history of Isle Royale National Park, Mich., by N. K. Huber. 1973. p. A1–A15; plate in pocket. \$1. (2401-02209) [I 19:16:754-A]
- 754-B. The Copper Harbor Conglomerate (middle Keweenaw) on Isle Royale, Mich., and its regional implications, by R. G. Wolff and N. K. Huber. 1973. p. B1–B15; plate in pocket. 95¢. (2401-00289) [I 19:16:754-B]
- 759-A. High-resolution seismic survey of an offshore area near Nome, Alaska, by A. R. Tagg and H. G. Greene. 1973. p. A1–A23. 60¢. (2401-00288) [I 19:16:759-A]
765. Geology of the oxidized uranium ore deposits of the Tordilla Hill-Deweeseville area, Karnes County, Tex.; A study of a district before mining, by C. M. Bunker and J. A. MacKallor. 1973. 37 p.; plate in pocket. \$1.25. (2401-00292) [I 19:16:765]
- 774-A. Reconnaissance geology of the northern Yukon-Koyukuk province, Alaska, by W. W. Patton, Jr. 1973. p. A1–A17. 40¢. (2401-00299) [I 19:16:774-A]
789. Geochemistry of lower Eocene sandstones in the Rocky Mountain region, by J. D. Vine and E. B. Tourtelot, *with a section on Direct-reader spectrometric analyses*, by R. G. Havens and A. T. Myers. 1973. 36 p. 75¢. (2401-00275) [I 19:16:789]
- 1258-E. A new method for the determination of three-dimensional deformation anisotropy in rock specimens, by R. A. Farrow. 1973. p. E1–E12. 25¢. (2401-00269) [I 19:13:1258-E]
1265. Ancient lavas in Shenandoah National Park near Luray, Va., by J. C. Reed, Jr. 1969. 43 p.; plate in pocket. \$1.25. (Reprinted 1973).
- 1332-A. A preliminary report on the geology and gold deposits of the Rochford district, Black Hills, S. Dak., by R. W. Bayley. 1972 (1973). p. A1–A24; plates in pocket. \$2. (2401-2173) [I 19:3:1332-A]
1346. Bedrock geology of the Cupsuptic and Arnold Pond quadrangles, west-central Maine, by D. S. Harwood. 1973. 90 p.; plates in pocket. \$2.60. (2401-02205) [I 19:3:1346]
1349. General geology of the Hahns Peak and Farwell Mountain quadrangles, Routt County, Colo., by Kenneth Segerstrom and E. J. Young, *with a discussion of Upper Triassic and pre-Morrison Jurassic rocks*, by G. N. Pippingos. 1972 (1973). 63 p.; plate in pocket. \$1.25. (2401-2172) [I 19:3:1349]
1351. Geology and description of the thorium-bearing veins, Lemhi Pass quadrangle, Idaho and Montana, by M. H. Staatz. 1972 (1973). 94 p., plate in pocket. \$3.75. (2401-02207) [I 19:3:1351]
1357. Placer gold deposits of Utah, by M. G. Johnson. 1973. 26 p.; plate in pocket. \$1.25. (2401-00264) [I 19:3:1357]
1361. An integrated system of geologic mapping and geochemical sampling by light aircraft, by C. L. Sainsbury, K. J. Curry, and J. C. Hamilton. 1973. 28 p.; plates in pocket. 90¢. (2401-00265) [I 19:3:1361]
1369. Stratigraphy of the Washakie Formation in the Washakie Basin, Wyo., by H. W. Roehler. 1973. 40 p.; plates in pocket. 90¢. (2401-00286) [I 19:3:1369]
1371. Studies related to wilderness—primitive areas, 1972. Title page and contents for volume (published as separate chapters A–C). Free on application to the Geological Survey.
- 1372-D. The McHugh Complex of south-central Alaska, by S. H. B. Clark. 1973. p. D1–D10. 20¢. (2401-00273) [I 19:3:1372-D]
- 1372-G. The Lower Cretaceous Figuera Lava and Fajardo Formation in the stratigraphy of northeastern Puerto Rico, by R. P. Briggs. p. G1–G10. 20¢. (2401-00319) [I 19:3:1372-G]
1378. Geochemical prospecting using water from small streams in central South Carolina, by Henry Bell, III, and G. E. Siple. 1973. 26 p.; plates in pocket. \$1.15. (2401-00313) [I 19:3:1378]
1379. Radiometric ages of igneous rocks from Pima, Santa Cruz, and Cochise Counties, southeastern Arizona, by R. F. Marvin, T. W. Stern, S. C. Creasey, and H. H. Mehnert. 1973. 27 p. 35¢. (2401-00283) [I 19:3:1379]
- 1383-A. Pine Creek volcanic assemblage at Mount St. Helens, Wash., by D. R. Crandell and D. R. Mullineaux. 1973. p. A1–A23. 40¢. (Geology of Mount St. Helens volcano, Washington.) (2401-00318) [I 19:3:1383-A]

Water-Supply Papers

- 1827-E. Chemical interactions of aluminum with aqueous silica at 25°C, by J. D. Hem, C. E. Roberson, C. J. Lind, and W. L. Polzer. 1973. p. E1–E57. 70¢. (2401-00229) [I 19:13:1827-E]
1998. Water resources of Hempstead, Lafayette, Little River, Miller, and Nevada Counties, Ark., by A. H. Ludwig. 1972 (1973). 41 p.; text and plates in case. \$4. (2401-00215) [I 19:13:1998]
- 2009-C. Chemical quality of surface water in the Flaming Gorge Reservoir area, Wyoming and Utah, by R. J. Madison and K. M. Waddell. 1973. p. C1–C18; plate in pocket. 65¢. (2401-00266) [I 19:13:2009-C]
- 2009-D. Appraisal of ground water for irrigation in the Little Falls area, Morrison County, Minn., by J. O. Helgesen. 1973. p. D1–D40; plate in pocket. \$1.25. (2401-00270) [I 19:13:2009-D]

**U.S. GOVERNMENT
PRINTING OFFICE**
PUBLIC DOCUMENTS DEPARTMENT
WASHINGTON, D.C. 20402
OFFICIAL BUSINESS
PENALTY FOR PRIVATE USE \$300

POSTAGE AND FEES PAID
**U.S. GOVERNMENT
PRINTING OFFICE**
375

